Electron energy-loss spectroscopy: DFT modelling and application to experiment

Che Royce Seabourne

Submitted in accordance with the requirements for the degree of Doctor of Philosophy

The University of Leeds

School of Process, Environmental and Materials Engineering

September 2010

The candidate confirms that the work submitted is his own, except where work which has formed part of jointly-authored publications has been included. The contribution of the candidate and the other authors to this work has been explicitly indicated overleaf. The candidate confirms that appropriate credit has been given within the thesis where reference has been made to the work of others.

Acknowledgements

Chapters 5, 7 and 8 have been at least partially based on work from jointly-authored publications (included in an appendix in Chapter 11).

Chapter 5 incorporates work from the following peer-reviewed publications:

C.R. Seabourne, A.J. Scott, R. Brydson, R.J. Nicholls. A systematic approach to choosing parameters for modelling fine structure in electron energy-loss spectroscopy. Ultramicroscopy 109 (2009) 1374.

C.R. Seabourne, A.J. Scott, G. Vaughan, R. Brydson, R.J. Nicholls. The effect of the core-hole on predicted EELS K edges in aluminium metal, alpha-alumina and wurtzite aluminium nitride. Phys. Rev. B, to be submitted after revisions and completions.

For the first of these papers, I was responsible for the overwhelming majority of the work, supervised by Dr. Andrew Scott and Prof. Rik Brydson. Assistance in some aspects of interpretation of experimental work and core-hole effects was received from the following authors; A.J. Scott, R. Brydson and R.J. Nicholls.

For the second paper I carried out all modelling work, supervised by Dr. Andrew Scott and Prof. Rik Brydson.

Gareth Vaughan acted as operator in the practical EELS experiments, though these were of my original design. Some assistance in the interpretation of those experimental results and core-hole effects was given by; A.J. Scott, R. Brydson and R.J. Nicholls.

Chapter 7 incorporates work from the following peer-reviewed publications:

C.R. Seabourne, A.J. Scott, R. Brydson, V. Harncharna, S.G. Wang, R.C. Ward, C. Wang, A. Kohn. Computational EELS modelling of magnesium oxide systems. J. Phys.: Conf. Ser. 241 (2010) 012063.

C.R. Seabourne, A.J. Scott, G. Vaughan, R. Brydson, S.G. Wang, R.C.C. Ward, C. Wang, A. Kohn, B. Mendis, A.K. Petford-Long. Analysis of computational EELS modelling results for MgO-based systems. Ultramicroscopy 110 (2010) 1059.

For these papers, I was responsible for all modelling studies using the CASTEP code, and selected interpretation of experimental results, supervised by Dr. Andrew Scott and Prof. Rik Brydson.

The experimental EELS work was coordinated and performed by the following authors; C. Wang, A. Kohn, G. Vaughan, B. Mendis and A.K. Petford-Long. Synthesis of materials was carried out by the following authors; S.G. Wang and R.C.C. Ward. Advice on the structural properties of interfaces was given by V. Harncharna.

Chapter 8 incorporates work from the following peer-reviewed publications:

C.R. Seabourne, I.M. Ross, W.M. Rainforth, A.J. Scott, B.G. Mendis, P. Eh. Hovespian. EELS and ELNES studies of nano-scale nitride multilayers deposited by unbalanced magnetron sputtering. J. Phys.: Conf. Ser. 241 (2010) 012046.

I.M. Ross, W.M. Rainforth, C.R. Seabourne, A.J. Scott, P. Wang, B.G. Mendis, A.L. Bleloch, C. Reinhard and P.Eh. Hovsepian. Nano-scale electron energy loss spectroscopy of CrAlYN/CrN – CrAlY(O)N/Cr(O)N multilayer coatings deposited by unbalanced magnetron sputtering. Thin Solid Films 518 (2010) 5121.

For these papers, I was responsible for all modelling studies using the Wien2k code, and relevant interpretation of experimental results, supervised by Dr. Andrew Scott. The experimental EELS studies were carried out and coordinated by the following authors; I.M. Ross, W.M. Rainforth, W. Peng, A. Bleloch and B.G. Mendis. Synthesis of materials was carried out by P.Eh. Hovespian and C. Reinhard.

On a personal note, I would like to thank my supervisors Dr. Andrew Scott and Prof. Rik Brydson for their support over the past three years. They have patiently and skilfully guided me both academically and personally. Andrew, your pastoral care has been invaluable and meant a great deal to me. Working with Rik has been a privilege, from paper writing to journeying across Europe by train! Thanks to everyone in SPEME and IMR who has advised me in even the slightest way. In particular, thanks to our *de facto* EELS group; Andy Brown, Gareth Vaughan, V, Rozita and Nicole. Also Bilton and Rachel, you can have a mention too! Raul and Maria – I will never forget your Spanish humour in the Rockies. I acknowledge the Board of Graduate Studies for their flexibility in transferring my funding to SPEME, and thank the Frank Parkinson Scholarship managers for their support. My gratitude also to Jason Lander and the NGS, Alan Real and Mark Dixon of the Leeds HPC team, and Chris Armstrong of NAG / HECToR.

To my family and friends – thank you so much for supporting me through my work, especially the Philps, the Wrights, the Petries and other St George's friends, the Coles, the Seawards, the two Janets, Coopers, Trevor and company. My love, affection and gratitude to all of you.

I dedicate this work to the memories of Royce Seabourne, Barry Cooper and Larry Seaward. You are missed, and loved always.

Che Seabourne, Leeds, 2010. Deus vobiscum.

Abstract

The all-electron density functional theory (DFT) code Wien2k has an established track record of modelling energy-loss near-edge structure (ELNES). The pseudopotential DFT code CASTEP can reproduce results found using Wien2k. A methodology was developed for DFT code parameter selection, based on converging parameters to the ELNES prediction. Various aluminium systems were studied; aluminium, aluminium nitride and aluminium oxide. Uniquely for aluminium metal, a ground state calculation provided strong agreement with experiment, as the core-hole is well screened. It was quantitatively demonstrated that the core-hole causes ionisation edge peaks to shift towards the Fermi level, and increases the intensity of those peaks - effects found to be larger for the cationic species. Group 4 and 5 transition metal carbides were modelled using CASTEP. Systems with vacancies were considered; $TiC_{0.79}$, $TiC_{0.58}N_{0.30}$, $TiC_{0.45}N_{0.43}$, $TiC_{0.19}N_{0.65}$ and $TiN_{0.82}$. By comparison with experimental data, structures for these systems were proposed. CASTEP was used to model oxygen K edges in various systems. For bulk MgO, acceptable experimental agreement was found using a ground state calculation. This was rationalised by observing that the introduction of a core-hole had relatively little effect on the *p* orbital DOS prediction for oxygen. For the interface of Fe (001) / MgO (001), it was demonstrated by careful comparison of theory and experiment that some degree of oxidation was present. Nanoscale analysis of multilayered CrAlYN/CrN coatings was performed. Experimentally observed ELNES was reproduced using ground state Wien2k calculations. Combined experimental and theoretical analysis indicated that the nominal CrN layers were close to stoichiometric CrN, the Cr/N ratio being 1.05 ± 0.1. For the CrAlYN layers, the theoretical system showing the best agreement was $Cr_{0.5}Al_{0.5}N$. This thesis has established methodologies for utilising DFT codes, illustrating how links between experimental and theoretical ELNES can be used in the nanoscale characterisation of technologically important materials.

Table of contents

1 Introduction

2 Electron energy-loss spectroscopy (EELS) in the (S)TEM

3 Computational EELS modelling

4 Initial modelling studies and experiments

5 The core-hole effect - a series of aluminium compounds

6 Detailed study of transition metal carbides

7 Studies of magnesium oxide systems

8 CrAlYN/CrN multilayer coatings

9 Future directions and conclusions

11 Appendices

List of abbreviations

ADF	Annular dark field
BCC	Body-centred cubic
BF	Bright field
BFGS	Broyden-Fletcher–Goldfarb–Shanno

BSE	Bethe-Salpeter equation
CASTEP	CAmbridge Serial Total Energy Package
CCD	Charge-coupled device
CEMES	Centre d'Elaboration de Matériaux et d'Etudes Structurales
DDSCS	Double differential scattering cross section
DFT	Density functional theory
DOS	Density of states
EDGE	Enhanced data generated by electrons
EELS	Electron energy-loss spectroscopy
ELNES	Energy-loss near-edge structure
EXELFS	Extended energy-loss fine structure
FCC	Face-centred cubic
FEG	Field emission gun
FEM	Free-electron metal
FWHM	Full-width half maximum
GGA	Generalized gradient approximation
HAADF	High-Angle Annular Dark Field
HREM	High Resolution Electron Microscopy
IR	Infra-red
KKR	Korringa, Kohn and Rostoker
LAPW	Linear augmented plane wave
LDA	Local density approximation
MBE	Molecular beam epitaxy
MLLS	Multiple linear least squares
MS	Multiple scattering
MTJ	Magnetic tunnel junction

MVSA	Multi-variate statistical analysis
NGS	National Grid Service
ONETEP	Order-N Electronic Total Energy Package
OP	Overlap population
OTF	On-the-fly
PAW	Projector augmented wave
PIPS	Precise Ion Polishing System
PVD	Physical vapour deposition
RAM	Random access memory
SCF	Self-consistent field
SIC	Self-interactions correction
(S)TEM	Scanning transmission electron microscopy
TM	Transition metal
TMR	Tunnelling magnetoresistance
UBM	Unbalanced magnetron sputtering
USP	Ultra-soft pseudopotential
UV	Ultra-violet
VCA	Virtual crystal approximation
VSM	Voltage scan module
XANES	X-ray Absorption Near Edge Structure
XC	EXchange correlational
ZLP	Zero-loss peak

List of figures

List of tables

Chapter 1

Introduction

1.1 Nanotechnology

Nanotechnology can reasonably be defined as the manipulation of matter on the atomic scale for technological advantage. Though the prefix ‘nano’ strictly means 10^{-9} m in scale, the term ‘nanotechnology’ is widely applied to somewhat larger systems.

At this scale, matter can display novel properties that tend to relate to the fact that the system is somewhere between a bulk solid and an atom or molecule. These properties typically arise due to quantum confinement effects and the high surface to bulk ratio of nanostructures which can lead to structural and electronic rearrangements in order to minimise total energy for the particular metastable nanoscale state (Buzea, 2007). Therefore, it is clear that in order to predict and understand these novel properties, there is a strong need for accurate understanding and characterisation of nanoscale systems, which is one of the ultimate aims of this thesis.

1.2 Nanoscale characterisation techniques

Concurrent with nanotechnology developments has been the refinement of techniques which can characterise the systems involved and influence their synthesis and further development. Table 1.1 summarises nanoscale characterisation techniques with relevant examples:

	X-ray analysis	Atomic force microscopy (AFM)	Scanning tunnelling microscope (STM)	Field ion microscope (FIM)	Transmission electron microscopy
Description	X-rays can be generated by a synchrotron and then fired at a sample. The electronic states can then be probed using X-ray absorption spectroscopy, or a diffraction map obtained.	Cantilever fine tip is scanned across the sample close to the surface, deflections of the tip due to various forces are then measured. The technique can therefore probe mechanical properties.	Small probe is brought close to a sample, electrons can tunnel between the surface and the tip, producing an electrical signal. In order for this signal to be constant, the tip is moved slightly, this movement indicating the 3D structure of the material. Also, scanning tunnelling spectroscopy is possible, local electronic structure information can be deduced, as the tunnelling current is a function of the local density of states.	Sharp tip placed into a high-vacuum, which is then backfilled with an imaging gas. The tip is then cooled to less than 100K. A positive voltage is applied to the tip, thus charging the imaging gas, which is repelled from the tip. A detector collects the repelled ions, the interaction of which with the sample is indicative of structure. Subsequently, 3D atom-probe tomography (3DAP) was developed. A recent review describes the usage of 3DAP to give information regarding sample composition as well as images (Seidman, 2007).	An electron beam is fired at an ultrathin sample, the scattering of that beam indicates structural properties. Energy losses in the transmitted beam can also be analysed as part of a form of spectroscopic analysis.
Spatial resolution	10-30nm (de Groot, 2009).	Sub-angstrom (Tortonese, 1993).	1Å / atomic (Renner, 1998).	1Å / atomic (Müller, 1970).	Sub-angstrom (Batson, 2002).
Sample information	Samples can be solid, liquid or gas.	Surface techniques, so can be several mm thick.		Thin wire, which is then fabricated to a fine tip.	Nanoparticulate, or ultrathin, less than 100nm.
Summary of information revealed	• Elements present in sample. • Bond order and coordination information.	• Mechanical properties. • 3D material structure. • Local structural information.		• Sample imaging. • Dynamic phenomena at the surface.	• Elements present in sample. • Ratio of elements present. • Bond order and coordination information.
Example	Zinc oxide nanostructured film deposition (Ingham, 2008).	Atomic resolution imaging of both graphite and boron nitride (Tortonese, 1993).	Determination of the structural properties of palladium clusters (Reetz, 1995).	Carbon concentration at a grain boundary in steels (Atrens, 2006).	Study of *Balanus amphitrite Amphitrite (Clare, 1994)*, characterisation of magnetic tunnel junctions (Wang, 2007).

Table 1.1: Summary of nanoscale characterisation techniques.

Electron microscopy (with excellent spatial resolution) forms the major focus of this thesis.

1.3 The electron microscope

The major focus of this thesis is on a form of spectroscopy (subsequently discussed) as part of the electron microscope. It was arguably Ruska and Knoll that developed the first prototype electron microscope in the 1930s, though a research group at the University of Toronto and the Siemens company were ultimately responsible for the first practically operable device (Ruska, 1943), (Hillier, 1946).

A description of the original device, the transmission electron microscope (TEM) forms the main part of Chapter 2, but an overview is given in this section. In the TEM, the electron beam itself is ultimately used to generate an image of the sample. An electron gun (the specifics of which are discussed in Chapter 2) fires electrons at the sample, the beam being focussed by a series of electromagnetic lenses. The electron beam is partially transmitted through the sample, and scattered. The scattered beam can be used to construct an image of the sample (principally via elastically scattered electrons), but also to carry out a form of spectroscopy discussed subsequently (using inelastically scattered electrons).

As can perhaps be deduced intuitively, firing a high energy electron beam at a sample has the potential to cause damage. Indeed, this is a major issue in electron microscopy. Indeed, a researcher outside the field might reasonably enquire as to the advantages of the technique as compared to photon-based methodologies, in particular X-ray absorption spectroscopy. Photon based techniques are certainly less likely to cause sample damage.

However, X-ray spectroscopy has a poorer spatial resolution than electron microscopy, spatial resolution being a major consideration when characterising nanomaterials. Being a photonic source, X-rays are hard to focus, whereas it is a much more straightforward process to focus a charged particle electron beam using electromagnetic lenses.

1.4 Electron spectroscopy

Thus far only the potential for imaging in the microscope has been discussed in any depth. However, the major focus of this work is electron spectroscopy. When the electron beam passes through the sample, it can excite electrons within the atoms of the sample, changing their energy levels. These transitions have fixed probabilities and energies, and can be indicative therefore of elemental composition. In electron spectroscopy, a spectrum of energy losses for the transmitted beam is collected, discussed at length in Chapter 2.

If the usefulness of electron energy-loss spectroscopy (EELS) was limited to elemental identification, this would be interesting, but unlikely to make electron microscopy at the heart of nanoscale materials characterisation. The particular elegance of electron spectroscopy is the link between electronic structure, and the structure of the material itself.

In the solid state, rather than being localised to individual atoms, electronic energy levels form a band structure dependent on bonding and coordination for the material in question. The fine structure in the electron energy-loss spectrum can be related to the electronic structure of the material, and therefore its structural properties.

Figure 1.1 is a graphical representation of the relationship between the electronic structure of a material and the electron energy-loss spectrum:

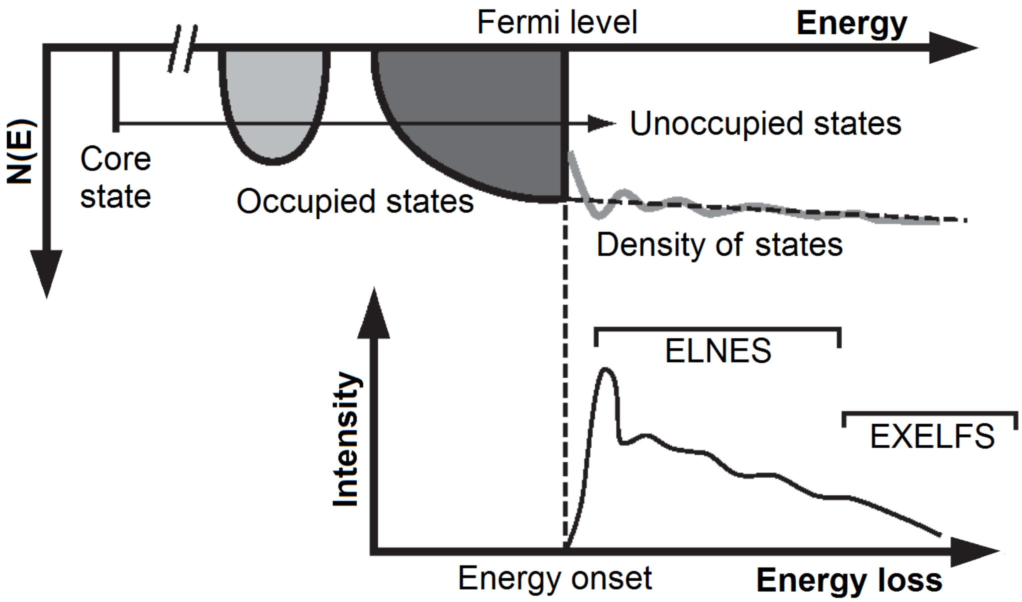

Figure 1.1: Illustration of the relationship between electronic structure and the EELS spectrum (Brydson, 2001).

As described above, a high energy electron beam can cause an electron within an atom of the sample can be promoted to an unoccupied state above the Fermi level. The nature of these unoccupied states is influenced by local bonding and structure. The unoccupied density of states (combined with transitional matrix elements) forms a major part of the core-loss region of the EELS spectrum (discussed in full in Chapter 2).

1.5 Computational modelling

The interpretation of EELS (in terms of fine structure especially) is however not straightforward. The main purpose of the work in thesis is to develop coherent methodologies for the computational modelling of electron spectroscopy, partially to assist in this endeavour.

The prediction of spectra from known models can be achieved using various methodologies discussed in Chapter 3 of the thesis, though the methodology used in this work is density functional theory (DFT).

Predicted EELS spectra can be used to assist in the assignment of experimental spectra (which is a major area of study in this work), but also modelling has the potential to influence experimental work, and be important in the characterisation of frontier nanomaterials.

1.6 Summary and research aims

This short chapter has briefly introduced various nanoscale characterisation techniques, the particular focus of this work being electron microscopy, and specifically EELS.

This thesis aims to achieve the following:

- Present an overview of condensed matter theory.
- Outline density functional theory and its application to EELS.
- Develop an understanding of high performance computing strategies.
- Devise coherent methodologies for modelling electron spectroscopy results, using density functional theory based codes.
- Evaluate the suitability of various codes for this purpose, and develop new styles of applying the codes.
- Demonstrate the capability of modelling to assist in the assignment of spectra obtained experimentally for nanoscale materials.
- Deduce structural properties of materials from modelling studies.
- Suggest characterisation approaches as a result of modelling.

The thesis work will therefore centre on the relationship between the electronic band structure of materials and the EELS spectrum.

In terms of structure, Chapters 2 and 3 respectively outline background information and relevant detail in terms of experimental electron spectroscopy and modelling thereof. Chapter 4 outlines more on the practical application of DFT codes to EELS modelling, and gives the results of initial tests.

Chapter 5 explores the impact of the core-hole in electron spectroscopy modelling by considering a number of aluminium compounds. Chapter 6 again begins with bulk modelling of group 4 and 5 transition metal carbides, but then considers if systems with vacancies can be successfully modelled.

Chapters 7 and 8 show the deduction of structural information for real materials by utilising a combination of experimental and theoretical electron spectroscopy. The materials studied are respectively magnetic tunnel junctions and nanoscale coatings.

Chapter 9 summarises the thesis work, and discusses the extent to which the original aims were met, as well as discussing possible future work.

Chapter 2

Electron energy-loss spectroscopy (EELS) in the (S)TEM

2.1 Introduction

Though the main body of this thesis discusses theoretical modelling of electron energy-loss spectroscopy, the consistent application of the results to experiment means it is important to present an appropriately detailed section on experimental EELS.

EELS can be considered to be a form of absorption spectroscopy utilising a transmission technique. An electron beam is fired through an thin sample (typically less than 100nm in thickness), and the energy loss of the transmitted electrons can be used to deduce materials properties such as local structure, coordination and bonding environments. The usage of an electron-based rather than photonic excitation source means a spatial resolution on the nanometre scale is possible (Egerton, 2005). Efficient characterisation of materials is essential in industry, making EELS an important technique in a wide range of fields. This chapter gives a brief overview of the EELS technique being used as part of the (S)TEM. In the standard TEM the EELS technique is analogous, but the optics of the microscope differ. In the case of the TEM there are post-specimen optics which direct the scattered electrons to the spectrometer, through the objective aperture, which is before the specimen in the (S)TEM.

Consider firstly the processes that can occur upon the interaction of the incident electron beam with the sample, summarised in Figure 2.1:

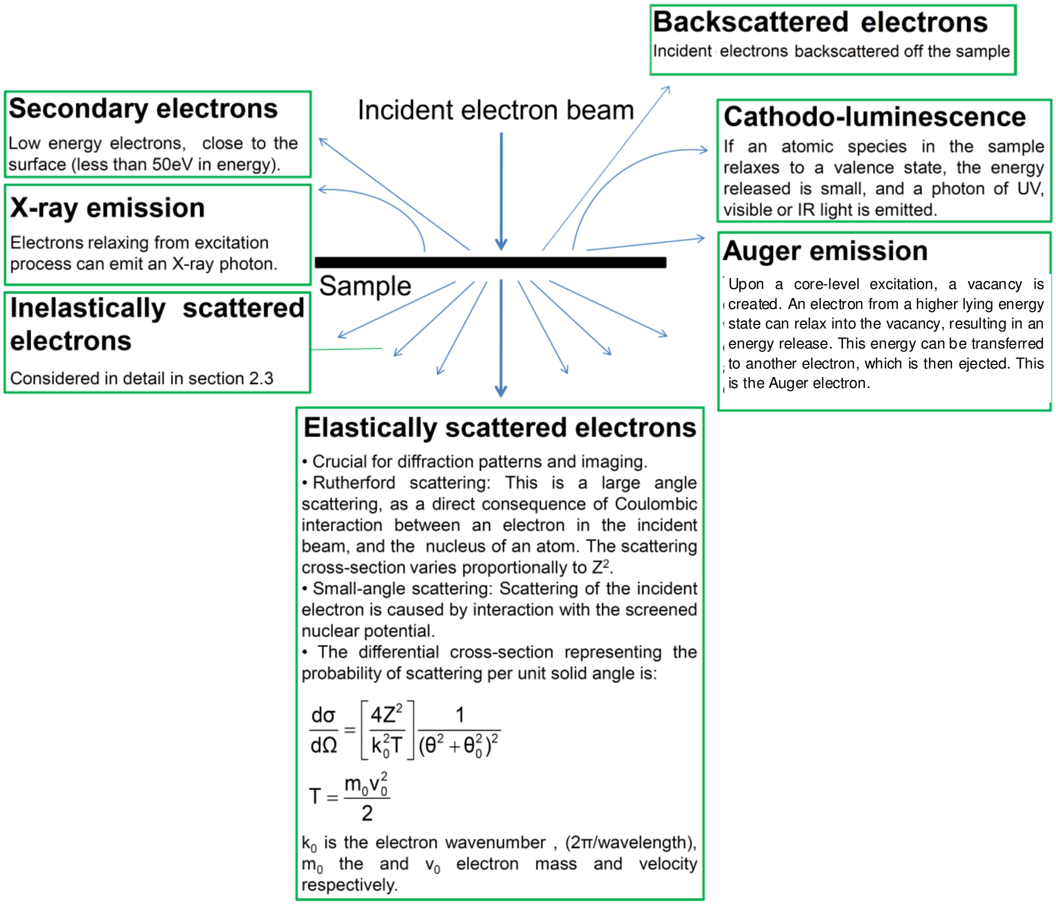

Backscattered electrons

Incident electrons backscattered off the sample

Secondary electrons

Low energy electrons, close to the surface (less than 50eV in energy).

Cathodo-luminescence

If an atomic species in the sample relaxes to a valence state, the energy released is small, and a photon of UV, visible or IR light is emitted.

X-ray emission

Electrons relaxing from excitation process can emit an X-ray photon.

Auger emission

Upon a core-level excitation, a vacancy is created. An electron from a higher lying energy state can relax into the vacancy, resulting in an energy release. This energy can be transferred to another electron, which is then ejected. This is the Auger electron.

Inelastically scattered electrons

Considered in detail in section 2.3

Elastically scattered electrons

- Crucial for diffraction patterns and imaging.
- Rutherford scattering: This is a large angle scattering, as a direct consequence of Coulombic interaction between an electron in the incident beam, and the nucleus of an atom. The scattering cross-section varies proportionally to Z^2.
- Small-angle scattering: Scattering of the incident electron is caused by interaction with the screened nuclear potential.
- The differential cross-section representing the probability of scattering per unit solid angle is:

$$\frac{d\sigma}{d\Omega} = \left[\frac{4Z^2}{k_0^2 T}\right] \frac{1}{(\theta^2 + \theta_0^2)^2}$$

$$T = \frac{m_0 v_0^2}{2}$$

k_0 is the electron wavenumber , (2π/wavelength), m_0 the and v_0 electron mass and velocity respectively.

Figure 2.1: Summary of interaction processes for the incident electron beam with the sample (Brydson, 2001), (Egerton, 1996), (Egerton, 2009).

Inelastic scattering events form the basis of the EELS process, as discussed at length in Section 2.3.

2.2 The experimental EELS method

EELS was pioneered by Hillier and Baker in 1944 (Hillier, 1943), (Hillier, 1944). At this point in the history of electron microscopy, an omission from the technique was the ability to establish elemental compositions. It was recognised that there was a strong possibility of measuring the energy losses of the exciting electron beam as it passes through a sample. A spectrum of electron energy losses can then be derived, which can reveal elemental compositions and structural information as is discussed subsequently.

For the purposes of high spatial resolution analysis of nanostructures, EELS is often used as part of the scanning TEM ((S)TEM), in which a focused probe scans in two-dimensions across the specimen. Fig. 2.2 adapts an existing schematic for the usage of EELS in the (S)TEM (Brydson, 2001). Other schematics are available in the literature (Liu, 2005), (Luo, 2006).

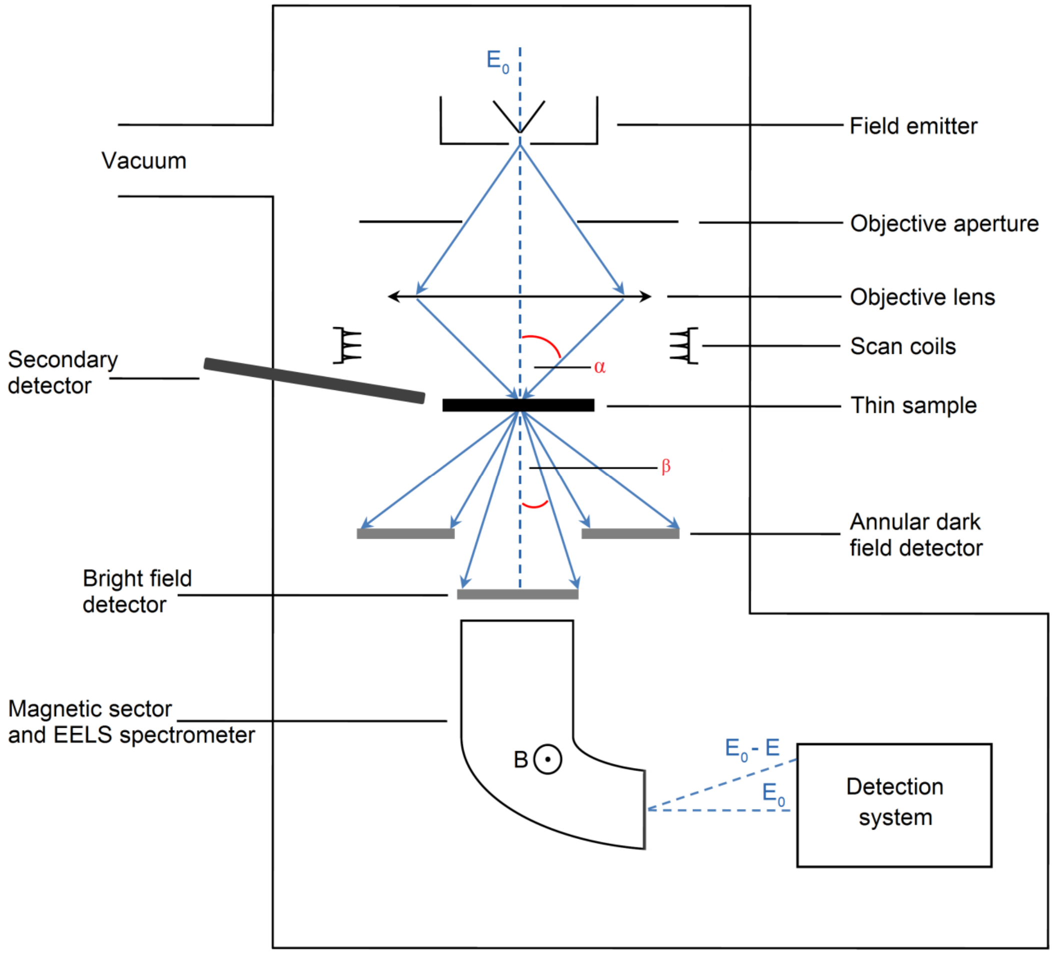

Figure 2.2: Schematic of EELS in the (S)TEM, with labelled components. α is the convergence semi-angle, and β the collection semi-angle (Brydson, 2001).

As Figure 2.2 illustrates, an electron beam is generated, accelerated towards the sample, and focussed using a series of lenses. Whilst passing through the sample, the electron beam is scattered elastically and inelastically, and the various scattered components enter the magnetic sector (B), in which velocity (and energy) analysis takes place. The magnetic sector is based on perpendicular electric and magnetic fields, shown in more detail in Figure 2.3 (Brydson, 2001).

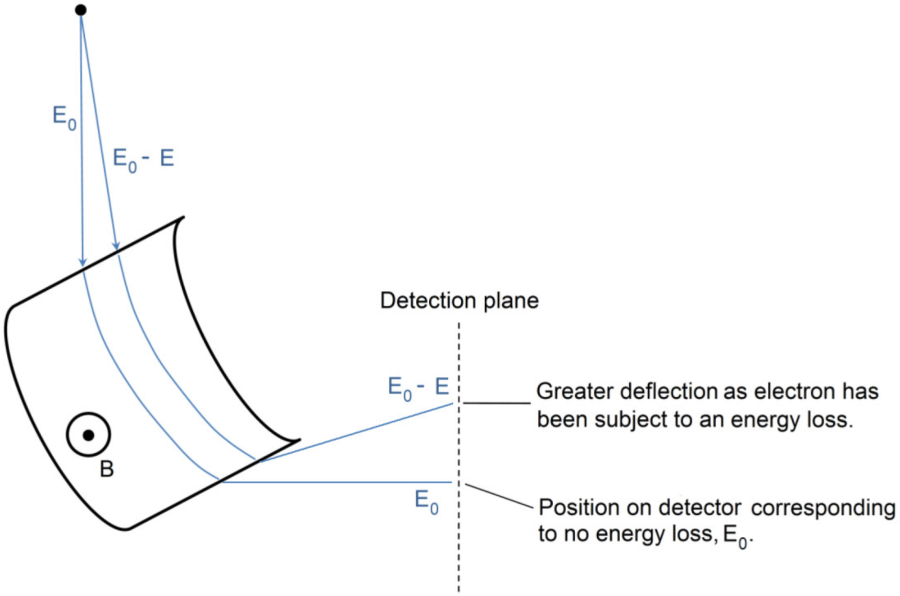

Figure 2.3: The magnetic sector of the EELS-(S)TEM apparatus (Brydson, 2001).

The position of the electron on the detection plane can be correlated to its velocity, such that the greater the energy loss of the electron, the lower its energy and hence velocity and so the more it is deflected in the magnetic sector as shown. The radius of curvature can be determined thus (Egerton, 2009):

$$R = (m_0 v/eB) \tag{2.1}$$

Where m_0 is the electron mass. The smaller the particle velocity therefore, the less the beam will be deflected. If mv is taken as a relativistic moment, then this expression is relativistically correct.

2.3 Relating the EELS spectrum to structure

2.3.1 Overview of EELS physics

In EELS, the incident electron beam collides with the atoms of the sample, and loses energy. One measures the extent of the inelastic energy losses by finding scattering angles, and relating these to the energy losses of the incident beam.

Consider initially the process that occurs in terms of momentum changes for an incident electron beam:

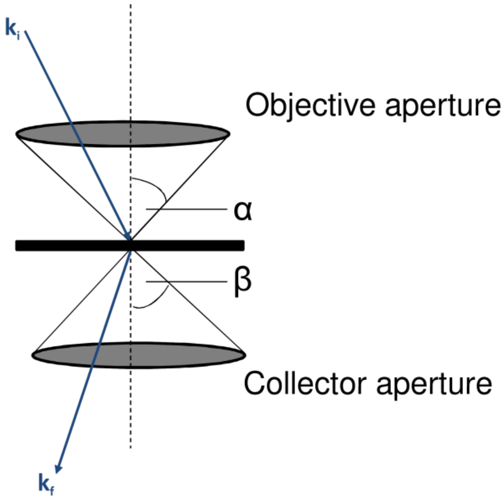

Figure 2.4: Momentum changes upon an incident electron beam interacting with a sample. The convergence and collection angles are illustrated.

The incident electron has an energy E_0, and initial momentum k_i, final momentum after scattering k_f. The most commonly used method to mathematically rationalise an EELS spectrum is the quantum mechanical approach of Bethe (Bethe, 1997). Before the electron beams hits the sample, the atomic electrons exist in an initial state described by the wavefunction ψ_i, altered by interaction with the electron beam to ψ_f. The differential scattering cross section calculates the probability of observing a scattered particle in a given quantum state per solid angle unit. Bethe showed it can be expressed in terms of initial and final momentums and wavefunctions:

$$\frac{d\sigma}{d\Omega} = \frac{4\gamma^2}{a_0{}^2 q^4} \frac{k_f}{k_i} \left| \int \Psi_f e^{i\bar{q}.\bar{r}} \, \Psi_i d^3 r \right|^2 \qquad (2.2)$$

Where q is the momentum transfer, γ the relativistic factor (see Eqn. 2.2), and a_0 the Bohr radius. The final state wavefunction can then be normalised with respect to energy loss, giving an expression for the double-differential scattering cross-section (DDSCS), expressing the probability of finding a scattered electron per unit solid angle, per unit of energy lost, i.e. the basis of a spectrum of electron energy-losses. This equation is written in 2.3 (Brydson, 2001):

$$\frac{d^2\sigma}{dEd\Omega}=\frac{4\gamma^2}{{a_0}^2q^4}\frac{k_f}{k_i}\left|\left\langle f\middle|e^{i\bar{q}.\bar{r}}\middle|i\right\rangle\right|^2 \tag{2.3}$$

Other expressions exist for the DDSCS in the literature, for example (Hébert, 2003), (Jorissen, 2005):

$$\frac{\delta^2\sigma}{\delta\Omega\delta E}=\left[\frac{4\gamma^2}{a_0^2q^4}\right]\frac{k_f}{k_i}\sum_{i,f}\left|\left\langle f\middle|e^{i\bar{q}\cdot\bar{r}}\middle|i\right\rangle\right|^2\delta(E-E_f+E_i) \tag{2.4}$$

E represents the energy loss, E_f and E_i the energies of the final and initial states respectively. σ is the total inelastic cross-section for scattering, and Ω the solid scattering angle. The summation is performed over all occupied initial and empty one-electron final states represented by the wavefunctions $\left|i\right\rangle$ and $\left|f\right\rangle$. The Dirac delta function ($\delta(E-E_f+E_i)$) selects all transitions from the initial state to final states such that E_f - E_i (Paxton, 2003). The resulting EELS spectrum can roughly be divided into a number of regions, as depicted schematically in Figure 2.5 (Brydson, 2001).

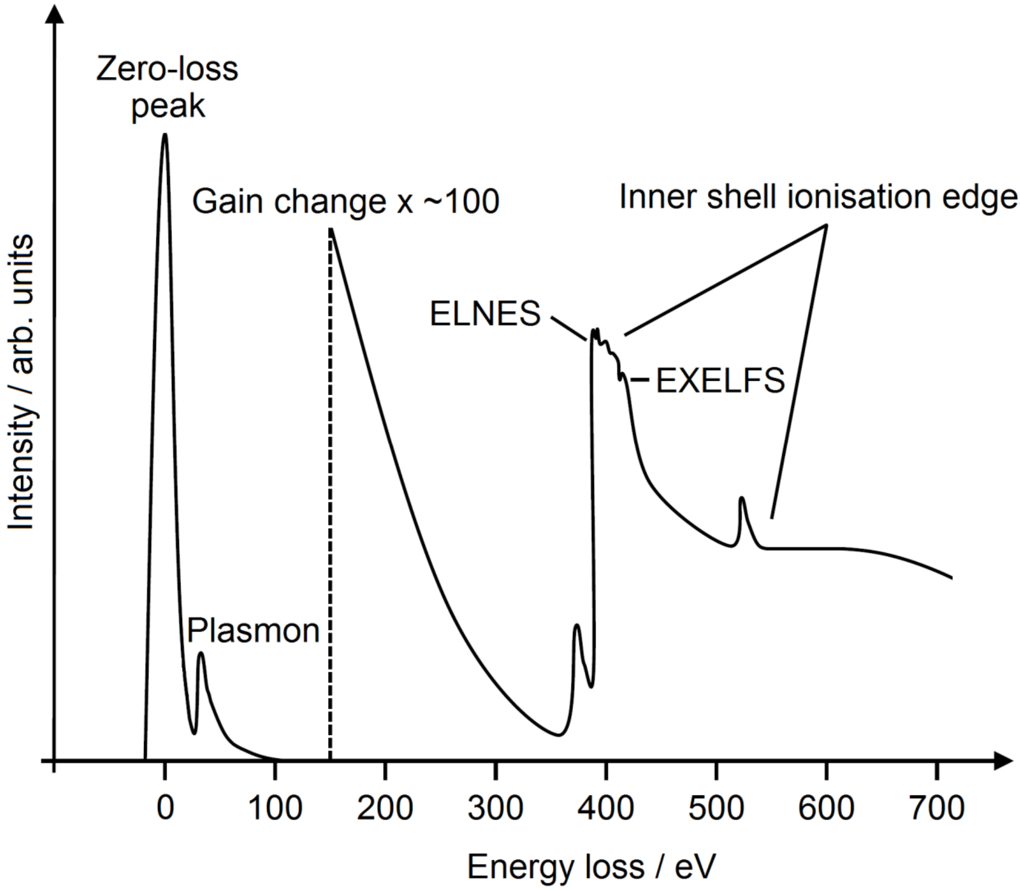

Figure 2.5: Schematic depiction of the various regions of an EELS spectrum. The energy losses shown act purely as a guideline (Brydson, 2001).

The x-axis merely reflects the energy losses of the incident electron beam, but expressed in units of electron-volts (1eV = 1.602×10^{-19} J). The y-axis describes the number of these energy losses. A summary of the major features is given below, more detailed descriptions follow in the subsequent pages.

- The **zero-loss peak** is always the most intense peak in the spectrum – a narrow feature corresponding to the large number of electrons that do not undergo energy loss when passing through the sample.
- **‘Plasmon’** is a term for the ‘vibration’ of free electrons against the heavy nuclei when stimulated by the electron beam.
- In the **core-loss** region, we observe ionisation edges corresponding to the excitation of electrons in single atoms (e.g. localised electrons in 1*s* (K) shells) to unoccupied sites above the Fermi level (highest occupied energy level). These are highly indicative of elemental composition.

- These **ionisation edges** also display fine structure due to local bonding and coordination. Specifically, the two major forms of fine structure are **electron energy-loss near-edge structure** (ELNES), and **extended electron energy loss fine structure** (EXELFS). As illustrated, the ionisation edge features are of vastly lower intensity than low-loss features.

EELS has the capability to characterise a sample in a variety of fashions. The major focus of this work is the core-loss region. The energy onset values of ionisation edges indicate the elements present in the sample. For example, for a carbon K ionisation edge, there is a fixed energy difference between the carbon 1*s* level and the Fermi level which is observed in the EELS spectrum. By finding relative areas under ionisation edges for different elements in a sample, the ratio of those elements can be estimated. ELNES fine structure probes the distribution of the unoccupied density of states, containing information on bonding, coordination environments and local structure.

2.3.2 Low energy loss region of the EELS spectrum

The zero-loss peak (ZLP) is always the most intense feature observed in an experimental EELS spectrum, corresponding to electrons that upon transmission (i.e. passing through the sample) are not subject to an energy loss (or very small losses). The ZLP therefore has two principal usages. The full-width half maximum (FWHM) of the ZLP is almost always used to describe the energy resolution of the EELS spectrum (the potential flaws of this approach are discussed in section 5.6 of this thesis). Furthermore, the ZLP can be used to estimate sample thickness. As the sample thickness increases, the probability of an inelastic scattering event occurring increases. The following equation can be used to estimate sample thickness (Brydson, 2001):

$$\text{thickness} = \Lambda.\ln\left(\frac{I_T}{I_{ZL}}\right)$$

(2.5)

Where Λ is the mean free path (for inelastic scattering), I_T being the total spectral intensity, and I_{ZL} the intensity for the ZLP.

The other major features typically observed in the low-loss region are bulk plasmon excitation peaks. Using an approximation based on a free-electron model of bulk materials, we can simply describe a plasmon excitation as the vibration of a valence electron cloud (bound by nuclear attraction) as a response to the incident electron beam. Again, assuming a free-electron model, the energy of a plasmon peak can be reasonably estimated thus (Brydson, 2001), (Egerton, 1996):

$$\text{plasmon energy} = \frac{h}{2\pi}\sqrt{\frac{Ne^2}{m_0\varepsilon_0}} \tag{2.6}$$

Where N is the valence electron density, m_0 the electron mass, and ε_0 the permittivity of the vacuum. The plasmon peak energy is sensitive to the density of valence electronic states, and therefore changes to the structure of the material can shift the plasmon energy, and also the shape of the peak.

2.3.3 Core-loss region

Hillier and Baker recognised that there was considerable relevance in measuring the energy lost by exciting electrons, and relating this to the specific energy levels of electrons in various atomic orbitals in the sample (for example when the principal quantum number n=1, a 'K' level or for n=2, an 'L' level) (Hillier, 1943), (Hillier, 1944). These 'ionisation edges' have a unique fine structure, for example, energy-loss near edge fine structure (ELNES).

$\left|\left\langle f\left|e^{i\vec{q}\cdot\vec{r}}\right|i\right\rangle\right|$ (See Eqn. 2.4) is generally referred to as a dipole matrix element term – expressing the probability of given initial to final state transitions occurring. As was outlined in Chapter 1, in condensed matter, the destination final states exist as part of a band structure, determined by local coordination environments. An EELS ionisation edge can therefore be considered to be local density of states (DOS) transformed by matrix elements terms. Continuing the mathematical assessment of EELS, the exponential term in equation 2.4 can be expanded thus:

$$\exp(i\vec{q}\bullet\vec{r}) = 1 + i\vec{q}\bullet\vec{r} + \frac{(i\vec{q}\bullet\vec{r})^2}{2}\ldots$$

(2.7)

In electron microscopy, two ‘types’ of electron intensities are recorded:

i) On-axis bright field intensity (BF). For electrons with small scattering angles (predominantly those with no energy loss, or subject to small inelastic scattering).
ii) Annular dark field intensity (ADF) - collects electrons subject to higher angle scattering, with large energy losses.

Annular dark field electrons are of importance in imaging using the electron microscope. Such images are formed by high scattering angle electrons which are incoherent, the image formed being sensitive to atomic number. Some high angle annular dark field (HAADF) images are presented later in the thesis. Another imaging mode is based on ‘diffraction contrast’. At certain orientations of a crystalline sample, the electron beam undergoes Bragg scattering, dispersing electrons into discrete locations (in the back focal plane). By placing apertures in that plane, Bragg reflections can be selected or excluded. For example, the apparatus can be designed such that only regions of the sample causing scattering to the relevant reflections appear in the image.

In conventional EELS one collects small scattering angle electrons by retracting the BF detector, thus ensuring the momentum transfer $\vec{q}$ is small. Therefore, higher order terms in equation 2.7 can be ignored, therefore:

$$\exp(i\,\vec{q}\bullet\vec{r}) = 1 + i\vec{q}\bullet\vec{r} + \frac{(i\vec{q}\bullet\vec{r})^2}{2}\ldots$$

$$\because \text{q is small}$$

$$\exp(i\,\vec{q}\bullet\vec{r}) \approx 1 + i\vec{q}\bullet\vec{r}$$

$$\because \Psi_f \text{ and } \Psi_i \text{ are orthogonal}$$

$$\left|\left\langle f\left|e^{i\vec{q}\cdot\vec{r}}\right|i\right\rangle\right|^2 \approx \left|\left\langle f\left|\vec{q}.\vec{r}\right|i\right\rangle\right|^2$$

For the final integral to be non-zero, ψ_i and ψ_f must not have the same symmetry (i.e. they should not both be even or odd functions). Thus for small scattering angles, the dipole selection rule exists, such that for ionisation edges the orbital angular momentum quantum number *l* will change by ±1 in order to avoid the matrix element integral being zero (Brydson, 2001). Therefore, from a 1*s* core-level, an electron must move to a state with *p* symmetry (symmetry projection). Table 2.1 summarises therefore the nomenclature used to describe these ionisation edges (Egerton, 1996), (Keast, 2001).

		Initial state quantum numbers			
Edge	**Initial state**	*n*	*l*	*j*	**Final state symmetry**
K	$1s^{1/2}$	1	0	1/2	*p*
L_1	$2s^{1/2}$	2	0	1/2	*p*
L_2	$2p^{1/2}$	2	1	1/2	*s* or *d*
L_3	$2p^{3/2}$	2	1	3/2	*s* or *d*
M_1	$3s^{1/2}$	3	0	1/2	*p*
M_2	$3p^{1/2}$	3	1	1/2	*s* or *d*
M_3	$3p^{3/2}$	3	1	3/2	*s* or *d*
M_4	$3d^{3/2}$	3	2	3/2	*p* or *f*
M_5	$3d^{5/2}$	3	2	5/2	*p* or *f*
N_1	$4s^{1/2}$	4	0	1/2	*p*
N_2	$4p^{1/2}$	4	1	1/2	*s* or *d*
N_3	$4p^{3/2}$	4	1	3/2	*s* or *d*
N_4	$4d^{3/2}$	4	2	3/2	*p* or *f*
N_5	$4d^{5/2}$	4	2	5/2	*p* or *f*
N_6	$4f^{5/2}$	4	3	5/2	*d or 'g'*
N_7	$4f^{7/2}$	4	3	7/2	*d or 'g'*

Table 2.1: Nomenclature used to describe ionisation edges that occur in EELS (Egerton, 1996), (Keast, 2001).

n is the principal quantum number, *l* is the orbital angular momentum quantum number, and *j* describes spin-orbit coupling effects. *j* is found as $l\pm1/2$, except for $l=0$ (i.e. an *s* orbital) where $j=1/2$ only. Therefore, for each *p*, *d* or *f* orbital there are two possible initial states (regardless of increasing *n* values), and therefore two parts of a multiplet edge. One example of a multiplet is an $L_{2,3}$ edge. The two components of these multiplets can be difficult to observe experimentally for lighter elements, though monochromation can resolve them in certain circumstances. Even with this selection rule in place, the analysis of ionisation edges is still potentially complex. Computational modelling of EELS can be important in this regard. Modelling studies allow us to control the theoretical structure of a material and predict the associated ELNES result, and indeed the assignment and better understanding of experimental spectra is an important area of research, forming the main body of this thesis. A description of modelling applications and approaches is therefore given in Chapter 3. Another feature in the core-loss region, the extended energy-loss fine structure (EXELFS) is not further considered in the thesis. On the tail of core-loss edges, weaker extended oscillations occur – called EXELFS. The amplitude of those oscillations can be used to infer coordination properties, their period to deduce bond distances (Brydson, 2001). Figure 2.6 summarises the relationship between materials structure and the core-loss region of the EELS spectrum, placing particular emphasis on the physical background to the technique, and specific properties that can be deduced. Modelling considerations are also outlined briefly, further detailed in Chapter 3:

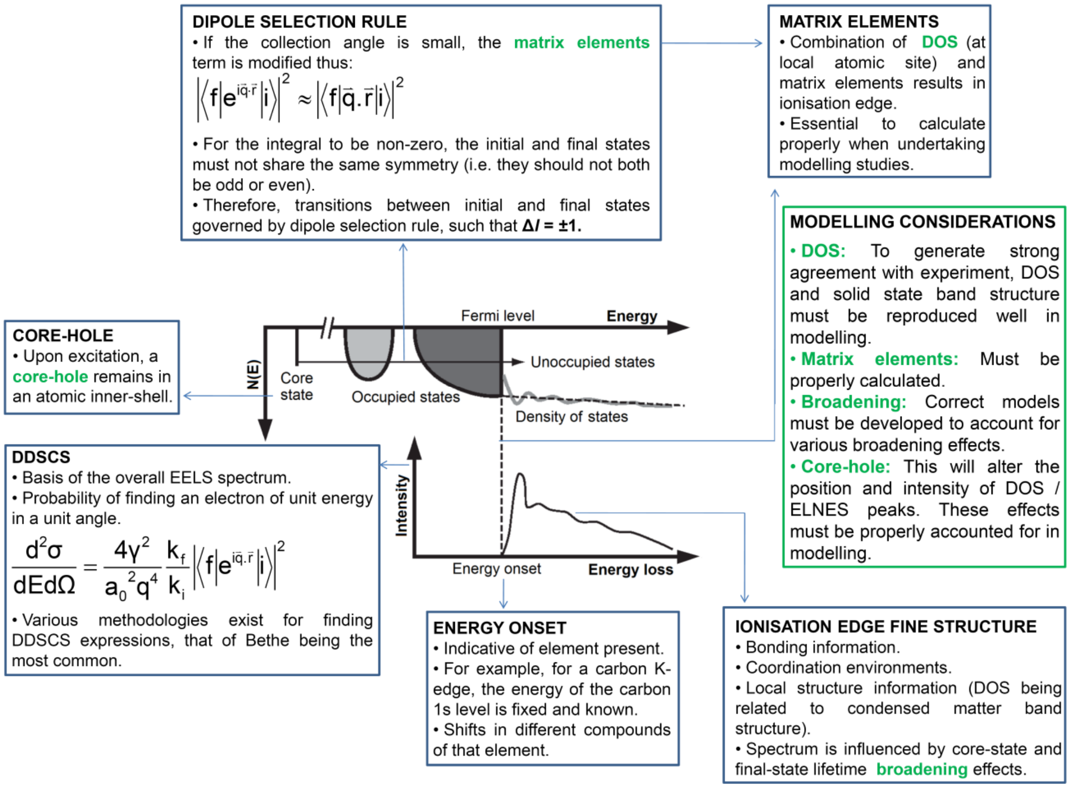

DIPOLE SELECTION RULE
- If the collection angle is small, the **matrix elements** term is modified thus:

$$\left|\langle f|e^{i\bar{q}.\bar{r}}|i\rangle\right|^2 \approx \left|\langle f|\bar{q}.\bar{r}|i\rangle\right|^2$$

- For the integral to be non-zero, the initial and final states must not share the same symmetry (i.e. they should not both be odd or even).
- Therefore, transitions between initial and final states governed by dipole selection rule, such that **$\Delta l = \pm 1$.**

MATRIX ELEMENTS
- Combination of **DOS** (at local atomic site) and matrix elements results in ionisation edge.
- Essential to calculate properly when undertaking modelling studies.

MODELLING CONSIDERATIONS
- **DOS:** To generate strong agreement with experiment, DOS and solid state band structure must be reproduced well in modelling.
- **Matrix elements:** Must be properly calculated.
- **Broadening:** Correct models must be developed to account for various broadening effects.
- **Core-hole:** This will alter the position and intensity of DOS / ELNES peaks. These effects must be properly accounted for in modelling.

CORE-HOLE
- Upon excitation, a **core-hole** remains in an atomic inner-shell.

DDSCS
- Basis of the overall EELS spectrum.
- Probability of finding an electron of unit energy in a unit angle.

$$\frac{d^2\sigma}{dEd\Omega} = \frac{4\gamma^2}{a_0^2 q^4}\frac{k_f}{k_i}\left|\langle f|e^{i\bar{q}.\bar{r}}|i\rangle\right|^2$$

- Various methodologies exist for finding DDSCS expressions, that of Bethe being the most common.

ENERGY ONSET
- Indicative of element present.
- For example, for a carbon K-edge, the energy of the carbon 1s level is fixed and known.
- Shifts in different compounds of that element.

IONISATION EDGE FINE STRUCTURE
- Bonding information.
- Coordination environments.
- Local structure information (DOS being related to condensed matter band structure).
- Spectrum is influenced by core-state and final-state lifetime **broadening** effects.

Figure 2.6: Summary of EELS physics, and possible links with modelling. A summary of key modelling considerations is then listed, in terms of generating strong agreement with experiment.

2.4 Electron source technologies

Frequently quoted throughout this thesis is the concept of electron source energy resolution in the EELS spectrum. It should be noted that this refers to the observable energy resolution of the spectrum. Specifically, the standard resolution quoted by experimentalists is the full-width half maximum of the zero-loss peak. The choice of electron source technology is crucial therefore in obtaining high spatial and energy resolutions.

2.4.1 Thermionic electron sources

A thorough description of electron source technologies is available in the literature (Bognor, 2007). The original electron source for microscopy was the thermionic gun; a V-shaped tungsten filament which is heated electrically. A later thermionic source was the LaB_6 filament, a material with a low work function, this being the minimum energy required to move an electron from the Fermi energy to vacuum. Table 2.2 summarises thermionic emission sources. (Bognor, 2007), (Keast, 2001).

Source	Description	Resolution / eV	Advantages	Disadvantages
Tungsten filament	- V-shaped hairpin. - Radius 100µm.	1-3	- Inexpensive. - Requires only low vacuum.	- Short lifetime. - Difficult to obtain good resolution.
LaB_6	- LaB_6 single crystal. - 100µm diameter, 1µm radius of tip.	~1	- Low work function means less heating, and better resolution. - Comparatively longer lifetime.	- Resolution still poor compared to field emission sources. - Lifetime limited compared to field emission sources.

Table 2.2: Summary of thermionic electron sources. Resolutions are based on the zero-loss peak (Bognor, 2007), (Keast, 2001).

2.4.2 Field emission electron sources

Field emission sources are a more recent development. For a metal in vacuum, there is an energy gap between the Fermi level, and the vacuum state. This energy gap is called the work function. In a classical model, energy must be provided to an electron at the Fermi level to overcome the work function. However, if the tip is at a negative potential to a nearby electrode, a potential gradient exists, allowing some part of the electron wave function to pass through the emission barrier without thermal stimulation. At higher energies, the barrier is thinner, leader to asymmetry in the energy profile of the beam.

Schottky-FEG tips are coated with zirconium oxide – which unusually increases in electronic conductivity with temperature (Iiyoshi, 1996). The resulting low work function of the material means only limited heating is required for a high beam intensity. Note that in contrast to cold-FEG, it is direct thermal stimulation which ultimately overcomes the work function. Again, this leads to an asymmetric energy profile of the electron beam, as some electrons escape the potential well with excess energy. The usage of some heating means that maintaining the tip in good condition is also relatively straightforward. Table 2.3 summarises field emission sources (Bognor, 2007), (Rainforth, 2000).

Source	Description	Resolution / eV	Advantages	Disadvantages
Cold-FEG	- Very fine cathode wire. - Electric field creates potential gradient, allowing emission.	0.3	- Good lifetime compared to thermionic sources. - Narrow probe size and high brightness.	- Not using a heated source means the tip is harder to maintain. - Extra magnetic shielding is required.
Schottky-FEG	- Narrow wire coated with zirconium oxide. - Emission stimulated using heat.	0.3-1.0	- Heating the source allows comparatively easy maintenance.	- The use of heating will sometimes lead to a lower resolution compared to a cold-FEG.

Table 2.3: Summary of field emission sources (Bognor, 2007), (Rainforth, 2000).

2.4.3 Monochromation

FEG sources are increasingly common in modern microscopes, and in some cases the source will be subject to monochromation to further improve the resolution. The principle of monochromation is to select a series of wavelengths (and therefore energies for example) from a larger input range. Complex designs are somewhat beyond the scope of this thesis, but a detailed monograph is available (Palmer, 2005), as is a 2008 introduction to monochromation developments (Grogger, 2008). This paper contains information on resolutions obtained using the technique, usefully applied to a number of different materials systems. The introduction in this thesis does however aim to give a brief overview of some electromagnetic principles utilised in monochromation.

The ‘Wien’ filter uses magnetic and electric fields to achieve monochromation. Fig. 2.7 is a schematic of the Wien filter, based on various literature (Curtis, 1971), (Kothleitner, 2003), (Martínez, 2004).

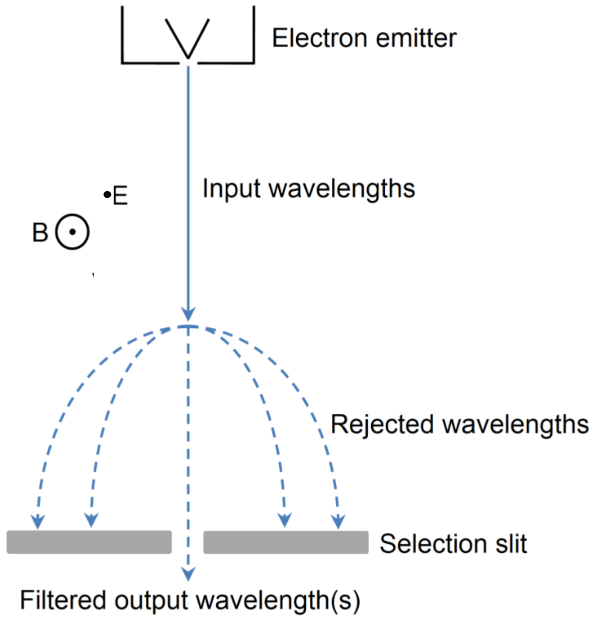

Figure 2.7: Schematic of a Wien filter (Curtis, 1971), (Martínez, 2004), (Kothleitner, 2003).

As depicted in Figure 2.7, a number of input electron ‘wavelengths’ enter the Wien filter, and are subject to perpendicular magnetic and electric fields. Electrons input into the device are subject to a force $\vec{F}$:

$$\vec{F} = e(\vec{E} + (\vec{v} \times \vec{B})) \tag{2.8}$$

$\vec{E}$ is the electric field, $\vec{B}$ the magnetic field, and $\vec{v}$ the particle velocity. One selects a wavelength (related to energy, E=hc/λ) by modifying $\vec{E}$ and $\vec{B}$ with appropriate slit positioning. Specifically, if one ensures that the vector product $(\vec{v} \, x \, \vec{B})$ is equal in magnitude and opposite in sign to $\vec{E}$ the net force on the electron is zero, and it will be undeflected

In this thesis, results are presented from a microscope with a monochromated source, specifically the FEI Titan 80/300 device at Imperial College. This instrument uses a Wien type monochromator, and testing has suggested the monochromator can improve the energy resolution from ~0.5eV to ~0.2eV (Perkins, 2007).

In order to successfully utilise monochromation for EELS, source tips need to have both good energy resolution and be bright – such that when we focus the beam down to achieve atomic scale information the signal is still sufficiently high. A considerable amount of beam current is lost via the energy selection process.

2.5 Aberration correction

2.5.1 Spherical lens aberrations

Optical lenses as used in electron microscopes are subject to numerous aberrations. A full discussion can be found in various references (Guenther, 1990), (Hecht, 2001), (Pedrotti, 2006), (Welford, 1986). It is necessary to give a brief description of spherical and chromatic aberrations. A standard optical lens will refract input waves more at its edge than centre, leading to a blurring called spherical aberration when looking at the beam on the viewing platform. Chromatic aberration is when images are unclear due to 'coloured' distortions at their edge, as a result of different wavelengths being refracted by slightly different amounts (Urban, 2008).

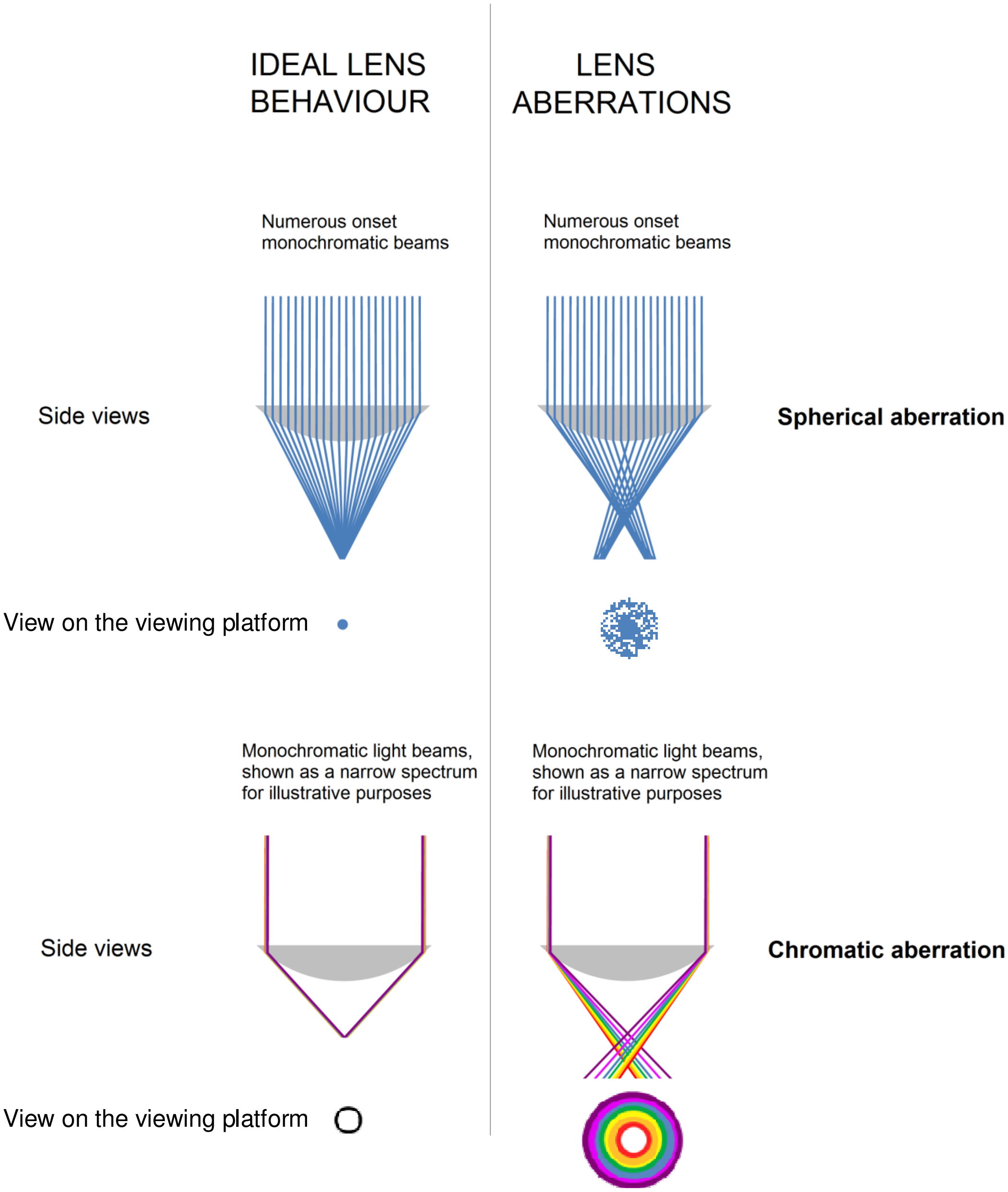

Figure 2.8: Schematic illustration of lens aberrations (Urban, 2008).

2.5.2 Correction of spherical aberrations

There are limits to resolution as described by the Scherzer theorem. The original paper describing the theorem is from the 1930s, but more recent papers have discussed the concept (Liu, 2001), (Scherzer, 1936), (Schonhense, 2006). The theorem states that spherical and chromatic aberrations cannot be avoided for a rotationally-symmetric electromagnetic lens. Therefore, to achieve aberration correction researchers design lenses that circumvent this constraint – multipoles.

Correction of chromatic aberrations has not been addressed in detail in the literature. It is confirmed possible however to correct for spherical aberrations using a hexapole-type lens system. Advanced descriptions of the device can be found in the literature (Baranova, 2008). An attempt is made to schematically depict an aberration correction system in Figure 2.9, utilising concepts from other papers (Browning, 2005), (Terauchi, 1999).

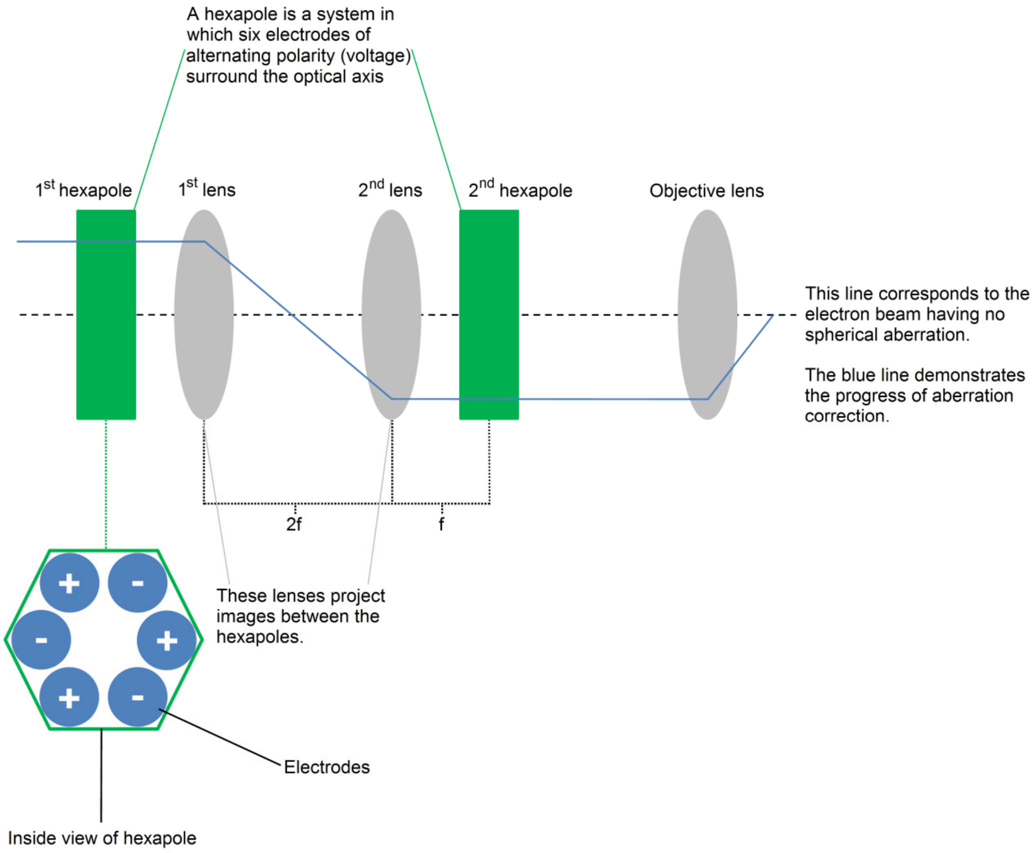

Figure 2.9: Schematic of hexapole lens system (Baranova, 2008), (Browning, 2005), (Terauchi, 1999).

f represents the focal lengths as described in an existing paper (Baranova, 2008). The dotted line represents a situation with no spherical aberration. As can be observed on the far right of the plot, the objective lens will cause a spherical aberration of ‘sign’ and magnitude. In this schematic the objective lens causes an aberration in an ‘upwards’ direction. The basis of the aberration correction is to deliberately introduce into the system a spherical aberration of equal magnitude to that of the objective lens, but of opposite ‘sign’. A pair of hexapole lens sets is used to achieve this. The first set of lenses generates a spherical aberration, the second set ‘over-corrects’ this by the precise extent of the spherical aberration of the objective lens itself. Thus, aberration correction is achieved (Baranova, 2008), (Browning, 2005), (Terauchi, 1999).

At the SuperSTEM facility in Daresbury, a similar (though in this instance a Quadrupole-Octupole) aberration corrector is fitted, to perform image correction. Work is presented in the thesis whereby the enhanced spatial resolution this offers was crucial to being able to accurately characterise the materials in Chapters 7 and 8. The boundary at a magnetic tunnel junction is considered in fine detail in Chapter 7, and in Chapter 8 nanoscale (layered) materials coatings are studied, in which high spatial resolution (as a result of aberration correction) is essential in distinguishing between the very thin layers.

2.6 Detection and acquisition

2.6.1 Basic overview of detection

As described in the original paper reporting EELS, a photographic plate can be used for detection (Hillier, 1944). It was demonstrated that edge onset values could be determined with good accuracy. However, photographic plates are time-consuming to process, and somewhat impractical. The modern standard alternative has rapidly become the charge-coupled device (CCD) (Boyle, 1970). A comprehensive review of CCD technology is available in the literature (Fan, 2000). CCDs consist of a grid of silicon substrates. Electrons are incident on a phosphorescent screen and are then converted to light. Light is channelled (via a fibre optic cable for example) to the CCD, which ultimately detects photonic intensity.

2.6.2 Novel acquisition methodologies

It is important to modify the detection system and parameters in an appropriate fashion depending on the region of the EELS spectrum one wishes accurately to collect, principally high and low electron energy loss regions. This is challenging, as the intensity of the EELS spectrum drops off rapidly with increasing energy loss.

A recent paper outlines a detection system that enables both these different energy regions to be probed for the same pixel (Scott, 2008). Figure 2.10 provides an outline schematic of the device utilised.

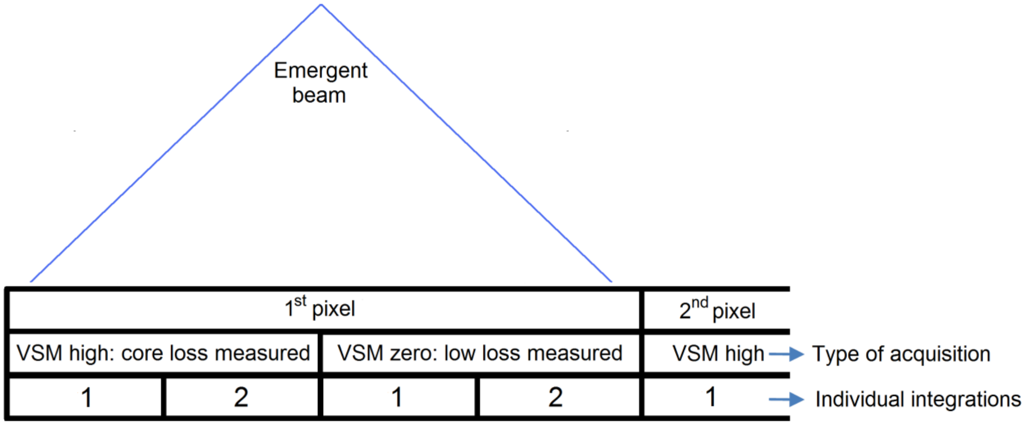

Figure 2.10: Schematic of dual detection scheme (Scott, 2008).

Using a computer, a voltage scan module (VSM) is set, which determines if the spectrometer drift tube is set to measure low-loss electrons, or high loss electrons. The probe starts on what is labelled as the '1st pixel'. The VSM is set high so core-loss is measured on the first integration sector. Computing elements ensure the information from this sector is recorded, then the second sector is integrated. The probe is not yet moved. With the probe still in position, the VSM is set to zero. This allows low-loss spectra to be measured from the same area and under the same experimental conditions as the core loss. A fast shutter speed is essential to limit the integration time. The probe can then be moved to the next pixel (Scott, 2008).

This whole process is technically challenging, as the ZLP / low-loss region is of a much higher intensity than the core-loss region. However, this collection of different spectral regions near simultaneously allows a more rapid acquisition of the spectrum, which can minimise the impact of noise. However this technique is still in its relative infancy, particularly in terms of its data acquisition procedures, as the authors state.

2.7 Summary

This thesis will address how DFT modelling of EELS can be used in combination with experimental spectra to deduce a variety of information. The information presented in this chapter is returned to throughout the rest of the document. Of particular importance with regard to EELS modelling is the dipole selection rule, and its relevance to ionisation edges. Modelling the fine structure of ionisation edges is a major component of the thesis. Chapter 3 compliments this experimental chapter by describing the major modelling methodologies in similar detail, an important theme being the relationship between electronic structure and materials properties.

Chapter 3

Computational EELS modelling

3.1 Introduction

The principle aim of this thesis is to illustrate the development of new approaches to EELS modelling, and their application to experiment. This chapter summarises methodologies used for modelling, and then describes in more detail the specific approaches used for the most part in this thesis.

In experimental EELS, a major challenge in terms of relating the spectrum to structural properties is being certain of the precise structure of the material being characterised. Modelling studies allow us to control the structure of a material and predict the ELNES result. Therefore, the potential for assignment and better understanding of experimental spectra is an important area of research. A concise description of modelling applications is available in the literature (Zhu, 2005), with a more detailed discussion also available (Rez, 2008).

The rest of this chapter describes in detail the DFT methodology used for EELS modelling. A small flow chart of the process is given below, each of the concepts being discussed in more detail subsequently:

Schrödinger equation → Kohn-Sham (DFT) solution → Initial estimate of electron density → System energy found → Used as a basis to refine electron density (SCF cycle) → Satisfactory electron density model → Key DFT parameters chosen (Chapter 4) → Band structure predicted → DOS predicted → **EELS prediction**

3.2 Band structure calculations and DFT

As outlined in Chapter 2, to accurately model EELS, it is necessary to correctly determine the electronic band structure of the system. The most common methodology currently used is density functional theory (DFT). It is necessary to further understand DFT, and the wider problems it was intended to solve (Hohenberg, 1964), (Kohn, 1965), (Martin, 2004). Further detail will then be given on the two codes used throughout the thesis; Wien2k and CASTEP.

3.2.1 The Kohn-Sham formalism

Previous models (such as Hartree-Fock) had attempted to use the many-electron wavefunction in solutions to the Schrödinger equation. Density functional theory (as the name suggests) uses electron density as an alternative. There is an immediate advantage to this method. Any method involving calculating wavefunctions in the Hartree-Fock form for example will clearly require 3N variables (the '3' relating to the number of dimensions of physical space, N the number of atoms). Electron density however is dependent only on three positional variables.

A comprehensive text can be used to find a detailed description of the evolution of the theory from the Thomas-Fermi model (which attempted to use a statistical model to map electrons) (Martin, 2004). However, for the purposes of this introductory chapter it is sufficient to discuss the most widely implemented form of DFT – the Kohn-Sham methodology.

The method relies on the following concept. The ground state (electron) density of a system (with interacting electrons) is equal to that of a specially chosen system with non-interacting electrons (quasi-particles). In order to achieve this (simply speaking) the non-interacting electrons are considered to be moving in an effective potential. The effective potential incorporates an external potential and the effects of Coulombic interactions between the electrons - these are the correlation and exchange effects. Kohn-Sham theory groups these correlation and exchange effects together, separates them out of calculations, then attempts to reintroduce them subsequently. In terms of equations, the Kohn-Sham formalism begins with the familiar Born-Oppenheimer approximation (which allows the separation of nuclear and electronic wavefunctions, and sets an external potential V), which allows the Schrödinger equation to be written as:

$$H\psi = [T + V + U]\psi = E\psi \tag{3.1}$$

Where the additionally introduced terms are:

H – Hamiltonian operator
T – kinetic (energy) operator
U – electronic interaction term (recall the Kohn-Sham formalism allows the grouping of all these terms in this fashion).
E – energy

A variety of existing and potentially complicated methodologies exist to solve the equation for the energy term. Crucially in the Kohn-Sham methodology (as alluded to above) the electronic interaction term ‘U’ is simplified by using an electron density model, in which all the exchange and correlation effects are grouped together in a single term. This allows energy to be expressed as:

$$E = T_S[n] + \int drV_{ext}(r)n(r) + E_{Hartree}[n] + E_{II} + E_{XC}[n] \tag{3.2}$$

Where:

[n] – denotes a functional of the **density** n(r, σ) – i.e. a term that depends upon the position of electrons in space (r) and their spin σ.

T_S – independent-particle kinetic energy.

V_{ext} – external potential due to nuclei.

$E_{Hartree}$ - Hartree energy (known, defines the self-interaction energy of density n(r), calculated as a classical charge density).

E_{II} – Ion-ion (i.e. nucleus-nucleus) electrostatic term, dealt with in a classical manner.

E_{XC} – exchange correlation functional.

As previously mentioned, it is this last term - the exchange correlation functional - that must be estimated by a variety of methods.

3.2.2 Exchange correlation functionals

The first and most simple method was proposed by Kohn and Sham themselves (Kohn, 1965); the local-density approximation (LDA). Again, this method uses electron density as its basis. The exchange-correlation energy (XC energy) of an electron in a homogeneous electron gas is found, and this is applied directly to an electron of that density in the actual system, which is not homogeneous, and does have electronic interactions. The etymology of the ‘local’ density approximation is therefore obvious, as the XC energy is entirely determined by local density calculations. In other words, the LDA should give a minimum system energy that matches the energy of the equivalent homogeneous electron gas.

There are clearly a number of problems with this method, and it will certainly fail to account for certain XC interactions. For example there are certain peculiar effects in chemistry that are somewhat difficult to predict – such as materials where Coulomb repulsion occurs (making predicted conductors insulators for example). Nickel (II) oxide has a partially filled 3*d* subshell, and initially would be expected to be conducting. However, the strong Coulomb repulsion mentioned above between the *d* orbital electrons actually makes nickel (II) oxide an insulator. Instead the LDA will work well for more typical metallic systems best approximated by the free electron model (Martin, 2004).

More modern techniques do exist to model the XC term, for example the generalised-gradient approximation (GGA). This functional recognises that using a homogeneous electron gas as a basis is clearly going to lead to errors in a large number of systems – and that the actual electron density might vary significantly from a uniform value. It is however possible to partially account for this by using a higher order derivative of the electron density – obviously for the GGA this is the gradient. There are of course various subtle variations in GGAs, described at length in various literature (Burke, 1997), (Langreth, 1980), (Perdew, 1986), (Perdew, 1996). Be it LDA or GGA, the exchange correlation functional can be used as an input file in certain codes, based on valence electron properties (see CASTEP discussion below). It can also be calculated (sometimes termed on-the-fly, OTF) based on the full electronic configuration – though still according to an exchange-correlational model such as the GGA. This concept will be returned to subsequently.

All GGAs lead to an exchange energy lower than the equivalent LDA (Martin, 2004). Predictably, for atomic species where electron density varies rapidly, this effect can be highly significant. The GGA will often improve agreement with experiment therefore (for energy based calculations) (Koch, 2001). Within the context of the GGA – there are still however various subtleties if a pseudopotential method is used, as discussed below. Table 3.1 summarises the LDA and GGA:

E_{XC} Potential	Brief Description	Ideal systems
LDA	The exchange correlation energy (XC energy) of an electron in a homogeneous electron gas is found, and this is applied directly to an electron of that density in the actual system.	Metals well approximated by the free electron model may take the LDA with some success.
GGA	Uses the first derivative of the electron density.	Particularly improves on the LDA for molecular systems.

Table 3.1: Summary of LDA and GGA.

The LDA was expected to be a poor approximation for systems other than free-electron metals. However, it has proved to be useful for a wide range of materials with unexpected success for covalently bonded (directional) structures. The LDA tends to over-bind, i.e. optimised geometry gives significantly smaller lattice parameters, and it predicts for example that the ground state for iron should be non-magnetic and FCC, hence the refinement of various GGA models since the 1990s. However, it should be noted the GGA is not always superior to the LDA.

3.2.3 SCF cycle

Upon choosing an approximation for the exchange-correlational, an initial estimate of electron density is made. Using the Kohn-Sham formalism, this initial estimate is used to determine system wavefunctions, and the system energy. Depending on the code in question, that information is used in different ways to predict a new electron density, and in turn a new system energy (of lower value if the code is well designed). This process is repeated, as part of a self-consistent field (SCF) cycle. This cycle is stopped when the system energy varies only within a certain (usually small and ultimately user-defined) tolerance.

3.3 Modern DFT developments

Though the Kohn-Sham methodology as described above displays great elegance, a weakness is that no truly systematic method has been found to improve the various functionals in terms of their modelling of exchange and correlation effects. This section describes some of the approaches that have been attempted. The first logical approach is the so-called self-interactions correction (SIC) approach. This approach attempts to correct for the interaction of an electron with itself in the Hartree interaction. In the Hartree-Fock methodology this problem can be accounted for exactly. However for DFT in the exchange-correlation approximations, these errors can be very significant, given that the exchange-correlation terms involve sizeable Coulombic interactions. The basis of the method is therefore the subtraction of a ‘self-[interaction]-term’ for each state. This can lead to extensive delocalisation of states or localising certain states (Bylander, 1996). The latter point is especially interesting, as it can lead to essentially atomic-like states (Martin, 2004). This had led for example to considerable success in describing the magnetic state in transition metal oxides (Svane, 1990).

Another recent attempt at a systematic approach is the LDA+U methodology – which has been added to CASTEP from version 4.3 onwards. The method involves combining a standard LDA or GGA with an additional ‘U’ term - a specific additional orbital-dependent term (Anisimov, 1997). The ‘U’ term is designed to correct errors in the LDA or GGA by applying the correctional term to highly localised orbitals. Specifically, for elements with *d* or *f* orbitals present, a specific on-site *d-d* or *f-f* Coulomb interaction term is added. Nickel (II) oxide has already been mentioned as an example of a material with strong electronic correlation effects, which are difficult to model using standard exchange correlationals, even the GGA. As noted by Anisimov et al., standard GGA methods will find a band gap in the *d* electron states due to Coulombic repulsion – but that predicted band gap is too small (Anisimov, 1997). In this case therefore, the ‘U’ term serves to increase that band gap. The LDA+U approach is designed to correct total energy calculations, and find true ground states and band gaps – but it does not influence (to any significant extent) the unoccupied DOS prediction.

3.4 The basis set and sampling of reciprocal space

3.4.1 Basis sets

Both CASTEP and Wien2k use a plane-wave basis set to model wavefunctions in the Kohn-Sham formalism. A plane wave is a wave of constant frequency (dependent on energy), with wavefronts consisting of an infinite series of parallel planes (of the same amplitude). In a plane wave basis set, various waves of different frequency are used to represent the system wavefunctions. Sampling an infinite number of waves to properly form the basis set is of course impossible, and so a ‘kinetic energy cut-off’ is defined beyond which the plane wave basis set is not sampled. The choice of this parameter is crucial.

To further rationalise the concept of the ‘kinetic energy cut-off’, consider a ‘band theory’ type approach. The first assumption of elementary band theory is that a crystal exists in which the atoms are in a regular array (Smart, 2005):

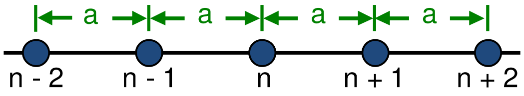

Figure 3.1: Regular array of atoms, interatomic distance ‘a’.

The crucial difference from the simpler free electron model is that we now apply a periodic rather than uniform potential, to create a periodic wavefunction, which has the general appearance of a sine wave:

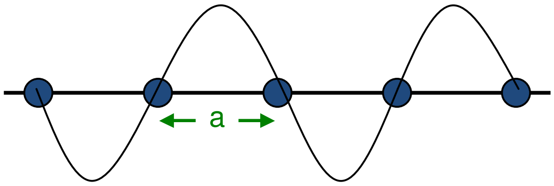

Figure 3.2: Periodic wavefunction.

Due to defining the atomic arrangement as periodic, the wavefunction at any position x along the chain is:

$$\psi(x)=\psi(x+\underset{\llcorner\text{N}^{\circ}\text{ of repeating ‘a’ units}}{N}a) \qquad (3.3)$$

To develop the model from this point the Bloch function is applied, which takes the form:

$$\psi(x)=\sum_{n} c_n \chi_n(x) \qquad (3.4)$$

Whereby $\chi_n(x)$ is the wavefunction of the atomic orbital, and c_n is the orbital coefficient, which takes the form $c_n = \exp(ikx)$, and because $x = na$ in this case, the Bloch function becomes:

$$\psi(x) = \sum_n \underbrace{\exp(ikna)}_{\text{Defines the phase of the orbital}} \chi_n(x) \tag{3.5}$$

In theory this series is infinite. However, as part of the plane-wave basis set one defines a kinetic energy cut-off beyond which the terms in equations 3.3 to 3.5 are ignored, i.e. in this analogy a value of n is chosen beyond which the function is no longer considered.

Good values of the kinetic energy-cut off (i.e. those leading to accurate data) will depend on the system in question. If researchers wish for example to study electrons in high energy orbitals close to the nucleus a high value is often required, due to the wavefunction oscillating rapidly close to the nucleus. DFT codes such as Wien2k and CASTEP will allow a user to select this value.

In CASTEP, this value is simply selected in electron volts (eV). In Wien2k the situation is slightly more complex. Although Wien2k is an all-electron code – it does make some utilisation of different potentials in different regions of space. So called Muffin-tin radii are defined around atoms (which are not allowed to overlap, wavefunctions in this region are modelled using spherical harmonics), and outside these there is an interstitial region in which the plane-wave basis set is used:

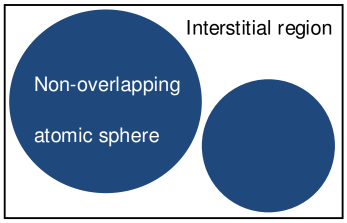

Figure 3.3: Wien2k's separation of a system into non-overlapping spheres and an interstitial region.

In Wien2k, 'RK_{MAX}' is user-defined whereby R is the smallest atomic sphere radius (described above) and K_{MAX} the maximum K (momentum) vector used, related to the kinetic energy cut-off.

3.4.2 *K*-point mesh

DFT codes calculate in reciprocal space. There are various significant constructs in reciprocal space. The Brillouin zone boundaries for example (Martin, 2004). The Wigner-Seitz cell can be used to depict the Brillouin zone. The construction method for the Wigner-Seitz cell is:

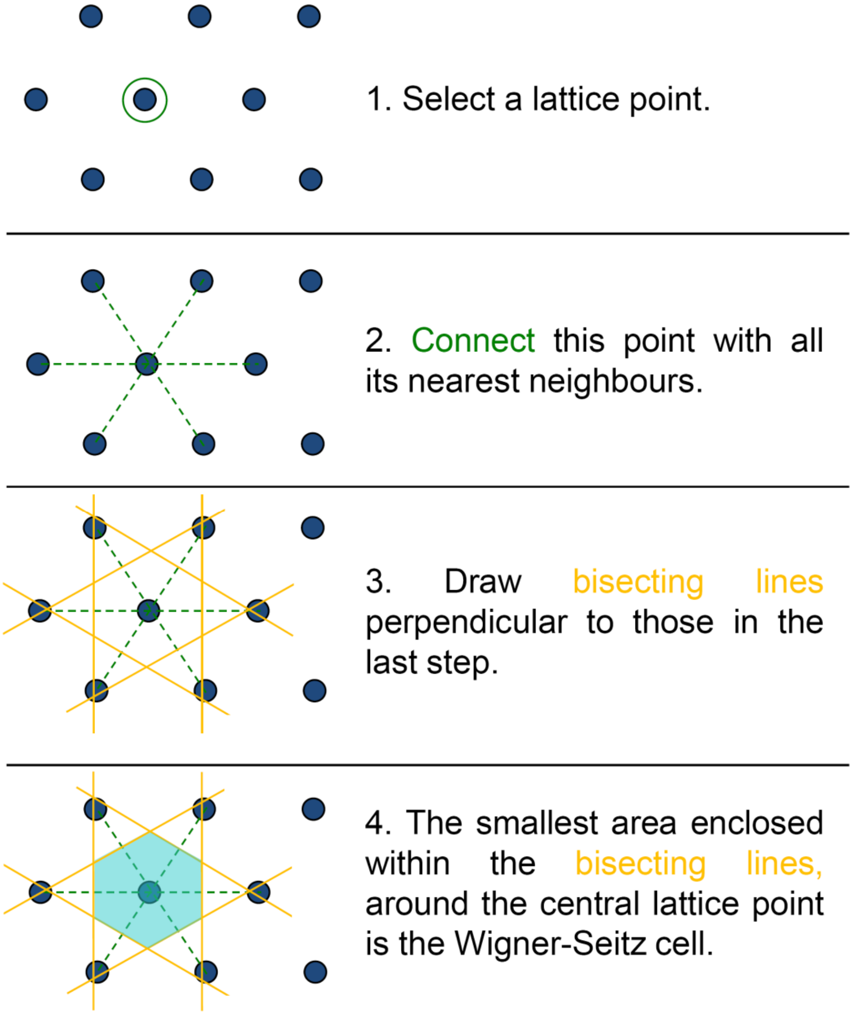

1. Select a lattice point.

2. Connect this point with all its nearest neighbours.

3. Draw bisecting lines perpendicular to those in the last step.

4. The smallest area enclosed within the bisecting lines, around the central lattice point is the Wigner-Seitz cell.

Figure 3.4: Constructing a Wigner-Seitz cell.

The Wigner-Seitz cell in real space is related to the Brillouin zone in reciprocal space. For example, the first Brillouin cell for the body-centred cubic lattice (reciprocal space) is also the Wigner-Seitz cell of a face-centred cubic lattice in real space. Indeed, when the Wigner-Seitz method is used to draw a cell in reciprocal space it will always represent a Brillouin zone.

Consider the Brillouin zone for a FCC lattice of aluminium which is the Wigner-Seitz cell for the BCC lattice in real space:

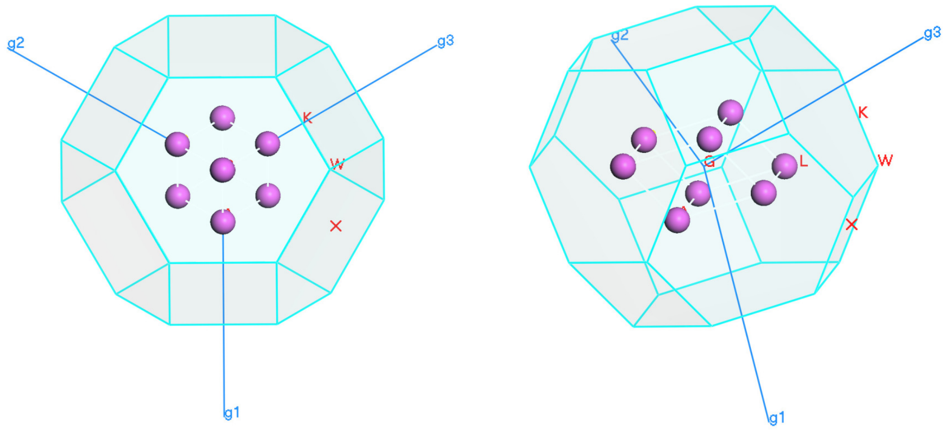

Figure 3.5: Brillouin zone for a FCC lattice of aluminium metal (shown in two different orientations). ‘G’ reciprocal lattice vectors are shown.

In these cells, there are regions of high symmetry given special designations, for example in this FCC case:

Γ / G	Centre of the Brillouin zone
L	Centre of a hexagonal face
K	Middle of an edge joining two hexagonal faces
W	Corner point
X	Centre of a square face

To perfectly represent this reciprocal space using DFT, it would be necessary to sample it at an infinite number of points. Instead, a grid of *k*-points is used to sample the Brillouin zone. If enough *k*-points are used, it is assumed that each *k*-point is sampling a small enough area of reciprocal space to compensate for the approximation of using a finite rather than infinite number of sampling positions. The most commonly used form of *k*-points is the Monkhorst-Pack grid (Monkhorst, 1976). This is a regular cubic grid in reciprocal space. For example, a grid of 4x4x4 *k*-points (64 in total) is shown within the FCC Brillouin zone below. Note that in typical calculations the DFT codes would deduce there are equivalent positions of *k*-points and atoms:

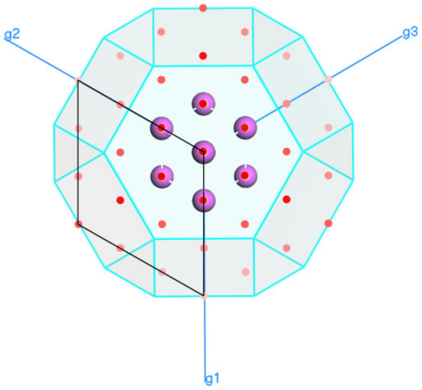

Figure 3.6: Depiction of 4x4x4 grid of *k*-points in the FCC Brillouin zone. The black rhomboid is designed to allow the eye to see the cubic nature of the *k*-point grid.

Crucially, solid state band structures are calculated by linking together energy states as found at the high symmetry points shown in Figure 3.5. Figure 3.7 for example is a band structure plot for aluminium metal:

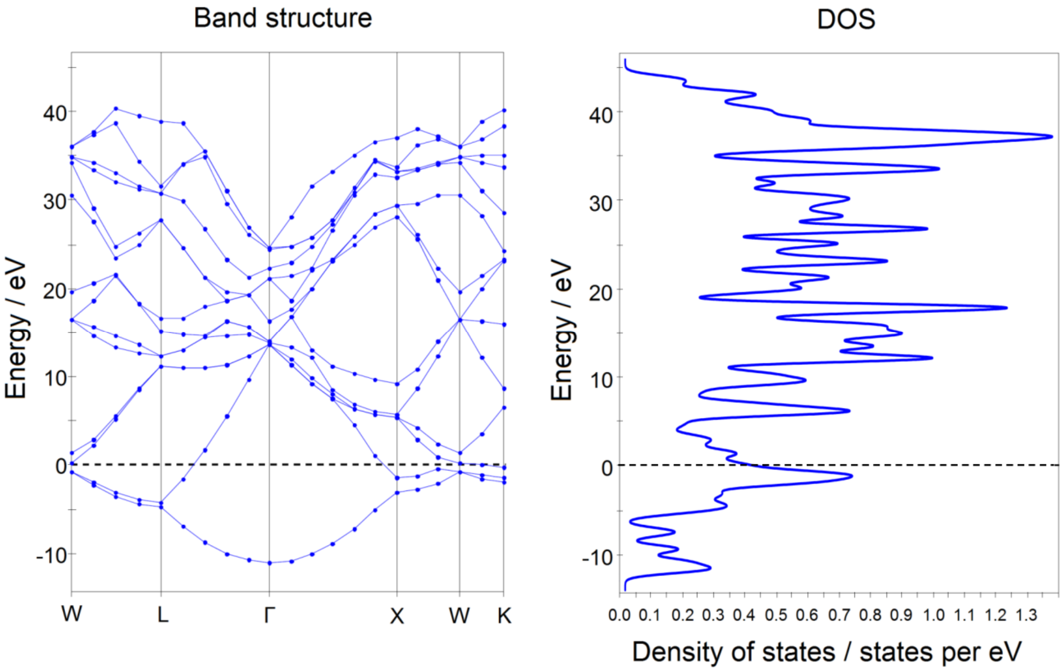

Figure 3.7: Band structure plot for aluminium metal found using CASTEP, also shown is the DOS plot.

Notice that for aluminium (a free-electron metal), as expected no band-gap is observed, and states cross the Fermi level.

3.5 Multiple scattering approach compared to DFT

3.5.1 Introductory remarks

Probably the first methodology used for modelling ELNES was the ‘multiple scattering’ (MS) approach. These codes originated from the analysis of X-ray absorption spectroscopy, initially considering simple elastic scattering of the ionised electron, which was later extended to multiple inelastic scattering. MS assumes that the absorbing atom in the centre of the solid cluster emits an electron, modelled as a spherical wave. The interference pattern of this wave and its reflections from surrounding atoms is considered to map out the density of unoccupied states (DOS). The density of states of a material in the solid state is closely related to the ELNES fine structure. Essentially the ELNES is the DOS following modification by mathematical matrix elements, a full discussion of which can be found in textbooks (Brydson, 2001), (Egerton, 1996). As the final interference pattern is a consequence of waves reflecting off atoms, removing atoms (to simulate vacancies for example) will have a controlled effect. This predictability and the time efficiency of the technique are its particular strengths (Arslan, 2002).

A commonly used formalism for the MS methodology is the Korringa, Kohn and Rostoker (KKR) approach (Martin, 2004). This formalism utilises a mathematical construct called a Green’s function. This function describes an independent particle propagating from point r to point r’ at energy E, clearly suitable given the description of MS given above. The most widely used code for the practical application of MS is FEFF (Ankudinov, 1998), (Ankudinov, 2000), (Rehr, 1992).

In terms of practicalities, the FEFF code can be operated without using an extensive parallel computing network. However, there are a number of potential problems with the MS approach, which have led some researchers to seek other methods (Mizoguchi, 2006). Cited as one issue with the MS approach is the difficulty in the selection of certain calculation parameters. More crucially, there is an argument that MS is not fundamentally suited to ELNES prediction (as opposed to EXELFS). Close to the edge onset (i.e. for electrons with relatively minimal energy upon leaving the atomic species) there are a very large number of scattering interactions which are difficult to model accurately.

This is a concern given that many experimental edges have complicated features at ionisation edge onsets.

As discussed in the introduction, electronic band structure is related to the bonding properties of the material. DFT is capable of predicting these bands structures. When compared to MS, a band structure methodology has three potential problems (Mizoguchi, 2006):

1) Introducing a core-hole (to simulate the effect of the ejected electron).
2) Avoiding artificial core-hole interactions / building complex cells.
3) The calculation of transitional matrix elements.

The major DFT codes in the field with respect to EELS are Wien2k, which is an all-electron code, and the pseudopotential code CASTEP, which elegantly uses a number of approximations to find sensible results despite only explicitly calculating valence electronic states (Clark, 2005) (Hébert, 2003), (Jorissen, 2005), (Schwarz, 2002), (Segall, 2002).

The three considerations above are now considered, with appropriate reference to those two major codes, utilised in the rest of the thesis.

3.5.2 Core-holes : Z+1 and other approaches

An early approach was the 'Z+1 approximation', in which the absorbing atom is replaced with the next higher element in the periodic table. A core-hole, which will be in close proximity to the atomic nucleus, can be considered as analogous to an additional positive charge. Therefore, the Z+1 approximation is a potentially useful approach (Buczko, 2000), (Fujikawa, 1983). The Z+1 approach can give good qualitative agreement between theoretical and experiment EELS edges. However, actual peak energies may need to be 'hard-shifted' along the energy axis (Buczko, 2000). The Z+1 approximation has been considered across a wide range of materials (Duscher, 2001). Semi-conductors and insulators were considered, and accounting for the core-hole is considered necessary for these material classes. It has been suggested in other sources that for free-electron metals this is somewhat unnecessary (Duscher, 2001), (Hébert, 2003). These principles are returned to and discussed at length throughout the thesis.

In the literature, the Z+1 approximation has been used to generate predicted edges for various systems. El-Barbary et al. studied a range of carbon materials using a DFT approach. Consider the following results (El-Barbary, 2006):

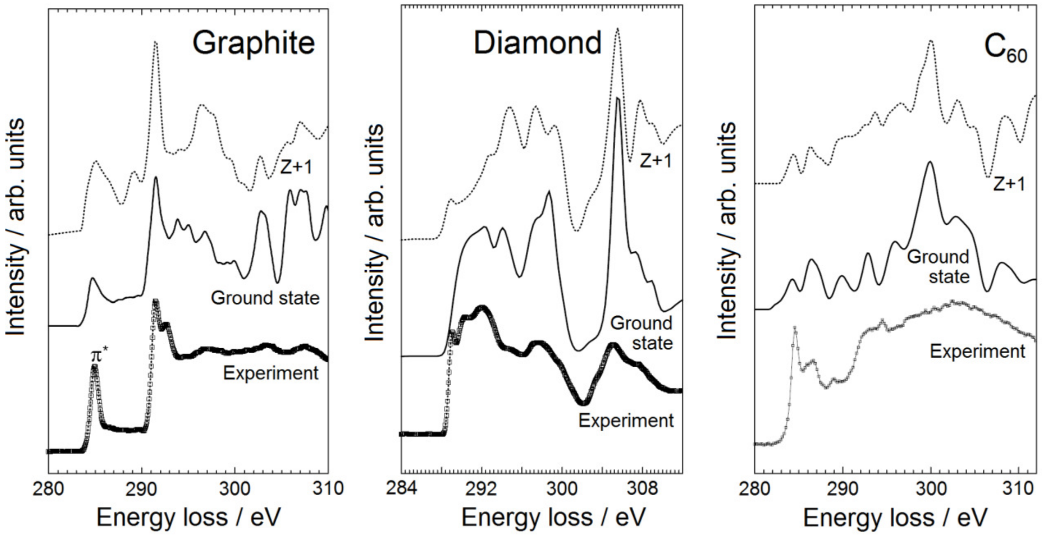

Figure 3.8: El-Barbary et al carbon allotrope K edges as labelled. Experimental spectra were acquired using a VG-HB501 STEM, 100kV, CCD camera detection, approximate resolution 0.7eV. In all cases from bottom to top experimental spectra, calculated ground state spectra, calculated spectra with Z+1 approximation used to simulate the core-hole (El-Barbary, 2006).

Observe firstly that the agreement with experiment is not particularly strong, perhaps with the exception of graphite. The authors acknowledge that the Z+1 approximation does not generally alter the spectra in these instances, with the exception of diamond. In this case the Z+1 approximation leads to an exciton peak (at 289eV) not seen for the ground state calculation.

Other researchers have been able to use the Z+1 to generate stronger agreement with experiment, comparable to that obtained by using an entirely revised electronic configuration. Lazar et al. considered various transition metal nitrides (Lazar, 2008).

The authors used DFT calculations to model the nitrogen K edge in bulk titanium nitride, and compared results for a ground state calculation (making no attempt to model the core-hole), a full electron core-hole and a Z+1 approximated core-hole to an experimental result:

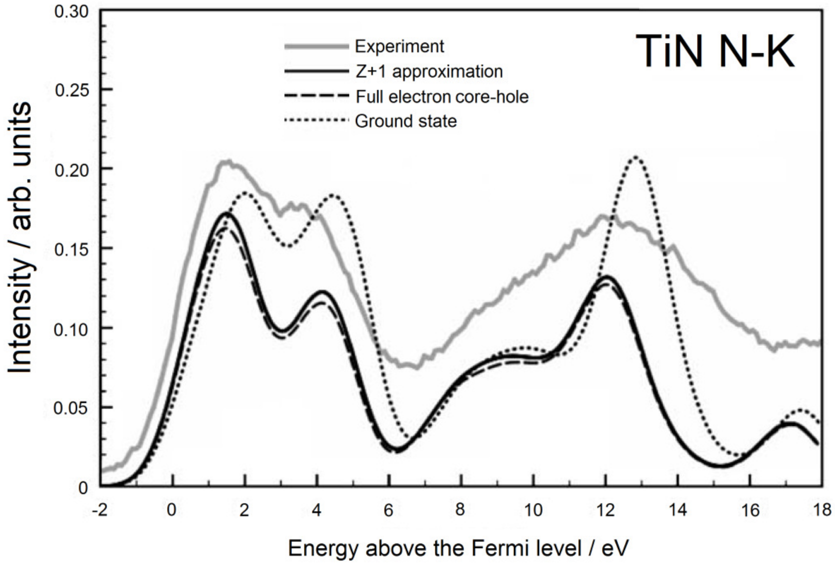

Figure 3.9: DFT calculations used to model the nitrogen K edge in bulk TiN, core-hole approximations as labelled (Lazar, 2008).

In terms of peak ratios (comparing to the experimental result) the usage of a core-hole approximation improves the agreement with experiment as compared to a ground state result. Furthermore, the Z+1 approximation result is highly similar to a calculation for a fully revised excited electronic configuration.

There are further examples in the literature of the Z+1 approximation yielding similar results to calculations for revised electronic configurations, for example the oxygen K edge in TeO_2 (Jiang, 2006):

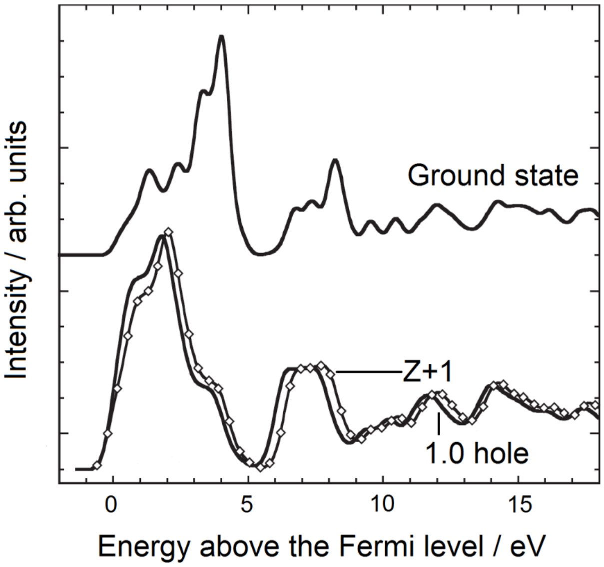

Figure 3.10: Models for the oxygen K edge in TeO_2, comparing different core-hole approximations. Again the Z+1 approximation provides a close agreement with a calculation for a fully modified electronic configuration (Jiang, 2006).

The Z+1 approximation has further been applied to the calculation of L edges, generating good agreement with experiment. For example the $L_{2,3}$ edge (silicon crystal) (Buczko, 2000):

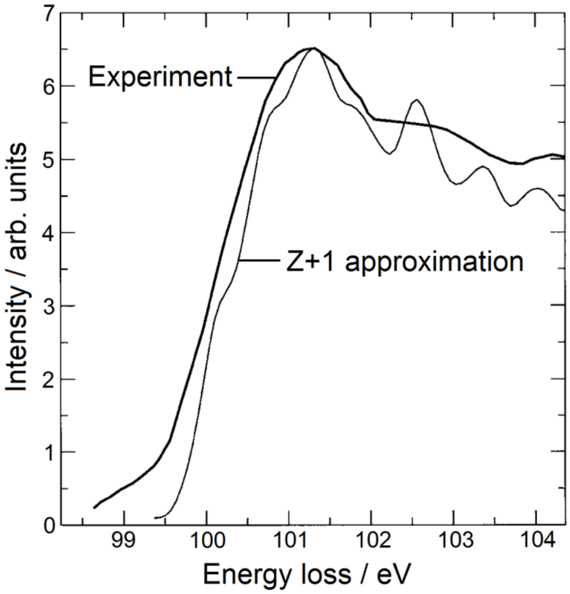

Figure 3.11: Comparison of modelled Z+1 Si $L_{2,3}$ edge with experiment (Buczko, 2000).

There are however a number of issues with the Z+1 approximation. Firstly, it suffers from a lack of specificity. One cannot specify the exact location of the core-hole (for example 1*s* or 2*p* orbital). Furthermore, it is not possible to use the Z+1 approximation to model the effect of a ‘fractional’ core-hole. For example, it has been argued a 0.5 electron core-hole (Slater’s transition state) is a valid means of modelling final state effects (Köstlmeier, 2001). For example, the Slater transition state has been shown to improve predictions of threshold energies (Paxton, 2003).

Further, as described subsequently (in the detailed description of codes used) it is not a complex process (as a user of the code) to carry out a full calculation for a revised electronic configuration as opposed to using the Z+1 approximation.

3.5.3 Other considerations in ELNES calculations

The second concern for the usage of DFT codes is avoiding artificial interactions between the core-hole created in our theoretical models, and creating complex cells. Core-hole interactions are returned to throughout the thesis, but simply put, to avoid artificial core-hole interactions large cells must be used. Similarly, a large number of atoms must be used to simulate complex systems such as defects and interfaces. Before the ready availability of paralleling computing facilities such calculations were not tractable.

The final consideration for accurate calculations is that DFT codes should find correct transition matrix elements. This has been successfully accomplished for modern DFT codes, described in sections 3.7 and 3.8.

In summary, in terms of the concerns for the usage of DFT codes as compared to an MS approach:

1) Introducing a core-hole (to simulate the effect of the ejected electron).

This can be accomplished relatively straightforwardly in modern DFT codes, or the Z+1 approximation can be used despite some potential problems.

2) Avoiding artificial core-hole interactions.

Large cells must be used, calculations of this sort being tractable given the ready availability of parallel computing facilities.

3) The calculation of transitional matrix elements.

This will be discussed subsequently for the Wien2k and CASTEP codes.

3.5.4 Other core-hole modelling strategies

de Groot has developed a charge-transfer multiplet methodology for the calculation (in particular) of L edges (and higher), arguing that traditional DFT or MS does not correctly account for the strong overlap of core and valance state wavefunctions (de Groot, 2008).

Consider an example de Groot presents (de Groot, 2005). In NiO, for a Ni $L_{2,3}$ edge a partially occupied $2p^5$ core-state will be present upon excitation by the incident electron beam. In NiO however, there is already a partially filled 3*d*-band, of configuration $3d^9$. The 2*p* and 3*d* core-holes interact significantly (via radial wavefunctions). Therefore, two-electron integrals (i.e. multiplets) are utilised in de Groot's code for the calculations of L edges and above.

In other systems, for example alkali metal halides such as LiF, there is a suggestion that upon excitation, an exciton pair is formed with the core-hole and ejected electron remaining strongly correlated (Rohlfing, 2003). An ideal methodology therefore in these cases might be the Bethe-Salpeter equation

(BSE), which explicitly accounts for the interaction of the excited electron and the electron-hole (Tanaka, 2009).

3.6 Previous observations regarding the core-hole as modelled by DFT

3.6.1 The core-hole effect

Previous literature has discussed what impact a core-hole should have on a predicted edge, and that is discussed at this juncture (Gao, 2008), (Henning, 1996), (Jiang, 2003).

Generally speaking, the inclusion of a core-hole is thought to shift edge features towards the Fermi level, and increase the intensity of features close to the Fermi level. These effects can be rationalised thus. When a core-state electron is removed, the electrostatic attraction on the remaining electrons from the nucleus is higher. This shifts the electronic states closer to the Fermi level. Similarly, this greater electrostatic force leads to the electronic states being contracted and pulled closer together, thus increasing the intensity of the edge close to the Fermi level.

These effects have been observed in a variety of different materials classes and compounds, a selection of examples being given in Table 3.2:

Class of material	**Examples in literature**
Ionic	• LiF, BeO, BN (1st row K edges) (Gao, 2008). • AlN (both edges) (Holec, 2008). • MgO, GaN, InN, ZnO (O and N K edges) (Lindner, 1986), (Mizoguchi, 2006).
Covalent	• SiC, diamond (1st row K edges) (Gao, 2008). • Graphite (carbon K edge) (El-Barbary, 2006). • Silicon (Si K edge) (Gao, 2009).

Table 3.2: Materials classes and selected examples in the literature where DFT modelling has reproduced the described core-hole effect.

In different materials classes, the magnitude of this core-hole effect is considered to be different, general trends being as given in Table 3.3 (Gao, 2008):

Class of material	**Discussion**
Ionic	Core-hole effect is more important for cations in ionic compounds.
Covalent	Core-hole effect is more important for elements with lesser electronegativity.
Same element in different compounds	Core-hole effect is more significant if the element is losing electrons.

Table 3.3: Suggested trends in terms of core-hole impact, derived from first row elements (Gao, 2008).

These effects are thought to occur because for any species already electron-deficient, further removing an electron in the form of a core-hole will have a comparatively larger effect than if the system was electron rich.

3.6.2 The importance of including a core-hole

The two codes considered in this work can account for a core-hole, and DFT codes have shown the nature of its impact and rationalised this. However, this does not necessarily answer the question of whether it is required (in all cases) to accurately model ELNES, and obtain for example good agreement with experiment.

The literature is heavily divided on this subject. The divisions might roughly be described thus;

- A view that a core-hole should always be included as this phenomenon will always occur in experiment. This is particularly true if quantitative effects are to be considered.
- A reasoning that in certain systems for known physical reasons a core-hole should definitely not be included.
- A pragmatic approach that good agreement with experiment can often be obtained using a ground state calculation.

The latter two viewpoints are not to be confused. The following papers have at least strongly suggested a core-hole should ideally be used in all cases (Mizoguchi, 2009), (Mo, 2000), (Zhu, 2005). Of course it is acknowledged that if a core-hole is to be included, a supercell must be used as to avoid artificial core-hole interactions, unless the standard unit cell is large enough.

In a short conference proceeding, Rez presented a different view, suggesting that there are specific cases in which a core-hole should definitely NOT be included, as in fact it does not represent the situation in experiment (Rez, 2006). Rez discusses the relevance of the core-hole lifetime with regard to EELS modelling of free-electron metals (FEMs) in particular. It is argued the core-hole relaxes extremely quickly, as do changes to local DOS, in such a timescale that the changes are not observable using the microscope, and therefore a core-hole should not be used.

This is somewhat different to the pragmatic viewpoint expressed in much literature, that a ground state calculation can often match experiment as well as a supercell / core-hole calculation, due to high screening of the core-hole (Muller, 2009). Listed below are examples of systems reported in the literature in which ground state calculations have been observed to give reasonable agreement due to ‘screening’ type effects:

- Aluminium K edge (this thesis and (Seabourne, 2009)).
- TiC, ZrC, HfC, VC, NbC, TaC (carbon K edges) (Scott, 2001).
- CrAlYN/CrN multilayer coatings (nitrogen K edges) (Ross, 2010).
- Nickel silicides (Ni and Si L edges) (Kawasaki, 2008).
- MgO (various edges) – reproduced ‘satisfactorily’ in the ground state (Mizoguchi, 2000).

Core-hole effects, and the inclusion thereof will be returned to throughout the thesis, and discussed as part of the conclusions.

3.7 Wien2k EELS modelling

3.7.1 Introduction to the Wien2k code

Wien2k is an all-electron DFT code, which uses the (linear) augmented plane wave (LAPW) method in electronic structure calculations, solving the Kohn-Sham formalism of DFT (Kohn, 1965), (Schwarz, 2002). The basis of this method is the separation of a cell into non-overlapping spheres and an interstitial region, a plane wave expansion being used for the latter. Throughout all calculations reported the generalised gradient approximation (GGA) was used to find the exchange-correlation functional (Perdew, 1996).

3.7.2 EELS calculations using Wien2k

Wien2k finds the EELS result as the double differential scattering cross section (DDSCS), which contains an expression for the transition matrix elements—which is especially simplified when the dipole approximation is in place (Brydson, 2001). The method used to find the DDSCS using Wien2k has been reported (Hébert, 2003), (Jorissen, 2005):

$$\frac{\delta^2\sigma}{\delta\Omega\delta E} = \left[\frac{4\gamma^2}{a_0^2 q^4}\right]\frac{k_f}{k_i}\sum_{i,f}\left|\left\langle f\left|e^{i\vec{q}\cdot\vec{r}}\right|i\right\rangle\right|^2 \delta(E - E_f + E_i) \qquad (3.6)$$

A summation is performed over all occupied initial and empty one-electron final states described by the wavefunctions $|i\rangle$ and $|f\rangle$ (Hébert, 2003). These wavefunctions are evaluated numerically using the Kohn–Sham formalism, following self-consistent field optimisation of the GGA approximated exchange-correlation potential and other approximations involved. The usage of a plane wave basis set allows DOS to be found and separated into partial-DOS components, and matrix elements found (Blöchl, 1994).

A core-hole (as part of an ionisation edge) can be directly accounted for by modifying the all-electron configuration of the atom in question.

3.7.3 Practical applications of the Wien2k code

This section aims to illustrate previous uses of the Wien code in the literature, and establish the capabilities of the code. It is however necessary to give some background as to its usage. The original code was simply Wien, which was then subject to various minor and major updates as it became Wien95, Wien97 and Wien2k (Schwarz, 2002), (Blaha, 1990).

As discussed above, strictly speaking DFT is a ground state methodology, i.e. it proposes that ground state electron density can be used to deduce system properties. Therefore initially, the code was not designed to perform calculations of any kind more than a few eV above the Fermi level. Various work was performed utilising system energy calculations for example. Other areas of investigation have been dielectric functions, geometry optimisation and ground state band structure calculations (Ambrosch-Draxl, 1997), (Blaha, 1995), (Kohler, 1996). (Persson, 1998), (Zhang, 1998).

The developers of the code and their associates responded to requests for the capability to calculate results above the Fermi level. Initially, X-ray absorption spectroscopy could be modelled, the physics of this being very similar to EELS. Ultimately, a specific ELNES calculation module was added to the Wien2k code (Jorissen, 2005). The following can be controlled as part of the calculation:

- Lattice parameter and atomic positions.
- Whether or not to account for transitions forbidden by the dipole selection rule.
- Whether or not to consider anisotropic effects.
- The inclusion or otherwise of a core-hole, and the 'nature' of that hole. For example a 0.5 electron core-hole etc...
- The position of the core-hole (which atomic shell it is in).
- The type of broadening applied to the ELNES result (discussed subsequently).

This section of the thesis considers some extreme capabilities of the Wien2k code in terms of ELNES modelling. The following areas are considered in more depth:

- Anisotropic effects.
- Ability to differentiate between allotropes and polymorphs.
- Modelling non-stoichiometric compounds and mixed alloys.

It is the demonstrated success (in the literature) of the Wien code to achieve such advanced modelling aims that has made the code the benchmark in DFT-based ELNES modelling.

The oxygen K edge in rutile-TiO_2 ($P4_2/mnm$) displays anisotropic effects. Wien2k is sufficiently advanced to be able to model this. For example, consider how the oxygen K edge alters when the orientation of the beam (relative to the crystal) is changed from (001) to (100) and then to (110) (Mauchamp, 2008):

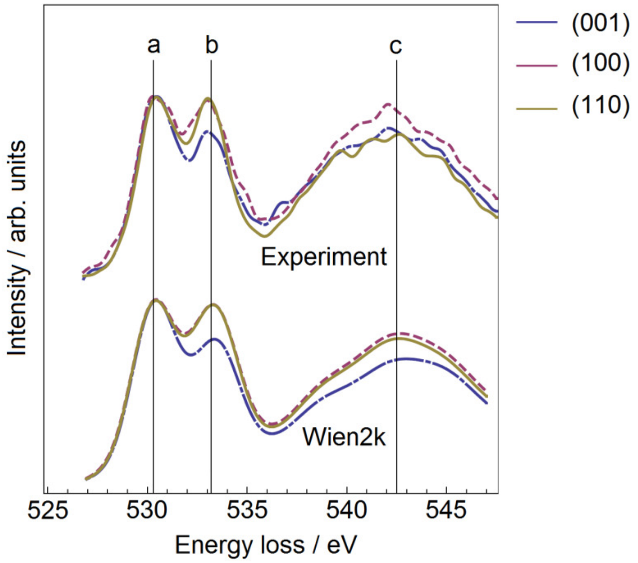

Figure 3.12: Anisotropic effect of the oxygen K edge in *r*-TiO_2 (Mauchamp, 2008).

As can be observed Wien2k successfully reproduces the change in peak ratios when tilting from the (100) to (001) orientation.

Similarly, consider the oxygen K edge in V_2O_5 (Su, 2003). Using a Philips CM200, ELNES was recorded, with the electron beam parallel the *c* direction of the V_2O_5 crystal. The experiment was carried out at various collection angles, as illustrated in Figure 3.13. Shown also in the figure are the equivalent modelling results found using Wien2k.

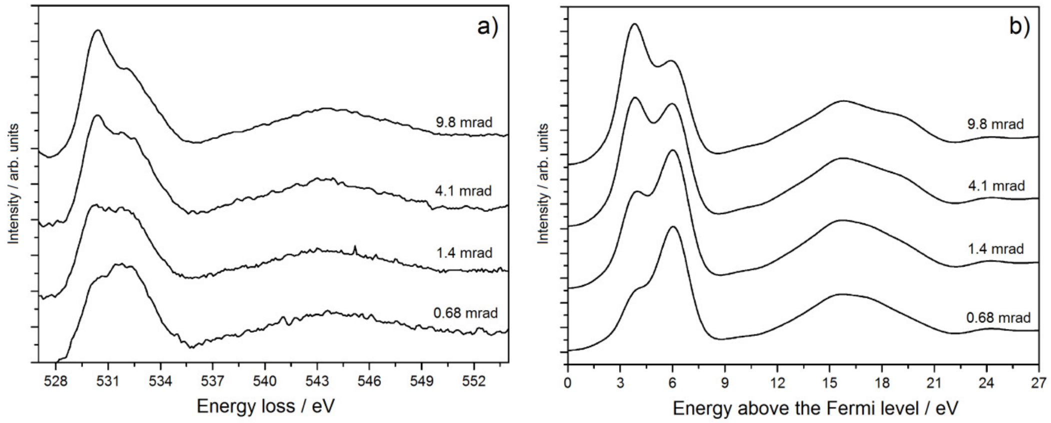

Figure 3.13: a) Oxygen K edge ELNES for V_2O_5, with various different collection angles, as labelled. b) Equivalent Wien2k modelling results (Su, 2003).

As can be observed, Wien2k is capable of predicting different fine structure at the different collection angles, as expected for the system. As the dipole selection rule begins to break down, additional final states are allowed. For a beam initially parallel to the crystal *c* axis, additional transitions into final π* states alter the ELNES.

Wien2k is furthermore sufficiently sensitive (as is experimental EELS) to differentiate between allotropes and polymorphs. An archetypal example is that of diamond and graphite (Dadsetani, 2010). Wien2k can replicate the experimental carbon K edges for these two allotropes, as well as for a carbon nanotube:

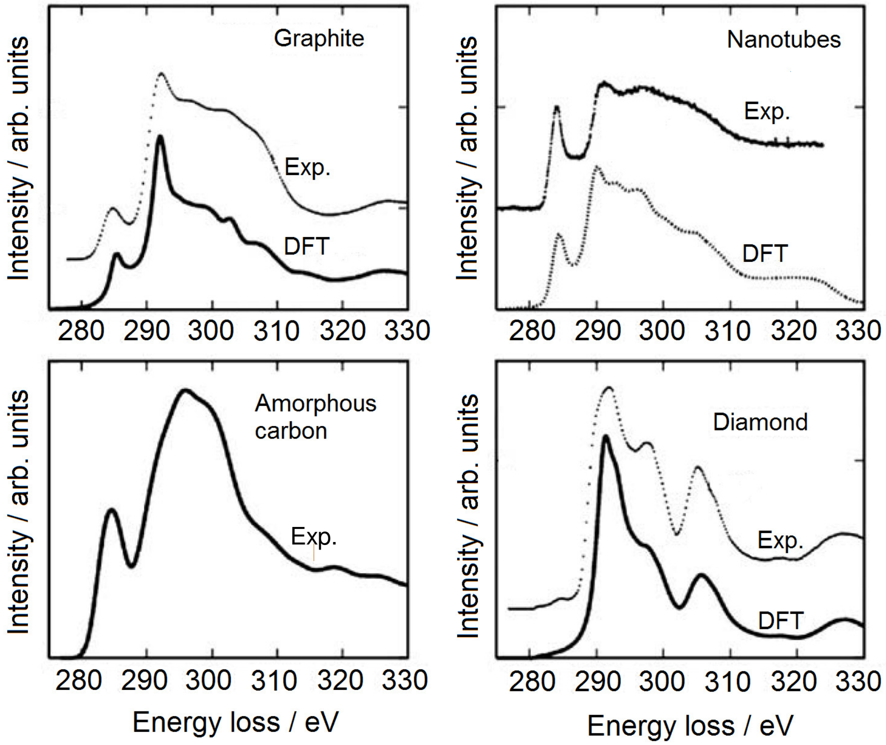

Figure 3.14: Carbon K edges for various allotropes as labelled, comparing experiment and Wien2k predictions (Dadsetani, 2010). An experimental result for amorphous carbon is shown for reference purposes.

Wien2k can also differentiate between cubic and hexagonal polymorphs, for example in GaN (Lazar, 2004).

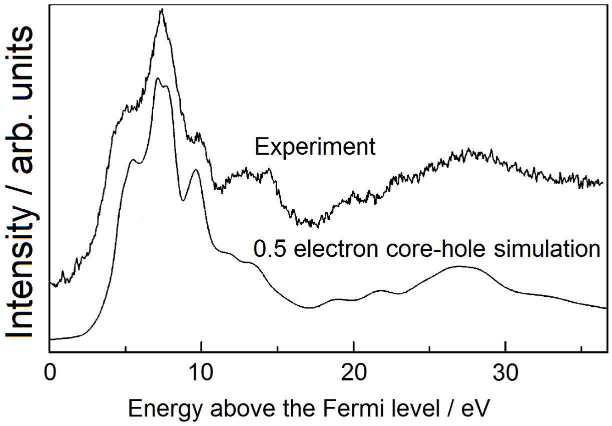

Figure 3.15: Comparison of experimental nitrogen K edge (for hexagonal GaN) with a theoretical simulation utilising a 0.5 electron core-hole (Lazar, 2004).

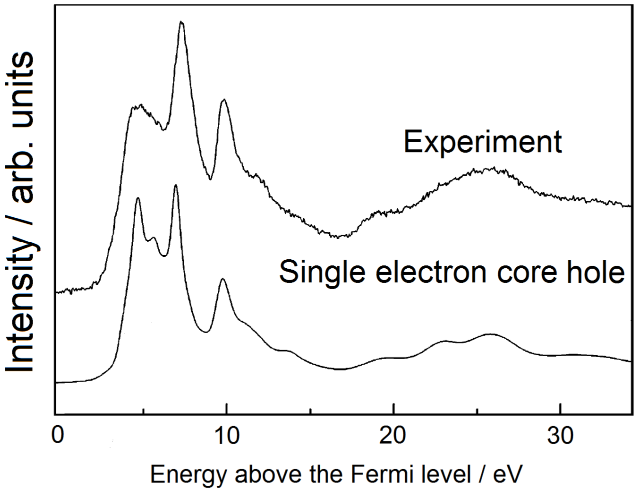

Figure 3.16: Comparison of experimental nitrogen K edge (for cubic GaN) with a theoretical simulation utilising a full electron core-hole (Lazar, 2004).

These examples also contain a system for which the strongest agreement with experiment is obtained via the usage of a 0.5 electron core-hole.

Vacancies are returned to in Chapter 6 of the thesis, with Wien2k having been used to model them in TiN_X (Tsujimoto, 2005). In this work, the authors modelled $TiN_{0.97}$, placing the defect in different sites relative to the core-hole, and considering how the changes in predicted spectra compared with experiment:

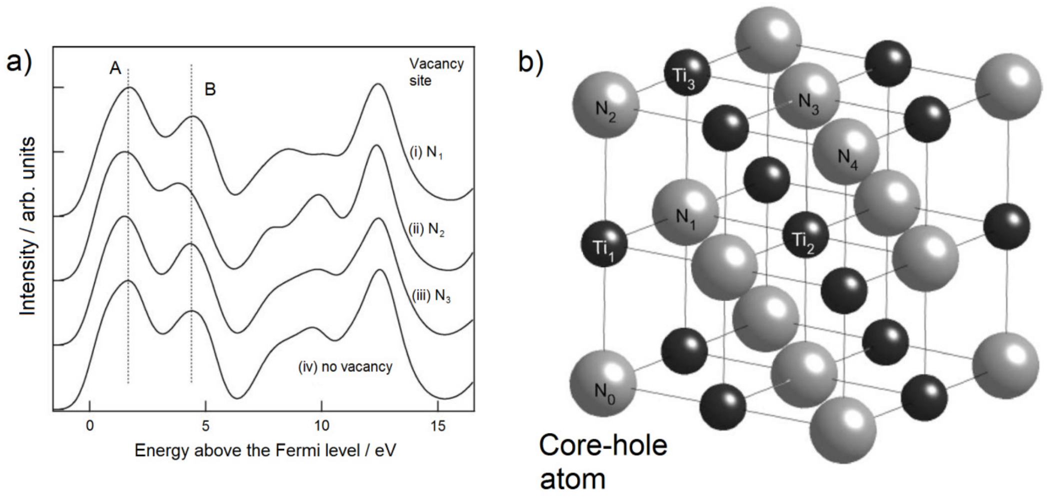

Figure 3.17: a) Nitrogen K edge predictions for $TiN_{0.97}$ using Wien2k for defect positions as labelled, relative to the 'core-hole' atom, b) Depictions of defect positions (Tsujimoto, 2005).

As can be observed, different defect positions alter the separation of peaks A and B. The authors suggest that only in position N_2 is a significant change in the edge prediction observed, rationalised in terms of the bonding character of the various peaks. These concepts are returned to in section 6.4 of this thesis.

In another level of sophistication, Wien2k has also been used to model 'mixed alloy' type systems of the form $Al_xGa_{1-x}N$ (Holec, 2008):

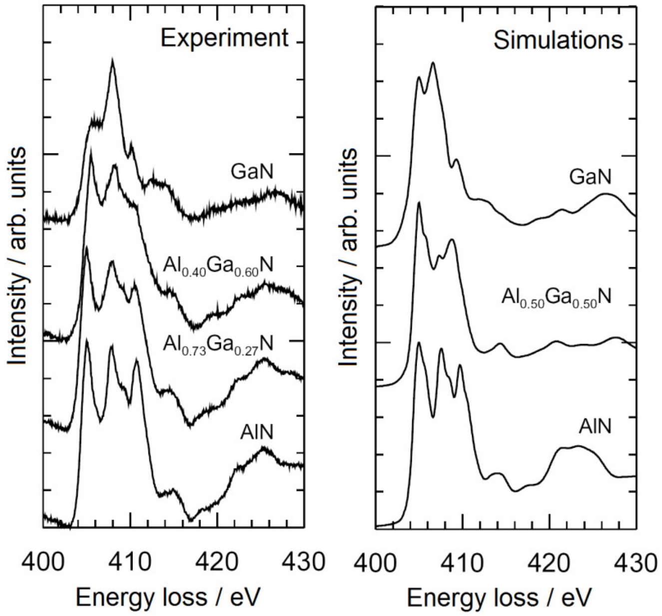

Figure 3.18: Comparison of experimental nitrogen K edges for various $Al_xGa_{1-x}N$ systems with a selection of theoretical simulations (Holec, 2008).

The code can be used to find reasonable agreement for this mixed alloy series, by using a symmetrical distribution of the various elements. This approach is adopted in new work for this thesis in Chapter 8.

3.8 CASTEP EELS modelling

3.8.1 Introduction to the CASTEP code

CASTEP is a DFT code using a plane wave basis set, with the added subtlety of using pseudopotentials in the Kohn–Sham DFT formalism (Kohn, 1965), (Payne, 1992). Pseudopotentials use approximations to model the atomic-like core wavefunctions, and only actively calculate valence electron states. Figure 3.19 illustrates this.

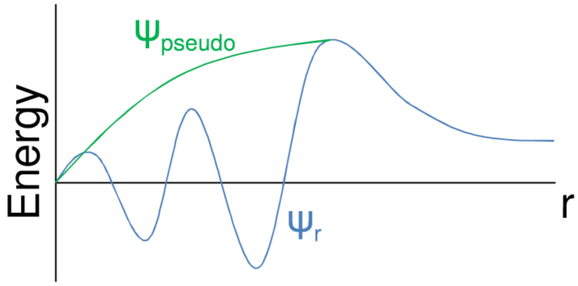

Figure 3.19: Illustrating pseudopotentials using wavefunction plots for a hypothetical atom.

ψ_r represents the true all-electron wavefunction. As can be observed, near the 'core' of the atom the real wavefunction varies rapidly. The pseudowavefunction 'smooths' over this region as illustrated, thus leading to a faster calculation.

It is necessarily to briefly justify why this approximation is valid. Each electronic state of the system is orthogonal to all the other states. As more and more states are filled, the wavefunctions begin to have more and more nodes in order to fulfil this condition. A large number of these nodes lie close to the nucleus, and the wavefunctions in this core-region are not subject to large changes. Most 'chemistry' is related to valence states, and indeed many of the core-states are highly localised in nature.

Therefore, wavefunctions in the core region are 'pseudised' and replaced with a pseudopotential. Therefore only the non core-state wavefunctions must now be orthogonal, thus reducing the number of required nodes, considerably simplifying the calculation.

The use of pseudopotentials dramatically reduces the number of plane waves required to represent the wavefunctions, whilst still giving good results. Throughout all calculations reported the generalised gradient approximation (GGA) was used to find the exchange-correlation functional (Perdew, 1996). The pseudopotential method can carry out system energy calculations (calculating for example energies of formation) with similar results to all-electron calculations. The possibility of introducing a core-hole despite using pseudopotentials is discussed subsequently.

3.8.2 EELS calculations using CASTEP

A customised version of CASTEP 4.1 supplied by the developers was used, although this was shown to produce identical EELS results to CASTEP 4.3, which has the EELS calculation module explicitly included. Subsequent versions of CASTEP (4.4, 5.0 etc...) also have the EELS module explicitly included.

The physical background behind the additions to the code has been reported by Gao et al., a summary of which follows (Gao, 2008). Firstly, the edge being found is very important. For a K edge, the dipole selection rule will mean *p* orbital partial DOS must be considered. The second key consideration is the prediction of transition matrix elements between the initial and final states, with existing work having addressed this consideration (Jayawardane, 2001) (Pickard, 1997). In particular, Pickard's doctoral thesis expands on the concept of a projector augmented wave (PAW) approach, initially established by Blöchl (Blöchl, 1994). This approach is designed to find matrix elements, and also separate the plane wave model DOS into partial DOS results for each class of orbital (for example *p* or *d*). As usual with matrix elements some expression of 'probability' is given for a transition between an initial and final state. As acknowledged, the initial state wavefunction can be calculated from an all-electron approach, based on atomic-like states. The developers in this case seek to use the PAW approach to calculate the 'excited' final state as a pseudowavefunction, allowing an expression for the matrix elements to be found.

To incorporate the core-hole, one uses an on-the-fly (OTF) customisable pseudopotential in the calculations. Although some of the methodology associated with CASTEP-EELS has been firmly established for some time, their integration into the accessible CASTEP code is relatively recent. There is little literature utilising the code. Indeed, one of the major developments of this thesis was to benchmark and consider what could be accomplished using the code.

However, there has been at least one major review printed discussing the integrated EELS module of CASTEP (Mizoguchi, 2009a). The aluminium K edge in aluminium nitride is returned to subsequently in the thesis.

In the review by Mizoguchi et al., the N K-edge in AlN was found, showing good agreement with experiment, also showing a distinct alteration in the predicted result for a core-hole result as compared to the ground state:

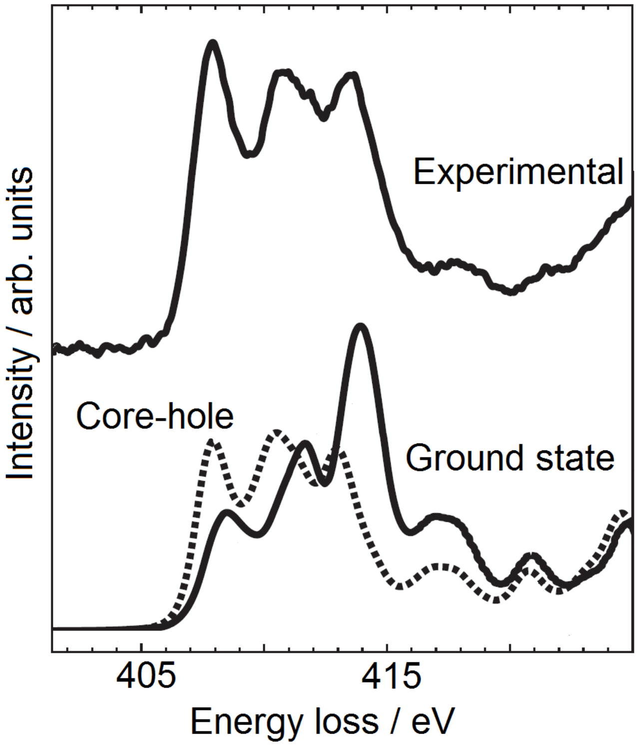

Figure 3.20: AlN nitrogen K edge predictions and comparison with experiment (Mizoguchi, 2009a).

3.9 Summary of modelling aims and background

Figure 3.21 summarises the background to the research undertaken in this thesis, and principal aims:

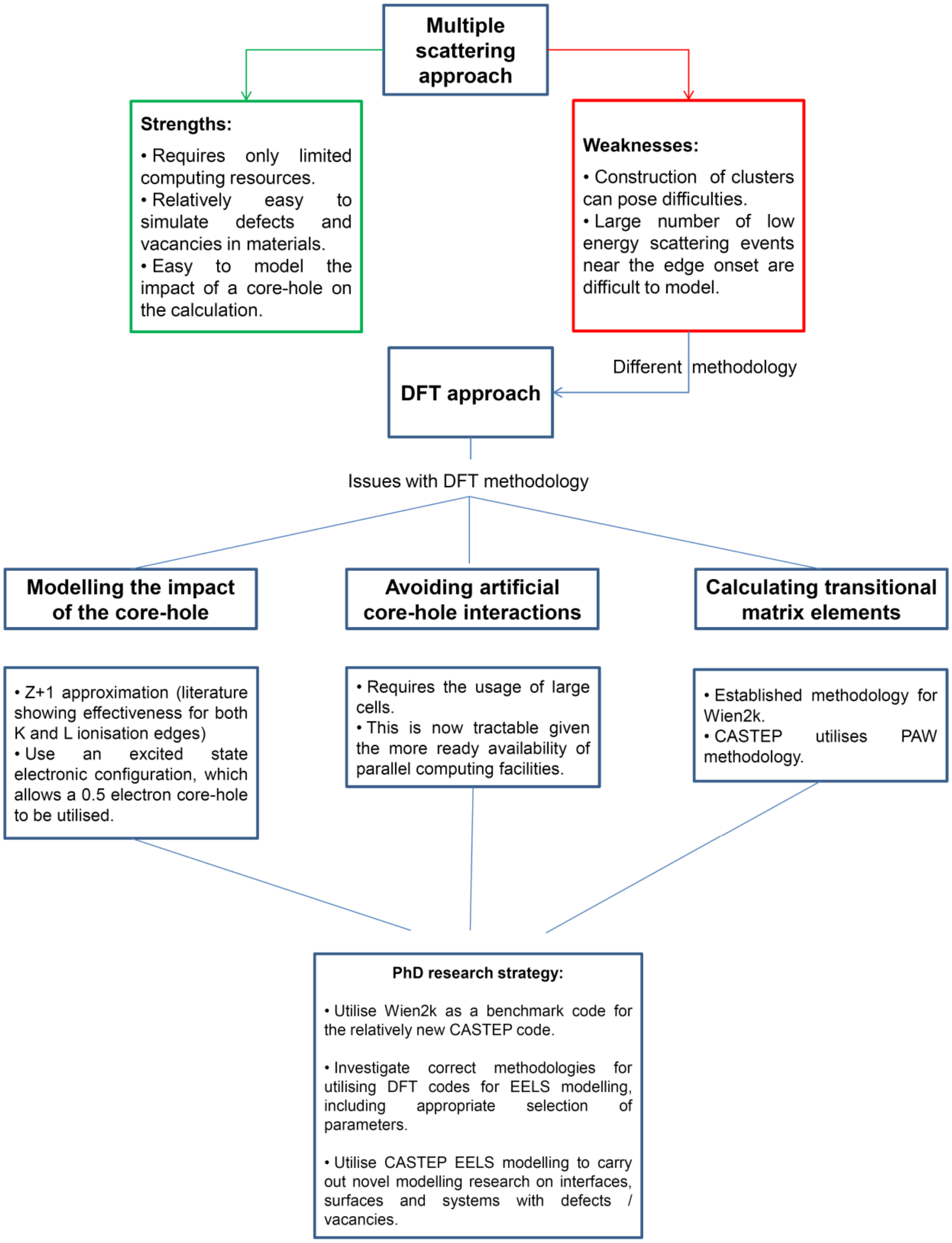

Strengths:

- Requires only limited computing resources.
- Relatively easy to simulate defects and vacancies in materials.
- Easy to model the impact of a core-hole on the calculation.

Weaknesses:

- Construction of clusters can pose difficulties.
- Large number of low energy scattering events near the edge onset are difficult to model.

- Z+1 approximation (literature showing effectiveness for both K and L ionisation edges)
- Use an excited state electronic configuration, which allows a 0.5 electron core-hole to be utilised.

- Requires the usage of large cells.
- This is now tractable given the more ready availability of parallel computing facilities.

- Established methodology for Wien2k.
- CASTEP utilises PAW methodology.

PhD research strategy:

- Utilise Wien2k as a benchmark code for the relatively new CASTEP code.

- Investigate correct methodologies for utilising DFT codes for EELS modelling, including appropriate selection of parameters.

- Utilise CASTEP EELS modelling to carry out novel modelling research on interfaces, surfaces and systems with defects / vacancies.

Figure 3.21: Summary of background research and literature, and aims for PhD research.

Chapter 4

Initial modelling studies and experiments

Chapter 3 established the theoretical background behind DFT, as well as the Wien2k and CASTEP codes. The first aim of this chapter is to outline some of the capabilities of the codes, including geometry optimisation, and accounting for spin polarisation. Initial testing of the CASTEP code is also presented, including a discussion of lifetime-based broadening effects.

The second aim of the chapter is to outline the correct procedure for using DFT codes to model ELNES results, in terms of properly choosing the key parameters involved in modelling; the basis-set size, and sampling density. Finally, the concept of a ‘supercell’ is rationalised, the physical basis behind the concept being explained.

4.1 Capabilities of DFT codes and geometry optimisation

4.1.1 System energies and geometry

DFT codes are able to find system energies. This has a variety of potential applications. For example, one can find reaction enthalpies by comparing the system energies of the reactants and products.

Furthermore, one can begin to predict structures *ab initio*. Consider aluminium metal, in the face-centred cubic (FCC) structure. The experimental lattice parameter is 4.05Å. One can find the system energy with this lattice parameter, and indeed any of choice. In this experiment, a range of lattice parameters from 3.95Å to 4.15Å were tested, and system energies found using the Wien2k code. The energy minimum was indeed centred around the experimental lattice parameter – thus providing *ab initio* evidence for the value.

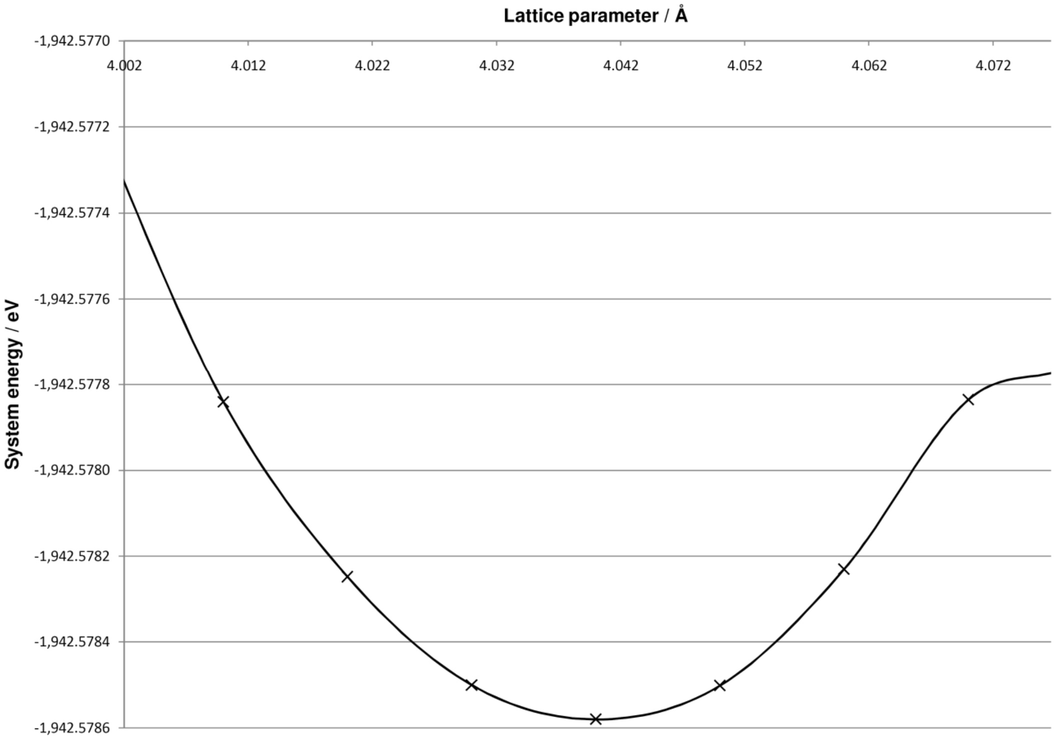

Figure 4.1: Depiction of system energy variation with lattice parameter alteration – single cell ground state calculation using Wien2k.

Using Wien2k, the energy minimum was predicted at 4.04Å, only 0.2% different from the experimental value.

Using DFT codes, system 'geometry optimisation' can be performed automatically under certain circumstances. The Broyden-Fletcher–Goldfarb–Shanno (BFGS) methodology is often used, applied in a fashion described by Pfrommer et al. (Pfrommer, 1997).

As Figure 4.1 indicates, the region immediately around an energy minimum (i.e. the energy surface) is 'quadratic' in nature providing changes to the lattice or atomic positions are small. When this is true, a so-called 'Hessian matrix' can describe the energy surface (this is the matrix of second derivatives of the energy with respect to position):

$$H = \begin{pmatrix} \partial^2 E / \partial x_1 \partial x_1 & & \partial^2 E / \partial x_1 \partial x_N \\ & \ddots & \\ \partial^2 E / \partial x_N \partial x_1 & & \partial^2 E / \partial x_N \partial x_N \end{pmatrix} \tag{4.1}$$

This matrix is not however known before the calculation begins, so the BFGS algorithm is used to approximate ‘H’, with increasing quality with successive iterations, until an energy minimum is found with certain user-defined constraints.

4.1.2 The importance of geometry variation with regard to the EELS result

In the previous section, using Wien2k the lattice parameter of FCC aluminium was optimised. However – it has been questioned in previous work how significant this optimisation will be in terms of predicted EELS results (Pickard, 1997). Clearly, if one is carrying out a reaction enthalpy calculation, or another equally precise energy calculation then cell geometry will be crucial, but small variations are unlikely to be crucial in EELS calculations as is illustrated subsequently. Often, predicted spectra are ‘hard-shifted’ on the energy axis to align with experiment, further lessening in the importance of geometry optimisation.

Using CASTEP, predicted aluminium K edges were found (in the ground state) at the experimental lattice parameter (4.05Å), and also; 3.95Å, 4.00Å, 4.10Å and 4.15Å – representing a 2.5% variation of the lattice parameter, ten times the alteration that occurred when the ‘geometry optimisation’ process was carried out above. Figure 4.2 illustrates the resulting edge predictions.

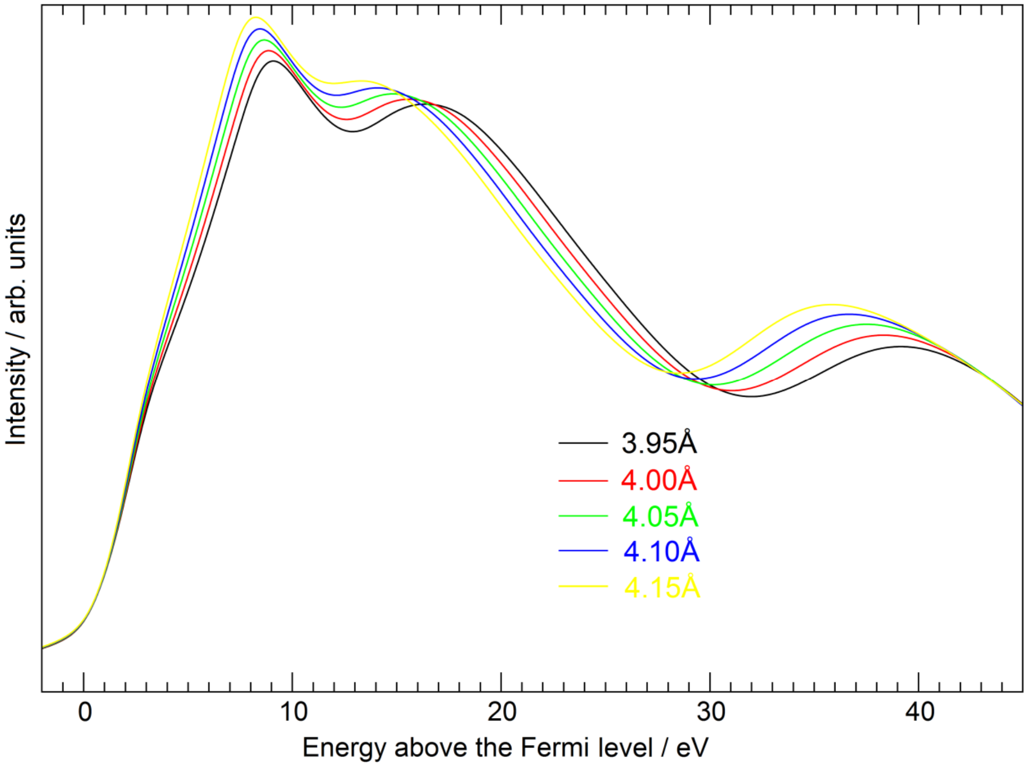

Figure 4.2: Effect on predicted aluminium K edge upon lattice parameter variation by approx. 2.5%. Shown with the addition of energy-dependent final state lifetime broadening (discussed subsequently). The experimental lattice parameter result is shown in green.

Qualitatively speaking, each result shows the same number of peaks, though the energy separations do vary with lattice size. However, these variations are extremely large compared to typical variation from experimental lattice parameters upon geometry optimisation, typically only a few per cent. Therefore, in Fig. 4.3 the predicted K edge for the experimental lattice parameter is compared to that for a lattice parameter of 4.04Å resulting from geometry optimisation.

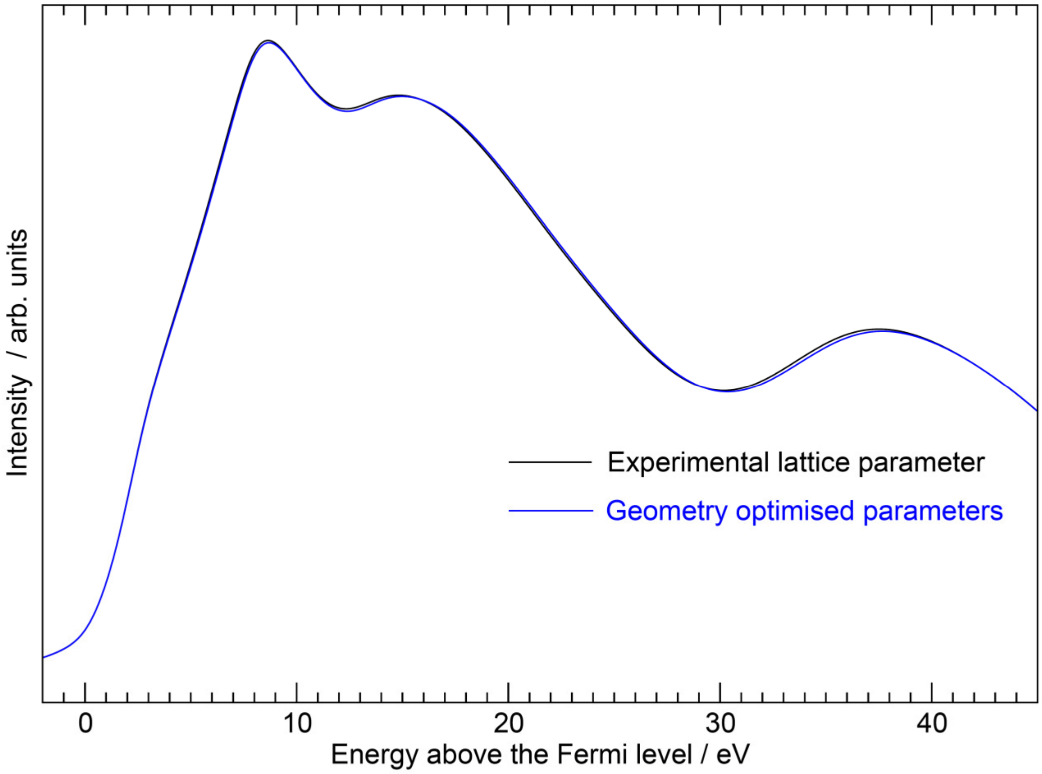

Figure 4.3: Comparing predicted aluminium K edge results for experimental lattice parameter (black line) and the dimensions resulting from geometry optimisation (blue line). All results are shown with the addition of energy-dependent final state lifetime broadening.

As can be seen in this instance the results are basically identical – further suggesting for bulk materials geometry optimisation is unnecessary in terms of ELNES predictions. This is a ‘pragmatic’ observation of course. Being strictly physically accurate, relaxation effects are of importance. A situation might for example exist where relaxation alters which states occur before or above the Fermi level. The conclusions of Chapters 6 and 7 further discuss structural energy minimisation, as does the final conclusion of the thesis.

DFT codes have the potential to explicitly account for ferromagnetism, by instructing the code to allow a net electron spin. Therefore, the ferromagnetism of a material can be verified by DFT thus; find the system energy (in the ground state) without allowing a net electron spin, and then find that energy with net spin allowed. This process can also be combined with lattice parameter refinement. Consider this example for nickel metal (FCC structure, standard lattice parameter 3.52Å):

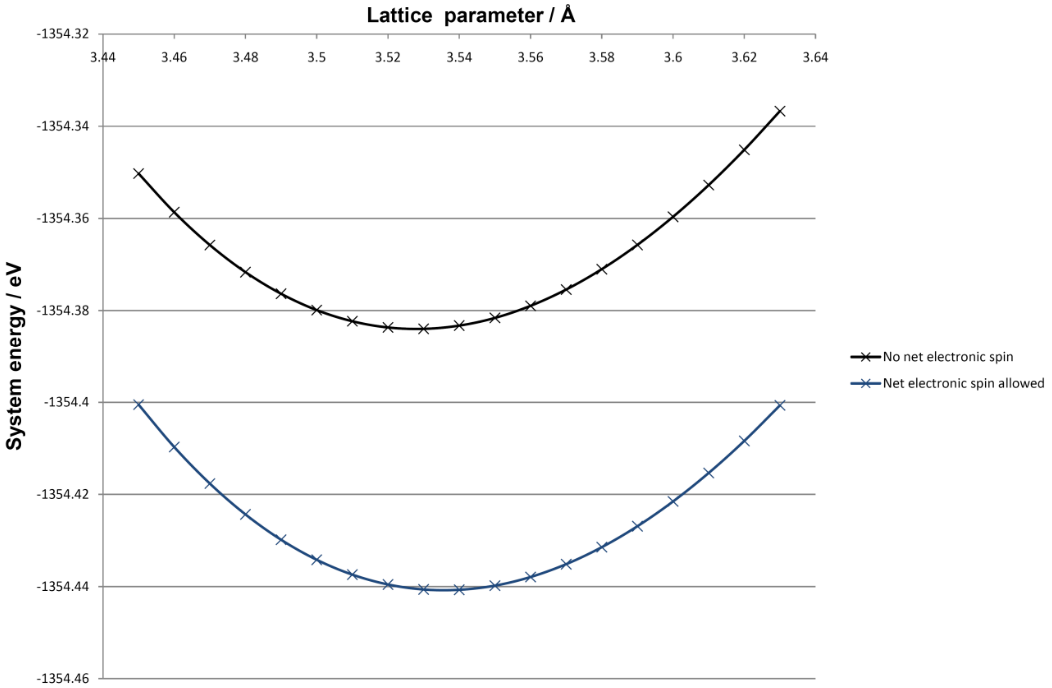

Figure 4.4: Various system energy predictions for nickel metal, for different lattice parameters, and with net electronic spin both allowed and disallowed.

When net electronic spin is allowed, the overall system energy is correctly predicted to be lower. Different optimised lattice parameters are also obtained.

4.2 Initial modelling studies and experiments

4.2.1 Group 4 transition metal carbides and broadening: Initial comparisons between Wien97 and CASTEP

A first significant modelling step was to test the EELS module of the CASTEP code, it being a relatively new addition. Important research has been carried out at Leeds on EELS modelling of group 4 and 5 transition metal carbides (Craven, 1995), (Scott, 2001). In that paper, various carbon K edges were predicted and compared with experiment. Zirconium carbide (ZrC) was chosen for initial testing, as the K edge in this case has a number of features. In the 2001 paper from Leeds, Wien97 was used to calculate a predicted carbon K edge for zirconium carbide in the cubic rock salt structure, with lattice parameter 0.470nm. This calculation was carried out in ground electronic state.

CASTEP was used to predict this edge, again in the ground state. Figure 4.5 is an overlay plot of the previous Wien97 result and the current CASTEP result. In this case, numerical energy-independent broadenings were used, and it was assumed in both cases that the dipole selection rule applied:

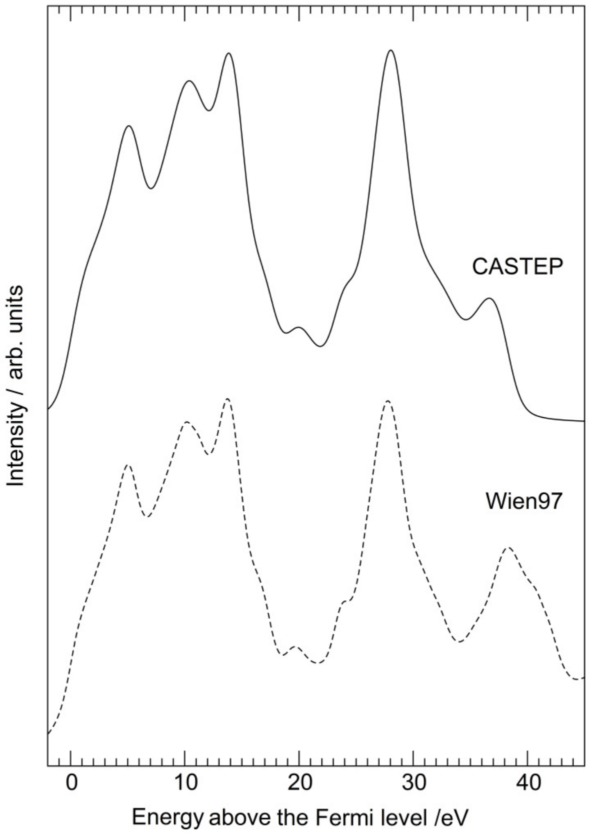

Figure 4.5: Overlay plot of zirconium carbide carbon K edge predicted results. Dashed line is the Wien97 result, solid line is the modern CASTEP result. Both calculations were in the ground state, without the addition of any energy-dependent broadening scheme. The modern CASTEP result calculated in this thesis is subject to 0.2eV Lorentzian and 0.4eV Gaussian broadenings. The CASTEP result has been aligned to the edge onset of the Wien97 result (Scott, 2001).

In this figure, numerical broadenings of 0.2eV Lorentzian and 0.4eV Gaussian were applied to the CASTEP result. These values were chosen to match those used in the first major paper reporting the modified version of CASTEP (Gao, 2008). As in that paper, these values allow the main peaks to be seen in the ELNES, without the spectrum becoming confusing. If only very small numerical broadenings are used, the theoretical spectra have the appearance of hundreds of intense narrow lines that are difficult to interpret in a useful fashion. These Lorentzian and Gaussian broadenings do not rigorously account for core-state broadening effects or for source broadening. When comparing the results to experiment these effects are accounted for as is subsequently described.

4.2.2 Initial thoughts on broadening

Broadening effects in ELNES were briefly mentioned in Chapter 2 of the thesis. It is necessary at this point to give a more detailed description. Generally, for an EELS ionisation event, the following broadening effects exist:

- Core-state broadening (for the inner-shell from which an electron is promoted as part of the excitation event). A simple numerical broadening can be used, with tabulated values available (Fuggle, 1992).
- Final state broadening. The mean free path of the emitted electron (undergoing scattering) will determine a final state lifetime. This broadening is discussed in depth subsequently.
- Instrumental broadening. The ZLP width (in eV) must be accounted for, typically using a simple Gaussian.

As can be readily observed, the results for ZrC are a very good match to the existing Wien result, which was an encouraging sign for the new EELS code module of CASTEP. It was recognised however that as compared to experiment, there are simulated peaks high above the edge onset that are far more intense than observed in practise. Therefore, an energy-dependent final state lifetime broadening function was added. This scheme is actively incorporated into Wien2k, though not as yet CASTEP (Moreau, 2006). This scheme also accounts for element-specific core-state broadening, and source broadening.

It should be noted that in the Wien2k broadening module as used throughout the thesis (including for CASTEP results), once the energy-dependent final state lifetime broadening component is added, varying the source broadening (when it is less than 1.0 eV) has minimal effect - the final state broadening massively dominates. Similarly within the input file used it is possible to vary the edge onset value, or the beam energy. Again, practically speaking variation of these parameters does not significantly alter the broadened result.

It should be recognised that other final state lifetime broadening schemes do exist. For example Wien2k also has the option of a broadening scheme based on a quadratic function of energy above the edge onset (Muller, 1998). This is practically speaking harder to implement than the energy-dependent final state lifetime broadening scheme, as one must specify additional parameters to utilise this quadratic scheme (the energy difference between the Fermi level and the bottom of the valence band, and the plasmon energy), which is a source of possible difficulty.

4.2.3 Full discussion of energy-dependent final state lifetime broadening

The developers of the method recognised that reliable expressions exist for the mean path-length of inelastically scattered electrons in the solid state, whereby the mean path-length is expressed as a function of energy (Seah, 1979). It is therefore possible to estimate the excited state lifetime, and subsequently using the Heisenberg uncertainty principle, estimate an energy-dependent Lorentzian final state broadening. The final expression for the broadening was obtained by the authors as (Moreau, 2006):

$$\Gamma(E)/\,eV = 0.3906\left(\frac{123}{(E-E_0)^{2.43}} + 0.056\right)^{-1} \tag{4.2}$$

Whereby $E-E_0$ are the various kinetic energies of the ejected electrons with E_0 the ionisation energy at the edge considered. Figure 4.12 compares the experimental data for ZrC with the current CASTEP theoretical result with the addition of the energy-dependent final state lifetime broadening function (with 0.5eV source broadening, carbon K level core-state broadening). The experimental data for ZrC was obtained using a VG HB5 electron microscope. This was fitted with a cold field-emission (FEG) (S)TEM, with convergence semiangle of 11 mrad and collection semi-angle of 12.5 mrad. The energy resolution was 0.3eV (Craven, 1995), (Scott, 2001).

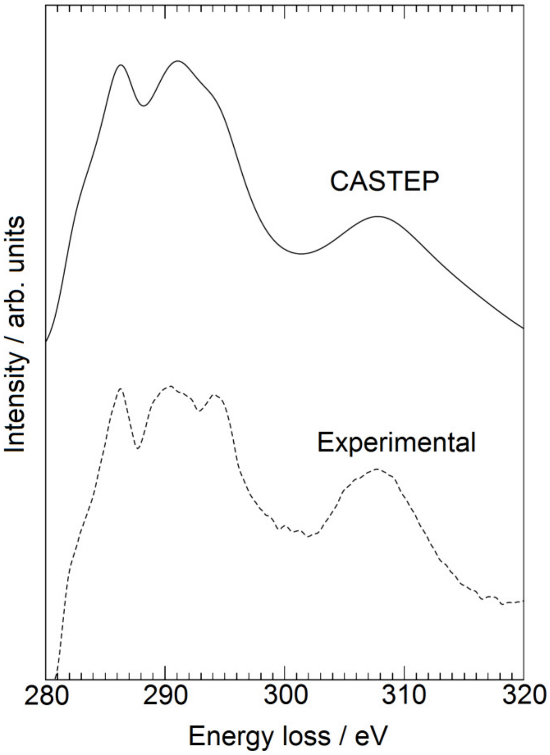

Figure 4.6: Overlay plot of CASTEP predicted zirconium carbide carbon K edge with experiment. The theoretical result has been treated with the energy-dependent final state lifetime broadening scheme (solid black line, source broadening 0.5 eV with carbon K level core-state broadening). The experimental zirconium carbide K edge (dashed line), was obtained using a VG HB5 cold FEG STEM, convergence semi-angle of 11 mrad, collection semi-angle of 12.5 mrad, 0.3 eV energy resolution. The results are aligned relative to the experimental data edge onset (Craven, 1995), (Scott, 2001).

Though not an ideal match (indeed perhaps the broadening removes certain experimental features near the edge onset) these results were deemed to be encouraging. Crucially, the choice of convergence/collection angles for the experimental data means the dipole approximation will apply, and for this isotropic cubic system therefore it was not considered necessary to investigate the impact of for example the collection angle on the modelled result as this would have no effect.

4.3 Convergence

4.3.1 Basic principles of convergence

Given the outline principles as described, it is necessary to consider how to treat the two important user-controlled parameters (kinetic energy cut-off and *k*-

point density) with regard to EELS modelling. Firstly, it is necessary to consider some known principles with regard to these parameters.

Firstly, consider the kinetic energy cut-off. As this is increased, the system energy always decreases until it converges. This is illustrated in Figure 4.7. When carrying out a system-energy type calculation, this is a useful form of convergence test.

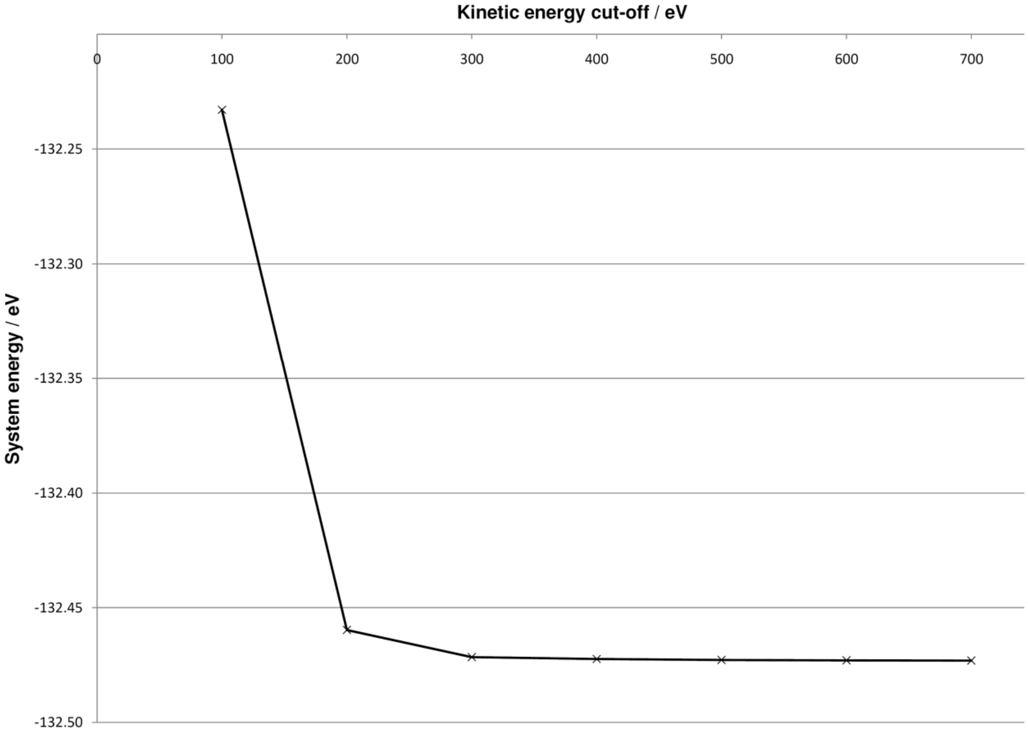

Figure 4.7: Depicting energy-based convergence of the kinetic energy cut-off value. Aluminium metal system (2x1x1 unit cell), using the CASTEP code, ground state calculation.

In terms of the *k*-point mesh, there is not a smooth trend in system energy as the *k*-point numbers are increased – however, the system energy does converge as enough *k*-points are added, as illustrated in Figure 4.8.

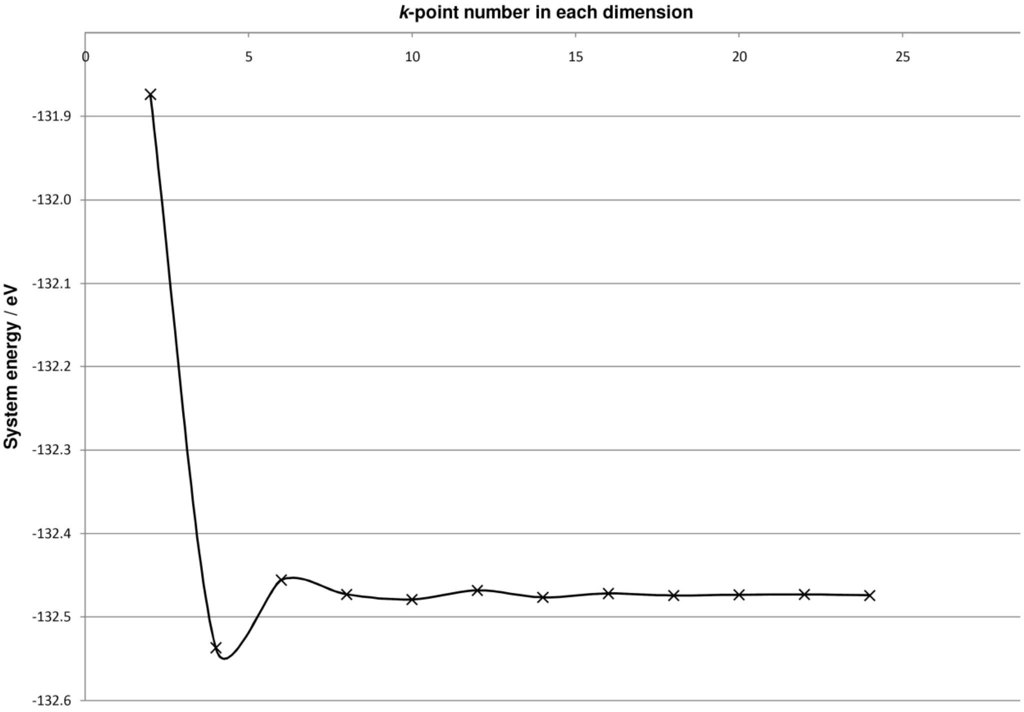

Figure 4.8: Depicting the convergence of system energy with respect to *k*-point mesh density. Aluminium metal system (2x1x1 unit cell), using the CASTEP code, ground state calculation.

However, I believe it is more sensible (if one is to undertake a convergence process) to converge these parameters to the feature of interest in this work – i.e. the ELNES edge prediction. So one should steadily increase the parameters (i.e. kinetic energy cut-off and *k*-point mesh density) and converge the ELNES result to those. For example, consider the aluminium metal ‘test-case’ that has been used throughout this section. In Figure 4.9, various ELNES (aluminium K) results are found upon increasing RK_{MAX}.

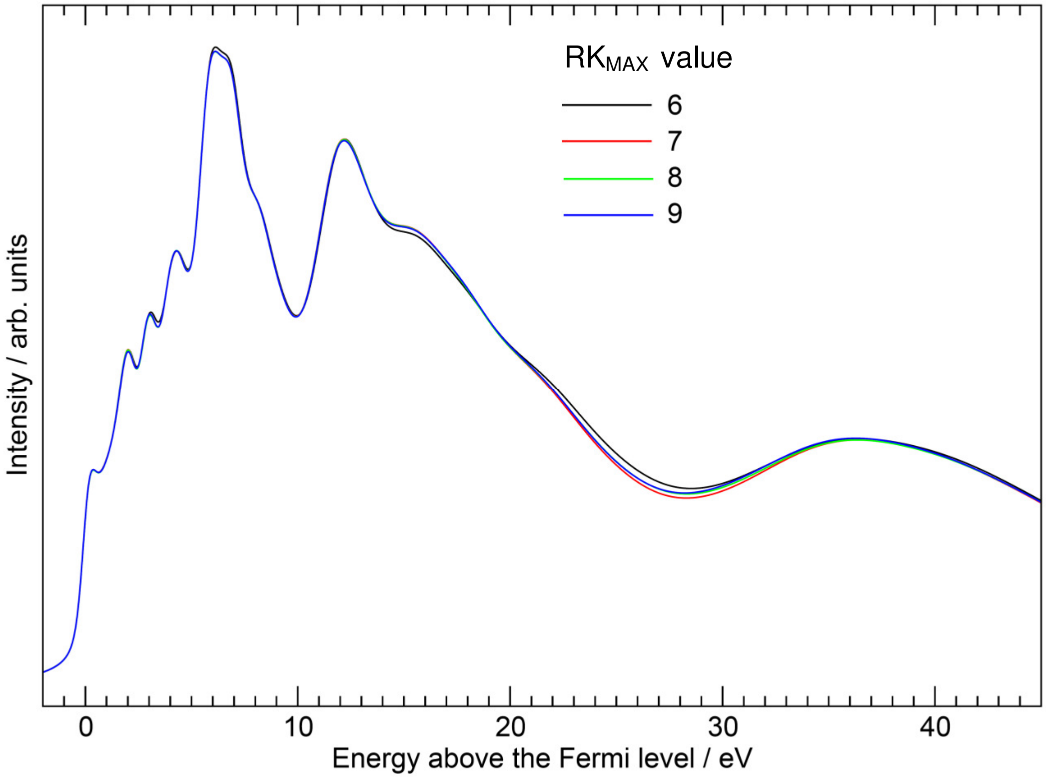

Figure 4.9: Depicting the convergence of kinetic energy cut-off with respect to the ELNES result. Labelled with colours are differing values of RK_{MAX} used in these Wien2k calculations.

As the RK_{MAX} value is increased, the predicted spectra become increasingly similar, and for values of 8 and 9 are almost identical. Therefore, convergence has been achieved. Once we have chosen a value of RK_{MAX}, we can repeat a similar process with respect to the *k*-point mesh density, illustrated in Figure 4.10.

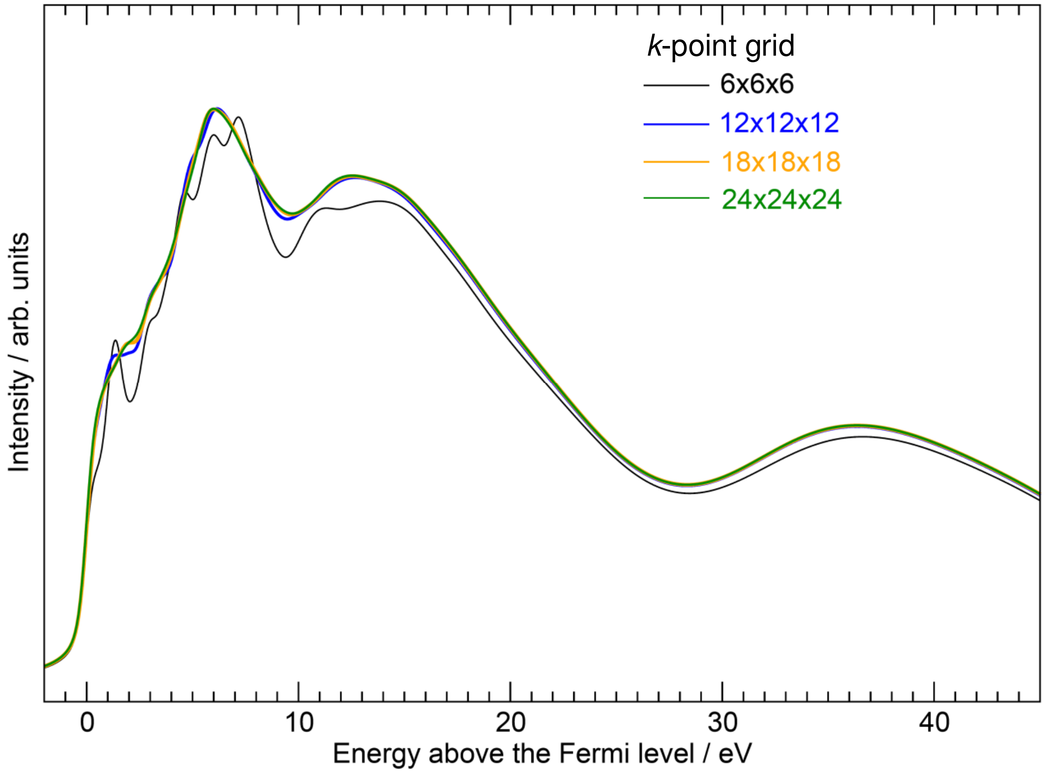

Figure 4.10: Depicting the convergence of *k*-point mesh density with respect to the ELNES result. Labelled with colours are differing densities of *k*-point meshes.

Again one can observe that upon increasing the *k*-point density, the predicted spectra become increasingly similar in nature. Upon moving from a grid of 18x18x18 *k*-points to 24x24x24 *k*-points, the predicted spectra are almost identical, and therefore convergence has been obtained. Note that upon increasing the number of *k*-points, the predicted edge begins to 'smoothen'. When the sampling density is too small, additional 'false' peaks are observed.

4.3.2 Advanced approaches in converging parameters to predict ELNES results

Having considered these outline principles, in a recent paper I proposed an 'ideal' method for converging ELNES predictions (see Appendix 11.1) (Seabourne, 2009). The method for each of the codes Wien2k and CASTEP is presented in Table 4.1:

Step	Parameter	Wien2k	CASTEP
1	Size of basis set	Converge the edge against the choice of RK_{MAX} value. Typically a starting value is 6, increasing in increments of 1. A small grid of *k*-points (i.e. 2x2x2) is sufficient at this stage.	Converge the edge against the choice of kinetic energy cut-off in eV. Typically a starting value is 300eV, increasing in 100eV intervals. A small grid of *k*-points (i.e. 2x2x2) is sufficient at this stage.
2	Number of *k*-points	Converge the edge against the number of *k*-points in the irreducible Brillouin zone.	In CASTEP, the EELS calculation can be considered part of the 'Band Structure' task. Theoretically, this can be run as a single step. However, as a band structure task requires a large number of additional empty bands (to probe above the Fermi energy) one generally runs a standard energy calculation first with a low number of extra bands to generate a .check continuation file, followed by the band structure calculation. Therefore in CASTEP one must: Converge the predicted results with the *k*-point mesh in the simple energy section of the calculation. Subsequently converge the predicted result with the *k*-point mesh in the band structure section of the calculation (i.e. the active EELS calculation). Generally the latter calculation is more demanding and may require a finer mesh for convergence.
3	Cell size	When an EELS ionisation event occurs a core-hole is left behind. If this is included in the above steps, the cell-size should be large enough to avoid artificial interaction. This concept is further explained in the main body of the thesis.	
Additional	Core-hole occupancy	If necessary at this stage, vary fractional core-hole occupancy, to achieve a better agreement with experiment for example. This is not truly an *ab initio* step.	

Table 4.1: Ideal selection procedure for converging parameters in ELNES modelling. It is practically speaking straight-forward to converge the basis-set first, as these changes do not have a large effect on calculation time or memory. The *k*-point convergence steps are the most computationally demanding. The additional step, as noted, is not strictly *ab initio*, but is designed to improve potential agreement with experiment. It should be considered (when altering core-hole occupancy) that by improving experimental agreement in this fashion, one might be obscuring fundamental problems with the other parameter choices if care is not exercised.

Often, a large ‘supercell’ is used to separate the core–holes (discussed in Chapters 2 and 3), to avoid unwanted interaction between them (Hébert, 2003). The term ‘supercell’ refers to the concept illustrated in Figure 4.11:

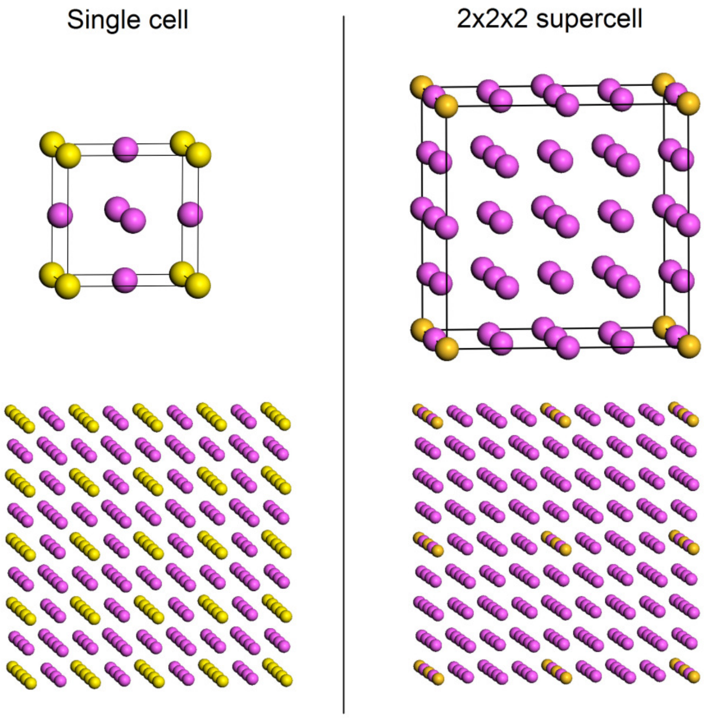

Figure 4.11: Depicting the concept of a supercell, using aluminium as an example, shown in the cubic (FCC) orientation. Single cells with a core-hole in place are shown (the core-hole atom labelled in yellow), and also 2x2x2 supercells. The top plots are the standard means of depicting the supercell, with the ‘core-hole’ atoms at the corners. However, one must recognise that these are periodic repeating structures. The bottom plots show a larger section of aluminium therefore, showing again where the core-hole atoms would be for a ‘single cell’ and for the ‘2x2x2 supercell’.

Although the term ‘supercell’ will be used in this thesis, due to its relative familiarity in this field of research, it should be noted the important consideration is the physical separation in space of the core-hole atoms, as shown in Figure 4.11.

Perhaps not considered so often however is the physical reason for this separation - i.e. the actual reason we do not want to observe interference between our theoretical core-holes. In order to do this one must consider the typical timescale of events in EELS.

One can define the incidence of an excitation electron as time 0 s. If we have an incident fast electron beam of energy 200 keV it will travel at around 2.7 x 10^8 ms^{-1}, meaning it will pass through for example an aluminium atom (of diameter ~ 0.25 nm) in approximately 10^{-18} s. The time taken to generate the core-hole in the first instance is likely to be around this order of magnitude or higher. However, the generation of a core-hole in absorption spectroscopy is a considerably quicker process than the relaxation of that core–hole, which is crucial (Ohno, 2006).

This core-hole can decay by either Auger emission or X-ray fluorescence (emission). Therefore, the core-hole lifetime is a combination of the Auger lifetime and the fluorescence lifetime:

$$\frac{1}{\tau} = \frac{1}{\tau_{Auger}} + \frac{1}{\tau_{Fluorescen\,ce}} \tag{4.3}$$

Based on tabulated core-state linewidths, this means for our aluminium example the core-hole has a lifetime of around 10^{-15} s (Brydson, 2001), (Krause, 1979).

This timescale is far longer than the excitation time. Therefore, if the fluence rate of the electron beam was high enough, other core-holes could be generated before this core-hole underwent relaxation. This would mean the various core-holes would interact, and the final state DOS (*p* DOS for an Al K edge for example) would be affected.

However, in reality a typical fluence rate is around 10^7 Am^{-2}, meaning that the core-hole is entirely relaxed some orders of magnitude before the next EELS excitation event occurs (approximately 10^{-8} s). Therefore, one must set up the theoretical cell to avoid unrealistic core-hole interactions. Furthermore, the Frank-Condon principle will apply in these cases such that the excitation process will be over long before any structural relaxation can take place, the time for a vibrational transition being in the region of 10^{-14} s. This adds further evidence that standard unit cell dimensions obtained from diffraction or high-resolution imaging experiments can be used for EELS predictions.

A brief point should be made at this juncture with regard to the role of the final state. As the above timescales reveal, the final state persists for longer than the exciting beam is in the proximity of the atom. The exact nature of the final state wavefunctions is determined by the way in which they decay, which is not clear until relaxation occurs and the ground state is restored. One might argue therefore that the 0.5 electron core-hole provides the best physical representation of an ELNES excitation / relaxation.

4.4 Summary

This section has outlined other *ab initio* capabilities of DFT codes, including the possibility of geometry optimisation. Furthermore, convergence of DFT parameters was discussed; specifically the kinetic energy cut-off and *k*-point mesh. Energy-based convergence can be used, but for ELNES predictions, it is more sensible to graphically converge against the ELNES prediction itself. The importance of supercells was also discussed, to avoid artificial core-hole interactions that do not realistically simulate experiment.

Chapter 5

The core-hole effect - a series of aluminium compounds

5.1 Introduction and systems studied

This section considers some fundamental bulk materials, using the methodology presented in Chapter 4. Specifically, the effect of the core-hole on the following edges was considered; aluminium K in aluminium metal, aluminium and oxygen K in α-alumina and aluminium and nitrogen K in aluminium nitride (wurtzite structural form). These three bulk materials were chosen as they have a common element, and cover a range of materials classes, namely a conductor, insulator, and semi-conductor. It is assumed throughout theory and experiment that the dipole selection rule operates (applicable for small momentum transfer), so the crucial consideration for the K edges presented is the partial *p* orbital density of states (DOS) (Brydson, 2001).

For each of the three bulk materials, each elemental K edge was found in the ground state, with a 0.5 electron core-hole in the 1*s* level, and a full-electron core-hole in the 1*s* level. This process was then repeated for a 2x2x2 'supercell' of the material, i.e. one in which the core-hole separation had been increased so as to minimise artificial core-hole interactions. Various qualitative and quantitative comparisons with experiment were then carried out. Comparisons with experiment allow one to observe which systems and edges required a core-hole to be in place to obtain reasonable and physically sensible results. The fractional core-hole experiments assist in rationalising these observations.

A final consideration in the theoretical experiments relates specifically to the compound systems, i.e. alumina and aluminium nitride. It has been suggested that for such systems, the cation K edge should show a greater alteration upon the addition of a core-hole (Rez, 2006). The cationic species is already electron-deficient, so further removal of electrons is considered to have a greater impact on the predicted result. An attempt is therefore made to quantitatively compare the 'impact' of the core-hole for the anionic and cationic species in alumina and aluminium nitride.

5.2 Methodologies of calculations used

5.2.1 Code specific considerations

This section considers one approach towards treating the core-hole in CASTEP, which is to ‘promote’ the core-hole electron to the lowest unoccupied orbital. For example, for the aluminium atom core-hole, the configuration was modified to $1s^1 2s^2 2p^6 3s^2 3p^2$.

For Wien2k, the core-hole electron was removed from the cell, and smeared across the whole system as a positive charge. This process makes the practical operation of the Wien2k code somewhat more straightforward. The initial step in Wien2k is to generate a series of input files using the ‘init_lapw’ command. One must take care with this command, and ensure that the code does not for example reduce the cell from standard FCC to primitive if this is not desired.

Practical experience has shown that in terms of the core-hole, the key factor influencing the unoccupied DOS is the site of the core-hole in the local atom in which it is generated, rather than whether the core-electron is promoted to a higher-lying orbital or smeared across the whole system as a charge. In Chapter 7 (Figure 7.11), a CASTEP experiment is carried out where a charge is smeared across the whole cell. Equivalent trends to those seen in this section (where the core-hole electron is promoted within the same atom) are observed.

5.2.2 Parameter selection

The selection method was that as described in Chapter 4 (Table 4.1). For CASTEP, the kinetic energy cut-off value was altered in 100eV intervals from 300eV to 600eV. After each sequential alteration, for each energy axis data point the change in the predicted result (found as a percentage) was determined. The percentage changes were averaged to a single value across all the energy axis points obtained. To increase the speed of calculations, when this averaged value was 5% or less, the parameter was considered to be converged.

For the CASTEP convergence process, broadenings of 0.2eV Lorentzian and 0.4eV Gaussian were applied, to allow visual inspection of the results during the tests. These broadenings were used in the original paper reporting the PAW method being applied to the CASTEP code (Gao, 2008).

For *k*-point mesh convergence the calculations were as described in Table 4.1. The process was divided into two steps; the first to generate basic model data and system energies, and a second which calculates a large number of bands above the Fermi level. In the first step, the *k*-point mesh (for a single cell) was doubled from 12x12x12 to 24x24x24 and so on until convergence was achieved. The same process was used for the second step which calculates the EELS result.

Table 5.1 lists the resulting converged parameters obtained for all systems and edges using the CASTEP code, including details of the theoretical cells that were utilised.

	Aluminium metal	**Alumina**		**Aluminium nitride**	
Cell details	2x1x1 aluminium cell (primitive), a = 5.73 Å, b = c = 2.86 Å, α = β = γ = 60˚, single-electron core-hole in place for one of the Al atoms. All other atoms at all times standard USP (GGA) pseudopotentials.	Single alumina cell, rhombohedral form, a = b = c = 5.13Å, single electron core-hole in place for one atom. All other atoms at all times standard USP (GGA) pseudopotentials.		Single aluminium nitride cell in the wurtzite form (space-group $P6_3$mc), a = b = 3.11 Å, c = 4.98 Å, α = β = 90˚, γ = 120˚. Single electron core–hole in place for one atom. All other atoms standard USP (GGA) pseudopotentials.	
Edge	Aluminium K	Aluminium K	Oxygen K	Aluminium K	Nitrogen K
Kinetic energy cut-off	600eV	400eV	600eV	500eV	500eV
k-point mesh in energy calculation step	12x24x24, spacing in reciprocal space of 0.018Å^{-1}	24x24x24, spacing in reciprocal space of 0.011 Å^{-1}	24x24x24, spacing in reciprocal space of 0.011 Å^{-1}	24x24x12, spacing in reciprocal space of at least 0.017Å^{-1}	24x24x12, spacing in reciprocal space of at least 0.017Å^{-1}
k-point mesh in band structure step	24x48x48, spacing in reciprocal space of 0.009 Å^{-1}	24x24x24, spacing in reciprocal space of 0.011 Å^{-1}	24x24x24, spacing in reciprocal space of 0.011 Å^{-1}	24x24x12, spacing in reciprocal space of at least 0.017Å^{-1}	24x24x12, spacing in reciprocal space of at least 0.017Å^{-1}

Table 5.1: Chosen parameters for CASTEP calculations, and details of the systems considered.

For Wien2k, the convergence process is somewhat more straightforward, as there are not two *k*-point meshes involved in the calculation. In the case of

Wien2k, with regard to the 'kinetic energy cut-off' the key variable is the RK_{MAX} value. RK_{MAX} was increased from 7 in steps of 1, with the 5% variation convergence criterion applied. The *k*-point mesh was doubled in size from 4x4x4 until convergence was achieved. Throughout the Wien2k convergence experiments, the energy-dependent final state lifetime broadening scheme was applied (Moreau, 2006), which is a straightforward process in Wien2k even for relatively trivial convergence calculations. This level of broadening was considered acceptable as no Wien2k theoretical result (or indeed CASTEP result) is presented without this broadening scheme applied in this chapter.

The converged parameters, and details of the theoretical cells used are as given in Table 5.2. It is unsurprising - given the approach used for parameter variation as part of the convergence process - that for several systems similar sets of calculation parameters were ultimately used.

	Aluminium metal	**Alumina**		**Aluminium nitride**	
Cell details	Single aluminium cell in primitive orientation, $a = b = c = 2.86$Å, $\alpha = \beta = \gamma = 60^\circ$, single electron core-hole in place.	Single alumina cell, rhombohedral form, $a = b = c = 5.13$Å, single electron core-hole in place for one atom. All other atoms at all times standard USP (GGA) pseudopotentials.		Single aluminium nitride cell in the wurtzite form (space-group $P6_3mc$), $a = b = 3.11$Å , $c = 4.98$ Å , $\alpha = \beta = 90^\circ$, $\gamma = 120^\circ$. Single electron core-hole in place for one of the atoms. All other atoms standard GGA pseudopotentials.	
Edge	Aluminium K	Aluminium K	Oxygen K	Aluminium K	Nitrogen K
RK_{MAX}	10	8	8	8	8
k-point mesh	18x18x18	8x8x8	8x8x8	8x8x4	8x8x4

Table 5.2: Chosen parameters for Wien2k calculations, and details of the systems addressed.

5.3 Results and comparisons with experiment for bulk materials

5.3.1 Comparisons of Wien2k and CASTEP K edge predictions across the three bulk materials

For the three bulk materials, each elemental K edge was predicted using both CASTEP and Wien2k. In each instance, predictions were found for a single cell (or a 2x1x1 cell for aluminium, see Tables 5.1 and 5.2), and for a 2x2x2 supercell, which was designed to minimise the interaction of the theoretical core-holes. For each of those cell sizes, a ground state calculation was carried out, as well as a calculation with a 0.5 electron core-hole in the 1*s* level, and a single electron core-hole in the 1*s* level. In all cases the results are shown with an energy-dependent final state lifetime broadening applied.

The results are also ‘hard-shifted’ on the energy axis so that the edge onset occurs at 0eV. In the case of CASTEP, the shift required is small. In Wien2k it can be quite large, for example the ‘edge-onset’ might be 6eV, which suggests Wien2k is displaying the band-gap as part of the ELNES prediction. On the various figures depicting the theoretical results, the x-axis is therefore labelled as the ‘shifted-energy’.

Consider firstly results for the aluminium metal K edge, shown in Figure 5.1.

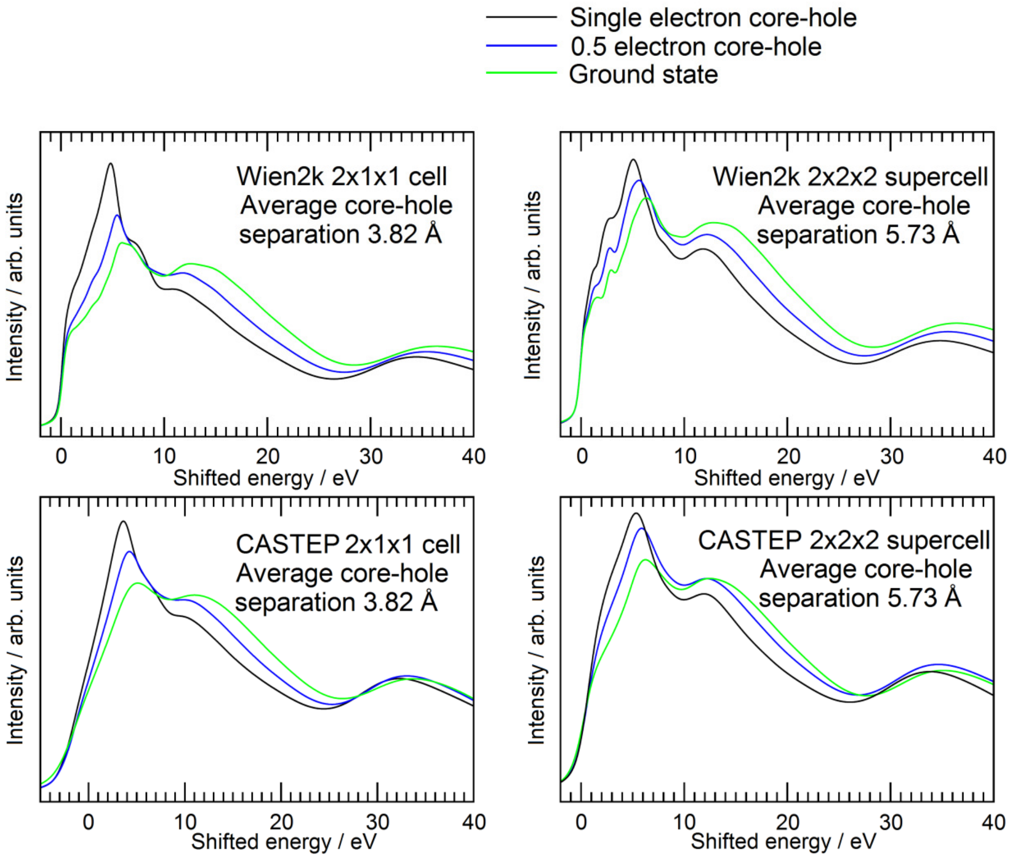

Figure 5.1: Various aluminium metal aluminium K edge predictions, found using Wien2k and CASTEP. The top plots are Wien2k results, the bottom plots CASTEP. The left-hand plots are those for the 2x1x1 cell, on the right are shown the 2x2x2 supercell results. The core-hole ‘strength’ is as labelled using colour-coding.

The left-hand plots show respectively Wien2k and CASTEP results for 2x1x1 cells (average core-hole separation distance 3.82Å). The right-hand plots show the corresponding results for the 2x2x2 supercells (core-hole separation distance 5.73Å).

The reasons for using a 2x1x1 cell are as explained in the literature (Seabourme, 2009). Crucially, it is observed that the general agreement between results for the two codes is good. In both instances, generally speaking upon the introduction of a core-hole there is an increase in edge intensity close to the edge onset, and a shift in the energy of the first peak towards the Fermi level, as expected (Gao, 2008), (Rez, 2006). The core-hole effect is perhaps slightly larger in the Wien2k case for the 2x1x1 cell, given the sharper rise in intensity for the single electron core-hole as compared with CASTEP. However, this difference in impact is not observed for the 2x2x2 supercells, suggesting this is not a physically significant effect.

Furthermore, the fractional core-hole experiments are arguably indicative. Examining the 2x1x1 cell results as compared to the 2x2x2 supercells (for both codes), for the 2x1x1 cells variation of the core-hole ‘strength’ has a considerably larger effect than for the 2x2x2 supercells, particularly in the case of Wien2k. This suggests (as previously reported for valid Wien2k calculations (Seabourne, 2009)) that for the 2x2x2 supercells in particular there is some extent of core-hole ‘screening’, such that the exact core-hole approximation utilised does not massively alter the predicted result. The extent of core-hole screening implies ground state calculations may provide good agreement with experiment, as discussed subsequently.

Figs. 5.2 and 5.3 present (respectively) the aluminium and oxygen K edges from α-alumina (core-hole separation distance for single alumina cell 5.13Å, 2x2x2 supercell core-hole separation distance 10.26Å).

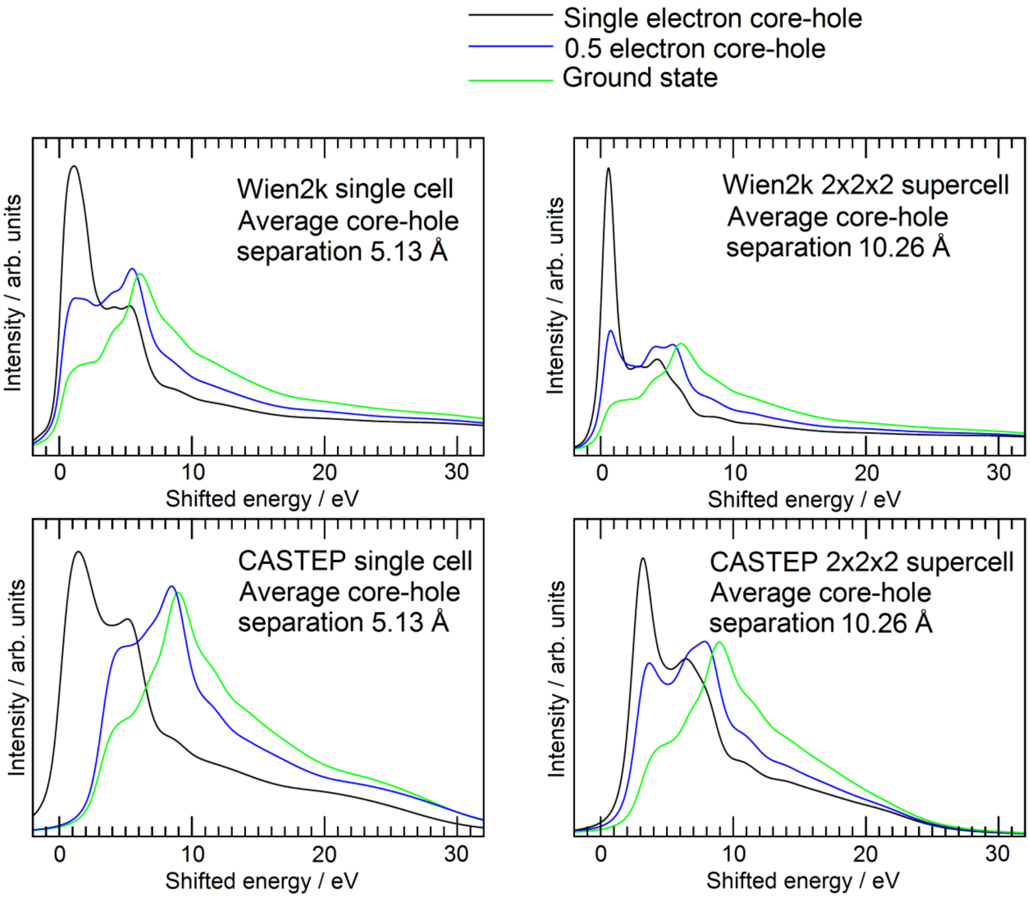

Figure 5.2: Various aluminium oxide aluminium K edge predictions, found using Wien2k and CASTEP. The top plots are Wien2k results, the bottom plots CASTEP. The left-hand plots are those for the single cell, on the right are shown the 2x2x2 supercell results. The core-hole ‘strength’ is as labelled using colour-coding.

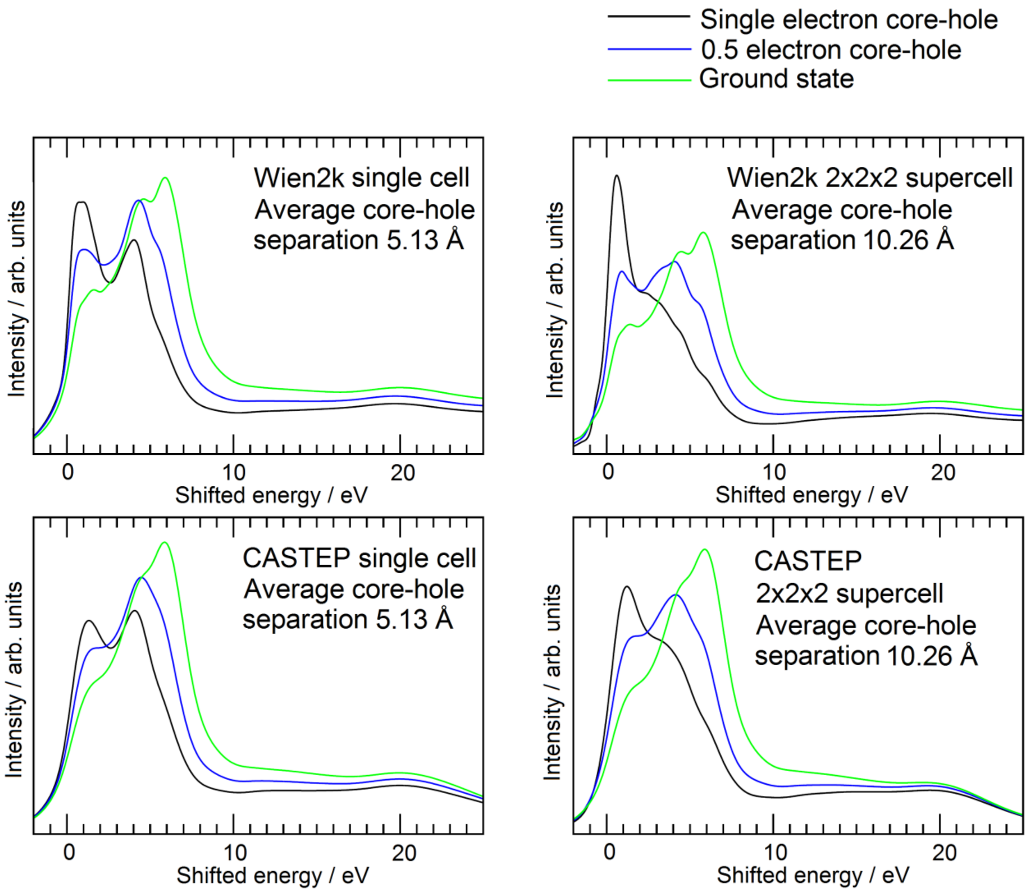

Figure 5.3: Various aluminium oxide oxygen K edge predictions, found using Wien2k and CASTEP. The top plots are Wien2k results, the bottom plots CASTEP. The left-hand plots are those for the single cell, on the right are shown the 2x2x2 supercell results. The core-hole 'strength' is as labelled using colour-coding.

Consider firstly the aluminium edge predictions. Comparing the Wien2k and CASTEP results, there is in both cases the expected behaviour upon the addition of a core-hole (shift in the edge peaks towards the Fermi level, and an energy increase in that region). However, for the single electron core-hole result, the first peak in the spectrum is somewhat sharper for the Wien2k results, and is of higher intensity relative to the second peak, particularly for the Wien2k 2x2x2 supercell result.

Excluding the single electron core-hole results, the other predictions (when comparing the two codes) are similar, which is an encouraging sign in terms of the validity of the various approximations CASTEP uses to reintroduce core-state information. As compared to the aluminium edge in aluminium metal, variation of core-hole 'strength' has a similar effect in the single and 2x2x2 supercells. It is indeed arguable (comparing the various core-hole results) that a single alumina cell may be large enough to screen the core-hole.

Upon initial inspection of the oxygen K edge results, generally speaking the addition of a core-hole brings about a lesser change in the edge intensity near the Fermi level as compared to the aluminium (cationic) edge, which is consistent with expected trends when comparing anionic and cationic edges (Gao, 2008), (Rez, 2006). The various theoretical results are qualitatively consistent when comparisons are made between the two codes, with particular exception of the single electron core-hole result for the various single cells. Comparing the Wien2k and CASTEP results, the first two peaks (black lines) are in the opposite intensity pattern, i.e. in the Wien2k spectrum the first peak is more intense than the second, and vice versa for CASTEP. Again, as was observed for the aluminium edge, the variation of core-hole ‘strength’ has a similar effect for the single and 2x2x2 supercells.

Figs. 5.4 and 5.5 present (respectively) aluminium and nitrogen K edge predictions for aluminium nitride (wurtzite structural form, average core-hole separation in single cell 3.73Å, in 2x2x2 supercell 7.46Å).

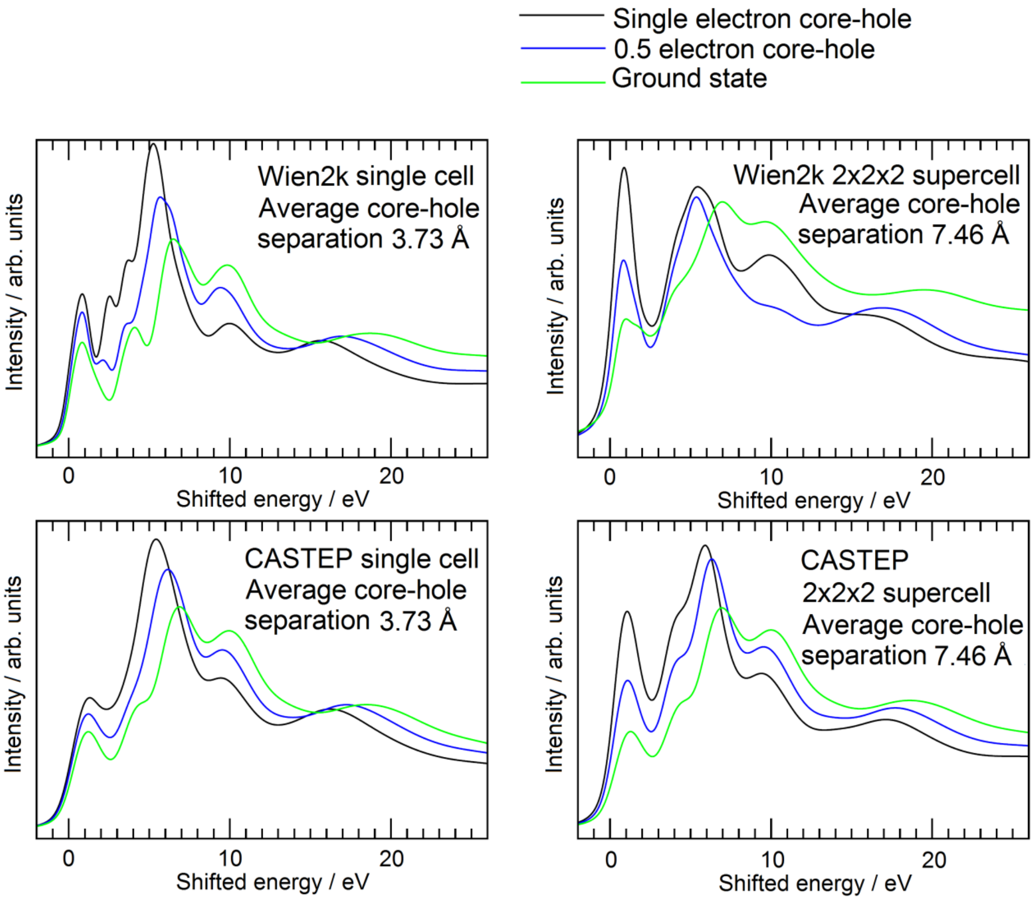

Figure 5.4: Various aluminium nitride aluminium K edge predictions, found using Wien2k and CASTEP. The top plots are Wien2k results, the bottom plots CASTEP. The left-hand plots are those for the single cell, on the right are shown the 2x2x2 supercell results. The core-hole 'strength' is as labelled using colour-coding.

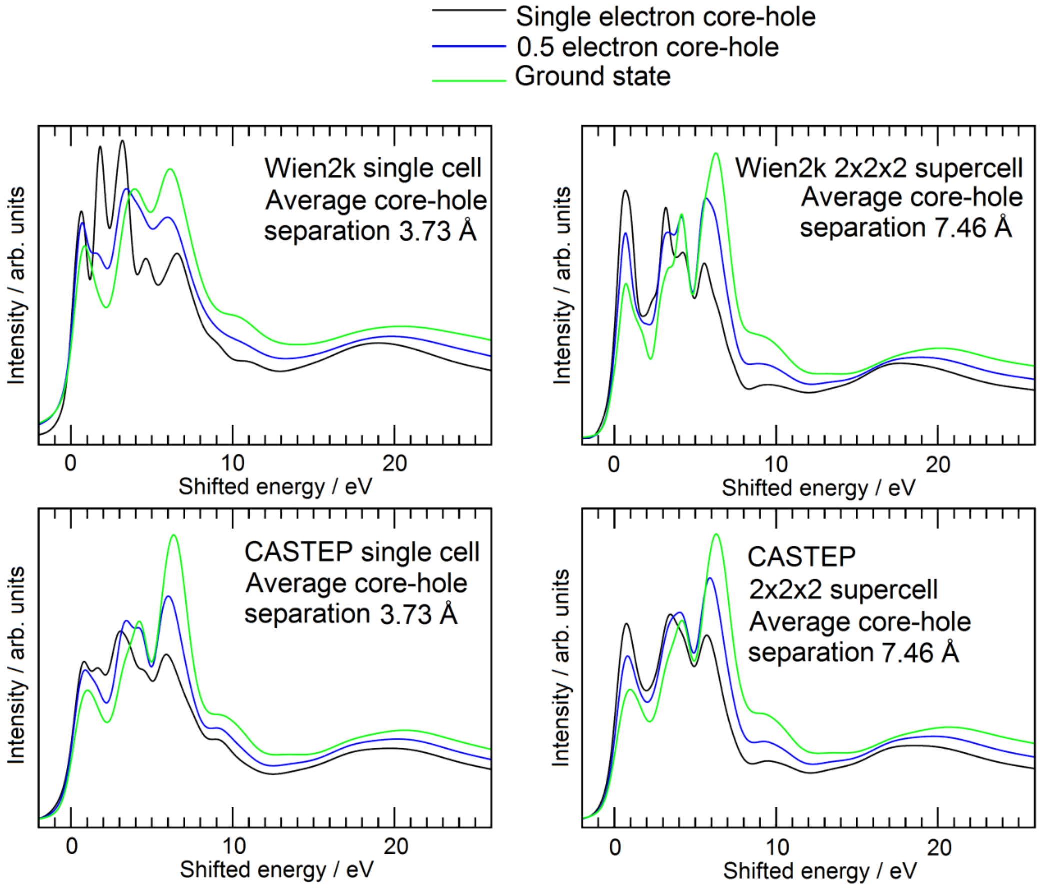

Figure 5.5: Various aluminium nitride nitrogen K edge predictions, found using Wien2k and CASTEP. The top plots are Wien2k results, the bottom plots CASTEP. The left-hand plots are those for the single cell, on the right are shown the 2x2x2 supercell results. The core-hole 'strength' is as labelled using colour-coding.

With regard to the aluminium edge predictions, the results appear largely qualitatively similar when the two codes are compared, and the observed edge changes when a core-hole is introduced are as expected. For the single cell results, there is a more definite shift towards the Fermi level for the core-hole results in the Wien2k case as compared to CASTEP, and there is furthermore a degree of fine structure not observed in the CASTEP case. In the case of the 2x2x2 supercells, the single-electron core-hole results differ significantly in terms of the intensity of the first peak in the spectrum relative to the second.

Compared to aluminium oxide and indeed aluminium, variation of the core-hole 'strength' has a marked difference in effect for the two cell sizes. For the single-cell results the various fractional core-hole results are fairly similar in nature, and a far more dramatic effect is observed for the 2x2x2 supercells.

The nitrogen K edge predictions show a larger number of peaks, particularly in the single cell cases. The anion K edge also shows on initial inspection (as compared to the aluminium cation edge) a lesser intensity shift upon the addition of the core-hole, particularly for the 2x2x2 supercell results. Some minor differences are observed between the codes for the core-hole results for the 2x2x2 supercells. Significant differences are observed for the core-hole results for the single cell systems. Examining the left-hand plots in Fig. 5.5, although the single electron core-hole results (black lines) both display 5 peaks between 0-10eV, these peaks display significantly different relative intensities.

The nitrogen K edge for AlN (see also experimental result, Figure 5.8) is relatively complex and detailed close to the Fermi level. The core-hole interactions may well be particularly strong in this instance, and this may be influencing each of the codes in a somewhat different fashion. Crucially, the ground state results are in both cases similar, which further supports this idea. In the structural form used for alumina for example, the system is isotropic, which is not true of aluminium nitride. This will lead to further edge complexity, particularly ‘disrupted’ by core-hole interactions in the single cell.

5.4 Quantitative analysis of experimental comparisons

5.4.1 Aluminium metal

A sample of aluminium (0.9% Cu by weight, characterised at the University of Birmingham) was treating using a Precision Ion Polishing System (PIPS) machine, operating at 5keV, for 2.5 minutes on each side of the sample disc. This sample was analysed in-house at Leeds using a Philips CM200 FEG TEM (Gatan imaging filter / EELS spectrometer). The zero-loss energy resolution was 0.7eV. As stated in the acknowledgements section, Gareth Vaughan acted as operator for these experiments.

Figure 5.6 shows an initial comparison of various theoretical results with experiment:

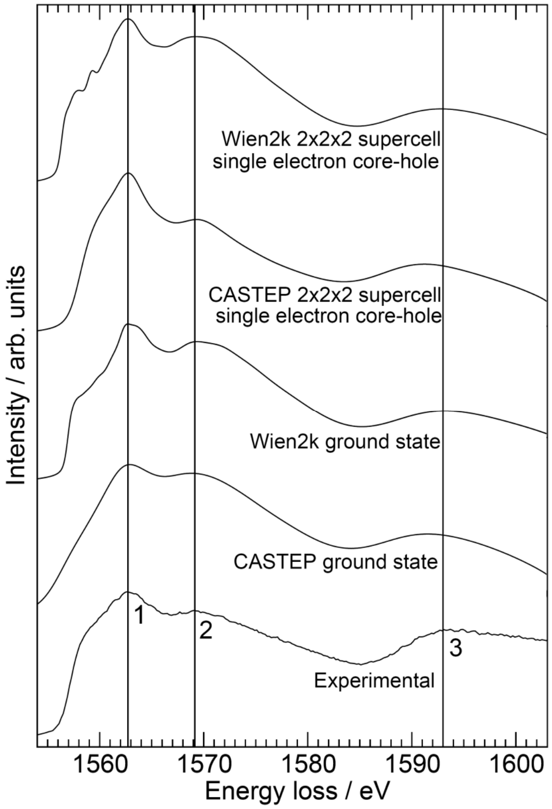

Figure 5.6: Aluminium K edges in aluminium metal compared to an experimental result (0.9% Cu by weight), resolution 0.7eV. The various theoretical results are as labelled in the figure, and are shown with energy-dependent final state lifetime broadening in all cases.

Peak labels have been added to the figure to assist with inspection. We observe that the qualitative agreement is not improved by using a supercell and core-hole. All the results offer reasonable agreement in terms of energy positions and relative intensities, with the CASTEP ground state result arguably providing the best agreement for the various peak positions, though the Wien2k results show a ‘shoulder’ feature before peak ‘1’ which is arguably observed in experiment.

Rez suggests that for free-electron metals (FEMs) such as aluminium, a ground state calculation will provide good agreement with experiment (Rez, 2006). Relatively diffuse electrons will mean the core-hole is well screened, lessening its impact. Muller further discusses this in a recent Nature Materials review (Muller, 2009).

Rez also discusses the relevance of the core-hole lifetime with regard to EELS modelling of FEMs. It is argued the core-hole relaxes extremely quickly, as do changes to local DOS, in such a timescale that the changes are not observable using the microscope.

5.4.2 Aluminium oxide

A crystalline alumina sample was again characterised using our in-house microscope (Philips CM200 FEG TEM). Figures 5.7 and 5.8 respectively show overlay comparisons of theoretical and experimental aluminium and oxygen K edges:

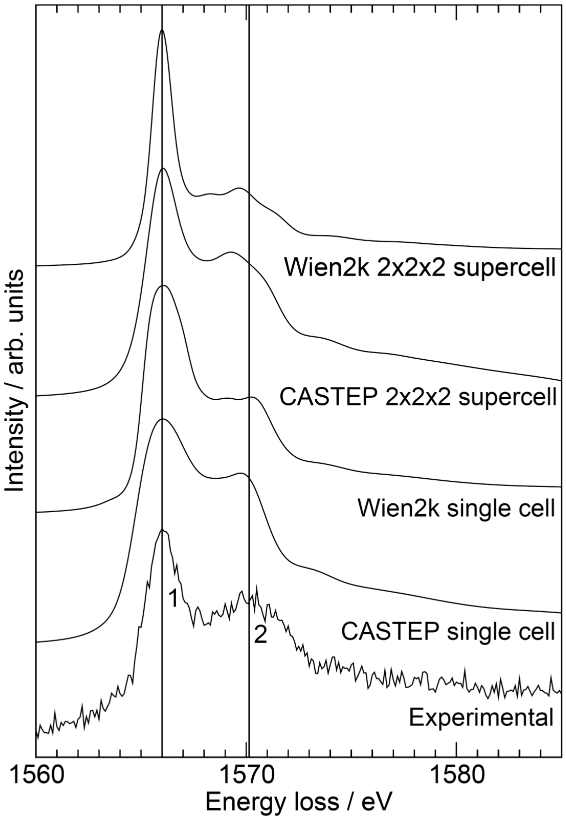

Figure 5.7: Aluminium K edges in alumina compared to an experimental result, resolution 0.7eV. The various theoretical results are as labelled in the figure, and are shown with energy-dependent final state lifetime broadening in all cases. A single electron core-hole was used for all the presented theoretical results.

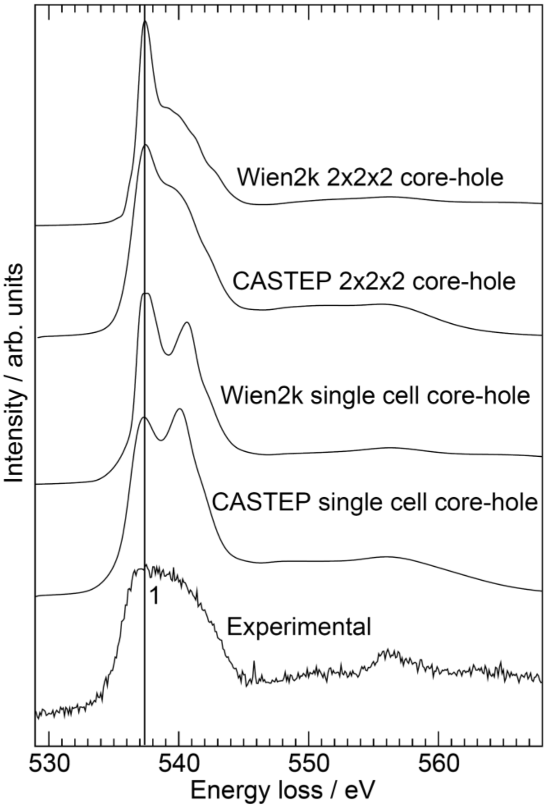

Figure 5.8: Oxygen K edges in alumina compared to an experimental result, resolution 0.7eV. The various theoretical results are as labelled in the figure, and are shown with energy-dependent final state lifetime broadening in all cases.

In contrast to aluminium metal, alumina is an insulating material, with poor screening of the core-hole. For both K edges good qualitative agreement with experiment is only observed when a core-hole is used.

For the aluminium edge, agreement with experiment is not particularly improved when a supercell is used. Indeed these results in isolation imply that the single cell is large enough to avoid artificial core-hole interactions (given the similarity of the single cell predictions with experiment). However, the supercell calculations for the oxygen edges are somewhat different to those for the single cell, casting potential doubt on this analysis. A brief point should also be made with regard to the fact that the experimental (oxygen K) edge does not display the second peak / shoulder observed in all the theoretical results. This is likely to be due to specimen damage, rather than broadening effects as considered subsequently in section 5.6.

5.4.3 Wurtzite aluminium nitride

In the case of aluminium nitride, Figs. 5.9 and 5.10 respectively present overlay comparisons of the aluminium and nitrogen K edges (theory and experiment). In these cases the experimental data was obtained from an external source:

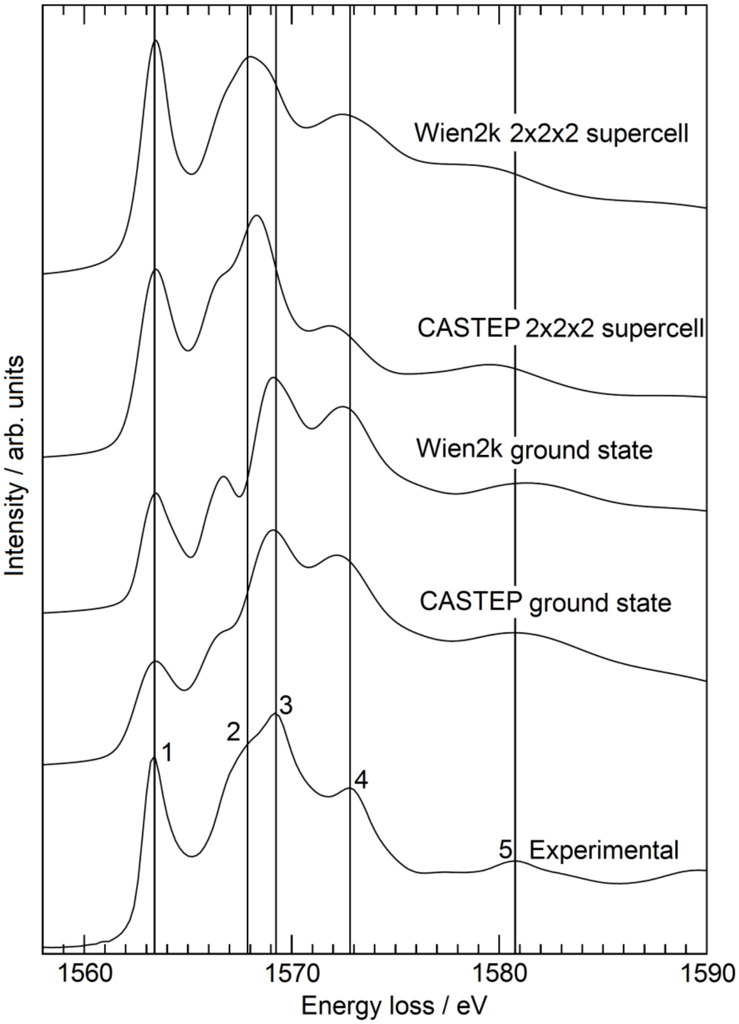

Figure 5.9: Aluminium K edges in aluminium nitride compared to an experimental XANES result (as obtained by Flank et al (CEMES EELS database, <http:// www.cemes.fr>)) resolution 0.8eV. The various theoretical results are as labelled in the figure, and are shown with energy-dependent final state lifetime broadening. The supercell results include a single electron core-hole.

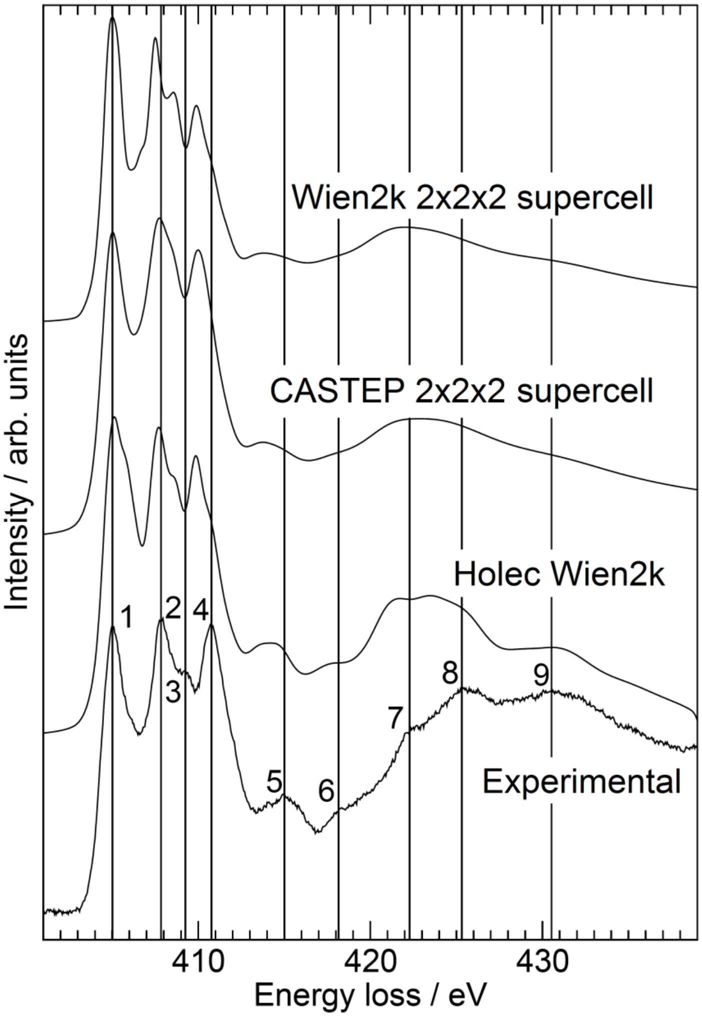

Figure 5.10: Nitrogen K edges in aluminium nitride compared to an experimental result (as obtained by Holec et al, resolution 0.15eV (Holec, 2008). Various other theoretical results are labelled in the figure. In the case of those calculated for the thesis, they are shown with energy-dependent final state lifetime broadening. The Holec et al theoretical result is broadened with a 0.4eV Gaussian.

The aluminium edge data was obtained by Flank et al., and downloaded from the CEMES EELS database (<http://www.cemes.fr>). The nitrogen K edge data was provided by kind permission of Holec et al. (Holec, 2008). This was not originally background corrected but has been for the purposes of this work. Considering firstly the aluminium edge, the 2x2x2 supercells present an improved agreement with experiment. Also shown are ground state results, which were considered to be qualitatively useful in previous work (Seabourne, 2009). Particularly for the CASTEP ground state result, although the peak ratios are not in the correct intensity pattern, the energy values are approximately correct. However, arguably the best qualitative agreement with experiment is observed for the 2x2x2 CASTEP supercell result.

The initial overlay plot for the nitrogen K edge includes experimental and theoretical data from another research group (Holec, 2008). Our results for 2x2x2 supercells compare well to the experimental result, and also to the previously obtained theoretical result (which uses a single-electron core-hole and a 2x2x2 supercell). The Holec et al. work perhaps shows some more (smaller) peak features not observed in the work from this thesis.

5.4.4 Quantitative comparisons

An aim of this section of work was to move away from purely qualitative comparisons with experiment. In order to accomplish this, a method I developed (since published) was utilised (Seabourne, 2010). For the edge in question, the various sets of theoretical data were appropriately scaled and shifted relative to the experimental result. In order to do this, each theoretical result was shifted on the energy axis so that the energy of the first spectral peak matched that of experiment. Secondly, the intensity of the theoretical peak was scaled to match that of experiment. Subsequently, the theoretical results were interpolated onto the same x-axis abscissas as the experiment result (i.e. simulation values are found at the energy values of the experimental data). At each point on the new x-axis, for each theoretical result, the difference from experiment was found, and squared. The average of these squared differences was obtained over a sensible energy range and square rooted. This gives a ‘goodness of fit measure’ and is effectively a form of chi-squared analysis. Finally that value was normalised against the intensity of the scaled peak. The energy range chosen will alter the resultant values, and therefore it was decided to standardise the energy window for the edges considered as from 5eV before the first peak to 20eV after that peak. Different energy windows are shown in the plots below for illustrative purposes.

There are other possible methodologies. Peak areas might have been used for the normalisation section, however it would be difficult in some cases to determine the correct area of the spectrum to use. Furthermore, there may be some systematic effects resulting from the choice of energy window. The experimental data is not in all cases treated to remove multiple scattering effects, which are particularly bad towards the higher value of the chosen energy window. This may obscure otherwise good fit in the region of the Fermi level. However, this work represents a significant beginning to measuring goodness of fit.

Figures 5.11 to 5.15 illustrate the results of the described process:

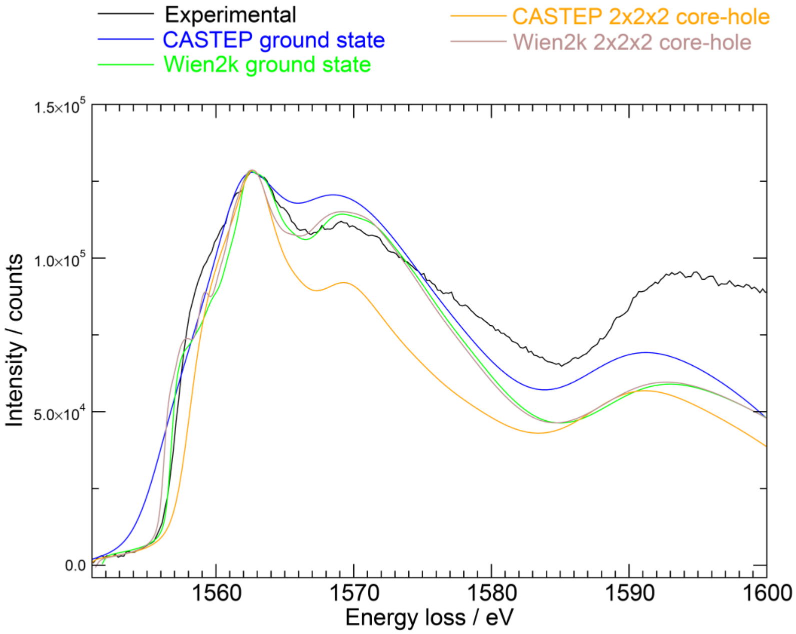

Figure 5.11: Various aluminium K edges in aluminium metal. The experimental result is unaltered. The theoretical results are shifted in energy and intensity to match the principal peak in the experimental spectrum.

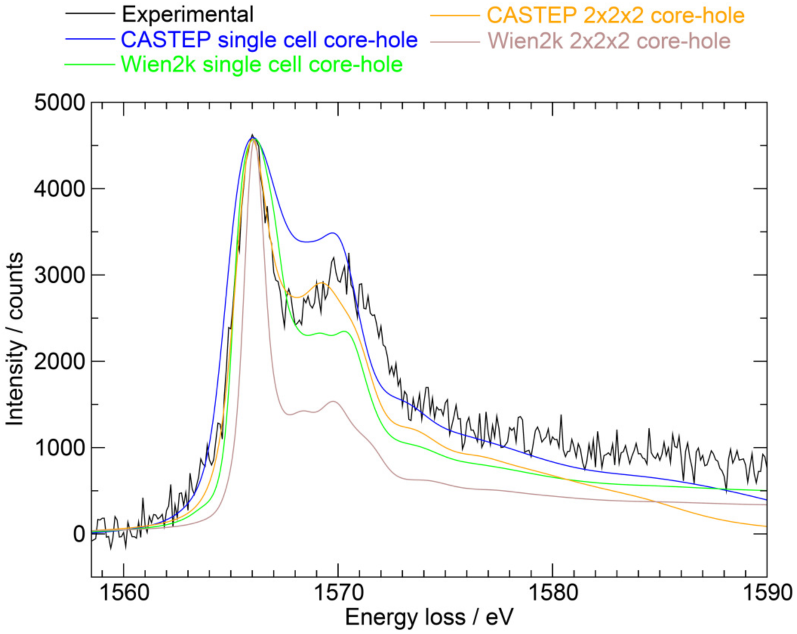

Figure 5.12: Various aluminium K edges in alumina. The experimental result is unaltered. The theoretical results are shifted in energy and intensity to match the principal peak in the experimental spectrum.

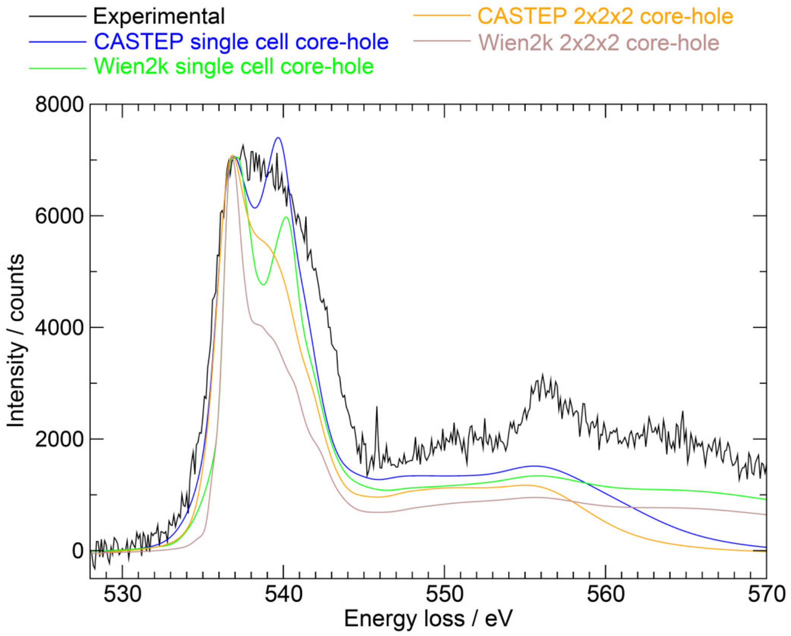

Figure 5.13: Various oxygen K edges in alumina. The experimental result is unaltered. The theoretical results are shifted in energy and intensity to match the principal peak in the experimental spectrum.

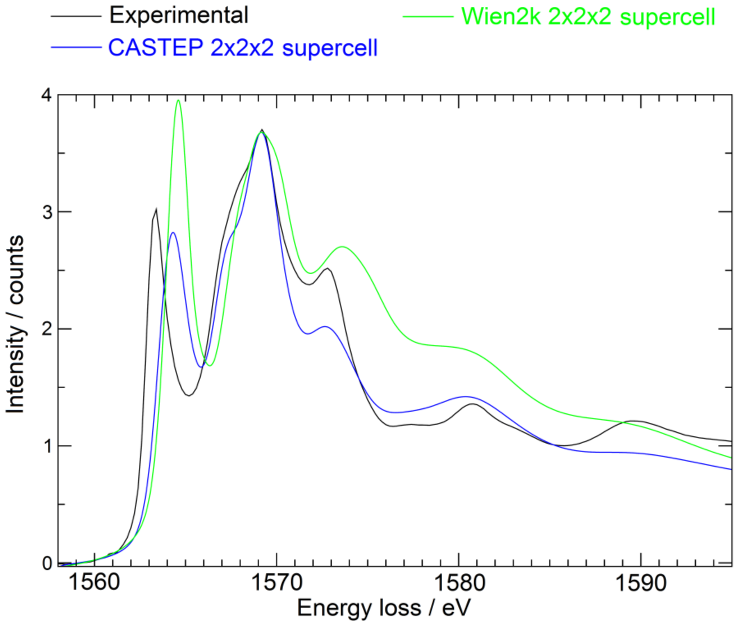

Figure 5.14: Various aluminium K edges in aluminium nitride. The experimental result is unaltered. The two theoretical results are shifted in energy and intensity to match the second peak of the theoretical spectrum.

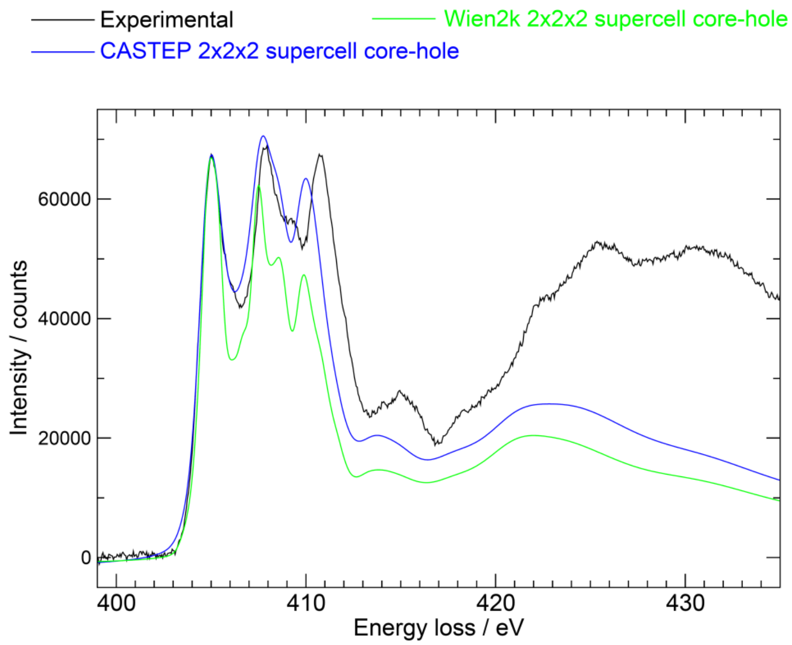

Figure 5.15: Various nitrogen K edges in aluminium nitride. The experimental result is unaltered. The two theoretical results are shifted in energy and scaled in intensity so that the first peak in all the spectra has the same intensity.

Table 5.3 summarises the results of the various reduced chi-squared type analyses:

Material	EDGE	Energy range for analysis / eV	CASTEP single cell ground state normalised result	Wien2k single cell ground state normalised result	CASTEP single cell core-hole normalised result	Wien2k single cell core-hole normalised result	CASTEP 2x2x2 supercell core-hole normalised result	Wien2k 2x2x2 supercell core-hole normalised result	Additional comments
Aluminium	Aluminium K	1557.3 - 1582.3	0.059	0.075	N/A	N/A	0.179	0.076	As the numerical values do indicate, there is also strong agreement for the two Wien2k results; indeed for the two major peaks the agreement is better for the Wien2k results.
Al_2O_3	Aluminium K	1561.0 – 1586.0	N/A	N/A	0.091	0.104	0.086	0.200	Visual inspection further indicates better agreement for the CASTEP results.
	Oxygen K	532.4 - 557.4	N/A	N/A	0.119	0.174	0.178	0.267	The best numerical match in this instance (CASTEP) shows inconsistent peak ratios.
w-AlN	Aluminium K	1558.4 - 1583.4	N/A	N/A	N/A	N/A	0.111	0.205	Visual inspection further indicates better agreement for the CASTEP results.
	Nitrogen K	400.0 – 425.0	N/A	N/A	N/A	N/A	0.154	0.228	Wien2k prediction arguably shows fine detail not observed for the CASTEP result.

Table 5.3: Summary results for the various reduced chi-squared type analyses. The results highlighted in green represent the best 'numerical' agreement.

Various comments are given regarding numerical agreements in Table 5.3, and clearly this methodology is not ideal. It is however the beginning of a quantitative methodology. Future work might involve developing an 'iterative' broadening scheme, in which comparison with experiment is used to optimise the various broadening parameters used in the codes.

5.5 Quantitatively measuring the ‘impact’ of the core-hole

It is generally thought that the addition of a core-hole causes a shift in the edge features towards the Fermi level, and increases the intensity of those features (Gao, 2008), (Rez, 2006). In this section of the thesis, it was aimed to place some kind of quantitative measure on the extent of these shifts.

For each compound edge (and code), the total intensity from 0-20eV was found. The ‘midpoint’ of that intensity was then found, i.e. the energy at which the integral from 0eV to that energy resulted in an intensity half that for the total integral from 0-20eV. I term this the ‘intensity moment’ of the edge, as depicted in Figure 5.16. I then found the shift in this value for the spectrum with the core-hole in place (as compared to a ground state calculation).

In terms of measuring an intensity shift near the Fermi level, the total spectral intensity was found for each edge over 0-20eV. Then, for an energy range of 0-10eV the intensity was found, and normalised against that for the whole spectrum from 0-20eV. This analysis was performed for the ground state and single electron core-hole results. The percentage shift in the intensity for the addition of the core-hole was then found.

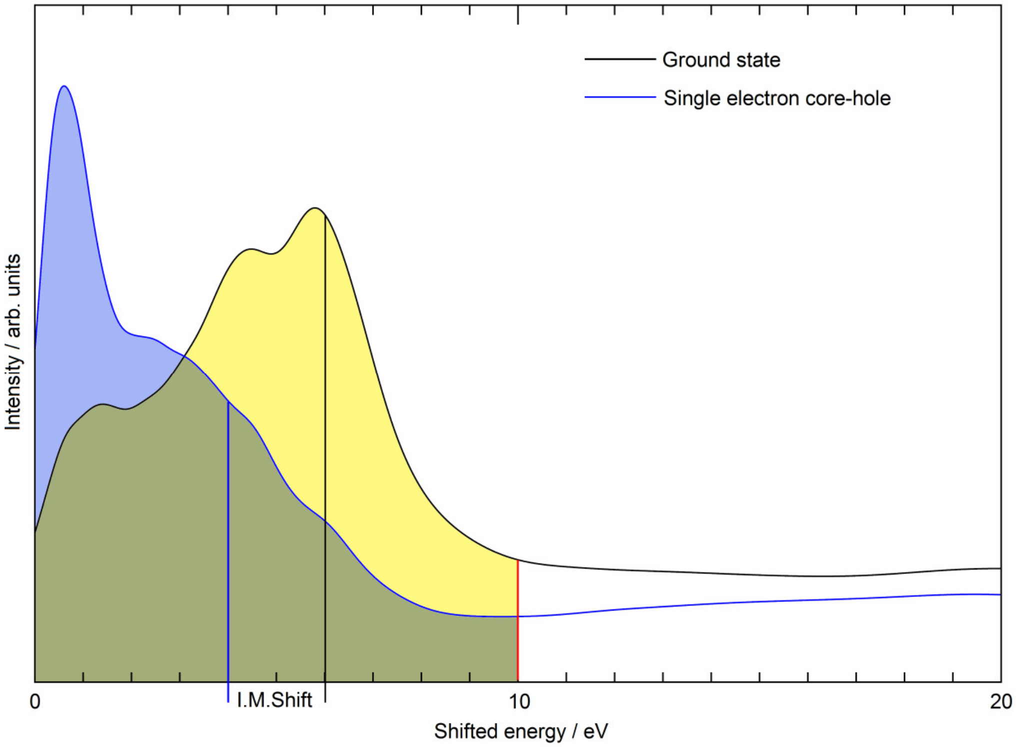

FIGURE 5.16: Depicting the process of determining the ‘intensity-moment’ shift, and percentage change upon the addition of a core-hole. The edges shown are for the sake of example the oxygen K edges from alumina (Wien2k). The shift in the ‘intensity-moment’ is illustrated, as explained in the main body of text. Further, the integrals for each spectrum (core-hole and ground state) are carried out from 0-10eV, and then normalised against the intensity of the spectrum from 0-20eV. The blue shading shows the core-hole spectrum integral, and the yellow shading that for the ground state. Areas of overlap are in green.

Tables 5.4 and 5.5 list the observed results for CASTEP and Wien2k respectively. Figure 5.17 visually depicts the various shifts in energy and intensity using a labelled scatter plot.

System / edge	I.M ground state spectrum / eV	I.M core hole spectrum / eV	I.M. shift / eV	Ground state integration 0-10eV / spectrum intensity from 0-20eV	Core-hole integration 0-10eV / spectrum intensity from 0-20eV	Percentage change in intensity upon addition of core-hole
Alumina oxygen K edge	6.0	4.3	-1.7	0.75	0.76	1.3
Alumina aluminium K edge	7.7	4.8	-2.9	0.66	0.78	18.2
Aluminium nitride nitrogen K edge	7.0	6.0	-1.0	0.66	0.67	1.5
Aluminium nitride aluminium K edge	9.9	7.5	-2.4	0.51	0.63	23.5

Table 5.4: Exploring the impact of the core-hole for the various CASTEP results. Listed are the shifts in the ‘intensity-moments’ when a core-hole is added, as well as the normalised intensity shift over the first 10eV of the spectrum.

System / edge	I.M ground state spectrum / eV	I.M core hole spectrum / eV	I.M. shift / eV	Ground state integration 0-10eV / spectrum intensity from 0-20eV	Core-hole integration 0-10eV / spectrum intensity from 0-20eV	Percentage change in intensity upon addition of core-hole
Alumina oxygen K edge	6.0	4.0	-2.0	0.73	0.75	2.7
Alumina aluminium K edge	8.0	4.3	-3.7	0.62	0.76	22.6
Aluminium nitride nitrogen K edge	6.9	5.8	-1.1	0.66	0.68	3.0
Aluminium nitride aluminium K edge	9.9	8.5	-1.4	0.51	0.58	13.7

Table 5.5: Exploring the impact of the core-hole for the various Wien2k results. Listed are the shifts in the ‘intensity-moments’ when a core-hole is added, as well as the normalised intensity shift over the first 10eV of the spectrum.

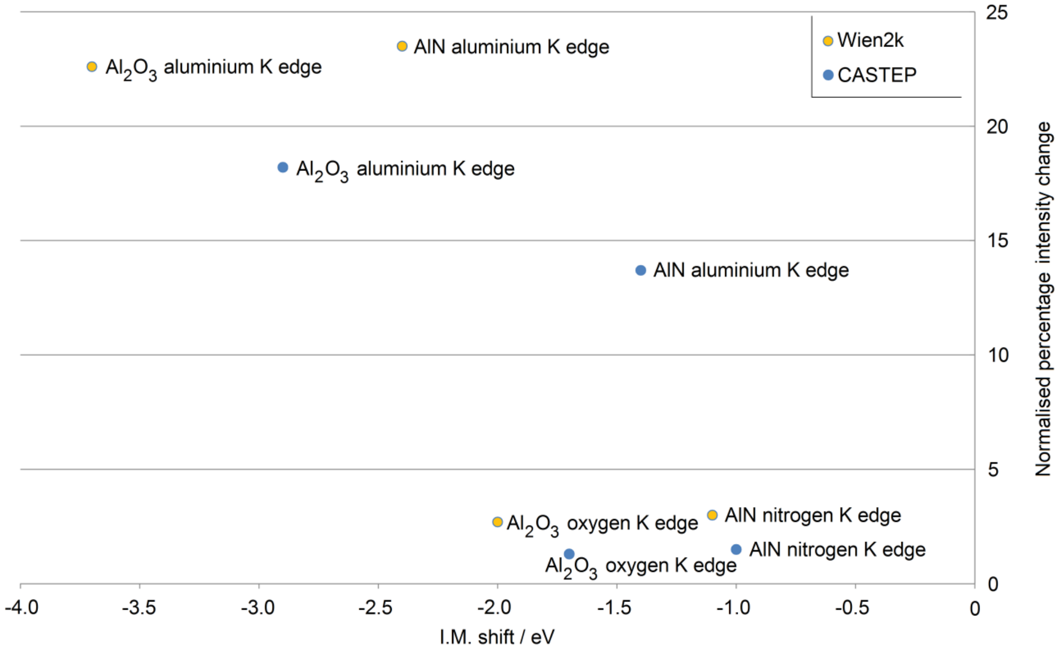

FIGURE 5.17: Scatter-plot indicating (for each code and edge) the 'intensity-moment' shift and normalised intensity change upon the addition of the core-hole.

As can be observed, in all cases the addition of a core-hole causes an intensity increase near the Fermi level, and an 'intensity-moment' (energy) shift towards the Fermi level, consistent with expected trends (Gao, 2008), (Rez, 2006). Furthermore, it has been suggested that these effects will be greater for the cation in a compound, as these species are already electron deficient (Rez, 2006). In contrast, in the anionic species there are additional valence electrons in place that can screen the core-hole. This trend is observed quantitatively for each compound and code. Comparing the two compounds, generally speaking the alumina 'intensity-moment' energy shifts (on the x-axis) are larger. Given the greater electronegativity of oxygen as compared to nitrogen, alumina is arguably more ionic in nature, leading to a greater alteration in properties upon the introduction of an electrostatic alteration to the system.

Comparing results across the two codes, for the anion edges in both compounds the results are highly similar in terms of both intensity and energy shifts. For the various aluminium edges, the differences between the codes are somewhat larger, particularly in the case of aluminium nitride. However, as mentioned (and as is crucial) the general trends for each compound (in terms of there being a greater effect for each cation edge) are consistent between the two codes.

5.6 Broadening effects

I successfully applied for time on Imperial's monochromated FEI TITAN 80/300 machine, through the EPSRC Equipment Access scheme (<http://www.epsrc.ac.uk/funding/facilities/epsrc/Pages/default.aspx>). There were two major themes planned for these experiments, related to the systems explored in this chapter. The experimental operator for this section of work was Dr. James Perkins (Imperial).

The first was to investigate how different nominal energy resolutions (based on the width of the zero-loss peak) would alter experimentally observed ELNES edges, including those modelled in this section.

Monochromation can reduce the overall beam current (see Chapter 2) and hence immediate (and predictable) problems were observed when trying to obtain good signal-to-noise ratio for the higher energy edges owing to the steep fall off in EELS spectral intensity with increasing energy loss. However, for various aluminium $L_{2,3}$ edges an attempt was made to obtain the edges at a series of different energy resolutions. Figure 5.18 illustrates the edge obtained at different energy resolutions:

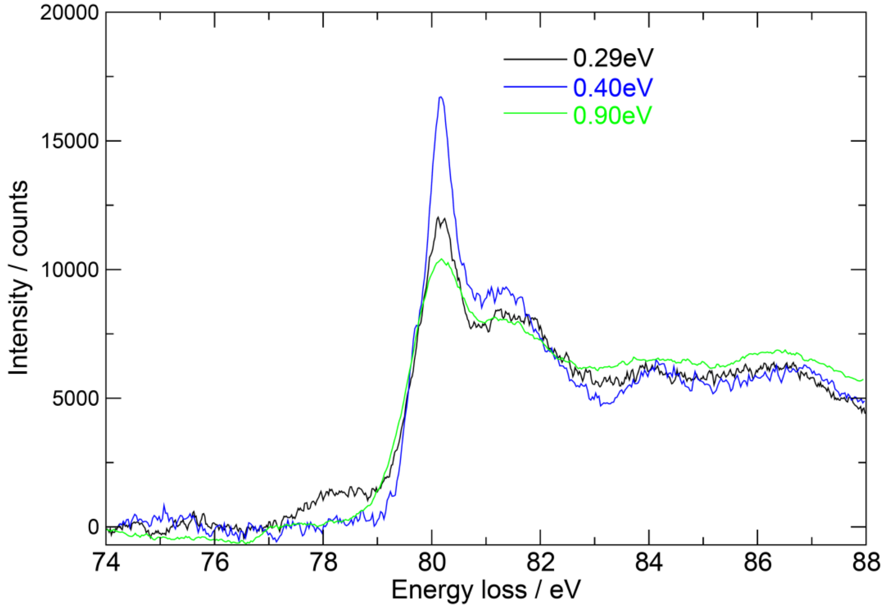

Figure 5.18: Illustrating the aluminium $L_{2,3}$ edge in alumina obtained at a series of different zero-loss resolutions, using FEI TITAN 80/300 with monochromator installed, with correction of spherical aberrations. The spectra have been normalised by intensity over the region shown in the figure, relative to the 0.29eV resolution result.

Unsurprisingly, for the better resolutions the second peak is more distinct, and better separated from the first. However, it should be noted that the 0.40eV resolution data seems to have a narrower first peak than the 0.29eV data set. For this latter result, there is a ‘bump’ in the edge at around 78eV, arguably corresponding to aluminium metal, indicating sample damage by the time this resolution had been reached. This sample damage may alter the nature of the first peak in the spectrum. Generally speaking, the first peak is perhaps too high in energy when compared to other literature (Kimoto, 2003). However, generally speaking at even a 0.90eV resolution, two peaks are still observable.

Using parameters from Table 5.1, the aluminium $L_{2,3}$ was modelled, with various broadenings applied as outlined in Figure 5.19 below:

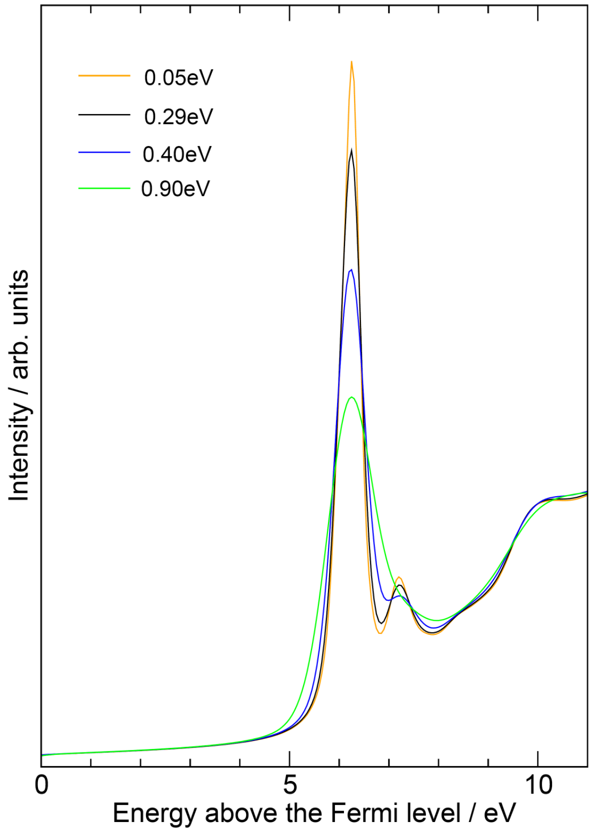

Figure 5.19: Ground state CASTEP modelling of the aluminium $L_{2,3}$ edge for alumina. The edges are shown with core and final state lifetime broadenings, but different Gaussian broadenings, designed to represent the instrumental resolution. The results have again been normalised by intensity.

Clearly the theoretical results do not particularly well reproduce peak ratios. There is also a suggestion that for these two peaks close in energy, the

Gaussian broadening used is ‘over-broadening’ the results as compared to experiment. Consider Figure 5.20, which compares experiment and theory for the 0.29eV and 0.90eV resolutions, these clearly illustrate the ‘overbroadening’ of the Gaussian for the latter resolution, but shows good peak energy separations when comparing experiment and theory for the 0.29eV resolution data, though peak ratios are not particularly well reproduced.

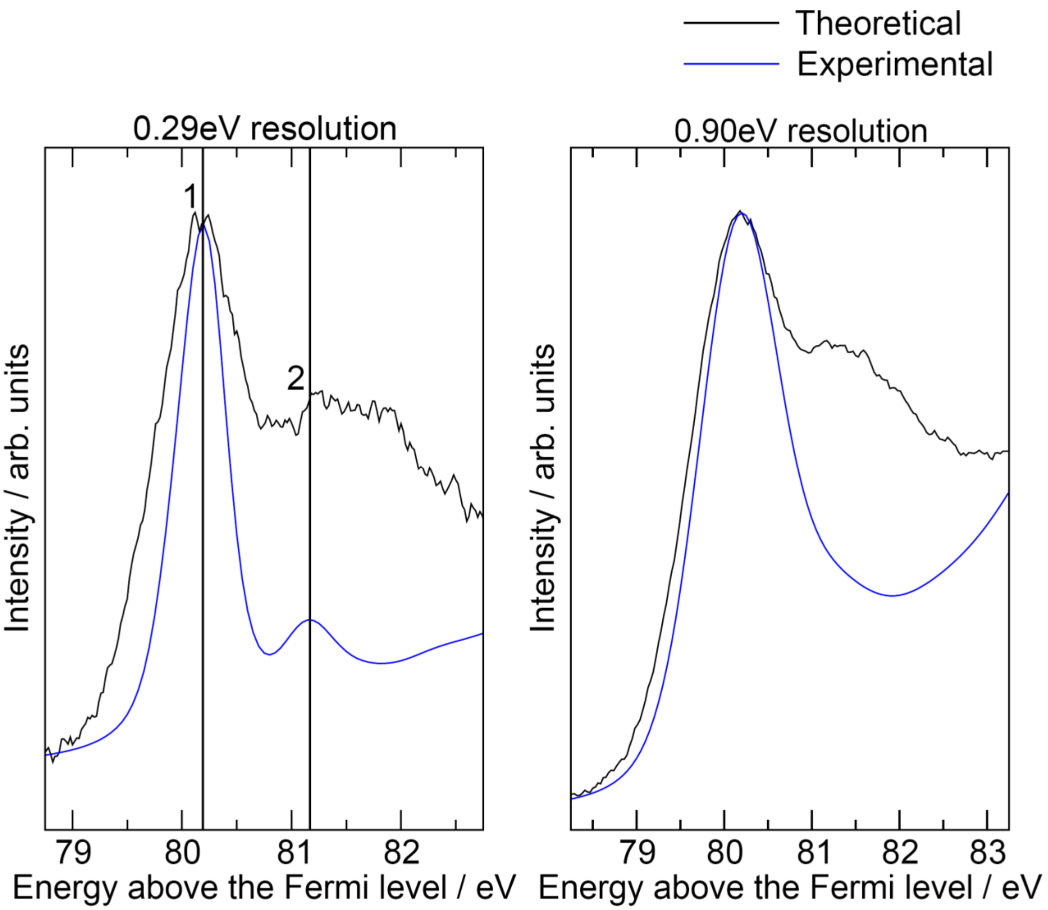

Figure 5.20: Comparison of experimental and theoretical alumina Al $L_{2,3}$ edges as labelled. The theoretical results are aligned with experiment by energy, and intensity.

Another interesting consideration is how the inherent source broadening alters with energy loss, an effect rationalised by considering the spectrometer itself as a lens (Egerton, 1996). Again, some preliminary results were obtained using the Imperial Titan. The monochromator was switched off, as on the day used for this experiment it could not be properly tuned. For a zero energy adjust, the ZLP FWHM was obtained. The energy adjust value was then altered, and the ZLP obtained again. The results were as shown in Figure 5.21:

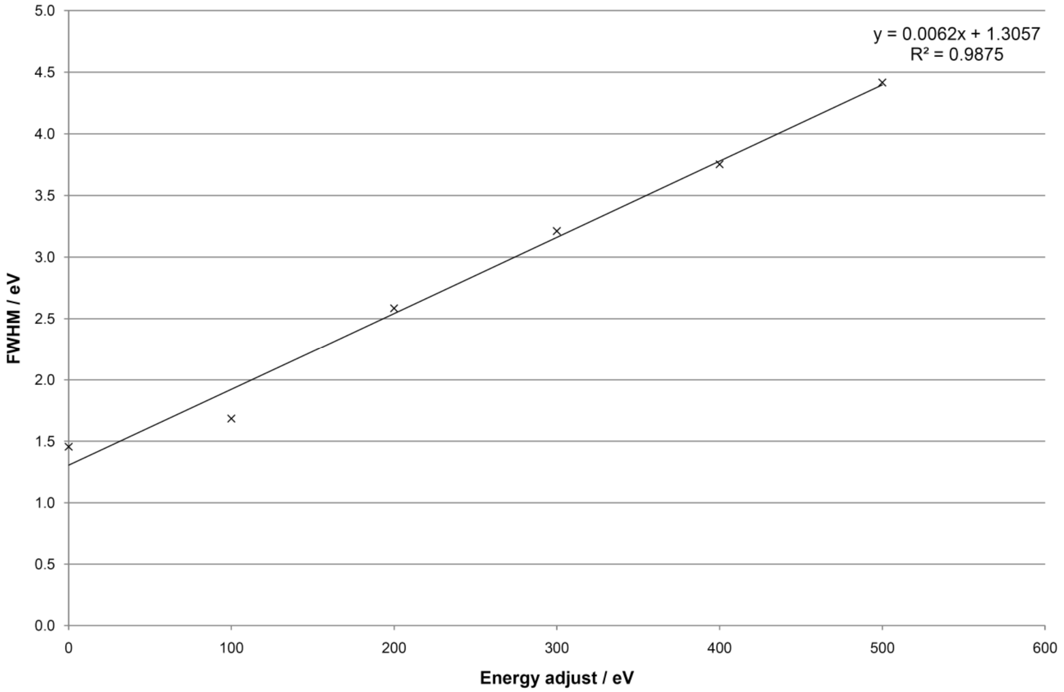

Figure 5.21: Comparison of ZLP FWHM values with energy adjust, with other conditions unaltered.

It would be interesting to attempt to repeat this experiment with the monochromator in place, but a distinct worsening is observed in the energy resolution as the energy adjust value is increased (simulating an energy loss as in a core-ionisation edge). This is due to a chromatic aberration type effect (in the spectrometer and related optics). In a typical experiment we initially focus the spectrometer on the zero-loss peak at a particular position on the detector. These (preliminary) results suggest the resolution defined at the ZLP could be around three times worse at a 500eV energy-loss. In a large number of (good quality) experimental studies, the spectrometer is properly refocused at core-loss edges to avoid this problem. However, this is not always the case.

5.7 Summary and conclusions

Careful DFT calculations have been presented across a range of aluminium compounds, and predicted results are similar for the pseudopotential code CASTEP and the all-electron code Wien2k. Quantitative techniques have been applied to determine agreement with experiment, and good agreement was generally observed. The parameters used for the calculations were converged, though the convergence criteria were relatively ‘generous’ so to allow faster calculations. This concept has been considered previously in the literature (Nicholls, 2008). It has further been shown with a quantitative analysis that the addition of a theoretical core-hole does move the edge features towards the Fermi level, and lead to an increase in intensity in that region. These effects were also proven to be larger for the cationic species in a particular compound.

Chapter 6

Detailed study of transition metal carbides

6.1 Introduction and systems considered

In initial testing (see Chapter 4) the carbon K edge for zirconium carbide was modelled in the ground state for direct comparison with previous work carried out by Scott et al. (Scott, 2001). In this paper, the full series of groups 4 and 5 transition metal carbides were studied, i.e. TiC, ZrC, HfC, VC, NbC and TaC. It was considered necessary to consider these systems using the CASTEP code in more detail, using the rigorous methodology developed in thesis, to supplement the existing work in the literature using the Wien2k code (Scott, 2001). Investigated in this instance were the carbon K edges in all cases, in addition to selected $L_{2,3}$ edges.

Also considered were a series of carbonitride systems with vacancies present; $TiC_{0.79}$, $TiC_{0.58}N_{0.30}$, $TiC_{0.45}N_{0.43}$, $TiC_{0.19}N_{0.65}$ and $TiN_{0.82}$ (MacKenzie et al., unpublished data). Previous work has suggested that for TiC_x type systems, different 'X' values will alter the microhardness of the system, and influence properties such as conductivity and thermal expansion behaviour (Ivanov, 1978), (Zueva, 2000). An ultimate aim of this work is to suggest structural characteristics for these systems by combining experimental and theoretical EELS.

6.2 Bulk group 4 and 5 transition metal carbides

6.2.1 Introduction

Transition metal (TM) carbides have various applications in materials science. Due to their high melting points, they are referred to as 'refractory carbides' (Scott, 2001), (Storms, 1967). TM carbides are also hard, this in combination with their stability at high temperature makes them ideal candidates for usage in industrial cutting machines, or as wear-resistant coatings (as they also have low chemical reactivity).

This section considers the ELNES characterisation of the group 4 and 5 carbides (TiC, ZrC, HfC, VC, NbC, TaC), ZrC having been briefly considered before in the thesis. The carbon K edges for all the materials are modelled, and in the case of TiC, also the Ti $L_{2,3}$ edge.

6.2.2 Parameter selection

The established method (as previously described in this thesis) was used to determine suitable parameters. Table 6.1 lists the chosen parameters, which were determined to be suitable for all six compounds, for a tolerance of 5% based on the carbon K edge upon doubling *k*-point mesh parameters from 6x6x6, or increasing the kinetic energy cut-off by 100eV intervals.

Parameter	Chosen value
Standard cell dimensions	Cubic cell of the carbide in the rock-salt structure, ($\alpha=\beta=\gamma = 90^\circ$): TiC, $a=b=c$ = 4.33Å ZrC, $a=b=c$ = 4.70Å HfC, $a=b=c$ = 4.64Å VC, $a=b=c$ = 4.17Å NbC, $a=b=c$ = 4.47Å TaC, $a=b=c$ = 4.46Å
Kinetic energy cut-off	600eV
Energy step *k*-point mesh	12x12x12 or better, actual reciprocal space separations (single cell): TiC = 0.019Å^{-1} ZrC = 0.018Å^{-1} HfC = 0.018Å^{-1} VC = 0.020Å^{-1} NbC = 0.019Å^{-1} TaC = 0.019Å^{-1} For 2x2x2 supercell calculations, convergence tolerance increased to allow sensible calculation times, therefore new reciprocal space separations: TiC = 0.029Å^{-1} ZrC = 0.027Å^{-1} HfC = 0.027Å^{-1} VC = 0.030Å^{-1} NbC = 0.028Å^{-1} TaC = 0.028Å^{-1}
EELS calculation *k*-point mesh	12x12x12 or better, actual reciprocal space separations: TiC = 0.019Å^{-1} ZrC = 0.018Å^{-1} HfC = 0.018Å^{-1} VC = 0.020Å^{-1} NbC = 0.019Å^{-1} TaC = 0.019Å^{-1} For 2x2x2 supercell calculations, convergence tolerance increased to allow sensible calculation times, therefore new reciprocal space separations: TiC = 0.029Å^{-1} ZrC = 0.027Å^{-1} HfC = 0.027Å^{-1} VC = 0.030Å^{-1} NbC = 0.028Å^{-1} TaC = 0.028Å^{-1}
Core-hole / pseudopotentials	Single electron core-hole in place for one of the carbon atoms, using an on-the-fly (OTF) pseudopotential. All other atoms – standard ground state GGA pseudopotentials.

Table 6.1: Chosen parameters (CASTEP) for groups 4 and 5 transition metal carbides**.**

6.3 Bulk material carbon K edge results

In the style of work presented in Chapter 5 of this thesis, for the six bulk materials considered, predicted carbon K edge results were found for both single and 2x2x2 supercells, in the ground state and using 0.5 electron, and single electron core-holes in the 1*s* level.

6.3.1 Titanium carbide carbon K edge

Firstly consider Figure 6.1, which shows results for the TiC carbon K edge modelling. Presented throughout this section on the carbon K edges are three plots for each core-hole approximation and cell size; a partial (*p* orbital) density of states shown with 0.2eV smearing, an ELNES result also shown with a 0.2eV smearing (i.e. directly comparable to the *p*-DOS broadening), and an ELNES result shown with energy-dependent final state lifetime broadening:

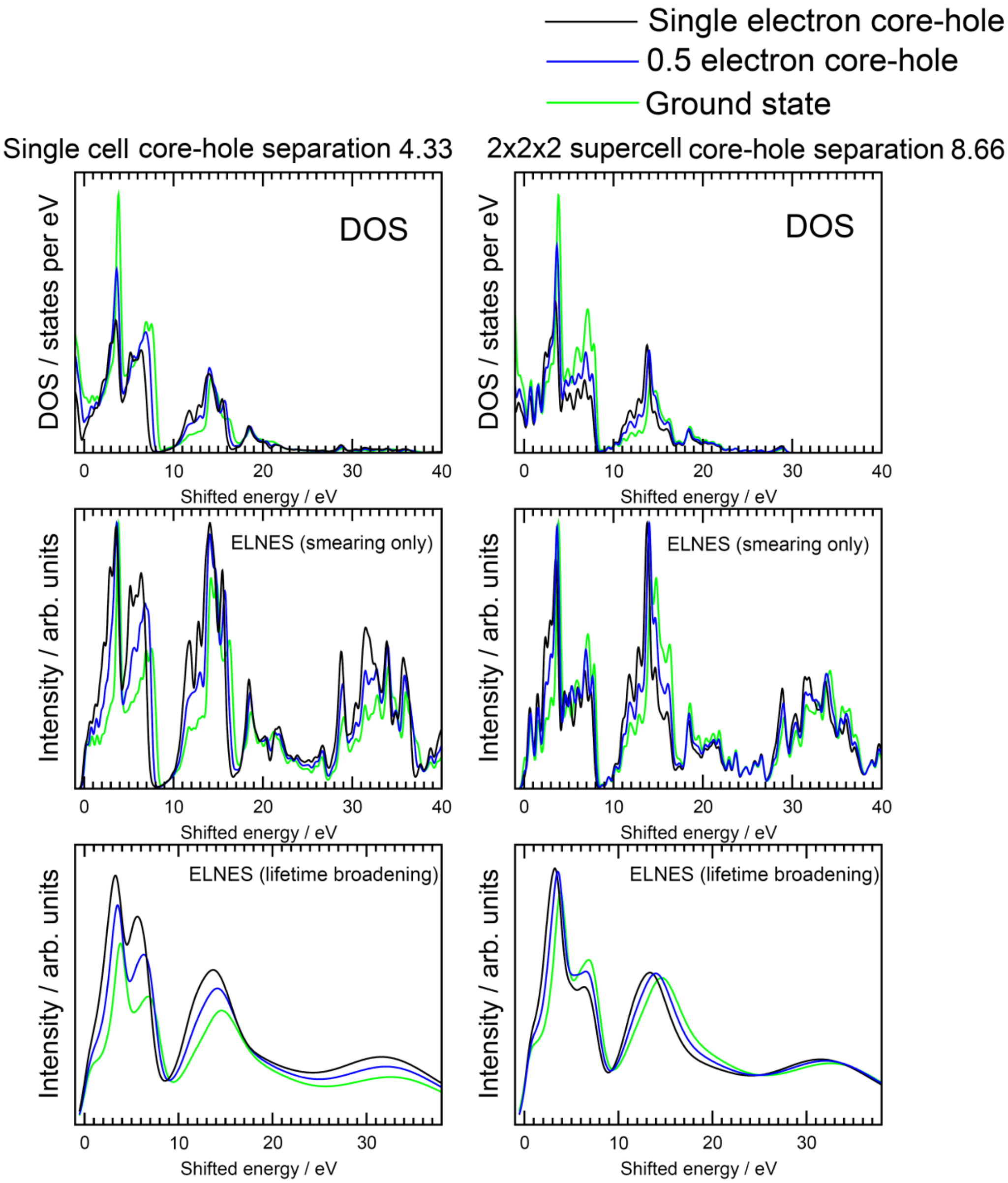

Figure 6.1: Various TiC carbon K edge predictions and DOS results. The top plot shows the *p* orbital partial density of states, shown simply with a 0.2eV smearing. The middle plots are the carbon K edge predictions again shown with only a 0.2eV smearing added. Finally, the bottom plots are the carbon K edge predictions with the addition of energy-dependent final state lifetime broadening.

There is broad qualitative similarity between the various *p* partial DOS predictions and the respective ELNES predictions (when the same broadening is applied). Certainly, the energy positions of the peaks are similar, though relative peak intensities alter comparing the partial *p* DOS and ELNES.

The more broadened ELNES predictions allow the easiest observation of trends with regard to the importance of core-hole strength. For both cell sizes, generally upon increasing the core-hole strength there is a shift in the edge towards the Fermi level. These changes are larger in the single cell case, though this is likely to be due to artificial interference of core-holes. The variation of core-hole strength (i.e. when comparing the 0.5 and single electron core-hole results) is similar to that observed in previous work (Paxton, 2000).

Qualitatively speaking, the single cell ground state result appears similar to the various larger cell supercell results. The 2x2x2 supercell calculations take six times longer than the single cell calculations (example given for TiC with a single electron core-hole in place). As the partial *p* DOS plots indicate, altering the core-hole strength does significantly change the intensity of the first major peak in the DOS, but the energy positions of the peaks are approximately unchanged. Therefore, Figure 6.2 compares the experimental TiC carbon K edge (VG HB5 cold FEG STEM, 0.3eV energy resolution) with the single cell ground state result, and 2x2x2 supercell core hole results. In this instance the results are again shown with the further addition of energy-dependent final state lifetime broadening:

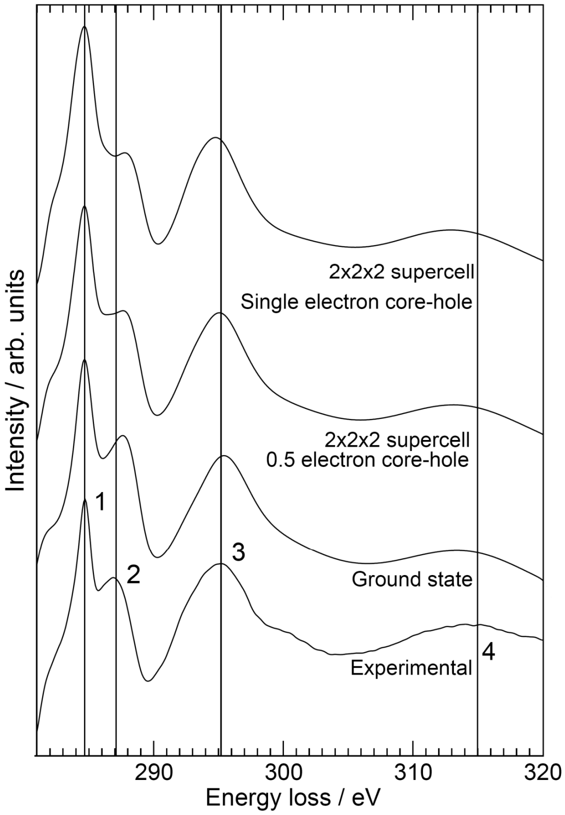

Figure 6.2: Comparison of TiC experimental carbon K edge (VG HB5 cold FEG STEM, 0.3eV energy resolution) with various theoretical simulations carried out using the CASTEP code. Guidelines have been added with peak labels (Craven, 1995), (Scott, 2001).

We can clearly observe in terms of peak ratios (for 1 and 2) that the closest agreement with experiment is the ground state result. Certainly this does not appear to be improved by the much more computationally demanding 2x2x2 supercell calculations. The partial *p* DOS results suggest that for this largely metallic system the core-hole is well screened, and therefore a ground state calculation is highly viable.

None of the results correctly predict the separation of peaks 1 and 2.

6.3.2 TiC titanium L edge

For TiC, the Ti $L_{2,3}$ edge was also considered with the same rigour as the carbon K edge. Again presented are three plots for each core-hole approximation and cell size; a partial (*s* and *d* orbital) density of states shown with 0.2eV smearing, an ELNES result also shown with a 0.2eV smearing (i.e. directly comparable to the *p*-DOS broadening), and an ELNES result shown with energy-dependent final state lifetime broadening:

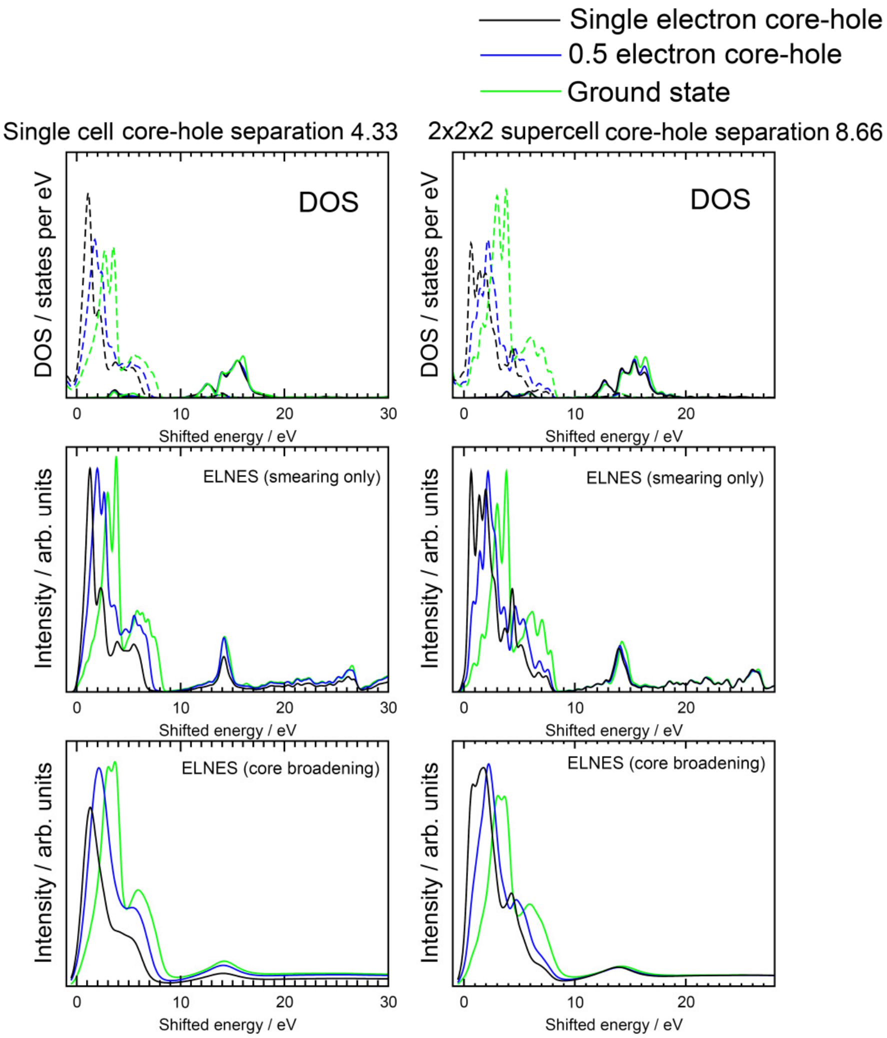

Figure 6.3: Various TiC Ti $L_{2,3}$ edge predictions and DOS results. The top plot shows the *s* and *d* orbital partial density of states, shown simply with a 0.2eV smearing. The solid lines are the *s* orbital partial DOS, and dashed lines are the *d*-orbital equivalents. The middle plots are the Ti $L_{2,3}$ edge predictions again shown with only a 0.2eV smearing added. Finally, the bottom plots are the Ti $L_{2,3}$ edge predictions with the addition of energy-dependent final state lifetime broadening.

Encouragingly, the ground state results are similar for the different cell sizes, which is expected. The overall ELNES predictions bear a strong similarity to the partial *d* DOS predictions in most cases. For the $L_{2,3}$ edges (and indeed *d* DOS predictions), the introduction of a core-hole has a great qualitative effect. In particular, consider the *d* DOS predictions (for both cell sizes), which show a clear shift from a doublet (in the ground state) to a completely different shape upon the addition of a core-hole.

Agreement with experiment is relatively poor in terms of peak separations, as illustrated in Figure 6.4. The code has been assumed to be correctly accounting for spin-orbit coupling. The core-hole result arguably also shows a shoulder that is also observed in experiment:

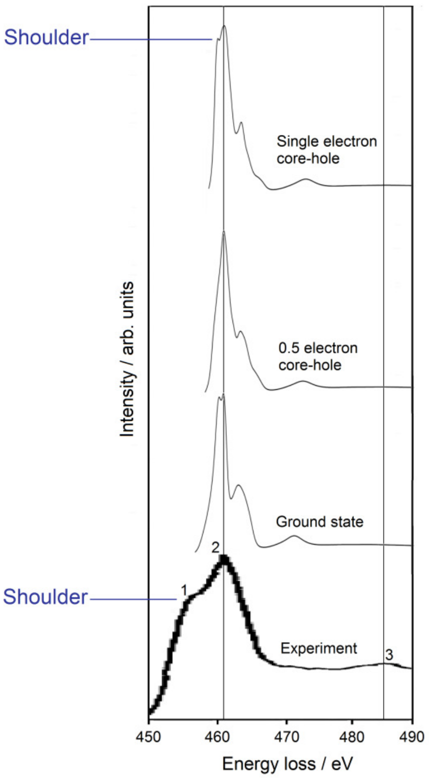

Figure 6.4: Comparison of various theoretical TiC Ti $L_{2,3}$ edges with a digitised experimental result (Hofer, 1990). The theoretical results are shown with appropriate core and final state lifetime broadenings, and an appropriate Gaussian broadening.

At this juncture, it is necessary to give some consideration of the relative contribution of *s* and *d* states to the overall $L_{2,3}$ edge. Note this is not an active consideration of the 'branching ratio' – i.e. the L_3 to L_2 ratio which is calculated by the code, the standard statistical ratio for which is (2l + 2) / 2l = 2 (where l=1 for a *p* orbital (Ogasawara, 2001).

Some attempt was made to use a multiple linear least squares (MLLS) methodology, whereby a fit of the *s* and *d* partial DOS was carried out against the ELNES results without lifetime broadening effects. This process was carried out for a 2x2x2 supercell with a single electron core-hole in place, experimental comparisons being most encouraging at least in this case. Figure 6.5 compares the ELNES prediction for a 2x2x2 supercell (Ti $L_{2,3}$ edge) with a MLLS fit of the *s* and *d* partial DOS which contribute to the edge. Note that no effort has been made to account for matrix elements:

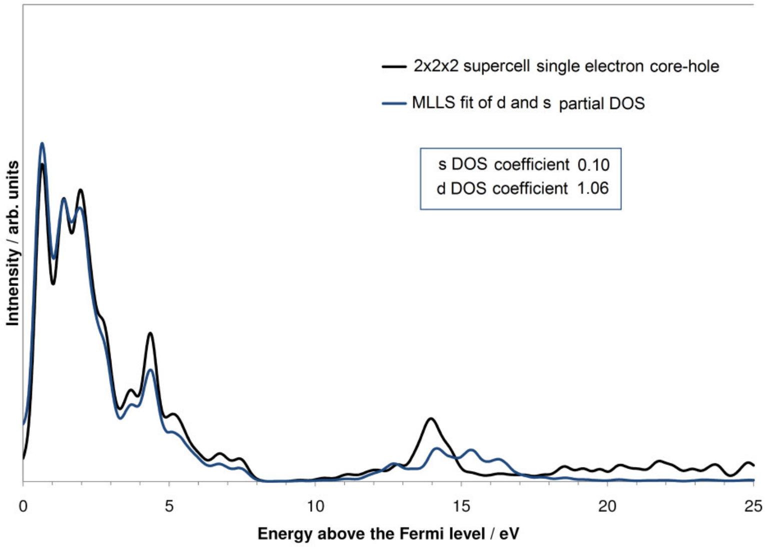

Figure 6.5: Comparison of ELNES ($L_{2,3}$) prediction for Ti with a MLLS fit of the *d* and *s* partial DOS.

Visual inspection, and MLLS coefficients clearly indicate the dominance of the *d* states in these $L_{2,3}$ edges. Furthermore, the high similarity of the partial DOS results to the ELNES predictions shows minimal significance for the transitional matrix elements.

6.3.3 Other group 4 and 5 carbides carbon K edges

For the other group 4 and 5 carbides L edges were not considered. A full range of carbon K edges (in the style of Figures 6.1 and 6.2) were found for each compound, with experimental comparisons made.

Figures 6.6 to 6.10 show single cell and 2x2x2 supercell carbon K edge predictions (with lifetime broadening effects) with different core-hole approximations (as labelled) for ZrC, HfC, VC, NbC and TaC. Also shown for each compound are experimental comparisons. The following Table 6.2 then gives an overview discussion of interesting observations with regard to the modelling results. For the experimental comparisons, **all core-hole results are from 2x2x2 supercells.**

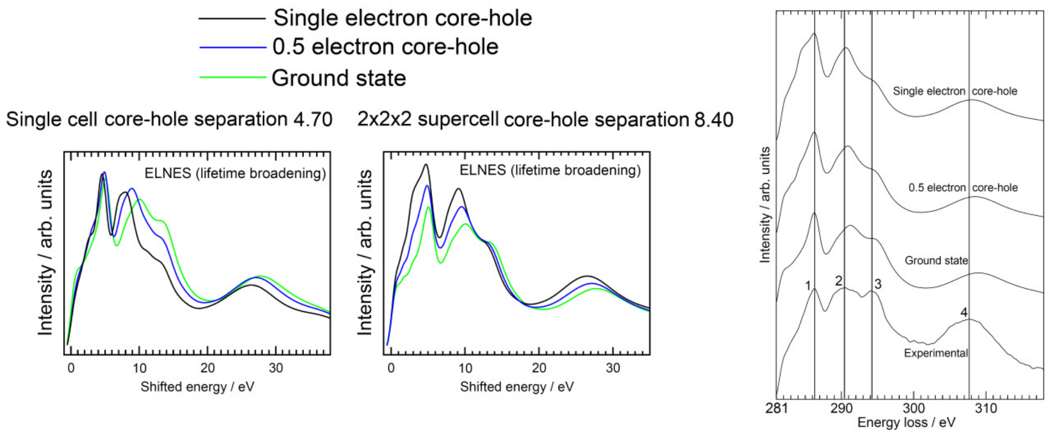

Figure 6.6: Various ZrC carbon K edge predictions and DOS results, also comparison of ZrC experimental carbon K edge with various theoretical simulations (Craven, 1995), (Scott, 2001).

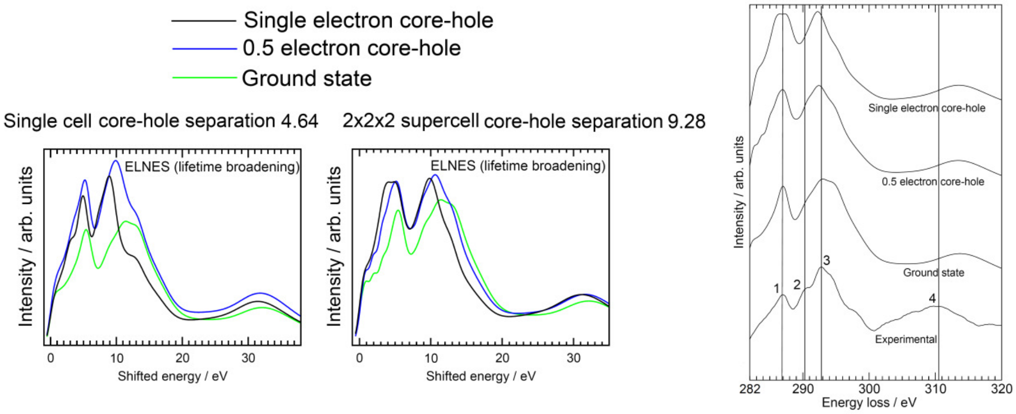

Figure 6.7: Various HfC carbon K edge predictions and DOS results, also comparison of HfC experimental carbon K edge with various theoretical simulations (Craven, 1995), (Scott, 2001).

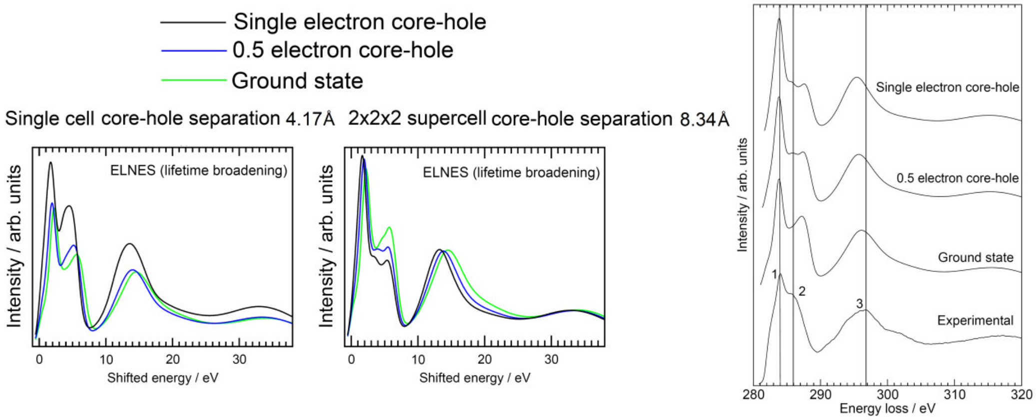

Figure 6.8: Various VC carbon K edge predictions and DOS results, also comparison of VC experimental carbon K edge with various theoretical simulations (Craven, 1995), (Scott, 2001).

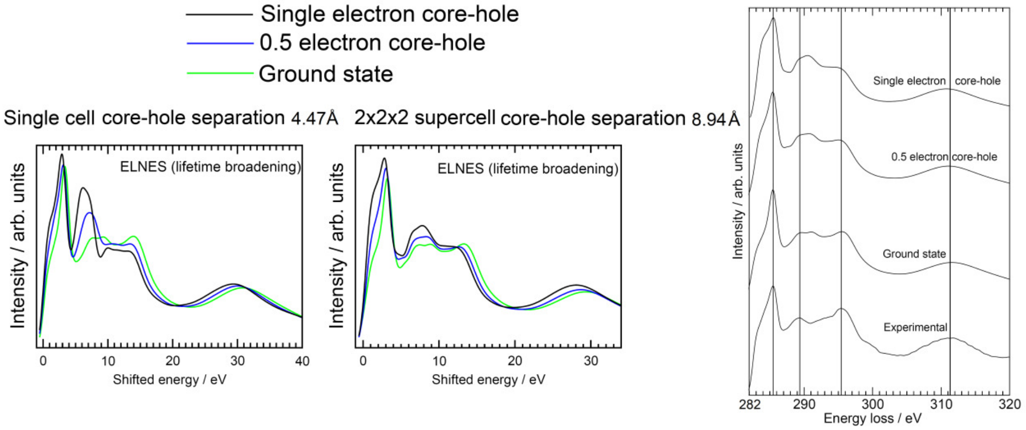

Figure 6.9: Various NbC carbon K edge predictions and DOS results, also comparison of NbC experimental carbon K edge with various theoretical simulations (Craven, 1995), (Scott, 2001).

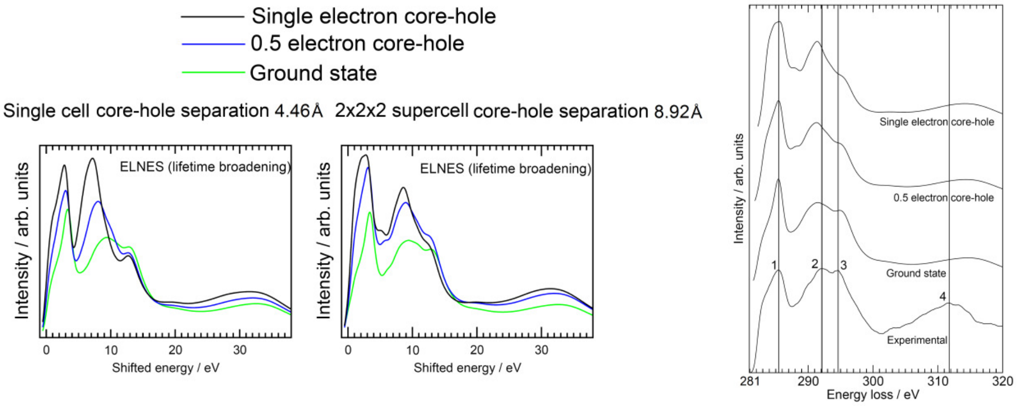

Figure 6.10: Various TaC carbon K edge predictions and DOS results, also comparison of TaC experimental carbon K edge with various theoretical simulations (Craven, 1995), (Scott, 2001).

Compound	**Observations relating to cell size and core-hole strengths**	**Experimental comparisons**
ZrC	For the 2x2x2 supercell as compared to the single cell peak separations are more similar for the different core-hole approximations.	In terms of peak intensity ratios, arguably the ground state result offers the best agreement. However, peak positions relative to experiment are slightly improved upon using a core-hole.
HfC	As with ZrC, changing core-hole strength has a lesser effect on peak separation for the 2x2x2 supercell.	Relative peak positions compared to experiment are not particularly improved by using a core-hole, nor are peak intensity ratios.
VC	For the 2x2x2 results as compared to single cells, the core-hole appears strongly screened, little qualitative difference is observed upon altering core-hole strengths.	Experimental peak ratios are best reproduced by the ground state simulation, though this agreement is not particularly good. Using a core-hole does not particularly improve the agreements.
NbC	Peak ratios are less dependent on core-hole strength for the 2x2x2 supercell results.	Arguably the best agreement is observed for the ground state result (particularly with regard to relative peak intensities).

TaC	The results are more qualitatively similar for the 2x2x2 supercells (in terms of core-hole strength).	Reasonable agreement is observed for all results, arguably the strongest agreement is again for the ground state calculation.

Table 6.2: Observations relating to core-hole strength and cell-size, and experimental comparisons for ZrC, HfC, VC, NbC and TaC.

In Scott et al.'s work on these systems using Wien, good qualitative agreement with experiment was observed for ground state results for the carbon K edges, though the results were not treated with a final state lifetime broadening scheme (Scott, 2001). In that work, single electron-core hole effects were considered for TiC and ZrC. In both instances, the usage of a core-hole improved agreement of peak positions with experiment. This is arguably observed with the modern CASTEP results also, which benefit from the usage of supercells.

Generally speaking for all the systems, when a supercell is used, variation of core-hole strength has a lesser effect on the predicted edges. Scott et al.'s previous work using Wien had indeed suggested that the general core-hole effect for these systems would be relatively small, improving peak positions, but not radically altering peak intensity ratios (Scott, 2001). The variation of core-hole strength having relatively little effect on the predicted edge was something previously observed in particular for aluminium metal. This is unsurprising given the numerous metallic characteristics of the transition metal carbides considered.

In terms of experimental comparisons, generally speaking, as was the case for the Scott et al. Wien work ground state results provide acceptable agreement with experiment (unsurprising considering the metallic nature of the systems). In limited cases, particularly ZrC, using a core-hole improves peak positions as compared to experiment.

6.4 Non-stoichiometric carbonitrides

6.4.1 Introduction

Having modelled bulk carbides systems and obtained sensible results, it was thought plausible to model non-stoichiometric systems. A long-running collaboration at the University of Leeds between my supervisor and the University of Glasgow was highlighted as an area to investigate (MacKenzie et al., unpublished data). As was described in the introduction to this chapter, titanium carbides have a wide range of industrial usages (Scott, 2001), (Storms, 1967). However non-stoichiometry is common for these systems, and crucially the physical properties of the materials are influenced by the extent of vacancies (Eibler, 2002).

Various carbon and nitrogen edges were obtained for a series of non-stoichiometric carbonitrides; $TiC_{0.79}$, $TiC_{0.58}N_{0.30}$, $TiC_{0.45}N_{0.43}$, $TiC_{0.19}N_{0.65}$ and $TiN_{0.82}$.

6.4.2 Structural considerations

Given these systems are sub-stoichiometric, it was necessary to design a sensible methodology for modelling the 'vacancy' positions. Literature confirms that the titanium sites are fully occupied, and it is the carbon / nitrogen positions that are the source of the vacancies (de Novion, 1985).

Generally speaking the structures are of the rock-salt form. It was decided to use 2x2x2 supercells, i.e. '$Ti_{32}C_{32}$' if no defects existed. This system allowed reasonable compositions to be constructed that at least well approximated the experimental systems. Certain compromises were made in terms of exactly matching the configurations to allow high symmetry, which would speed up calculations. Ground state calculations were used, so there was no disadvantage to using smaller cells if symmetry permitted. To further allow high symmetry, vacancies were assumed to exist in a regular symmetric 'array' ($Fd3m$). There is direct experimental evidence (X-ray diffraction study (Lorenzelli, 1986)) for this being the case, particularly in the range $0.5 \leq x \leq 0.7$, with this being assumed to be viable (at least as an approximation) for the systems given above (Eibler, 2002). Furthermore, this structure has been demonstrated to be a ground-state using DFT (Korzhavyi, 2002). Clearly other models are possible, but would be much more computationally complex.

Figure 6.11 depicts a '$Ti_{32}C_{32}$' cell showing an equal distribution of carbon atoms and vacancies, i.e. '$Ti_{32}C_{16}$' – $TiC_{0.5}$. Atom colour labels are as illustrated in the figure (Eibler, 2002):

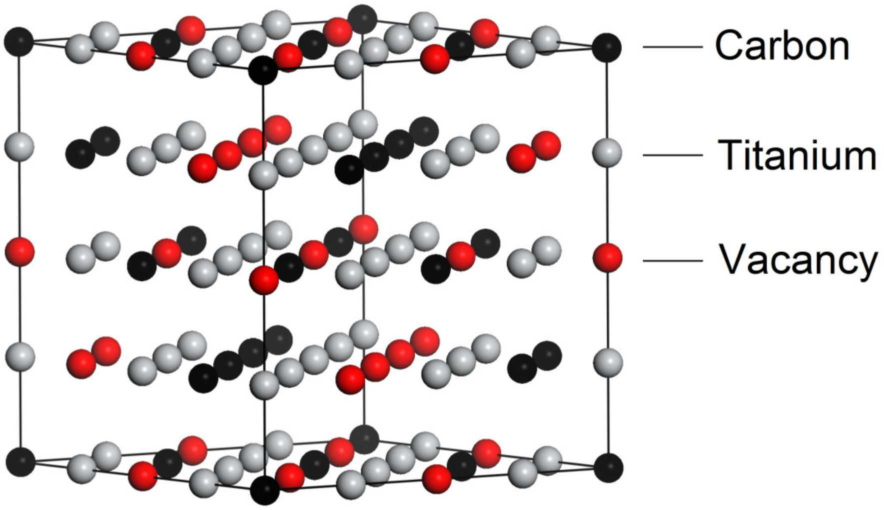

Figure 6.11: Showing the position of regular symmetry vacancies within a titanium carbide supercell, assuming half the carbon sites have vacancies. The 'silver' shaded atoms represent titanium, the grey carbon, and the red spheres represent the vacancies (Eibler, 2002).

Having established this methodology, a remaining challenge was using a sensible lattice parameter for the cells. A literature survey indicated the difference between for example the lattice parameter for bulk TiC (4.33Å) and $TiC_{0.62}$ (4.31Å) was minimal (Smolik, 1999), (Tashmetov, 2002). Table 6.3 therefore gives the lattice parameters that were chosen, with appropriate justification:

System	Actual composition used for modelling	Lattice parameter / Å	Justification of lattice parameter choice
$TiC_{0.79}$	$TiC_{0.81}$	4.31	Literature value for $TiC_{0.62}$ (likely to be highly similar to $TiC_{0.81}$ given the similarity to the lattice parameter of bulk TiC) (Tashmetov, 2002).
$TiC_{0.58}N_{0.30}$	$TiC_{0.56}N_{0.31}$	4.28	The lattice parameters as used for $TiC_{0.79}$ and $TiN_{0.82}$ were assumed to be reasonably accurate end-members to represent $TiC_{0.88}$ / $TiC_{0.84}$ or $TiN_{0.88}$ / $TiN_{0.84}$ respectively. Vegard's rule was then used to find lattice parameters for the intermediate compositions, for example for $TiC_{0.58}N_{0.30}$: $a^3_{TiC_{0.58}N_{0.30}} = 0.58\times a^3_{TiC_{0.88}} + 0.30\times a^3_{TiN_{0.88}}$
$TiC_{0.45}N_{0.43}$	$TiC_{0.44}N_{0.44}$	4.27	
$TiC_{0.19}N_{0.65}$	$TiC_{0.19}N_{0.69}$	4.25	
$TiN_{0.82}$	$TiN_{0.81}$	4.23	$TiN_{0.82}$ lattice parameter (for a surface) from literature (Shin, 2003).

Table 6.3: Lattice parameters and compositions for the carbonitrides series with appropriate justification (Shin, 2003), (Tashmetov, 2002).

Usually if there are significant discrepancies between the experimental and theoretical compositions, this was due to generating high symmetry in the cells to allow for faster calculations.

In terms of computing practicalities, the parameters used for the calculations were as in Table 6.1 for the 2x2x2 supercells. In the first batch of calculations, for systems with a mixture of carbon and nitrogen, each element was distributed at high symmetry positions within the cell. Figures 6.12 and 6.13 illustrate the process used to build the various cells, and the resultant symmetry operations performed:

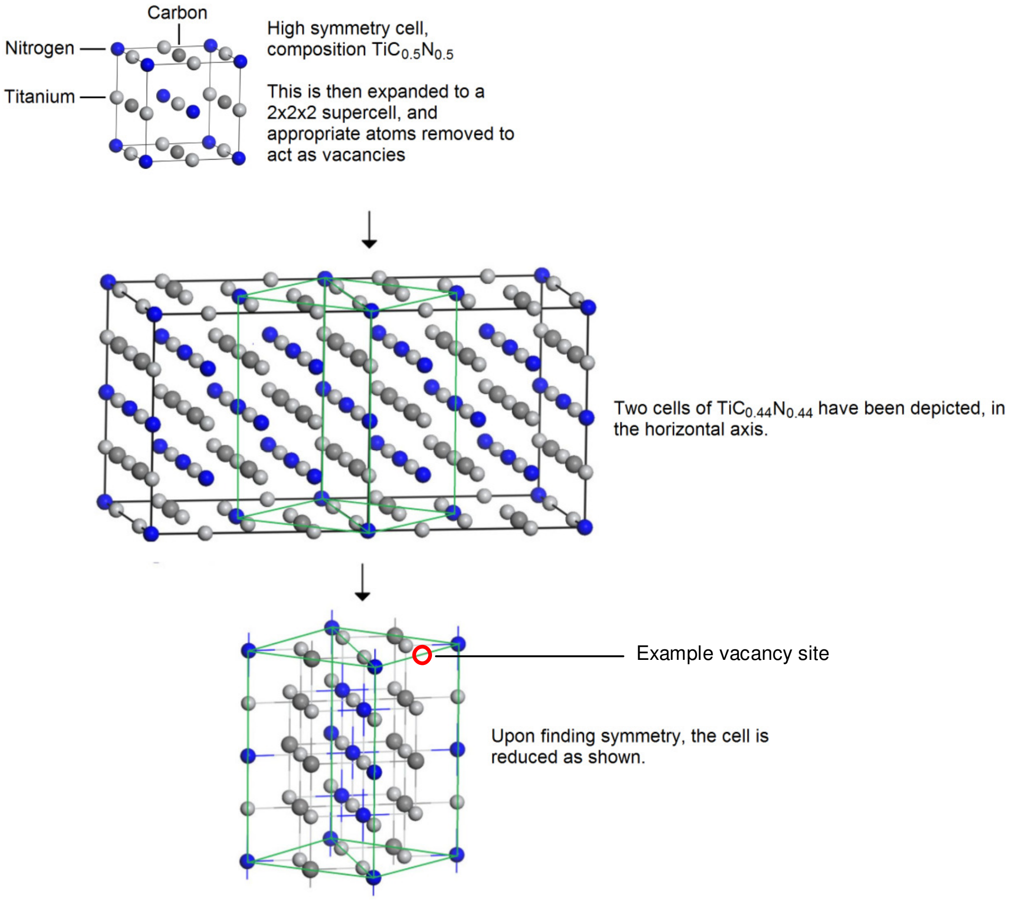

High symmetry cell, composition $TiC_{0.5}N_{0.5}$

This is then expanded to a 2x2x2 supercell, and appropriate atoms removed to act as vacancies

Two cells of $TiC_{0.44}N_{0.44}$ have been depicted, in the horizontal axis.

Example vacancy site

Upon finding symmetry, the cell is reduced as shown.

Figure 6.12: Depiction of the ultimate symmetrised structure used to simulate $TiC_{0.44}N_{0.44}$, elements as labelled. An example vacancy position has been highlighted with a red circle as a visual aid.

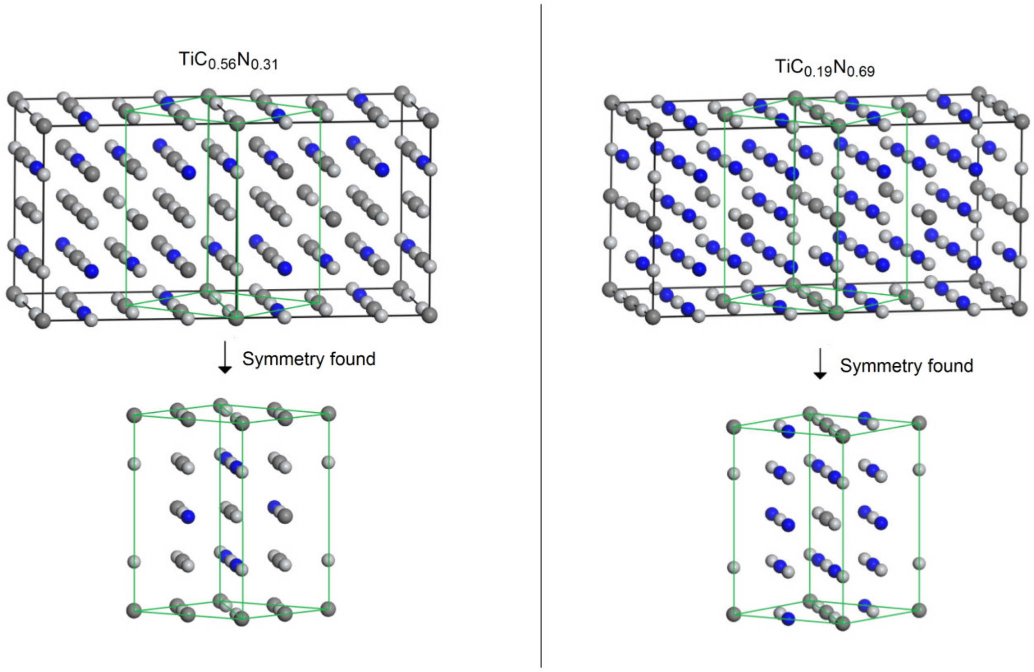

Figure 6.13: Symmetrised structures for $TiC_{0.56}N_{0.31}$ and $TiC_{0.19}N_{0.69}$, elemental labels as in Figure 6.12.

For the end-member compounds (i.e. $TiC_{0.81}$ and $TiN_{0.81}$), non symmetrical cells were utilised, as these were found to give better experimental agreement, the structures utilised in these cases are as shown below:

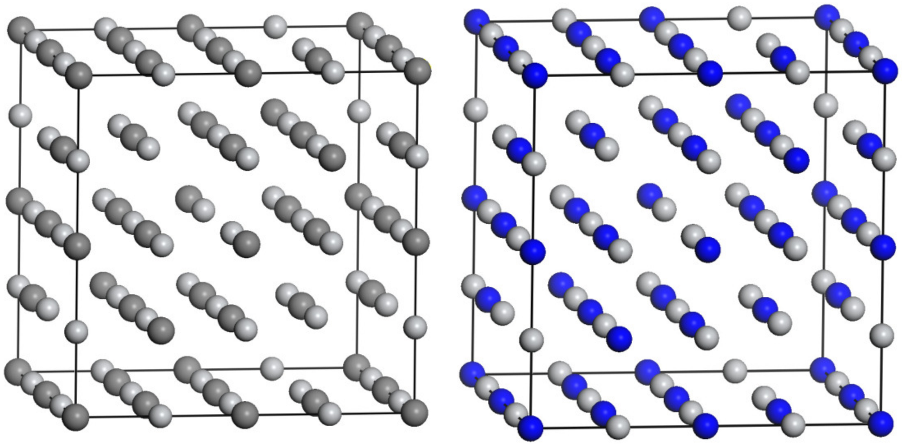

Figure 6.14: Structures (respectively) of $TiC_{0.81}$ and $TiN_{0.81}$.

6.4.3 Calculation details and results

Calculations were carried out in the ground electronic state. For each system, CASTEP finds a ground state edge prediction for each atom, these were then averaged to find the overall elemental edge for the system. This was considered to be a more realistic simulation of experiment. Furthermore, for the various bulk carbides, reasonable agreement with experiment was observed for ground state calculations. If a core-hole had been used, a large number of calculations would have had to be carried out, one for each atom being treated as the core-hole atom.

Figures 6.15 and 6.16 show the experimental and theoretical results for the carbon and nitrogen K edges respectively. Consider firstly the experimental carbon K edges in Figure 6.15. Generally, upon increasing the nitrogen content in the compound, peak 2 (as labelled) becomes more intense. The same trend is also observed for the nitrogen K edges (Figure 6.16), though is less striking in that instance.

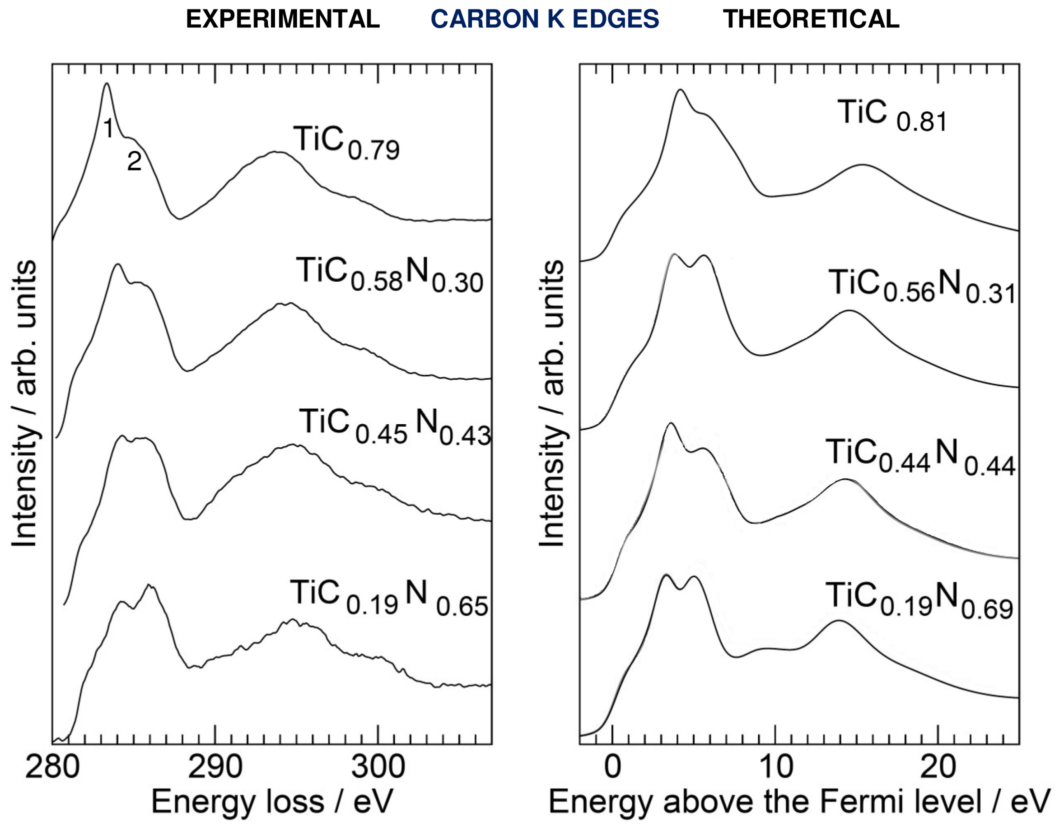

Figure 6.15: Comparison of experimental and theoretical carbon K edges for systems as labelled. The experimental data was obtained using the following conditions: VG HB5 cold FEG STEM, 0.3eV energy resolution (MacKenzie et al., unpublished data). The theoretical results were found using CASTEP in the ground electronic state as described, and are shown with the addition of energy-dependant final state lifetime broadening.

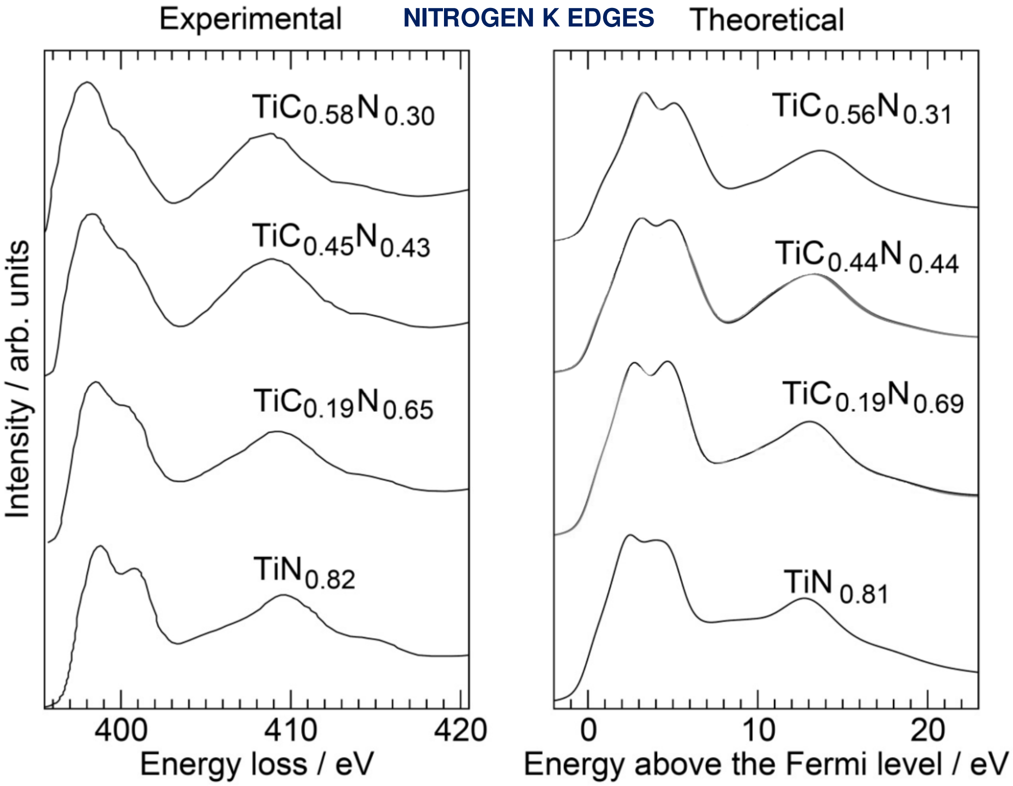

Figure 6.16: Comparison of experimental and theoretical nitrogen K edges for systems as labelled. The experimental data was obtained using the following conditions: VG HB5 cold FEG STEM, 0.3eV energy resolution (MacKenzie et al., unpublished data). The theoretical results were found using CASTEP in the ground electronic state as described, and are shown with the addition of energy-dependant final state lifetime broadening.

6.4.4 Discussion and required structural modifications

The experimentally observed trends in terms of peaks 1 and 2 are not properly observed with the symmetrical model structures as shown in Figures 6.12 and 6.13. Therefore, it was decided to carry out controlled structural modifications in an attempt to improve agreement with experiment. Tsujimoto et al. established a number of interesting observations regarding the analogous TiN_x system (Tsujimoto, 2005). They attribute peak 1 to $2p - 3d$ (t_{2g}) transitions (of σ character), and peak 2 to $2p - 3d$ (e_g) transitions. Consider Figure 6.17, which shows carbon K edge predictions for **all** atom positions in $TiC_{0.44}N_{0.44}$, rather than the average K edges presented in Figures 6.15 and 6.16:

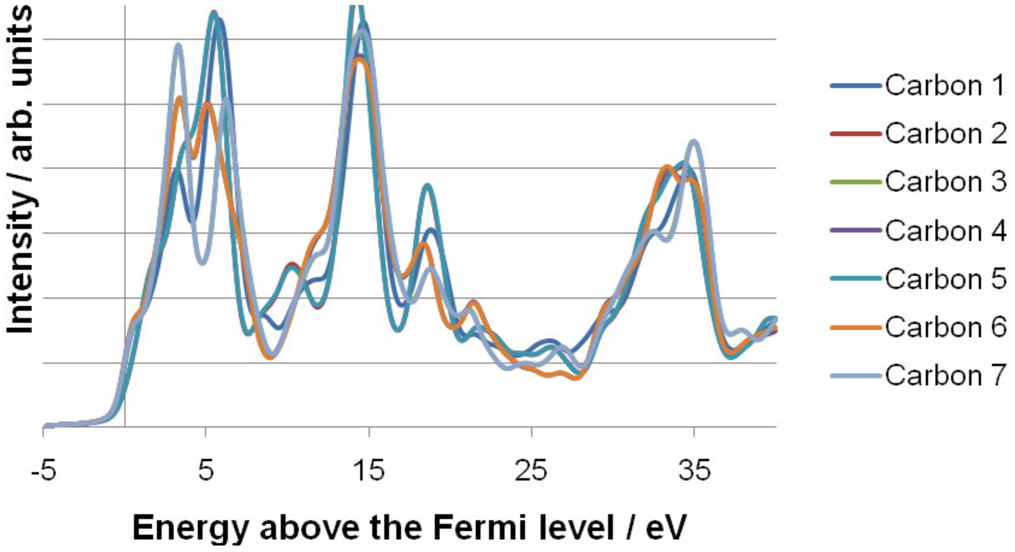

Figure 6.17: Illustrating (for $TiC_{0.44}N_{0.44}$) the carbon K edge predictions at different atomic positions in the cell.

Observe that there are certain positions in which the intensity of peak 1 (relative to peak 2) is significantly diminished. Tsujimoto et al. suggest that Ti forms σ bonding interactions with vacancies, and therefore in certain positions relative to the vacancy the intensity of peak 1 is significantly affected. Therefore, various structural modifications were made to the $TiC_{0.56}N_{0.31}$, $TiC_{0.44}N_{0.44}$ and $TiC_{0.19}N_{0.69}$ cells, utilising Tsujimoto's conclusions, and careful inspection of individual atom edge predictions (as in Figure 6.17). Figures 6.18 and 6.19 show the structural modifications that were made:

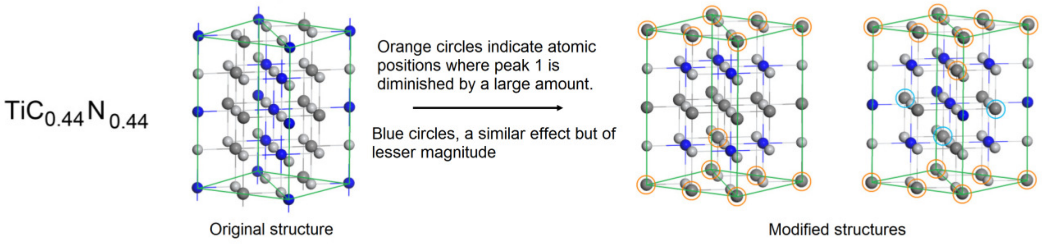

Figure 6.18: Depicting structural modifications made to $TiC_{0.44}N_{0.44}$.

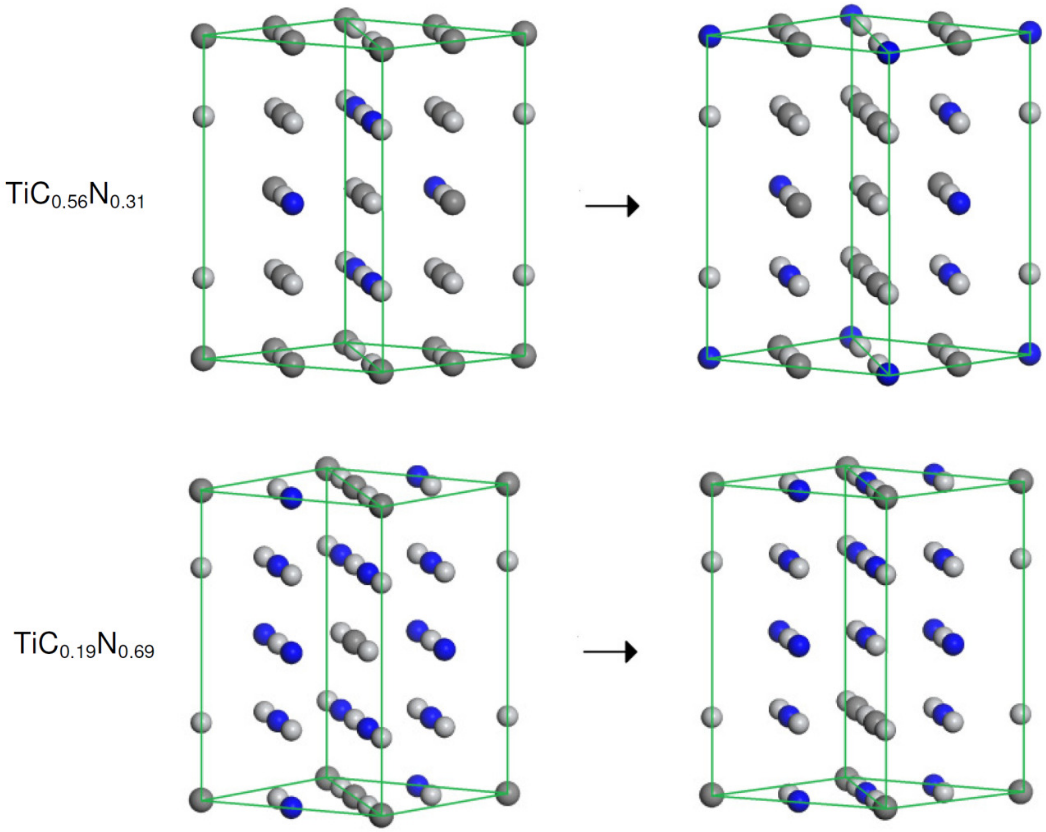

Figure 6.19: Depicting structural modifications made to $TiC_{0.56}N_{0.31}$ and $TiC_{0.19}N_{0.69}$.

Figures 6.20 and 6.21 now show experimental and theoretical comparisons for carbon and nitrogen K edges, with the original high symmetry structures, and the modified cells as given in Figures 6.18 and 6.19. Keys are given to explain which line corresponds to which structure:

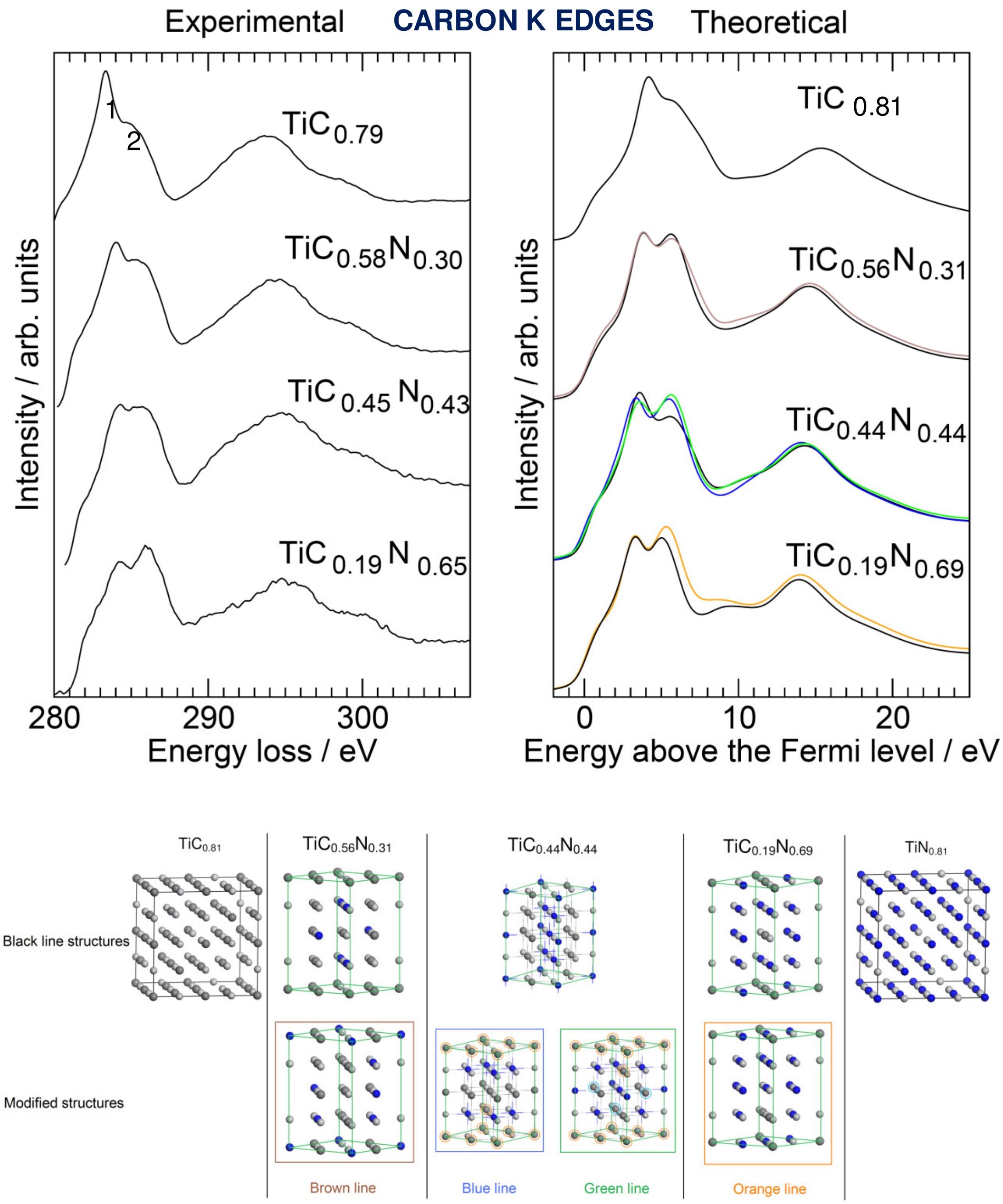

Figure 6.20: Comparison of experimental and theoretical carbon K edges for systems as labelled. The experimental data was obtained using the following conditions: VG HB5 cold FEG STEM, 0.3eV energy resolution (MacKenzie et al., unpublished data). The theoretical results were found using CASTEP in the ground electronic state as described, and are shown with the addition of energy-dependant final state lifetime broadening. The black lines represent the high-symmetry distribution of atoms as depicted in Figures 6.12 and 6.13 for systems containing both nitrogen and carbon, and also the modified structures of $TiC_{0.81}$ and $TiN_{0.81}$ given in Figure 6.14. The alternative colourations indicate different, modified structures, as illustrated by the key.

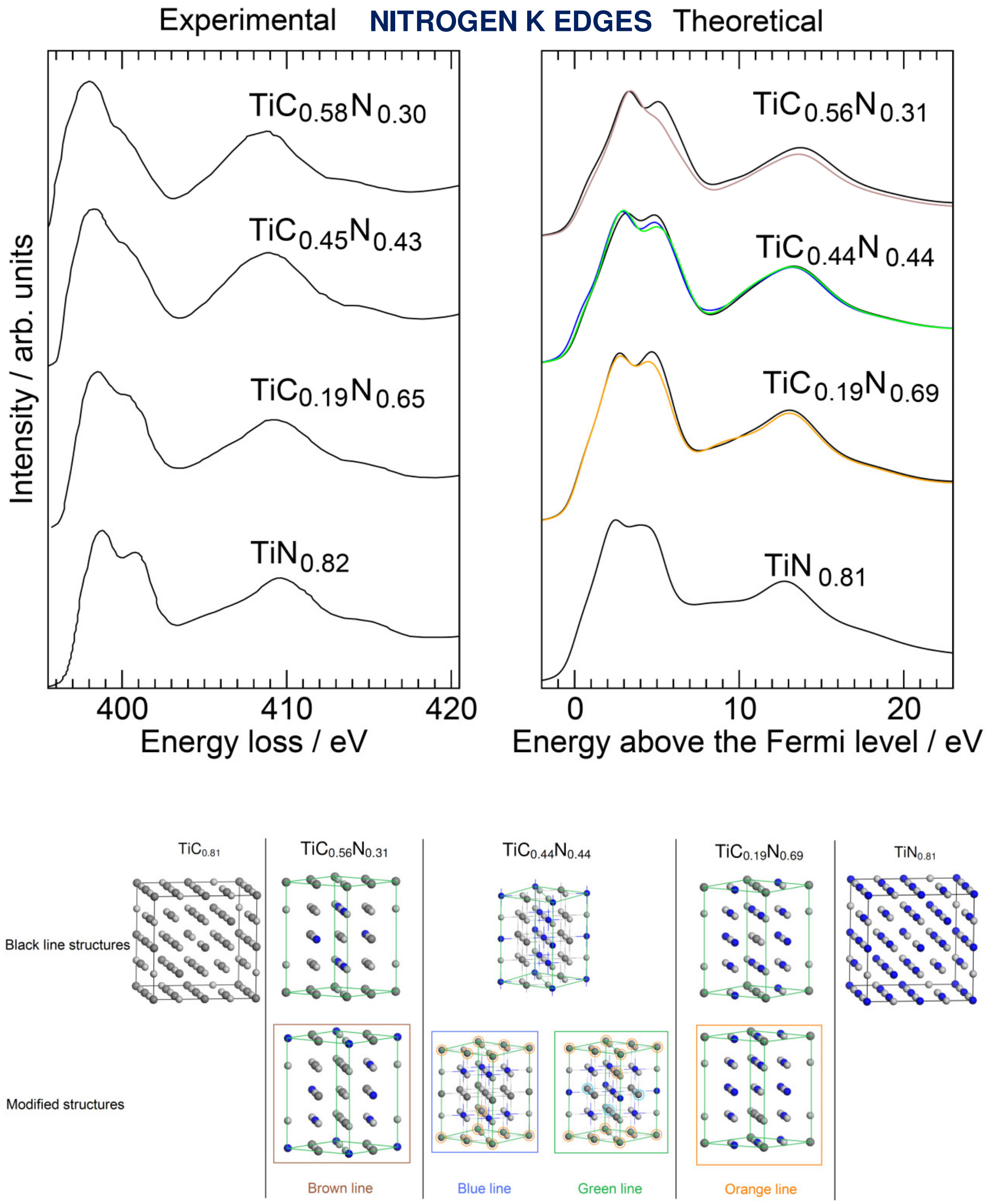

Figure 6.21: Comparison of experimental and theoretical nitrogen K edges for systems as labelled. The experimental data was obtained using the following conditions: VG HB5 cold FEG STEM, 0.3eV energy resolution (MacKenzie et al., unpublished data). The theoretical results were found using CASTEP in the ground electronic state as described, and are shown with the addition of energy-dependant final state lifetime broadening. The black lines represent the high-symmetry distribution of atoms as depicted in Figures 6.12 and 6.13 for systems containing both nitrogen and carbon, and also the modified structures of $TiC_{0.81}$ and $TiN_{0.81}$ given in Figure 6.14. The alternative colourations indicate different, modified structures, as illustrated by the key.

Following the structural modifications, the experimental trends as previously discussed are now observed. Arguably for $TiC_{0.56}N_{0.31}$ and $TiC_{0.19}N_{0.69}$ the modifications required to generate agreement with experiment involve increasing the amount of nitrogen in proximity to the defect, the opposite trend to that seen for $TiC_{0.44}N_{0.44}$ where carbon clustering at the vacancy improves agreement with experiment. Further study is however required, as discussed in the conclusions of this chapter, and those of the thesis itself.

6.5 Conclusions

For the six group 4 and 5 transition metal carbides, CASTEP was successfully used to obtain good agreement with experimental carbon K edge spectra, in the ground electronic state. For a series of titanium carbonitrides with vacancies present, ground state CASTEP calculations were once again utilised. In order to obtain strong agreement with experiment, structural modifications had to be made to the systems, arguably offering structural information. However, the structural suggestions made are by no means conclusive. In this work, spectra were used to converge the key DFT parameters, rather than system energy calculations. If the latter approach had been used, it may have been possible to find the most favourable structure (energetically) of the various vacancy systems. This is an area of possible future work. Furthermore, other approaches could have been used when considering the vacancy structures. Full structural relaxation might be attempted (with care used to avoid local minima), or 'empty' atoms might have been used in vacancy positions. Other models of defect positions have been postulated (for example a $R\bar{3}m$ symmetry arrangement), and the virtual crystal approximation (VCA) might also be of use. This is discussed further in the conclusion to the thesis.

Chapter 7

Studies of magnesium oxide systems

7.1 Introduction

This section of the thesis discusses the computational modelling of oxygen ionisation edges in electron energy loss spectra (EELS) for various magnesium oxide systems, namely bulk material, a (001) surface of MgO, and the interface between Fe (001) and MgO (001). This interface is present in magnetic tunnel junctions (MTJs). MTJs are made by the sandwiching of an insulating tunnel barrier (in this case MgO) between two ferromagnetic electrodes, composed of iron for example (Yuasa, 2004).

MTJs display a tunnelling current between the ferromagnetic layers, which can be controlled by the relative orientations of the magnetisations of those layers. This phenomenon is termed tunnelling magnetoresistance (TMR). MTJs have various potential applications, including magnetic memory devices for example. Crucially, the exact structure of the Fe (001) / MgO (001) interface is important in determining the precise TMR properties, and is therefore worthy of further study, and detailed characterisation in the electron microscope.

7.2 Methodology of EELS modelling

7.2.1 Initial considerations

The modelling studies in this section assume that the dipole selection rule operates (Brydson, 2001). All theoretical calculations in this section have been carried out using CASTEP, with the GGA used (Perdew, 1996). Specific choices of broadenings added to the various theoretical results have been given in the appropriate figure caption. These values are generally chosen to allow the main orbital transitions to be seen without the spectra becoming confusing, or to generate better agreement with experiment.

As per the CASTEP calculations in the previous sections, if a core-hole calculation was used, the core-state electron was promoted to a higher energy level within the atom in question. For example, for an oxygen K edge, the oxygen electronic configuration would be modified to; $1s^1 2s^2 2p^5$.

For the bulk material, it was not considered necessary to account for variation of crystal orientation effects. For the interface systems, this has not as yet been considered, though it may be an area of future work. The Wien2k code for example is capable of considering these effects (Blaha, 1990). The relevance of probe size is considered for the interface systems subsequently.

7.2.2 Parameter selection and convergence

The same convergence principles were used as described in the last two sections of the thesis. A cubic cell of MgO was constructed in the rock-salt structure (a=b=c=4.21Å, α=β=γ=90˚). For one oxygen atom a single electron core-hole was added. This was achieved by 'promoting' that electron into a higher lying valence state. The predicted oxygen K edge was then converged against the key parameters in the CASTEP code. Specifically, in the case of the kinetic energy cut-off, the value was changed in 100 eV intervals from 300 to 600 eV.

After each increase, for each data point (on the energy axis) the percentage variation in the result was found, and then those percentage variations were averaged into a single value across all the energy axis data points. When that value was 5% or less, the parameter was deemed to be converged. It should be noted that throughout this convergence process, broadenings of 0.2eV Lorentzian and 0.4eV Gaussian were applied to the results, as in previous sections to qualitatively verify (by visual inspection) that spectra are converging when parameters are altered as described above.

Again as previously for CASTEP, *k*-point mesh convergence was again divided into two steps (see particularly Chapter 4). In the case of simple energy calculation, the *k*-point mesh was increased from 12x12x12 to 36x36x36 in steps of 12x12x12, and the same percentage variation analysis was carried out to find the converged parameter choices. In the EELS section of the CASTEP calculations, the *k*-points were increased from 12x12x12 to 48x48x48 in steps of 12x12x12, convergence again being determined by analysis of the percentage variation in the predicted result.

Table 7.1 lists the chosen calculation parameters for a single MgO cell, subsequently used for all other simulations unless otherwise stated.

Parameter	Chosen value
Standard cell dimensions	Cubic cell of MgO in the rock-salt structure, (a=b=c=4.21 Å, α=β=γ = 90˚)
Kinetic energy cut-off	600eV
Energy step *k*-point mesh	24x24x24 or better unless otherwise stated (actual spacing – 0.0099Å^{-1}). Revised to 0.0197Å^{-1} for interface and surface studies.
EELS calculation *k*-point mesh	24x24x24 or better unless otherwise stated (actual spacing – 0.0099Å^{-1}). Revised to 0.0197Å^{-1} for interface and surface studies.
Core-hole / pseudopotentials	Single electron core-hole in place for one of the oxygen atoms, using an on-the-fly (OTF) pseudopotential. All other atoms – standard ground state GGA pseudopotentials.

Table 7.1: Chosen calculation parameters for a single MgO cell, subsequently used for all other simulations unless otherwise stated.

Subsequently, for the larger systems that were studied it was observed these parameter choices were not always feasible; hence they were revised as clarified in Table 7.1, these revised parameters being used throughout all surface and interface results presented in this section unless otherwise specified.

7.3 Initial results for bulk MgO

7.3.1 Approaches used for bulk MgO modelling

Using the parameters given in Table 7.1, an oxygen K edge was predicted in the ground state, for a single cell with a core hole in place, and for a 2x2x2 MgO supercell (core-hole separation distance of 8.42Å), also with a core hole in place. Further, geometry optimisation was considered, in the fashion as outlined in Chapter 4. The unit cell dimensions of MgO were altered to various values (with a core hole in place), and system total energies found. 'Geometry optimisation' was achieved for the set of parameters that resulted in the lowest system energy. These parameters were a=b=c = 4.47Å, α=β=γ = 90˚. Given the core-hole approximation used (i.e. the excited core electron was placed into a higher-lying orbital), the introduction of a core hole is not guaranteed to lead to a contraction of the unit cell when geometry optimisation is performed.

Geometry optimisation was not performed for the 2x2x2 supercell. To carry out the described methodology for the 2x2x2 supercell would be too computationally demanding. There is no sensible physical basis to speculate as to whether the results would be similar to the single cell case.

7.3.2 Bulk MgO modelling results

Various resultant supercell and single cell results (with and without core holes and geometry optimisation) are compared therefore in Fig. 7.1. As was established in section 4.3, the core-hole is likely to be relaxed before any vibrational relaxation can take place, but this section nonetheless illustrates the way the code deals with the alteration to the electron configuration. The ground state prediction uses the experimental lattice parameter, section 4.1 having illustrated how small variations as a result of geometry optimisation are unlikely to alter the ELNES prediction in these instances.

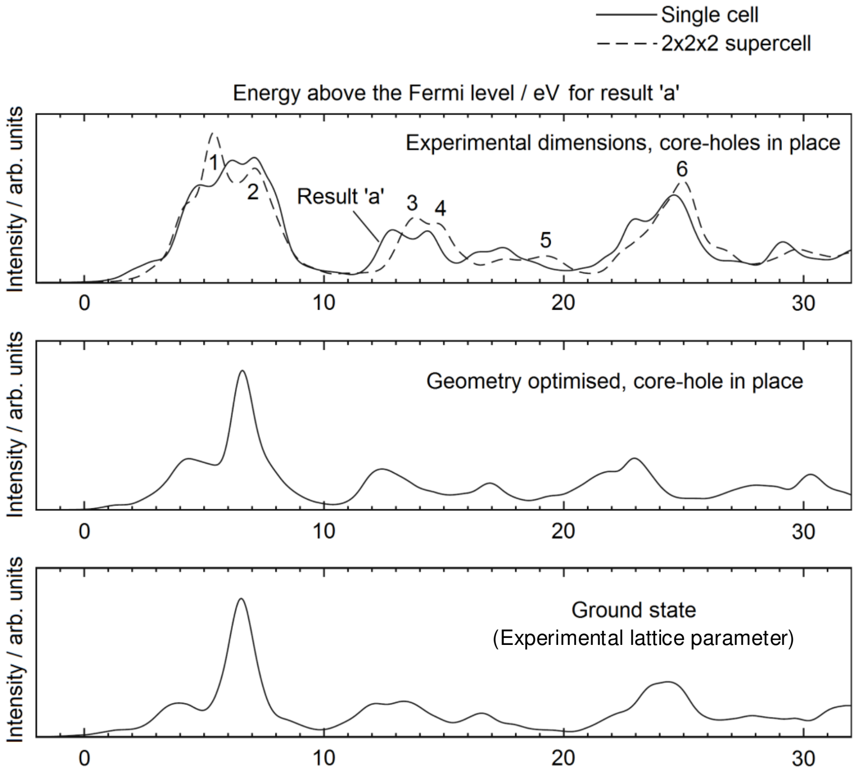

Figure 7.1: Various predicted oxygen K edges for bulk MgO systems as labelled. The results have been aligned by the energy value of the first peak in the spectrum for the non geometry optimised single electron core-hole result (result ‘a’). Other results have been directly labelled in the figure. All the spectra are shown with 0.8 eV Gaussian broadenings. Numerical peak labels have also been added; these are discussed in the main body of text.

With and without geometry optimisation, the results differ, though they might be argued to be qualitatively similar.

In both cases there are arguably four ‘sets’ of peaks, at approximately 6, 13, 17 and 23 eV (labelled from result ‘a’). Clearly within these ‘sets’ the peak ratios differ somewhat. The most prominent difference between results with and without geometry optimisation is the nature of peaks 1 and 2 i.e. without geometry optimisation (for the single and 2x2x2 supercells) a ‘doublet’ feature of some sort is observed, whereas this is more of a shoulder when geometry optimisation is in place.

A more subtle difference is to be found in the separation of the first and last peak ‘sets’ in the single cell cases with and without geometry optimisation. It is possible to argue that the lattice parameter variation (as a consequence of geometry optimisation) is directly responsible for the different peak separations, which are most visible between the first and last sets of peaks and are observed in other instances.

It has been shown that such a peak separation in transition metal oxides for example is likely to be proportional to the inverse square of the lattice parameter (Kurata, 1993). The trends observed in Figure 7.1 are at least arguably consistent with this, though obviously cannot be used to directly verify the exact inverse square relationship. However, in Figure 7.1 as the lattice parameter increases (in this case after geometry optimisation), the energy separation of the first and last sets of peaks decreases. It should be noted that the various CASTEP predictions do not appear to reproduce experiments particularly well beyond 20eV above the onset (Figure 7.2, discussed subsequently), and therefore this analysis is somewhat speculative - and the various levels of approximation involved in the calculations may be responsible for the observed ‘contractions’ in the spectra. Note also the comments given at the start of this section (7.3.2) with regard to the physical meaning (or lack of) in the geometry optimisation of a cell with a core-hole in place.

7.3.3 Bulk MgO comparisons with experiment

In Figure 5.2, the single cell result (without geometry optimisation, core hole in place), a ground state result, and a 2x2x2 supercell result with a core hole in place are compared to experiment (Gareth Vaughan acted as operator):

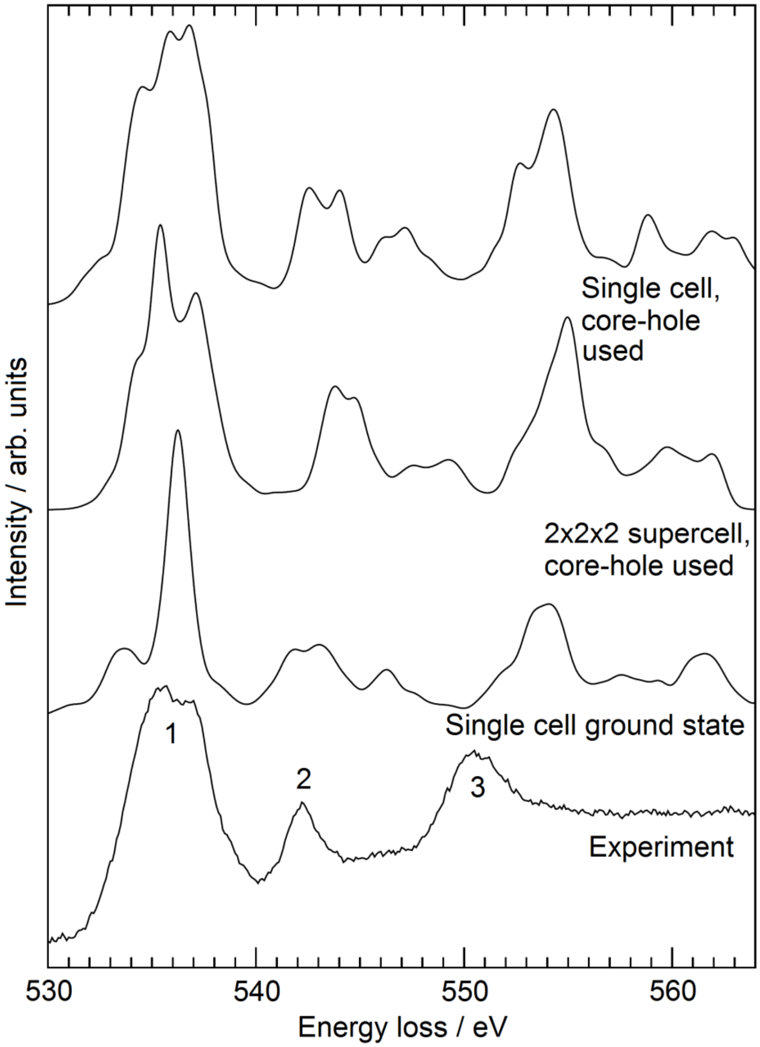

Figure 7.2: Comparison of experimental MgO oxygen K edge with various theoretical results (without geometry optimisation). The experimental result was obtained using a VG HB501 STEM retro-fitted with a Nion spherical aberration corrector and a Gatan Enfina electron energy loss spectrometer at the Daresbury Laboratories, UK (SuperSTEM1). The FWHM of the zero-loss peak was 0.7 eV. The theoretical results have been directly labelled in the figure, and are shown with 0.8 eV Gaussian broadenings.

The MgO sample was prepared by burning Mg ribbon in air and catching the smoke on a standard 400-mesh holey carbon film TEM grid (Agar Ltd.). Structural properties were verified by electron diffraction. No evidence was observed of contamination or non-stoichiometric MgO, an effect perhaps more common for thin films of MgO, grown on metals for example (Wollschläger, 1999), (Tamboli, 2009).

The spectrum has not been treated to compensate for multiple scattering effects, which were assumed to be negligible for this thin specimen. In terms of post-acquisition processing, the background was removed with a power-law fit to the background signal prior to the edge onset using a 40eV fitting window.

As can be observed the agreement between the results is encouraging, particularly in the cases with core holes in place. The relative peak ratios are similar, though peak positions vary. Certain features have also been attributed numerical labels; ‘1’ represents the first major peak or peak set in each of the spectra. In the experimental result, this peak is arguably a doublet. This ‘doublet’ is also observed in X-ray absorption spectroscopy (Hsieh, 2006). The theoretical results with core holes in place do show this doublet in some form. In the experimental result, ‘2’ is simply the next major peak in the spectrum. In all the theoretical results this peak is a doublet, which is then followed by at least a shoulder peak, which appears to be obscured in this particular experimental result. However, it is observed in the seminal paper of Lindner et al. on MgO ELNES fine structure (Lindner ,1986). The position (on the energy axis) of peak ‘3’ illustrates one of the major differences between the experimental and theoretical results.

A final note should be made with regard to the experimental result. The minimum intensity between peaks 2 and 3 varies somewhat. This may be a consequence of the background fitting model, or sample thickness. However, with reference to the latter consideration, specific measures were (as described) taken to avoid this, thus negating the need to consider multiple scattering effects. Further, it is arguably the higher minimum following peak 2, due to a small broad peak, which is noticeable in simulations (peak ‘5’ in Figure 5.1). This peak is clearly not well resolved as a distinct feature in the experimental spectrum but the simulations predict that extra intensity should be present in approximately this energy loss range.

It is necessary to acknowledge however that the ‘shoulder’ after peak 2 is somewhat better resolved for example in the paper of Lindner et al. (Lindner, 1986). Comparing our experimental spectrum (Figure 5.2) to that of Lindner et al., the energy resolution does appear worse, particularly with regard to the doublet feature, which is far-better resolved in the Lindner et al. result. The origin of the shoulder feature is unclear; the multiple scattering study of Lindner et al. does not explicitly rationalise it (Lindner, 1986).

7.3.4 Previous bulk MgO modelling studies and comparisons with experiment

A number of previous papers have carried out theoretical modelling of the oxygen K edge in MgO using a variety of methods (Lindner, 1986), (Mizoguchi, 2009), (Weng, 1989). Interesting considerations when examining these publications are the various attempts to reproduce the ‘doublet’ nature of the first peak in the experimental spectrum (‘1’ in Figure 7.2). The paper of Lindner et al. displays a doublet, but in the reverse intensity pattern to that observed in the experiment, where the first peak of the doublet has the highest intensity (Lindner, 1986). This is arguably similar to our result for a single cell with a core hole in place.

Perhaps the best effort to reproduce the feature in the current literature is that of Mizoguchi (Mizoguchi, 2009). In this paper, the doublet peak ratios are in the correct pattern, although the exact ratios are not entirely correct. This paper also illustrates the usage of overlap population (OP) diagrams to assign transitions in ELNES to specific orbital interactions in the system.

There are a number of possible explanations as to why this work (for the 2x2x2 supercell) and that of Mizoguchi display the doublet peak ratios in the correct pattern (relative to experiment), and the work of Lindner et al. does not. The multiple scattering calculation in Lindner et al.’s work is not self-consistent, and utilises the Z+1 approximation to model the core hole. In contrast the DFT calculations of this work and that of Mizoguchi are fully self-consistent, and use genuine excited state electronic configurations in calculations.

The generation of the doublet is shown in this work to be as a consequence of using a core-hole in the calculations. It is reasonable to suggest obtaining the correct peak ratios within this doublet is reliant on using a direct excited state electronic configuration as opposed to the Z+1 approximation for instance, further calling the work of Lindner et al. into question in this regard.

7.3.5 Summary of bulk modelling results

All results with a core-hole in place display some form of doublet. In the 2x2x2 supercell case this is arguably in the expected ‘ratio’ pattern. The ground state result, though not as encouraging a match with experiment, is useful in that it predicts approximate peak positions and relative intensities. There are however a number of remaining questions.

How can the effect the core-hole has on this occasion be rationalised, and why does the ground state calculation still give a relatively useful prediction? These matters are considered subsequently.

7.4 Beginnings of surface and interface studies

7.4.1 Introductory remarks

An ultimate aim of this work was to study certain model structures for the Fe (001) / MgO (001) interface - which forms the basis for a magnetic tunnel junction (MTJ), in this instance the epitaxial relation being Fe (001)[100]//MgO (001)[110]//Fe(001)[100] - a system that has various potential novel applications (Butler, 2001), (Yuasa, 2004).

An initial step was to model a (001) surface of MgO. The aim behind this was to verify that an MgO ‘slab’ could be constructed whereby within that slab the predicted oxygen K edge matched that of bulk. If this was verified it was then considered viable to extend the studies to interfacial systems.

7.4.2 Studies of MgO (001) surface

Figure 7.3 shows the slab that was studied—along with a number of labelled atomic oxygen positions, together with their distances from the ‘top layer’ of the surface.

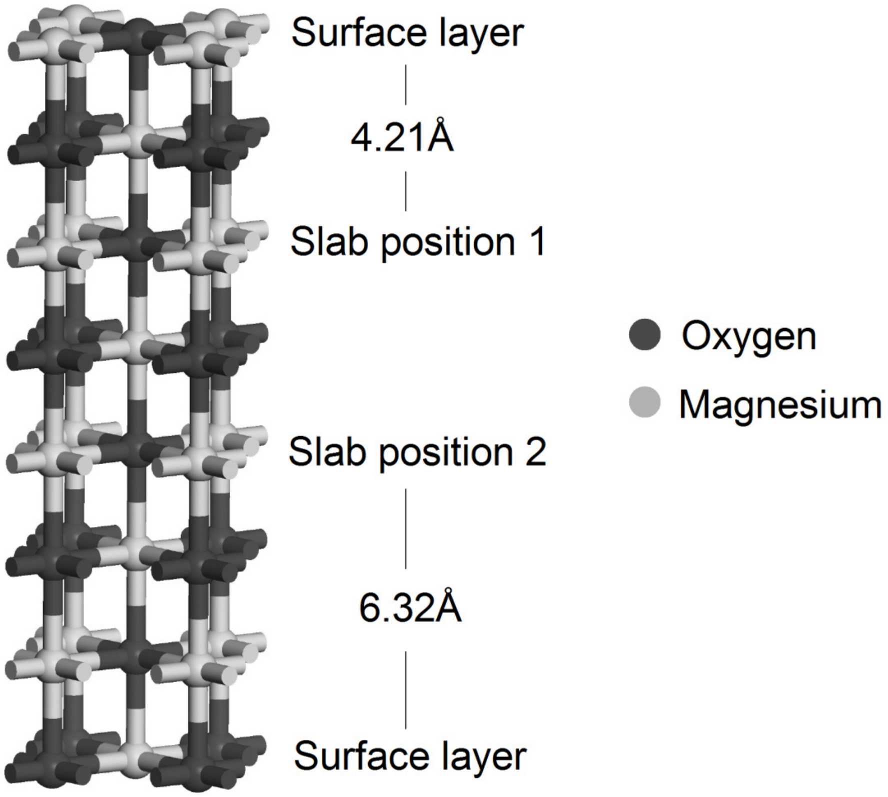

Figure 7.3: Structure of MgO (001) surface used. Labelled are the 'top' layers and the distances into the 'bulk' of the surface from which theoretical results were obtained. The dark-coloured atoms are oxygens, the light-coloured atoms magnesium. The dimensions of the surface are based on a non-geometry optimised cell of MgO.

The surface is both Mg and O terminated. Note a vacuum slab of thickness greater than 20Å was added although this is not depicted in the figure. This slab is based on the standard lattice parameters as given in Table 7.1. In this instance, it was decided to use ground state calculations. These had been shown to be at least qualitatively useful in studies of bulk materials, and therefore acceptable to observe interesting trends in these cases. The subsequent section of this Chapter offers a more detailed explanation of why ground state calculations are useful for the oxygen K edge in MgO, the principal explanation being that the oxygen 1*s* core hole is highly screened in MgO, so it has relatively little impact.

Further, as is observed in Figure 7.1 the geometry optimised core-hole model gives a similar predicted spectrum to the non-optimised ground state system. As Fig. 7.1 shows there are differences in for example the various bulk spectra predictions, but these differences are smaller and not significant when compared to the spectral variations observed for the various surface and interface systems as described in this section of the thesis.

Using ground state calculations also avoids the arguable necessity (see Figure 7.3) to expand the cell in the 'horizontal' direction to avoid unwanted core-hole interactions, thus saving considerable computational time. In these experiments, different 'layers' away from the surface of an MgO 'slab' were considered - and predicted oxygen K edges were calculated for these layers. Using parameters described in Table 7.1 (though on this occasion in the ground state), these predictions are compared to a calculation for bulk MgO (single cell result without geometry optimisation, ground state) in Figure 7.4.

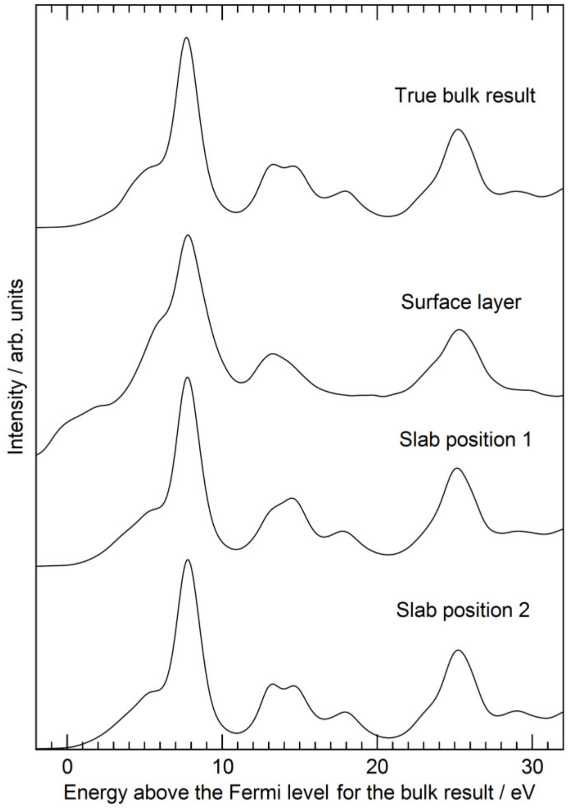

Figure 7.4: Comparison of MgO (001) oxygen K edge predictions at various labelled positions (see Fig. 5.3) with the bulk result for a single cell without geometry optimisation (all ground state calculations). All results are shown with broadenings of 0.2eV Lorentzian and 0.4eV Gaussian, aligned by the first peak of the true bulk result.

At a distance of 4.21Å from the surface, the result begins to approach the bulk, and by a distance of 6.32Å, the result begins to match the bulk extremely closely. Therefore, this is a large enough theoretical slab of MgO to use as part of the Fe (001)/ MgO (001) interface, i.e. if a distinct difference was calculated at the interface with iron itself, this result would be reliable only if at some point in the MgO slab the result matched that for standard bulk MgO. As is outlined subsequently, this is what is actually observed in experimental studies. It should be noted that no attempt was made to relax the surface, which would lead to an alteration in the structure. The key aim of this experiment was not to determine that behaviour, but to confirm that bulk-type behaviour is observed within a short distance of the surface.

7.4.3 Interface studies

It is possible to postulate various structures for the interface, including suggestions of a sharp interface, or one with a monolayer of FeO for example. Indeed, these two structural forms have been observed (by HREM imaging) and characterised experimentally (Meyerheim, 2002), (Wang, 2007), (Wang, 2008). Depictions of the structures are given in Figure 7.5:

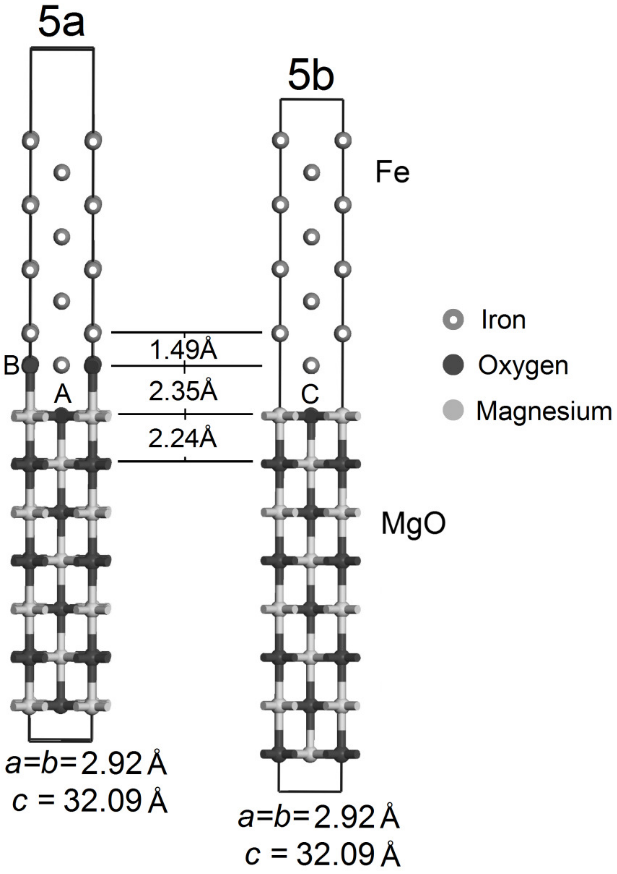

Figure 7.5: Postulated Fe (001)/MgO (001) interface structures; inter-layer distances as depicted, *a*=*b*=2.92Å, *c*=32.09Å. An interface with a monolayer is shown on the left (7.5a) and on the right a clean interface (7.5b) (Meyerheim, 2002), (Wang, 2007), (Wang, 2008).

Figure 7.5a shows an interface structure with a FeO monolayer, Fig. 7.5b a 'clean' interface. The monolayer structure and dimensions are based on previous work in the literature using X-ray analysis (Meyerheim, 2002). In Fig. 7.5b, the Fe–O distance is altered in accordance with experimental observations in the electron microscope (Wang, 2007), (Wang, 2008). In both cases, the MgO (001) surface has mixed oxygen/magnesium termination, and the first 'layer' of iron atoms at the interface is positioned above oxygen atoms.

The physical interface structures are considered to be structurally relaxed. Therefore, the theoretical structures presented are entirely coherent, with the a=b distances set as the average of the Fe (001) and MgO (001) surface values. The sample characterised in the electron microscope had a bottom Fe electrode of 50 nm thickness, then a 3 nm thick MgO barrier, and a 10 nm thick Fe layer on top. Arguably, as the Fe layers have a larger thickness, it is possible that to maintain coherence, the MgO lattice parameter will shift to match that of iron. However, the difference in lattice parameter between the mean average and the Fe (001) system is small, and unlikely to lead to a significant difference in predicted spectra given the level of broadening applied. In both cases no form of geometry relaxation was carried out during the calculations. Detailed descriptions are available of the experimental procedures used to epitaxially grow these structures (Wang, 2007), (Wang, 2008). In all cases, the magnetic tunnel junctions were grown in an ultrahigh vacuum molecular beam epitaxy (MBE) deposition system. In terms of the experimental EELS results, the spectra have been extracted from line scans perpendicular to the interfaces, obtained at SuperSTEM with 0.7 eV energy resolution. The experimental results have been further processed using multi-variate statistical analysis (MVSA) to improve the signal-to-noise ratio (Lozano-Perez, 2007), (Trebbia, 1990). A selection of theoretical and experimental interface results is presented in Fig. 7.6 (experimental operator Dr. B. Mendis, Durham / SuperSTEM):

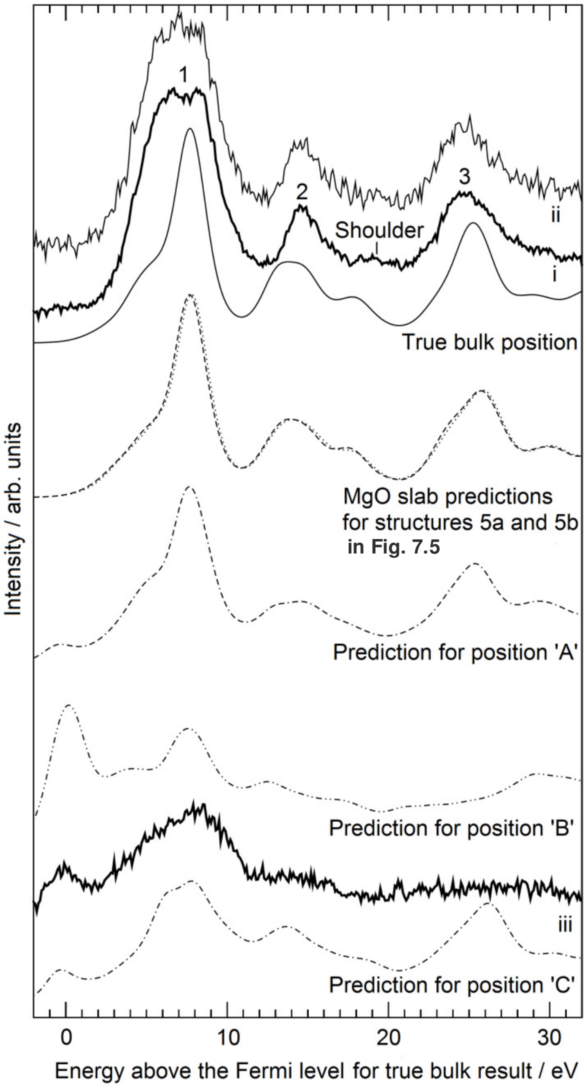

Figure 7.6: Various predicted and experimental results (oxygen K edges) for the interface systems, dimensions as shown in Fig. 7.5. The experimental results have been labelled (i)–(iii) and are as follows: (i) line scan within the MgO insulating slab, shown with MVSA, (ii) without MVSA, and (iii) line scan at the interface of MgO with Fe. These spectra are aligned against the ‘equivalent’ predicted results. All predictions are in the ground state, and are labelled directly in the plot. These results are aligned relative to the first peak of the true bulk predicted spectrum, and are all shown with a Gaussian broadening of 1.0 eV.

The theoretical results correspond to the labelled positions A–C in Fig. 7.5, and as was the case for the MgO (001) surface the calculations have been carried out for the ground state. Also shown are theoretical results obtained within the bulk of the MgO ‘slab’ for each interface structure, also found in the ground state.

The theoretical results show some rather interesting trends. At all interfaces (as compared to the bulk), pre-edge intensity is observed, particularly in the case of theoretical result ‘B’. One possible explanation is as follows. When an oxygen atom is in the proximity of an iron atom (as in the interface), interactions can occur between the oxygen 2*p* orbitals and the Fe 3*d* orbitals - creating additional, lower-lying hybridised states for oxygen K edge transitions. Indeed, in a paper discussing fine structure for various iron oxide systems, Colliex et al. carried out a detailed survey of existing explanations for the observation of pre-peaks in such systems (Colliex, 1991).

In this paper it is confirmed that for iron oxide systems (and by close analogy the interface presented), the 2*p* states involved in a K edge can be hybridised with 3*d* states. On initial inspection, one might question why the predicted spectra for positions A and C are so different—particularly with regard to the ‘pre-peak’ at ~0 eV and peak ‘1’. However, the coordinations of the two positions are different. In both cases, the nearest neighbouring atoms are Mg at a distance of 2.07Å, Mg at 2.24Å, Fe at 2.35Å and O at 3.05Å.

However, for position A there are additional O atoms at 3.13Å, altering the coordination sphere and therefore the ELNES of the atom in question, the importance of Fe 3*d* / O 2*p* orbital interactions having been emphasised previously. In structure 5.5a (which contains position ‘A’), there are more potential orbital interactions, which are quite different from those in structure 5.5b (containing position ‘C’). This further rationalises the differences in the predicted spectra between positions ‘C’ and ‘A’.

Now let us consider experimental results from a real interface, three of which have been included in Figure 7.6. The VG HB501 microscope was used again. This instrument has an approximate 1Å probe size (24 mrad probe semi-convergence angle and 19 mrad EELS collection semi-angle), the importance of which is discussed subsequently. It should again be noted that the experimental spectra have not been deconvoluted to account for multiple scattering effects. Importantly however, peak ratios appear plausible when compared to literature on bulk MgO (Lindner, 1986).

Firstly, a result from the ‘bulk’ MgO slab of the interface is compared with theory. In the experimental case, this was a result from a line scan at the centre of the MgO ‘sandwich’ of the MTJ, with MVSA in place (i). When compared with the bulk experimental result (Figure 5.2), MVSA does considerably reduce the spectral noise, and also the shoulder feature after peak ‘2’ is reasonably well resolved as compared with the true bulk experimental result. Also shown is a labelled result, which was not subject to MVSA (ii), to confirm that the technique improves signal-to-noise ratio, and does not affect relative peak intensities.

In the theoretical cases, the ‘bulk’ atom was chosen at least 6.7Å (in the *c*-axis) from positions B or C. As can be observed the agreement between theory and experiment is good, with analogous similarities to and differences from experiment as those discussed in Figure 7.2 for results with and without a core hole.

An experimental result from the interface boundary between Fe and MgO is also shown. In this instance the best match (based on comparison of peak ratios for the pre-edge peak and for the ‘first’ peak in the spectrum) is with theoretical result ‘C’ - i.e. that for a clean interface. In the paper of Colliex et al. (Colliex, 1991), various oxygen K edges are presented for FeO, Fe_3O_4, α-Fe_2O_3, and γ-Fe_2O_3. Theoretical result C (and the similar experimental result) is particularly similar (in terms of peak ratios) to the results for FeO and Fe_3O_4, and the paper explicitly rationalises the observation of a pre-peak for the FeO K edge for example.

7.5 Numerical processing of surface and interface results

7.5.1 Delocalisation and dechanneling.

There is another consideration however. As is discussed for example in Egerton’s recent review on the EELS technique, there are certain fundamental limits to the spatial resolution of EELS, and indeed some amount of delocalisation or dechanneling can occur (Egerton, 2009), (Kimoto, 2008).

Assuming an edge onset for the oxygen K edge of around 530 eV, this implies a resolution limit due to delocalisation of around 2Å (Egerton, 2009). The separation in space of positions A and B is around 2.77Å, and the probe width is no smaller than 1Å. Further, dechanneling (transfer of the electron probe to adjacent columns of atoms in propagation) will lessen the lateral resolution (Kimoto, 2008).

Therefore, theoretical result ‘C’ and the experimental result are compared to an ‘average’ theoretical spectrum of positions ‘A’ and B’. The results are shown in Figure 7.7, where all the theoretical results are found in the ground state, from dimensions given in Figure 7.5.

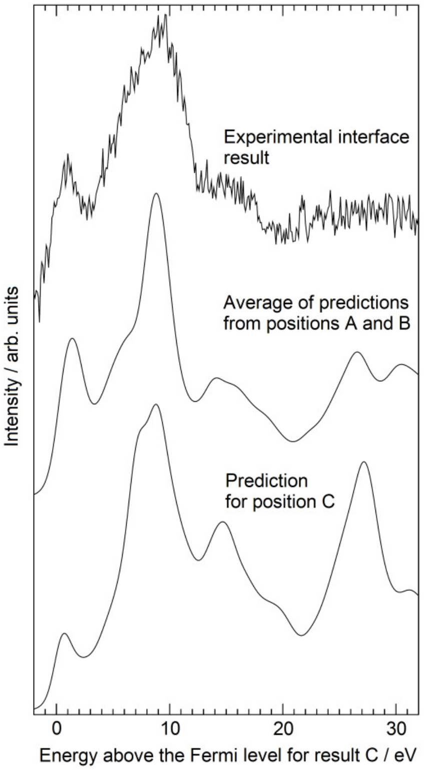

Figure 7.7: Comparison of various predicted and experimental oxygen K edges for the Fe/MgO interface. Both theoretical results have been shown with a Gaussian broadening of 1.0 eV, and are calculated in the ground state, based on dimensions shown in Figure 7.5. All results have been scaled such that the most intense peak in the spectrum has the same intensity, and the results have been hard shifted on the energy axis to align to that peak.

As can be observed, although the process of averaging results ‘A’ and ‘B’ is potentially dubious, this result probably best matches the experiment, the ratio of the first two peaks in the spectrum being fairly consistent. Further, the nature of the peak at around 14eV also seems to match the experiment well.

7.5.2 Beginnings of quantitative analysis

To further facilitate the comparison of various theoretical models, a numerical analysis was attempted. In order to facilitate this numerical comparison between experiment and theory, firstly a background removal was performed on the experimental result (using the power law).

Furthermore, scaling of the theoretical results had to be carried out as described in Chapter 5. For each theoretical result, this was a two-step process. Firstly, the magnitude of the most intense peak in the spectrum was made to match the equivalent peak in the experimental data. Secondly, the theoretical result was ‘hard shifted’ on the energy axis so that the most intense peak had the same energy as the equivalent peak in the experimental spectrum. The theoretical results were then interpolated onto the same energy axis abscissas as the experimental result, from 526 to 556 eV, in steps of 0.1 eV.

This energy range was chosen as this is the region in which simulations are most accurate. Multiple scattering effects were not considered, with the same potential consequences as described in section 5.4.4 where this form of analysis was first introduced. The results of this process are depicted in Figure 7.8 (which shows a wider energy range for illustrative purposes).

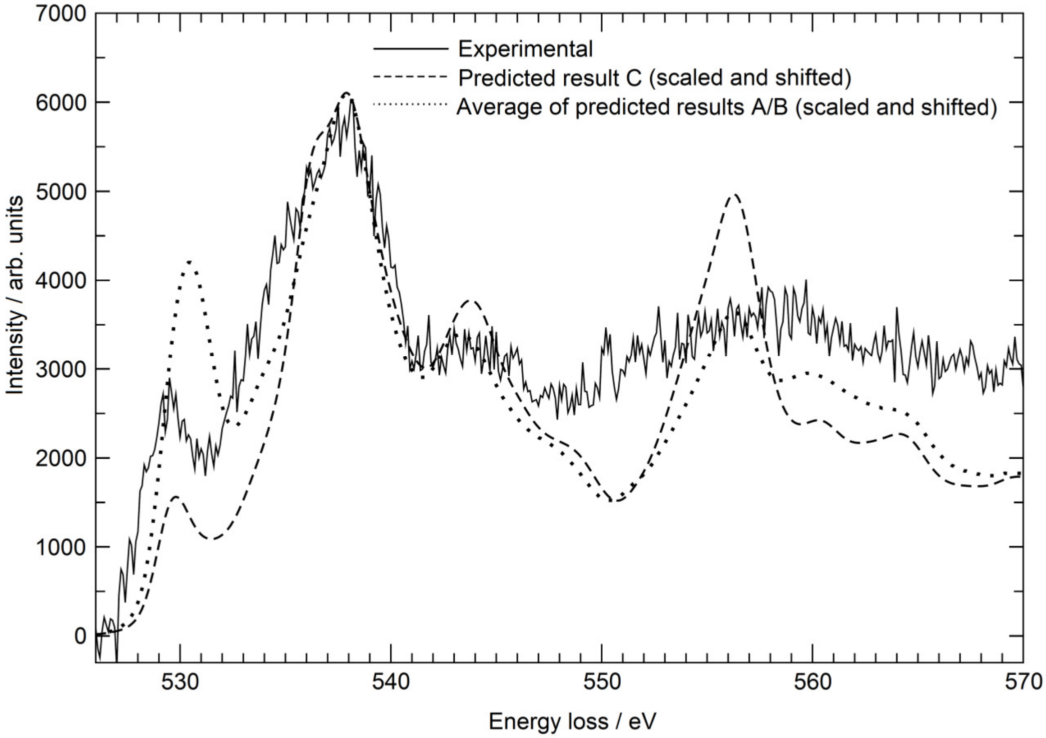

Figure 7.8: Predicted and experimental interface oxygen K edge predictions, adapted from Figure 7.7. As explained in the main body of text, the theoretical results have been hard shifted in energy, and scaled in intensity relative to the experimental result. As in Figs. 7.6 and 7.7, the theoretical results are shown with a Gaussian broadening of 1.0eV, and are calculated in the ground state, with dimensions from Fig. 7.5.

For each data point (for example, 526.0eV, 526.1eV, 526.2eV, etc...) the difference between the theoretical and experimental result was found, and squared. Across the full range of x-axis data points, those squared differences were mean averaged, and the square root was found. These values are effectively ‘standard deviations’ between observed and expected data. For theoretical result C versus experiment the result was 875 (counts), and for the average of A/B 818 (counts). This and the qualitative comparisons do suggest the averaged A/B spectrum is a better match with experiment.

7.5.3 The relevance of broadening in quantitative analysis

Another consideration is the nature of broadening used. In for example Figure 7.6, a simple Gaussian was used.

Another possible option is using the energy-dependent final state lifetime broadening scheme. This does not provide particularly good results for either the bulk MgO oxygen K edge or the MgO insulating slab in the interface. However, it does improve the general agreement of the interface theoretical results with experiment. At the boundary with Fe (a free-electron metal), it is logical to suggest the oxygen core-hole lifetime will be different from that in the bulk, and a different broadening approach may be beneficial. Therefore, in Figure 7.9, the experimental interface result is compared with the theoretical results from Figures 7.7 and 7.8, but these results have now been treated using the energy-dependent final state lifetime broadening scheme.

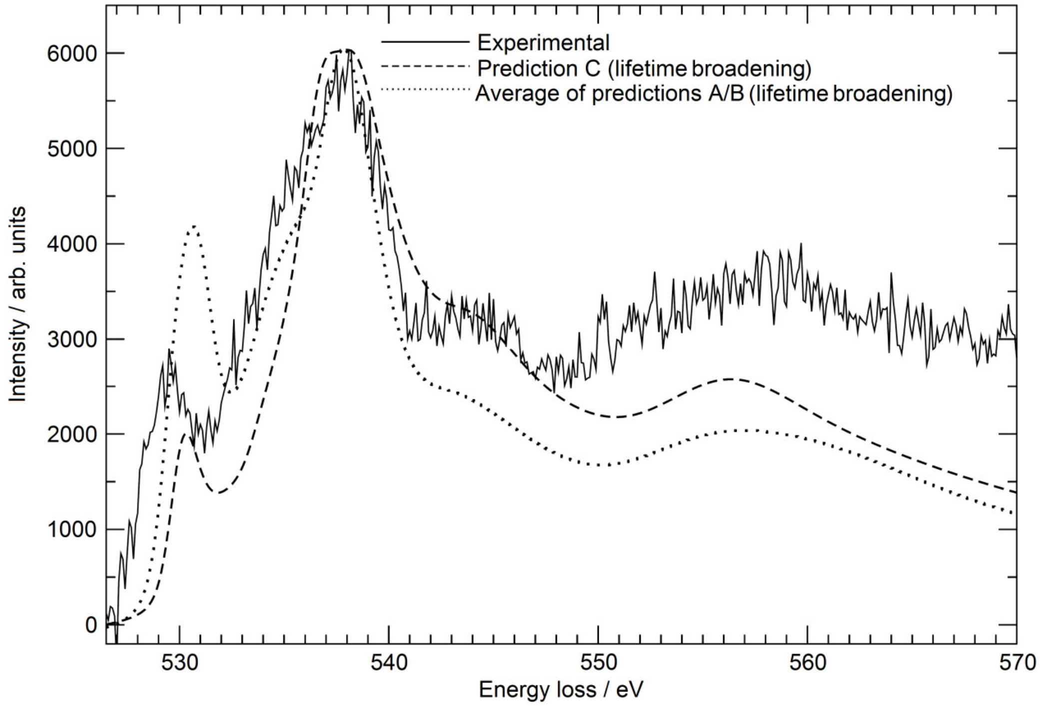

Figure 7.9: Predicted and experimental interface oxygen K edge predictions, adapted from Figure 7.7, but on this occasion the theoretical results are subjected to energy-dependent final state lifetime broadening. As in Figure 7.8, the theoretical results have been hard shifted in energy, and scaled in intensity relative to the experimental result. All the theoretical calculations were carried out in the ground state.

Again, as in Figure 7.8, scaling has been performed relative to the most intense peak in the spectrum. As can be seen in Figure 7.9, the addition of the lifetime-based broadening scheme appears to alter the relative similarities between the two sets of theoretical results. With this broadening scheme applied, for theoretical result C versus experiment the result of the least squares analysis was 821 (counts), and for the average of A/B 991 (counts). This (and visual inspection) suggests a better fit for position ‘C’ when this broadening is applied.

This work has made some effort to quantify ‘goodness of fit’ between modelled and experimental EELS results. However, future work is planned on investigating broadening in EELS, such that there can be confidence in the numerical analyses presented. I am however confident that the differences observed in the ‘standard deviations’ are statistically significant. I integrated the experimental spectrum from 526 to 556 eV, divided the value by 30 (the energy range), and found the square root. The resulting answer was 56, and I consider this a reasonable estimate of average spectral ‘noise’. The differences in standard deviations described above are as large or greater than the spectral noise, so would appear to be statistically significant, and the methodology presented is worthy of further investigation.

7.5.4 Multiple linear least squares analysis

Given the high standard of experimental result, it was possible to carry out a final form of analysis - a multiple linear least squares (MLLS) fit of the A/B model and C model to the experimental result. The results are shown in Fig. 7.10.

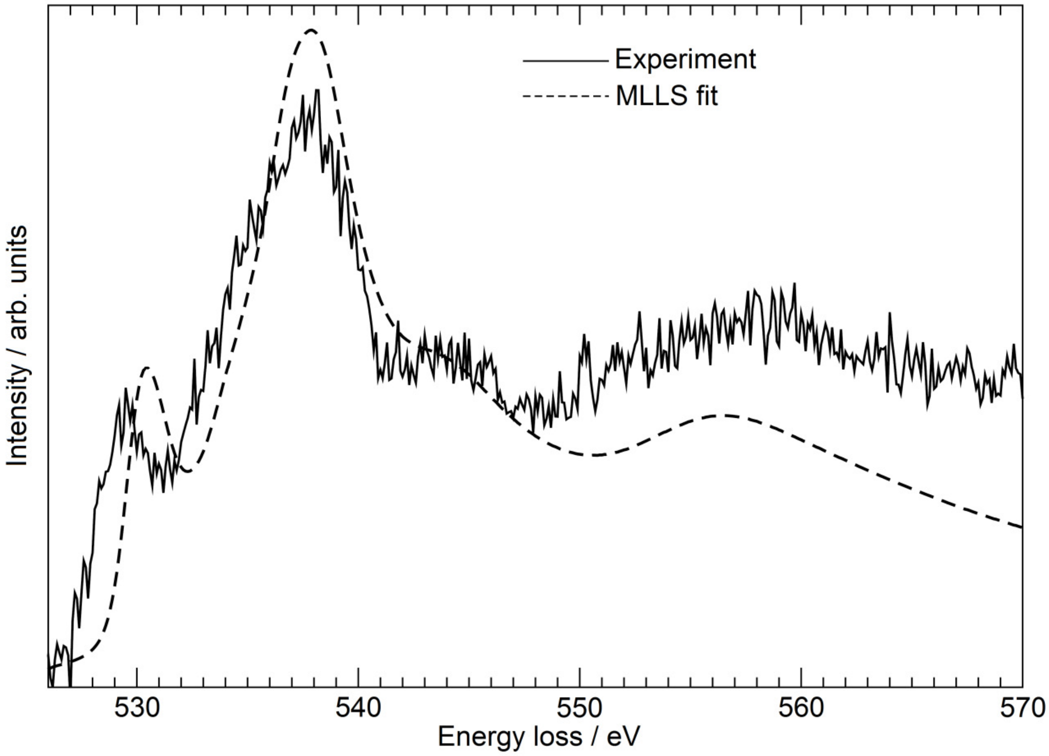

Figure 7.10: Results of MLLS fit (of theoretical result C and the average of A/B, both with lifetime-based broadening).

The analysis was carried out in an energy window of 526–556eV, using the model/experimental data as presented in Figure 7.9, meaning that the MLLS analysis was carried out on theoretical results normalised against experiment by setting the same maximum peak intensity. The MLLS fit coefficients were 0.43 for the A/B spectrum and 0.67 for the C spectrum, suggesting each theoretical set was of similar importance in the fit. One might postulate that the true experimental interface structure is a mixture of the models presented in Fig. 7.5, and the MLLS coefficients might indicate relative proportions in the mixture, though this concept requires further study.

It is aimed to carry out subsequent investigations of such interfaces. One system that could be considered for example is a Fe/MgO interface, where multilayers of FeO exist at the boundary.

Further, the ideal picture of the oxidised interface is certainly possible. However, one also needs to consider interface roughness, especially of the top MgO/Fe interface due to island growth of Fe. Therefore, the spectra may also reflect O–Fe bonding due to steps at the interface and not just an atomically flat monolayer of Fe-O. EELS measurements of roughness at this interface have been discussed in depth in a recent paper, for example (Serin, 2009). Further, there was evidence of charging, resulting in ‘elongated’ atoms at the interface, making it difficult to establish firm conclusions regarding the interface structure.

7.6 Why are ground state calculations viable in this case?

7.6.1 Introductory remarks

Though not as ideal a match with experiment as bulk core-hole results, ground state calculations (particularly those shown in Figures 7.4 and 7.6) are of qualitative usage. An overview of why this might be the case has been given previously in this Chapter, and this section considers the phenomenon in more detail.

One might suggest that if a material has high screening, a ground state calculation may be acceptable, the logic being that screening of the core-hole will lessen its impact on the predicted result. Magnesium oxide is an insulating material with a wide band gap. However, one might argue that as the oxygen species within MgO are (at least partially) ionic and hence ‘negatively charged’, some amount of screening may exist.

At EDGE conference 2009, a slightly different rationalisation was proposed by Mauchamp et al. which is now considered for MgO using the CASTEP code (Mauchamp, 2009), (Mauchamp, 2009a). A key consideration is the density of states (DOS), its nature in the ground state, and how this is impacted by the introduction of a core hole. The idea of different partial DOS (e.g. *s* DOS, *p*

DOS) being impacted to different extents by the introduction of a core hole has also been considered previously in the literature (Keast, 2001).

Consider firstly Figure 7.11. These are various CASTEP DOS predictions - for a single cell of MgO in the ground state. These predictions were carried out using the same parameters as given in Table 7.1 (for bulk material calculations). Two energy ranges are shown in the plot; above and below the Fermi level.

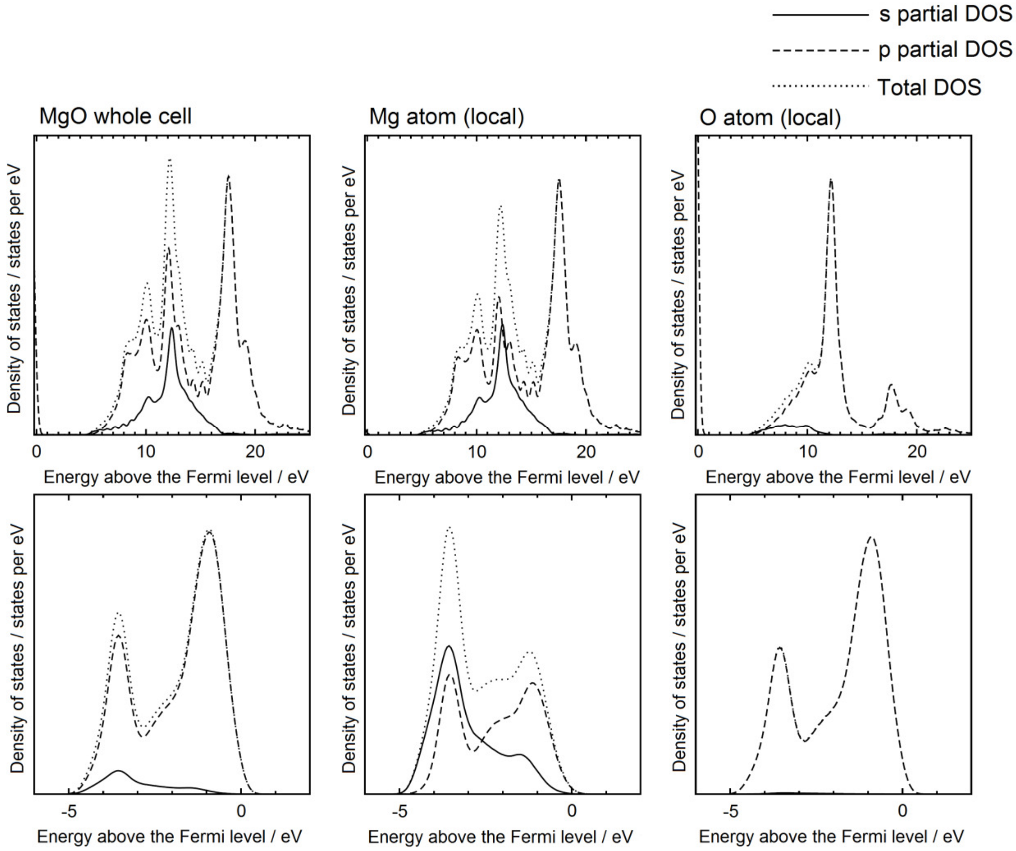

Figure 7.11: Various ground state DOS predictions (as labelled, found using CASTEP) for MgO, and localised atoms within a single cell of the material. The top plots focus on energy above the Fermi level (i.e. conduction bands), the bottom plots focus on upper valence states.

Firstly in the top plots are shown various unoccupied DOS predictions. As can be observed, the unoccupied DOS for the whole cell closely resembles the local DOS for the Mg atom, rather than the oxygen atom. In other words, the conduction bands in this material mostly have magnesium (2*p*) character. This may go some way towards explaining why for the oxygen K edge in this system, the introduction of a core hole does have an impact, but not such that the ground state cannot provide a reasonable agreement with experiment given the correct choice of broadening conditions.

In the plots that consider the valence bands just before the Fermi level, it is observed that the overall DOS character closely resembles that for oxygen, though arguably the *p* DOS is qualitatively similar in each case.

7.6.2 The core-hole effect for the oxygen K edge

The oxygen unoccupied partial *p* DOS was considered in the ground state (as found above), and compared to *p* DOS predictions for a single cell with a core hole in place. In this instance (for a single cell), the core hole was 'smeared' across the whole cell by adding a single positive charge to the cell to compensate for the missing core electron. The results are shown in Figure 7.12.

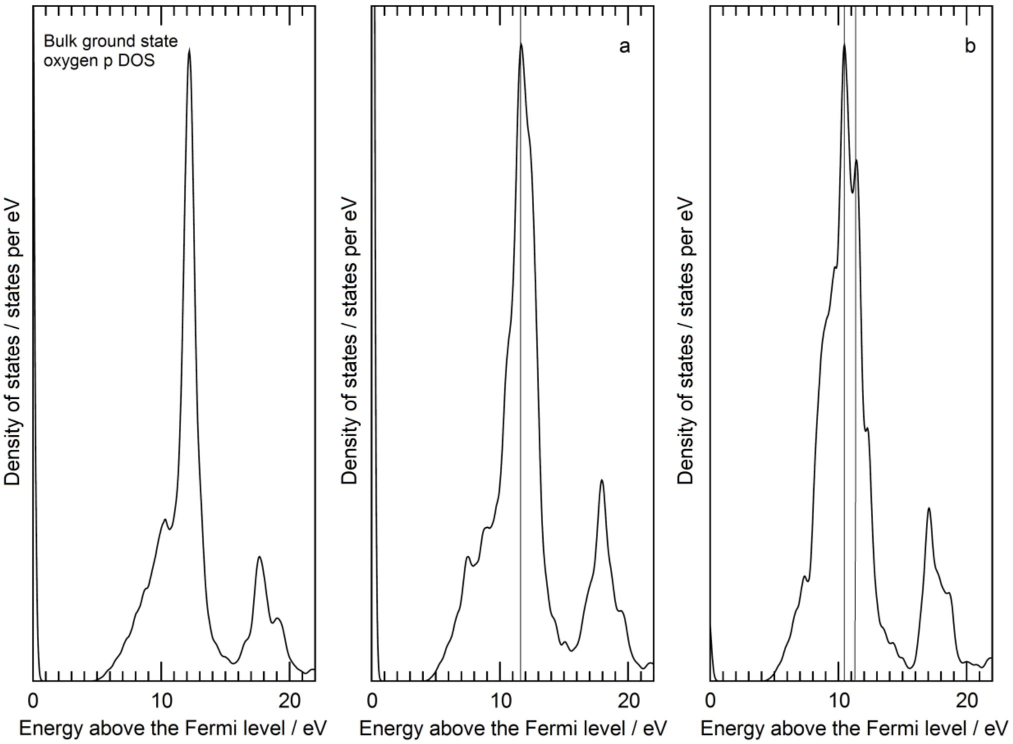

Figure 7.12: Various oxygen atom *p* DOS predictions. On the far left is the oxygen *p* DOS prediction from the bulk material in the true ground state. For plots (a) and (b) a single cell was created where one of the four oxygen atoms had a single electron core-hole in place. Plot (a) shows the *p* DOS prediction for one of the ground state oxygen atoms. Plot (b) shows the *p* DOS prediction for the oxygen atom that has the core-hole in place.

The first plot on the left is simply the *p* DOS prediction found from a single cell with all atoms in the ground electronic state, as labelled in the figure. For plots

(a) and (b), a single cell was then constructed in which one of the four oxygen atoms had a single electron core hole in the 1*s* level. The other three oxygen atoms were in the ground electronic state. Plot (a) shows the *p* DOS prediction for one of those ground state oxygen atoms. This result is highly similar to the result from the cell in which all atoms were in the ground state.

This suggested any differences observed for the core-hole atom would be significant and meaningful, and plot (b) shows the *p* DOS prediction for the oxygen that has the core hole in place. This result is qualitatively similar to the ground state result, and result (a). However, one can clearly observe the development of the 'doublet' feature previously discussed. Further, the core-hole result (b) displays a large-shoulder before the doublet, which is arguably an effect of the core hole also seen in Figure 7.2.

It is however reasonable to suggest (on comparing results (a) and (b)) that the oxygen 2*p* electrons in the valence band screen the core hole to an extent. This also goes some way towards explaining why the ground state result provides a reasonable qualitative match with experiment. In the Lindner et al. study using multiple scattering, a ground state partial *p* DOS for oxygen was found. This result was qualitatively similar to the various ground state predictions in this work. In Lindner et al.'s paper, the introduction of a core hole does also create a doublet at the first peak of the spectrum, though in the reverse ratio to experiment.

It does however remain, despite the relative subtlety of the effect, to understand why the addition of a core hole leads to the development of the 'doublet' feature. Figure 7.12 has a number of vertical lines added to parts 'a' and 'b' to aid inspection of the figures. One can observe that when the core hole is introduced, there is a definite shift in the energy of the first peak towards the Fermi level. Furthermore the intensity of this peak increases.

7.7 Summary and conclusions

Pseudopotential DFT modelling (in the form of the CASTEP code) was successfully used to model the oxygen K edge ELNES in various systems, from bulk magnesium oxide to the interface of Fe (001) / MgO (001), for which various interesting trends were observed with regard to pre-edge intensity.

MLLS fitting suggested there was likely to be some degree of oxidation at the interface. With regard to further work one option might be to examine elemental profiles of Mg, Fe and O at that the interface to provide further evidence of FeO formation.

In this work, spin polarisation was not considered (the relevance of this being that Fe has a magnetic moment). As was shown in Figure 4.4, the inclusion of spin in calculations can alter the system energy, therefore potentially influencing any associated ELNES prediction, as observed in analogous work (Eustace, 2010). Future work might involve the determination of the extent of this effect for this Fe/MgO system.

For bulk MgO, and indeed the other systems it was found that ground state calculations were qualitatively useful. This was rationalised by an analysis of the various DOS components for the system, a major consideration being that the *p* partial DOS for the oxygen atom did not massively vary when a core hole was added, though the core hole does create a doublet for the first peak in the spectrum. Interface and surface results will be studied further in future work, following the observations of interesting trends in the thesis. Possible experiments might include the energy minimisation of the surface and interface structures, and the usage of ‘empty’ atoms in the structures, negating the need for large vacuum slabs.

Chapter 8

CrAlYN/CrN multilayer coatings

8.1 Introduction

Mechanical engineering components are in frequent need of ultra-performance coatings to provide environmental protection and extend lifetimes. A particular challenge for surface engineers is to design coatings that provide environmental protection from 650℃ - 1000℃, without adversely affecting the properties of the mechanical component in question (Fröhlich, 2006), (Hovsepian, 2005). High-performance materials are coated depending on the particular application required, applications including automotive components coatings, and the coating of alloys used in the manufacture of aerospace components (Guzman, 2003), (Luo, 2005).

Coatings with a nano-scale multilayer structure (deposited using magnetron sputtering) have better hardness and oxidation resistance than monolithic coatings (Zhou, 2004). In particular, titanium-free multilayer coatings based on CrAlYN/CrN have shown good wear and oxidation performance (Hovsepian, 2006), (Yang, 2004). The structure and chemistry of these multilayer systems has not been studied in detail. A better understanding of the nano-chemistry in these cases may help to interpret properties such as oxidation resistance and tribological performance. The ultimate aim of this study, involving DFT modelling was to deduce structural and chemical information regarding the CrAlYN/CrN coatings, using an aberration corrected (S)TEM (see Chapter 2).

8.2 Experimental synthesis

8.2.1 Introductory remarks

Synthesis of materials was carried out by P. Eh. Hovespian and C. Reinhard. TEM characterisation by I.M. Ross, W.M. Rainforth and W. Peng, A. Bleloch and B. Mendis. The CrAlYN multilayer coating was deposited on a γ-TiAl substrate using unbalanced magnetron sputtering (UBM). The procedure used a Hauzer HTC 1000-4 PVD coater (Münz, 1992), following methodology previously outlined (Hovsepian, 2006a), (Münz, 2001). The γ-TiAl substrate was metal ion etched for enhanced adhesion and coating quality (Ehiasarian, 2007).

Following this a base layer of CrAlN was added (approximately 0.3µm thick) using UBM. The multilayer coating was then added – consisting of alternate layers of CrAlYN / CrN – leading to a total coating thickness of ~5µm. For the UBM deposition a substrate temperature of 450˚C was used, with a bias voltage of -75V.

Tribological properties and oxidation performance are thought to be improved by the pre-deposition of a partially oxidised surface layer (Tönshoff, 1998). Thus, for the final part of coating, the reactive deposition atmosphere was changed from nitrogen to dry air to form an oxy-nitride surface layer (CrAlYON/CrON), approximately 0.8µm thick (Seabourne, 2010a, see also Appendix 11.1).

8.2.2 Characterisation of multilayers using EELS

EELS data was obtained at the SuperSTEM facility using SuperSTEM1 (an HB501 with a NION spherical aberration corrector), with EELS spectrum imaging used (Dellby, 2001). The EELS data was acquired with an electron beam at 100kV, a convergence half-angle of 24 mrad and a spectrometer collection angle of 19 mrad (see Chapter 2 for discussion of these concepts). These convergence and collection angles are arguably at the limit of the dipole approximation, which was assumed to apply during modelling nonetheless.

High angle annular dark-field (HAADF) images were recorded with a detector acceptance angle 70-120 mrad. The electron source was a FEG, the convergence semi-angle 8 mrads, and the collection angle 4 mrads. This means the dipole selection rule applies (See Chapter 2 for further discussion).

The first figure below shows a bright-field (S)TEM image of the coating as deposited by UBM. Subsequently, there is a HAADF image of the actual multilayer structure, shown with a period of 3.8±0.2nm.

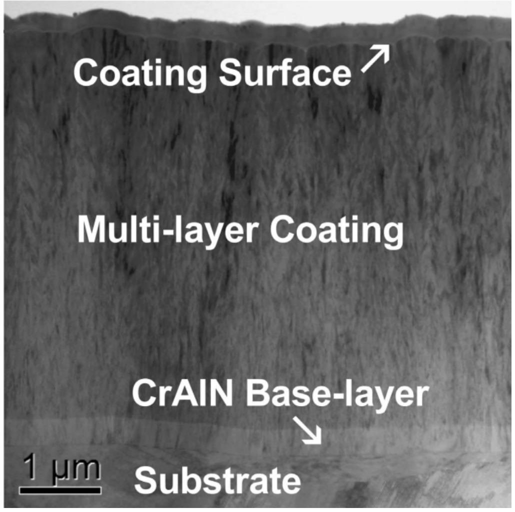

Figure 8.1: Bright-field STEM image of the deposited coating showing the various coating components. The band of grey contrast directly above the surface of the coating corresponds to a sputtered metal layer deposited during sample preparation.

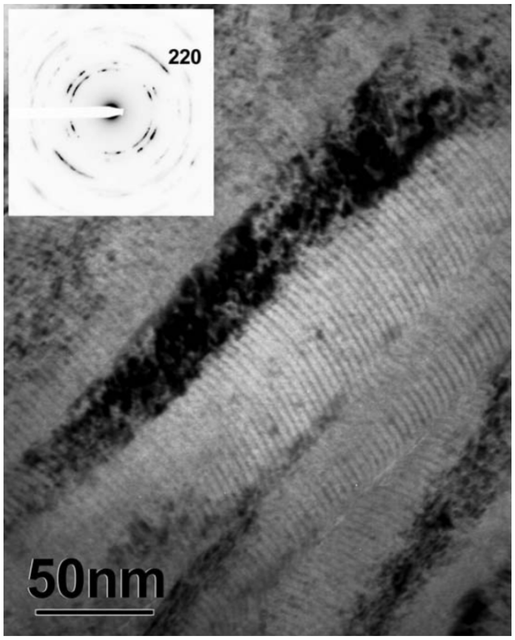

Figure 8.2: High magnification HAADF image of the multilayer coating structure. Period of 3.8±0.2nm.

The electron beam was scanned across the multilayers in a 'line scan'. The 'probe size' of the electron beam was approximately 1.6Å, and the step size of movement during the line scan was 2Å. This step size, and the exposure time in each instance was appropriately modified to minimise problems of drift and sample contamination. Figure 8.3 shows a line scan across the multilayer coatings:

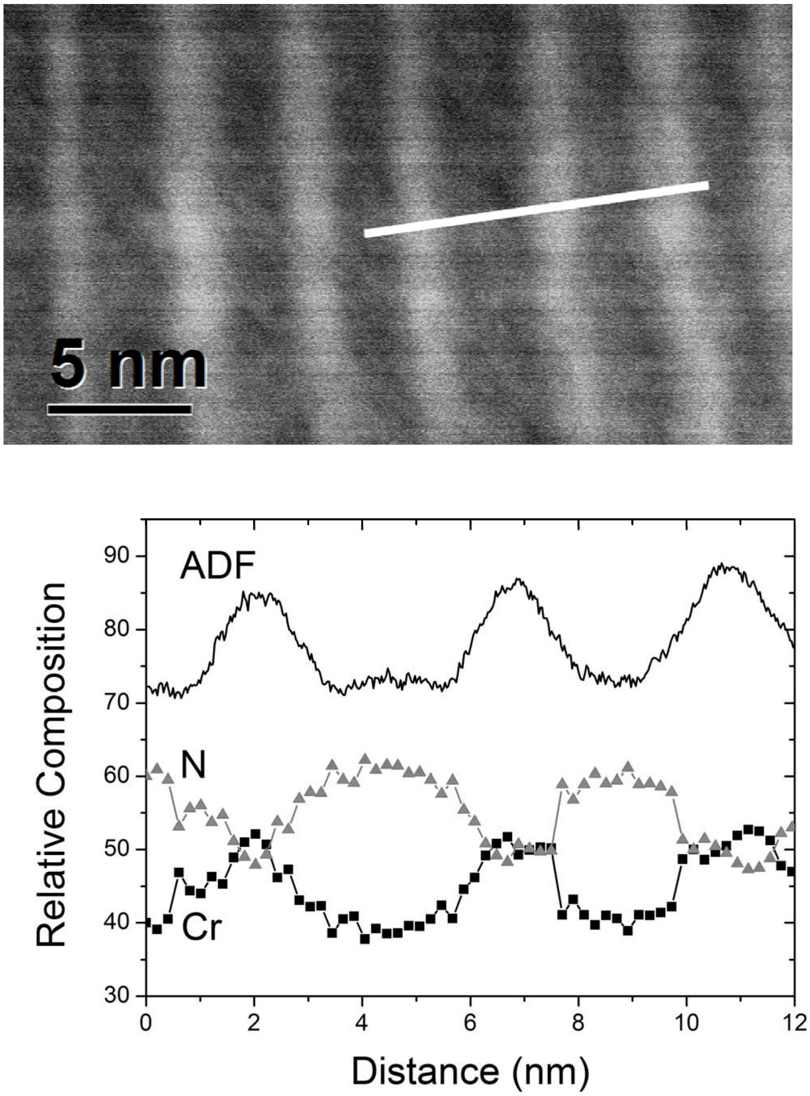

Figure 8.3: Depiction of the line scan across the multilayer coatings (top). Illustration of elemental content as the line scan progresses (bottom).

It was possible to obtain initial quantification results using a spectrum imaging technique. Two data sets were obtained for spectrum imaging, with corresponding HAADF images acquired at each location – one for the N K and O K edges and Cr $L_{2,3}$ edge , and the second for the Al K edge. To observe if there was contamination or specimen drift, the HAADF image was taken before and after the acquisition of the spectrum image line scan.

Two data sets had to be obtained due to the energy loss ranges in question, i.e. the N K (401eV), O K (532eV) and Cr $L_{2,3}$ (575eV) edges and the higher Al K edge (1560eV) could not be obtained on the same spectral scan, due to limits in spectrometer coupling optics. The lower energy Al $L_{2,3}$ edge at 73eV was not used. This is because it overlaps with the Cr M_1 edge at 73.5eV. Thus two sets of data were acquired, in each case a spectrometer energy dispersion of 0.5eV/pixel was used.

Finally therefore, intensity profiles were obtained. Edge integration of the O K, N K, Cr $L_{2,3}$ and Al K edges was carried out using background fitting and integration ranges as follows; O K (474eV-521eV, 532eV-575eV), N K (358eV-393eV, 401eV-426eV), Cr $L_{2,3}$ (513eV-563eV, 575eV-615eV), Al K (1392eV-1529eV, 1560eV – 1620eV). Relative concentrations could then be obtained by normalisation of the net edge intensities by corresponding inelastic Hartree-Slater cross sections.

When considering the individual coating layers as part of a more detailed EELS analysis, the probe size of the electron beam was focussed again to 1.6 Å, and positioned at the centre of the layer in question. The EELS spectrum was then carefully recorded at the N K edge and Cr $L_{2,3}$ edge, the spectrometer dispersion being 0.1eV/pixel.

8.3 Modelling methodology

Computational simulations were carried out using the Wien2k code (see Chapter 3 for a full description).

The structures of the end members of the Fm-3m series of CrN and AlN were chosen with lattice parameters 4.14Å and 4.05Å respectively (Panjan, 2007), (Zhu, 2008). Vegard's rule was then used to find plausible lattice parameters for the intermediate compositions ($Cr_{0.75}Al_{0.25}N$, $Cr_{0.625}Al_{0.375}N$, $Cr_{0.5}Al_{0.5}N$, $Cr_{0.325}Al_{0.625}N$, $Cr_{0.25}Al_{0.75}N$) nitrogen being the common element in all cases (Calmels, 2006), (Jhi, 1997):

$$a^3_{NCr_xAl_{(1-x)}} = xa^3_{NCr} + (1-x)a^3_{NAl} \tag{8.1}$$

The resulting lattice parameters are as given in Table 8.1:

Compound	**Lattice parameter / Å**
CrN	4.140
$Cr_{0.75}Al_{0.25}N$	4.118
$Cr_{0.625}Al_{0.375}N$	4.107
$Cr_{0.5}Al_{0.5}N$	4.095
$Cr_{0.325}Al_{0.625}N$	4.084
$Cr_{0.25}Al_{0.75}N$	4.073
AlN	4.050

Table 8.1: Resulting lattice parameters for mixed alloy compounds.

Using the calculated lattice parameters, unit cells were constructed, with calculations being in the ground state. A theoretical core-hole was therefore not included as it has been shown that for systems related to CrN the core-hole has only a small effect on the predicted ELNES result (Scott, 2001). This was also observed for analogous transition metal compounds in Chapter 6 in this thesis. It should be noted it is valid not to include Y in the theoretical cells, as this element localises to the boundaries between layers rather than the layers themselves (Ross, 2010). Wien2k was then used to find predicted nitrogen K edges. 1000 *k*-points were used in total in the reducible Brillouin zone, with RK_{MAX} of 7, l_{max} of 12, and energy and charge convergence criteria of ±0.0001Ry (Rydberg energy units).

When there was more than one nitrogen atom present in the cell, an 'average' K edge was determined. In the figures presenting the theoretical results, two types of broadening were applied. Firstly, a nominal energy-independent Lorentzian broadening (of magnitude 1eV), and secondly an energy-dependent final state lifetime broadening as described previously in the thesis.

8.4 Results and discussion

There are ultimately (as part of the multi-layer structure) three nominal 'types' of layer – CrN, CrAlN and CrAlYN. These labels are not attempts to accurately describe the stoichiometry of those layers. Indeed the purpose of characterisation in this instance is to move towards determining that stoichiometry.

Analysis of the ELNES at the N K edge from the individual layers was performed relative to the simulated N Kedges for CrN with varying Al contents as shown in Figure 8.4:

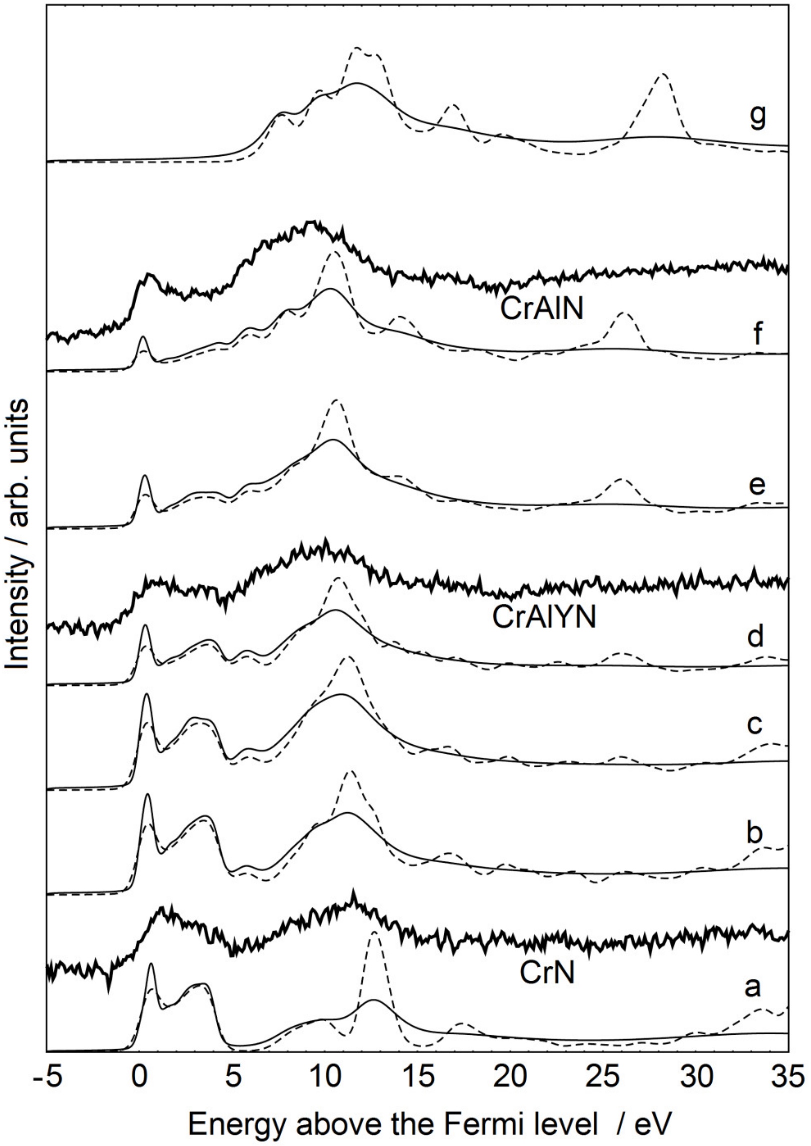

Figure 8.4: Comparison of the simulated ELNES and experimental observations for mixed alloy systems: a) CrN, b) $Cr_{0.75}Al_{0.25}N$, c) $Cr_{0.625}Al_{0.375}N$, d) $Cr_{0.5}Al_{0.5}N$, e) $Cr_{0.325}Al_{0.625}N$, f) $Cr_{0.25}Al_{0.75}N$ and g) AlN. In all cases the solid black line includes energy-dependent final state lifetime broadening, the dashed line is with minimal numerical broadening. The experimental results for CrN, CrAlYN and CrAlN are shown with solid bold lines as labelled, and aligned with the closest matching theoretical result.

Clear trends are observable for the theoretical results. Moving up the plot the change from a transition metal (chromium) to a *p*-block element (aluminium) is clear. The peaks in the region 0-5eV decrease in intensity and ultimately disappear. In the case of the transition metal the *p* orbitals (crucial to the K edge) are presumably modified due to interaction with *d* orbitals.

Considering the experimental ELNES results, spectra for the CrN, CrAlYN and CrAlN layers are shown in bold on Figure 8.4, shown next to the predicted result they appear closest to in appearance (based on comparisons of peak ratios).

For the nominal CrN layer, the shape and peak positions are comparable to those seen by Mitterbauer et al. for bulk CrN (Mitterbauer, 2004), and indeed the best match with the Wien2K calculations was also with stoichiometric CrN. This is in good agreement with the relative Cr/N ratio of 1.05±0.1 obtained from the initial EELS line scan shown in Figure 8.3.

In the case of CrAlYN the best agreement with the simulated edges was for $Cr_{0.5}Al_{0.5}N$, a system with half as much chromium as compared with nitrogen. This is consistent with the relative Cr/N ratio of 0.59±0.02 as observed by the line scans.

Previous studies have reported that for UBM deposited CrAlN, the nitrogen content of the coating was approximately 1:1 with respect to metal content (Ding, 2005). Further, incorporation of aluminium was seen to be beneficial in the formation of a more stoichiometric composition within the coating. The CrAlN base-layer in this instance was in best agreement with the theoretical result for $Cr_{0.25}Al_{0.75}N$. One problem with this conclusion is that it implies a slightly higher aluminium content than was observed by direct analytical (S)TEM measurements, which showed 47.8±5.6 at% N, 20.0±2.3 at% Cr and 32.2±3.8 Al. However, comparisons with theory do clearly show a greater aluminium content than the CrAlYN layers.

Table 8.2 summarises the observed trends when comparing theory and experiment.

Layer	Best agreement	Nitrogen content	Aluminium content
CrAlYN	$Cr_{0.5}Al_{0.5}N$	There was a suggestion that the EELS spectrum image line profiles reveal that the CrN layers for example contain significantly less N than the CrAlYN layers. Certainly according to the above, the amount of nitrogen relative to chromium is greater. For CrAlYN the best match to theory is $Cr_{0.5}Al_{0.5}N$ – i.e. where there is twice as much nitrogen as chromium. For CrN the best match with theory is CrN – an equal amount of nitrogen and chromium, i.e. less nitrogen relative to chromium.	The CrAlN layer is generally thought to be Al rich (compared to CrAlYN). The closest match for this layer theoretically was the $Cr_{0.25}Al_{0.75}N$ model - which seems highly consistent with that observation.
CrAlN	$Cr_{0.25}Al_{0.75}N$		
CrN	CrN		

Table 8.2: Summary of comparisons between theoretical and experimental nitrogen ELNES for CrN, CrAlYN and CrAlN.

8.5 Summary

Nanoscale characterisation of a CrAlYN/CrN multilayer coating was carried out using a combination of experimental and theoretical ELNES. For the nominal CrN layers a Cr/N ratio of near unity was observed; 1.05±0.01. In the nominal CrAlYN layers, quantitative analysis shows a Cr/N ratio of 0.59±0.02 consistent with target stoichiometry. The theoretical modelling showed a definite and logical trend in the ELNES as the ratio of transition metal to non-transitional metal was altered. By comparison of experimental and theoretical ELNES, the closest agreement for the nominal CrN layers was with the CrN model system, and for the nominal CrAlYN layers the closest agreement was for the $Cr_{0.5}Al_{0.5}N$ model system. This was consistent with quantitative analysis. Future work might involve the inclusion of spin polarisation, previous work having considered these effects for CrN nitrogen K edge modelling (Paxton, 2000).

Chapter 9

Future directions and conclusions

9.1 Linear scaling DFT methods

9.1.1 Introduction

Calculation time for a standard DFT code such as CASTEP scales cubically with the number of electrons involved in the calculation (Skylaris, 2005). In recent years a collaboration between the Universities of Southampton and Cambridge, and Imperial College London has resulted in the ‘ONETEP’ code.

ONETEP stands for ‘order-N electronic total energy package’. The software uses density functionals in a sophisticated manner to achieve the linear scaling. It is necessary to describe in outline how this is achieved. In one of the early papers reporting the ONETEP code, the authors suggest that;

“ONETEP is essentially a linear-scaling reformulation of the plane wave pseudopotential DFT approach”.

This is achieved by the usage of nonorthogonal generalized Wannier functions (NGWFs), which are best illustrated using a figure from the paper reporting the ONETEP code (Skylaris, 2005):

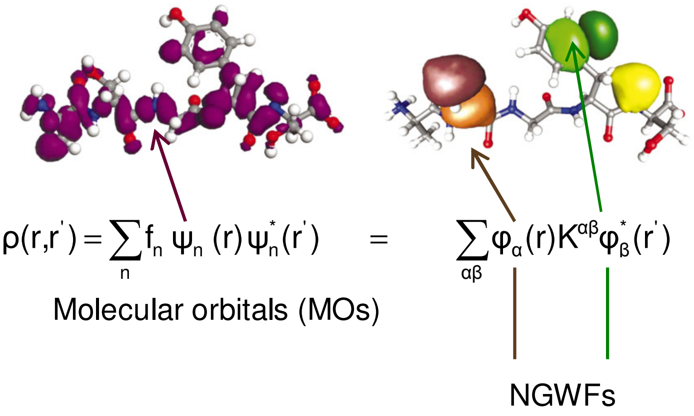

$$\rho(r,r') = \sum_n f_n \psi_n(r)\psi_n^*(r') \quad = \quad \sum_{\alpha\beta} \varphi_\alpha(r) K^{\alpha\beta} \varphi_\beta^*(r')$$

Figure 9.1: Illustrating NGWFs by comparison of the CASTEP and ONETEP codes. The system shown is a simple peptide (Skylaris, 2005).

The NGWFs effectively represent localised wavefunctions, centred on specific atomic sites. In order to maintain this approximation, the system must be an insulator or semi-conductor. In a free-electron metal for example, it would not be plausible to localise functions to specific atoms in this fashion.

Figure 9.1 is designed to illustrate the approach utilised by ONETEP as opposed to the CASTEP code. There are various fashions in which can frame DFT. In their paper reporting the ONETEP code, the authors use the Schrödinger equation (Skylaris, 2005).

$$\hat{H}\psi_i(r) = \left[-\frac{\hbar^2}{2m}\nabla^2 + V(r)\right]\psi_i(r) = \varepsilon_i\psi_i(r) \qquad (9.1)$$

$\hat{H}$ is the single particle Hamiltonian for a system with eigenvalues ε_i and orthogonal orbitals $\psi_i(r)$.

DFT proves that electron density is a universal variable that can be used to find ground state system properties such as energy (Hohenberg, 1964), (Kohn, 1965). As part of the Schrödinger / orthogonal orbital formalism, we can state for our ground state system, there is a single particle density matrix which contains all system information;

$$\rho(r,r') = \sum_n f_n\, \psi_n(r)\psi_n^*(r') \qquad (9.2)$$

(See Figure 9.1) f_n represents the occupation of state $\psi_i(r)$, restricted in value to 0 or 1 due to calculations being carried out 0K temperature. The diagonal elements of this density matrix give the charge density (the crucial quantity in DFT), allowing calculations to progress:

$$n(r) = 2\rho(r,r) \qquad (9.3)$$

As is implied in Figure 9.1, the key step towards linear scaling is the modification of equation 9.2.

When a band gap exists for a given system, the density matrix (9.2) exponentially decays as a function of the separation of r and r’ (He, 2001), (Skylaris, 2005).

Therefore, one can deliberately ‘truncate’ the density matrix so the information contained increases linearly with the size of the density matrix (see Figure 9.1):

$$\rho(r,r') = \sum_{\alpha\beta} \varphi_{\alpha}(r) K^{\alpha\beta} \varphi^{*}_{\beta}(r') \tag{9.4}$$

‘φ’ represents the NGWFs as shown in Figure 9.1. ‘K’ is called the ‘density kernel’, calculated by the code (McWeeny, 1960).

As rationalised above, the information contained in the density matrix increases linearly with the size of that matrix, i.e. linear scaling. Another means of rationalising this is to consider that effectively the ONETEP code reduces the standard DFT problem (the left hand side of Figure 9.1) to one in which there are NGWFs localised on each atom, and therefore the scaling is linear with the number of those NGWFs, and consequently the number of atomic species. There are various papers presenting different approaches to rationalising the theory behind the ONETEP code (Haynes, 2006), (Haynes, 2006a).

9.1.2 Core level spectroscopy

Core level spectroscopy calculations are not currently available as part of the ONETEP code. However, during a recent conference on the code this possibility was discussed by Ratcliff et al. (Ratcliff, 2010). A key problem is that in order to calculate core-level spectroscopy results, the density of states (DOS) needs to be found above the Fermi level. One suggested method of achieving this is to carry out a standard, fully consistent calculation in the ground state. This would then be followed by a non self-consistent calculation to find the DOS above the Fermi level. Potential methodologies to accomplish this are still in development at Imperial College London.

The linear scaling nature of the ONETEP code means large systems such as surfaces and interfaces might be increasingly tractable, and able to be studied in a shorter time. Practically speaking, DFT codes (for the purpose of studying core-level spectroscopy) are limited to 100s of atoms, whereas the ONETEP code may have the potential to move core-level spectroscopy calculations to systems of 1000s of atoms.

9.2 Computing considerations

9.2.1 Introduction

At various conferences on the general field of EELS or electron microscopy, seminars are devoted to EELS modelling. Usually, researchers with a specialism in experimental EELS are interesting in learning modelling principles. Theoreticians can give an overview of the techniques required, but often without relaying the difficulties of practical computing.

9.2.2 Parallelisation

For standard convergence and single cell experiments, parallel computing is not usually necessary, a quad-core desktop PC is sufficient. However, for supercell experiments parallel computing is essential. This is trivially thought to be in order to allow greater computational speed. There is however somewhat of a ‘bottleneck’ problem. Smaller jobs submitted to a parallel architecture will not necessarily run faster if the slowest step is the communication between the nodes rather than the calculation itself!

In fact, probably the greatest reason why parallel architectures are required is due to memory limitations. Typically, supercell calculations often require 30Gb of RAM, which is clearly not possible without the utilisation of a parallel computing network. Similarly, massive amounts of storage are required. The .check model data files that CASTEP produces can be 10-20Gb in size for example.

CASTEP is relatively straightforward to use in parallel, as it is a single executable. Wien2k is run by linking together a series of executables, which can be run in parallel, but this can be somewhat unreliable.

9.2.3 Parallel architectures used in this work

Initial work was carried out using the ‘Everest’ system based at the University of Leeds. Wien2k had been installed on the system for some time. I was able to coordinate the installation of the first trial version of CASTEP which incorporated EELS calculations. Everest was utilised throughout this work. Currently, I am guiding the installation of CASTEP and Wien2k on the new

‘Advanced Research Computing’ (ARC1) system at Leeds, which is likely to become one of the leading facilities in the UK.

In the interim I successfully applied for access on the HECToR UK supercomputing grid, again coordinating the installation of Wien2k and CASTEP. Concurrently, I accomplished the same on the National Grid Service network (NGS).

Establishing this wide range of computing support was essential in the accurate and reliable modelling of the larger systems presented in this thesis.

As alluded to above, improving the speed of communication between nodes in a parallel architecture is essential, and this should be an important consideration in the design of new systems. Indeed, it has been a major concern in the design of the ARC1 grid. Similarly, it is important to ensure there is minimal latency in the system. ‘Latency’ represents the time delay between an executable giving an instruction to hardware (to alter a voltage from on to off for example) and that transformation actually occurring.

The careful optimisation of these systems, and efforts made on my part with regard to code installation and management have made it definitively possible to move beyond relatively small unit cells, to the larger periodic units illustrated.

9.3 Conclusions and discussion of possible future work

The introduction to the thesis, and the main body of text stated the following research aims:

- Devise coherent methodologies for modelling electron spectroscopy results, using density functional theory based codes.
- Evaluate the suitability of various codes for this purpose, and develop new styles of applying the codes, using Wien2k as a benchmark.
- Demonstrate the capability of modelling to assist in the assignment of spectra obtained experimentally for nanoscale materials.
- Devise experiments based on modelling results.

- Deduce structural properties of materials from modelling studies, for novel systems including interfaces and systems with defects or vacancies.

In Chapter 4, a methodology was presented for the appropriate usage of DFT codes for ELNES modelling. The possibility of converging the kinetic energy cut-off and *k*-point mesh to the ELNES prediction itself was illustrated, and agreement with experimental spectra was improved by the application of an energy-dependent final state lifetime broadening scheme. It is interesting to note that having undertaken these rigorous processes, they were arguably unnecessary in terms of obtaining sensible experimental predictions, as previously considered in the literature (Nicholls, 2008). For example in Chapter 8, using practical experience derived from detailed experiments for analogous systems, reasonable parameters could be selected. However, for a relatively uncharacterised system (in terms of electronic structure), a rigorous convergence process should still be undertaken.

Chapter 5 studied a series of related aluminium compounds of different character; aluminium metal (free-electron metal), aluminium nitride (wurtzite form, semiconductor) and aluminium oxide (insulator). For each system, it was demonstrated that the CASTEP pseudopotential code correctly accounted for the core-hole, and was suitable for usage in EELS modelling. The nature of the CASTEP code means it is easier to operate in a parallel architecture, and theoretical cells are easier to construct.

Having demonstrated the suitability of the CASTEP code, and generated reliable methodologies, the remaining chapters sought to achieve the other stated aims. Modelling work has allowed some suggestions to be made to my experimental collaborators regarding possible future work. Considerable success has been achieved in deducing structural properties of materials and assigning spectra. In Chapter 6, some suggestions were made as to possible structures for a series of titanium carbonitride systems with vacancies. It was noted however that these structural postulations were far from conclusive. A $Fd3m$ vacancy symmetry was assumed, but other symmetry vacancies models are possible, and future work would ideally consider these in combination with the approach already presented. Furthermore, the virtual crystal approximation might be of considerable use in this instance. It was observed that different symmetries and positions of nitrogen and carbon atoms (specifically clustering certain species close to the vacancies) significantly altered agreement with experiment. In the virtual crystal approximation (VCA) it is possible (for a single atomic site) to set a ‘ratio’ of one element to another, i.e. simulate a ‘mixture’ of two atoms at a particular site. Future work utilising this approach might be prudent in this instance.

In Chapter 7, it was illustrated there was likely to be some degree of oxidation present at an interface found in magnetic tunnel junctions. Though it was the oxygen K edge that was modelled, future work might involve explicitly accounting for the ferromagnetism of the Fe layers, and the impact that may have on ELNES predictions for the oxygen K edge.

Finally, in Chapter 8 the compositions of a series of nanoscale coating layers were postulated. This work could be extended to include an analysis of the oxynitride layers these coatings also contain.

In this thesis, both the Wien2k and CASTEP DFT codes have been used for ELNES modelling. In terms of comparing the two codes, there are firstly a number of practical considerations. Due to the architecture of the CASTEP code it is more straightforward to operate on parallel architectures than Wien2k. Furthermore, the visualisation software associated with CASTEP (Accelrys’s *Materials Studio*) somewhat simplifies the construction of complex interfaces for example. There are however utility programs available to subsequently generate Wien2k input files (if care is exercised). Wien2k has an established track-record of ELNES modelling, with CASTEP having been seen to reproduce results correctly by comparison. It was not however a stated aim of the thesis to provide a physical justification for the choice of one code over the other for certain systems, nor has any such reasoning been discovered serendipitously. In this thesis work however, for large cells CASTEP has generally been chosen due to its greater reliability in parallel execution.

A persistently referred to area of potential future work has been structural energy minimisation of surfaces and interfaces, including cases in which little or no structural information is known. A potential problem – if this work is indeed carried out – is avoiding local minima being found if such as the BFGS methodology is utilised (see section 4.1). This risk can be minimised by a careful literature survey, such that the initial structure input into the DFT code is physically sensible. Furthermore, the key DFT parameters must be carefully converged against system energy variation, rather than spectra predictions for example (see section 4.3). CASTEP is known to be able to combine conventional DFT with a molecular dynamics type approach, which may also be of use in this field of work.

The introduction of a core-hole has been a major source of discussion throughout the thesis. Overall, it has been observed in this work that for free-electron metal systems, and transition metal compounds with high metallic character, a ground state calculation will provide good agreement with experiment. For certain insulating materials, ground state calculations have also shown acceptable agreement with appropriate broadening in place. However, in general for insulators and semiconductors, a core-hole calculation is required. Future work could involve different approaches to treating the core-hole, for example explicitly considering multiplet effects, or utilising a BSE approach to account for exciton pairs in certain materials classes.

10. References

Ambrosch-Draxl, C; Kouba, R; Knoll, P. 1997. First-principles band-structure calculations as a tool for the quantitative interpretation of Raman spectra of high temperature superconductors. *Z. Phys. B* **104**, 687.

Anisimov, V.I; Aryasetiawan, F; Lichtenstein, A.I. 1997. First principles calculations of the electronic structure and spectra of strongly correlated systems: The LDA + U method. *J. Phys.: Condens. Matter.* **9**, 767.

Ankudinov, A.L; Ravel, B; Rehr, J.J; Conradson, S.D. 1998. Real Space Multiple Scattering Calculation of XANES. *Phys. Rev. B* **58**, 7565.

Ankudinov, A.L; Rehr, J.J. 2000. Theory of solid state contributions to the x-ray elastic scattering amplitude. *Phys. Rev. B* **62**, 2437.

Arslan, I; Browning, N.D. 2002. Intrinsic electronic structure of threading dislocations in GaN. *Phys. Rev. B* **65**, 075310.

Atrens, A; Wang, J.Q; Stiller, K; Andren, H.O. 2006. Atom probe field ion microscope measurements of carbon segregation at an a:a grain boundary and service failures by intergranular stress corrosion cracking. *Corrosion Science* **48**, 79.

Baranova, L.A; Read, F.H; Cubric, D. 2008. Proceedings of the Seventh International Conference on Charged Particle Optics: Computer simulations of hexapole aberration correctors. *Physics Procedia* **1**, 185.

Batson, P.E; Dellby, N; Krivanek, O.L. 2002. Sub-ångstrom resolution using aberration corrected electron optics. *Nature* **418**, 617.

Bethe, H.A; Jackiw, R; Jackiw, R.W. 1997. *Intermediate quantum mechanics*. Addison-Wesley, Massachussets.

Blaha, P; Schwarz, K; Sorantin, P; Trickey, S.B. 1990. Full-potential, linearized augmented plane wave programs for crystalline systems. *Comput. Phys. Commun.* **59**, 399.

Blaha, P; Dufek, P; Schwarz, K. 1995. Electric field gradients, isomer shifts and hyperfine fields from band structure calculations in NiI_2. *Hyperf. Inter.* **95**, 257.

Blöchl, P.E; Jepsen, O; Andersen, O.K. 1994. Improved tetrahedron method for Brillouin-zone integrations. *Phys. Rev. B.* **49**, 16223.

Bogner, A; Jouneau, P-H; Thollet, G; Basset, D; Gauthier, C. 2007. A history of scanning electron microscopy developments: Towards "wet-STEM" imaging. *Micron* **38**, 390.

Boyle, W.S; Smith, G.E. 1970. Charge-coupled semiconductor devices. *Bell Labs Tech. J.* **49**, 587.

Browning, N.D; Erni, R.P; Idrobo, J.C; Ziegler, A; Kisielowski, C.F; Ritchie, R.O. 2005. High Spatial and Energy Resolution EELS using a Monochromated STEM. *Microsc. Microanal.* **11** (Suppl. 2), 1434.

Brydson, R. 2001. *Electron Energy Loss Spectroscopy*. Bios Scientific Publishers, Oxford.

Brydson, R; Scott, A.J; Brown, A. 2003. Some thoughts on source monochromation and the implications for electron energy loss spectroscopy. *Zeitschrift für Metallkunde* **94**, 277.

Buczko, R; Duscher, G; Pennycook, S.J; Pantelides, S.T. 2000. Excitonic Effects in Core-Excitation Spectra of Semiconductors. *Phys. Rev. Lett.* **85**, 2168.

Burke, K; Perdew, J.P; Ernzerhof, M. 1997. Why the Generalized Gradient Approximation Works and How to Go Beyond It. *International Journal of Quantum Chemistry* **61**, 287.

Butler, W.H; Zhang, X.G; Schulthess, T.C; MacLaren, J.M. 2001. Spin-dependent tunneling conductance of Fe|MgO|Fe sandwiches. *Phys. Rev. B* 63, 054416.

Buzea, C; Pacheco, I.I; Robbie, K. 2007. Nanomaterials and nanoparticles: Sources and toxicity. *Biointerphases* **2**, 17.

Bylander, D.M; Kleinman, L. 1996. The optimized effective potential for atoms and semiconductors. *Int. J. Mod. Phys.* **10**, 399.

Calmels, L; Mirguet, C; Kihn, Y. 2006. Evidence of alloying effects in TiC_xN_{1-x} compounds from calculated and experimental electron energy loss spectra. *Phys. Rev. B* **73**, 024207.

Clare, A.S; Nott, J.A. 1994. Scanning electron microscopy of the fourth antennular segement of Balanus amphitrite amphitrite. *Journal of the Marine Biological Association of the United Kingdom* **74**, 967.

Clark, S.J; Segall, M.D; Pickard, C.J; Hasnip, P.J; Probert, M.J; Refson, K; Payne, M.C. 2005. First principles methods using CASTEP*. Z. Kristallogr.* **220**, 567.

Colliex, C; Manoubi, T; Ortiz, C. 1991. Electron-energy-loss-spectroscopy near-edge fine structures in the iron-oxygen system*. Phys. Rev. B* **44**, 11402.

Craven, A.J; Garvie, L.A.J. 1995. Electron Energy Loss Near Edge Structure (ELNES) on the Carbon K-Edge in Transition Metal Carbides with the Rock Salt Structure. *Micros. Microanal. Microstruct.* **6**, 89.

Curtis, G.H; Silcox, J. 1971. A Wien Filter for Use as an Energy Analyzer with an Electron Microscope. *Rev. Sci. Instrum* **43**, 630.

Dadsetani, M; Titantah, J.T; Lamoen, D. 2010. Ab initio calculation of the energy-loss near-edge structure of some carbon allotropes: Comparison with n-diamond. *Diamond and Related Materials* **19**, 73.

Dellby, N; Krivanek, O.L; Nellist, P.D; Batson, P.E; Lupini, A.R. 2001. Progress in aberration-corrected scanning transmission electron microscopy. *J. Electron Microsc.* **50**, 177.

Ding, X-Z; Zeng, X.T. 2005. Structural, mechanical and tribological properties of CrAlN coatings deposited by reactive unbalanced magnetron sputtering. *Surf. Coat. Technol.* **200**, 1372.

Duscher, G; Buczko, R; Pennycook, S.J; Pantelides, S.T. 2001. Core-hole effects on energy-loss near-edge structure. *Ultramicroscopy* **86**, 355.

Egerton, R.F. 1996. *Electron Energy-Loss Spectroscopy in the Electron Microscope*, 2nd edn. Plenum Press, New York.

Egerton, R.F; Malac, M. 2005. EELS in the TEM. *J. Electron Spectrosc.* **143**, 43.

Egerton, R.F. 2009. Electron energy-loss spectroscopy in the TEM. *Rep. Prog. Phys.* **72**, 016502.

Ehiasarian, A.P; Wen, J.G; Petrov, I. 2007. Interface microstructure engineering by high power impulse magnetron sputtering for the enhancement of adhesion. *J. Appl. Phys.* **101**, 054301.

Eibler, R. 2002. Electronic structure and energetics of ordered titanium carbides of composition Ti_2C. *J. Phys.: Cond. Matter.* **14**, 4425.

El-Barbary, A.A; Trasobares, S; Ewels, C.P; Stephan, O; Okotrub, A.V; Bulusheva, L.G; Fall, C.J; Heggie, M.I. 2006. Electron spectroscopy of carbon materials: experiment and theory*. J. Phys.: Conf. Ser.* **26**, 149.

Eustace, D.A; McComb, D.W; Craven, A.J. 2010. Probing magnetic order in EELS of chromite spinels using both multiple scattering (FEFF8.2) and DFT (WIEN2k). *Micron* **41**, 547.

Fan, G.Y; Ellisman, M.H. 2000. Digital imaging in transmission electron microscopy. *J. Microscopy* **200**, 1.

Fröhlich, M; Braun, R; Leyens, C. 2006. Oxidation resistant coatings in combination with thermal barrier coatings on γ-TiAl alloys for high temperature applications. *Surf. Coat. Technol.* **201**, 3911.

Fuggle, J.C; Inglesfield, J.E. 1992. *Unoccupied Electronic States.* Springer, Berlin.

Fujikawa, T. 1983. Theory of the X-Ray Absorption Near Edge Structure (XANES) at a Deep $L_{2,3}$ Edge Studied by the Short-Range Order Multiple Scattering Theory. *J. Phys. Soc. Jpn.* **52**, 4001.

Gao, S.P; Pickard, C.J; Payne, MC; Zhu, J; Yuan, J. 2008. Theory of core-hole effects in 1*s* core-level spectroscopy of the first-row elements. *Phys. Rev. B* **77**, 115122.

Gao, S.P; Pickard, C.J; Perlov, A; Milman, V. 2009. Core-level spectroscopy calculation and the plane wave pseudopotential method. *J. Phys.: Condens. Matter* **21**, 104203.

Grogger, W; Hofer, F; Kothleitner, G; Schaffer, B. 2008. An Introduction to High-resolution EELS in Transmission Electron Microscopy. *Top. Catal.* **50**, 200.

de Groot, F. 2005. Multiplet effects in X-ray spectroscopy. *Coordination Chemistry Reviews* **249**, 31.

de Groot, F; Kotani, A. 2008. *Core Level Spectroscopy of Solids.* Taylor & Francis, London.

de Groot, F. 2009. XANES spectra of transition metal compounds. *J. Phys.: Conf. Ser.* **190**, 012004.

Guenther, R.D. 1990. *Modern Optics*. John Wiley & Sons, New York.

Guzman, L; Wolf, G.K; Davies, G.M. 2003. PVD–IBAD zinc coating development for automotive application. *Surf. Coat. Technol.* **174-175**, 665.

Haynes, P.D; Skylaris, C.-K; Mostofi, A.A; Payne, M.C. 2006. ONETEP: linear-scaling density-functional theory with local orbitals and plane waves. *phys. stat. sol. (b)* **243**, 2489.

Haynes, P.D; Mostofi, A.A; Skylaris, C.-K; Payne, M.C. 2006a. ONETEP: linear-scaling density-functional theory with plane-waves*. J. Phys.: Conf. Ser.* **26**, 143.

He, L; Vanderbilt, D. 2001. Exponential Decay Properties of Wannier Functions and Related Quantities. *Phys. Rev. Lett.* **86**, 5341.

Hébert, C; Luitz, J; Schattschneider, P. 2003. Improvement of energy loss near edge structure calculation using Wien2k. *Micron* **34**, 219.

Hecht, E. 2001. *Optics.* Addison-Wesley.

Henning, D; Ganduglia-Pirovano, M.V; Scheffler, M. 1996. Adlayer core-level shifts of admetal monolayers on transition-metal substrates and their relation to the surface chemical reactivity. *Phys. Rev. B* **53**, 10344.

Hillier, J. 1943. On Microanalysis by Electrons. *Phys. Rev.* **64**, 318.

Hillier, J; Baker, R.F. 1944. Microanalysis by Means of Electrons. *J. Appl. Phys.* 15, 663.

Hillier, J. 1946. Further improvement in the resolving power of the electron microscope. *J. App. Phys.* **17,** 307.

Hofer, F; Warbichler, P; Anderson, P.B; Pitonak, R. 1990. Investigation of Multi-Layer Coatings on Cemented Carbide Cutting Tools by Analytical Electron Microscopy. *Mikrochim. Acta.* **2**, 243.

Hohenberg, P; Kohn, W. 1964. Inhomogeneous Electron Gas. *Phys. Rev.* **136**, B864.

Holec, D; Costa, P.M.F.J; Cherns, P.D; Humphreys, C.J. 2008. A theoretical study of ELNES spectra of $Al_xGa_{1-x}N$ using Wien2k and Telnes programs. *Computational Materials Science* 44, 91.

Hovsepian, P. Eh; Lewis, D.B; Luo, Q; Münz, W.-D; Mayrhofer, P.H; Mitterer, C; Zhou, Z; Rainforth, W.M. 2005. TiAlN based nanoscale multilayer coatings designed to adapt their tribological properties at elevated temperatures. Thin Solid Films 485, 160.

Hovsepian, P. Eh; Luo, Q; Robinson, G; Pittman, M; Howarth, M; Doerwald, D; Tietema, R; Sim, W.M; Deeming, A; Zeus, T. 2006. TiAlN/VN superlattice structured PVD coatings: A new alternative in machining of aluminium alloys for aerospace and automotive components. *Surf. Coat. Technol.* **201**, 265.

Hovsepian, P. Eh; Reinhard, C; Ehiasarian, A.P. 2006a. CrAlYN/CrN superlattice coatings deposited by the combined high power impulse magnetron sputtering/unbalanced magnetron sputtering technique. *Surf. Coat. Technol.* **201**, 4105.

Hsieh, C.H; Chang, C.H; Chang, C.N; Sou, U.C; Sheu, H.S; Hsu, H.C; Yang, H.C. 2006. X-ray absorption spectroscopic study of a hot pressed MgB_2. *Solid State Commun.* **137**, 97.

Iiyoshi, R; Maruse, S. 1996. Tungsten-Point-Cathode Electron Gun Using Electron Bombardment for Cathode Tip Heating: Cathode Life and Operating

Characteristics at Cathode Temperatures above 2,800K. *J. Electron Microsc.* **45**, 128.

Ingham, B; Illy, B.N; Ryan, M.P. 2008. In situ synchrotron studies of ZnO nanostructures during electrochemical deposition. *Current Applied Physics* **8**, 455.

Ivanov, N.A; Andreeva, L.P; Gel'd; P.V. 1978. Thermal Conductivities, Electrical Resistivities, and Thermal Expansion of Titanium Carbonitrides and Oxycarbides. *Powder Metallurgy and Metal Ceramics* **17**, 613.

Jayawardane, D.N; Pickard, C.J; Brown, L.M; Payne, M.C. 2001. Cubic boron nitride: Experimental and theoretical energy-loss near-edge structure. *Phys. Rev. B* **64**, 115107.

Jhi, S-H; Ihm, J. 1997. Electronic structure and structural stability of TiC_xN_{1-x} alloys. *Phys. Rev. B* **56**, 13826.

Jiang, B; Jiang, N; Spence, J.C.H. 2003. Core-hole effects on the B K edge in MgB_2. *J. Phys.: Condens. Matter* **15**, 1299.

Jiang, N; Jiang, B; Erni, R; Browning, N.D; Spence, J.C.H. 2006. Experimental and theoretical improvements on understanding of the O K-edge of TeO_2. *Ultramicroscopy* **106**, 123.

Jorissen, K; Luitz, J; Hebert, C. 2005. A program for the calculation of Energy Loss Near Edge Structure. The new and improved TELNES.2 Code, in: D. Muller (Ed.), Enhanced Data Generated with Electrons (EDGE) Conference, TU Graz.

Kawasaki, N; Sugiyama, N; Otsuka, Y; Hashimoto, H; Tsujimoto, M; Kurata, H; Isoda, S. 2008. Energy-loss near-edge structure (ELNES) and first-principles calculation of electronic structure of nickel silicide systems. *Ultramicroscopy* **108**, 399.

Keast, V.J; Scott, A.J; Brydson, R; Williams, D.B; Bruley, J. 2001. Electron energy-loss near-edge structure – a tool for the investigation of electronic structure on the nanometre scale. *J. Microsc.* **203**, 135.

Kimoto, K; Ishizuka, K; Mizoguchi, T; Tanaka, I; Matsui, Y. 2003. The study of Al-L23 ELNES with resolution-enhancement software and first-principles calculation. *J. Electron Microsc.* **52**, 299.

Kimoto, K; Ishizuka, K; Matsui, Y. 2008. Decisive factors for realizing atomic-column resolution using STEM and EELS. *Micron* **39**, 653.

Koch, W; Holthausen, M.C. 2001. *A Chemists' Guide to Density Functional Theory*. Wiley-VCH, Weinheim.

Kohler, B; Wilke, S; Scheffler, M; Kouba, R; Ambrosch-Draxl, C. 1996. Force calculation and atomic-structure optimization for the full-potential linearized augmented plane-wave code WIEN. *Comp. Phys. Commun.* **94**, 31.

Kohn, W; Sham, L.J. 1965. Self-Consistent Equations Including Exchange and Correlation Effects. *Phys. Rev.* **140**, A1133.

Korzhavyi, P.A; Pourovskii, L.V; Hugosson, H.W; Ruban, A.V; Johansson, B. 2002. *Ab Initio* Study of Phase Equilibria in TiC_x. *Phys. Rev. Lett.* **88**, 015505.

Köstlmeier, S. 2001. Success and limits of common final-state approximations. *Ultramicroscopy* **86**, 319.

Kothleitner, G; Hofer, F. 2003. EELS performance measurements on a new high energy resolution imaging filter. *Micron* **34**, 211.

Krause, M.O; Oliver, J.H. 1979. Natural widths of atomic K and L levels, K_α X-ray lines and several KLL Auger lines. *Phys. Chem. Ref. Data* **8**, 329.

Kurata, H; Lefèvre, E; Colliex, C; Brydson, R. 1993. Electron-energy-loss near-edge structures in the oxygen K-edge spectra of transition-metal oxides*. Phys. Rev. B* **47**, 13763.

Langreth, D.C; Perdew, J.P. 1980. Theory of nonuniform electronic systems. I. Analysis of the gradient approximation and a generalization that works. *Phys. Rev. B* **21**, 5469.

Lazar, S; Hébert, C; Zandbergen, H.W. 2004. Investigation of hexagonal and cubic GaN by high-resolution electron energy-loss spectroscopy and density functional theory. *Ultramicroscopy* **98**, 249.

Lazar, P; Redinger, J; Strobl, J; Podloucky, R; Rashkova, B; Dehm, G; Kothleitner, G; Šturm, S; Kutschej, K; Mitterer, C; Scheu, C. 2008. N-K electron energy-loss near-edge structures for TiN/VN layers: an ab initio and experimental study. *Anal. Bioanal. Chem.* **390**, 1447.

Lindner, Th; Sauer, H; Engel, W; Kambe, K. 1986. Near-edge structure in electron-energy-loss spectra of MgO. *Phys. Rev. B* **33**, 22.

Liu, Z; Ximen, J. 2001. A theorem on high-order geometric spherical aberrations for Hutter's electrostatic lens. *Optik* **112**, 193.

Liu, J. 2005. Scanning transmission electron microscopy and its application to the study of nanoparticles and nanoparticle systems. *J. Electron Microsc.* **54**, 251.

Lorenzelli, N; Caudron, R; Landesman, J.P; de Novion, C.H. 1986. Influence of the ordering of carbon vacancies on the electronic properties of $TiC_{0.625}$. *Solid State Communications* **59**, 765.

Lozano-Perez, S. 2007. Multivariate Statistical Analysis of EFTEM data. *Microsc. Microanal.* **13** (Suppl. S02), 1258.

Luo, Q; Robinson, G; Pittman, M; Howarth, M; Sim, W.-M; Stalley, M.R; Leitner, H; Ebner, R; Caliskanoglu, D; Hovsepian, P.Eh. 2005. Performance of nano-structured multilayer PVD coating TiAlN/VN in dry high speed milling of aerospace aluminium 7010-T7651. *Surf. Coat. Technol.* **200**, 123.

Luo, T; Khursheed, A. 2006. Second-order aberration corrected electron energy loss spectroscopy attachment for scanning electron microscopes. *Rev. Sci. Instrum.* **77**, 043103.

Martin, R.M. 2004. *Electronic Structure: Basic Theory and Practical Methods*. Cambridge University Press, Cambridge.

Martínez, G; Tsuno, K. 2004. Design of Wien filters with high resolution. *Ultramicroscopy* **100**, 105.

Mauchamp, V; Épicier, T; Le Bossé, J.C. 2008. Application of a fully relativistic theory to the EELS investigation of anisotropy effects at the oxygen K edge in rutile and ZrO_2. *Phys. Rev. B* **77**, 235122.

Mauchamp, M; Jaouen, M; Schattschneider, P. 2009. Core-hole effect in the one-particle approximation revisited from density functional theory. *Phys. Rev. B* **79**, 235106.

Mauchamp, M; Jaouen, M; Schattschneider, P. 2009a. Core-hole effect in the one-particle approximation revisited from Density Functional Theory. EDGE Conference (Banff), private communication.

McWeeny, R. 1960. Some Recent Advances in Density Matrix Theory. *Rev. Mod. Phys.* **32**, 335.

Meyerheim, H.L; Popescu, R; Jedrecy, N; Vedpathak, M; Sauvage-Simkin, M; Pinchaux, R; Heinrich, B; Kirschner, J. 2002. Surface x-ray diffraction analysis of the MgO/Fe(001) interface: Evidence for an FeO layer. *Phys. Rev. B* **65**, 144433.

Mitterbauer, C; Hébert, C; Kothleitner, G; Hofer, F; Schattschneider, P; Zandbergen, H.W. 2004. Electron energy loss-near edge structure as a fingerprint for identifying chromium nitrides. *Solid State Comm.* **130**, 209.

Mizoguchi, T; Tanaka, I; Yoshiya, M; Oba, F; Ogasawara, K; Adachi, H. 2000. Core-hole effects on theoretical electron-energy-loss near-edge structure and near-edge x-ray absorption fine structure of MgO. *Phys. Rev. B* **61**, 2180.

Mizoguchi, T; Tatsumi, K; Tanaka, I. 2006. Peak assignments of ELNES and XANES using overlap population diagrams. *Ultramicroscopy* **106**, 1120.

Mizoguchi, T. 2009. Overlap population diagram for ELNES and XANES: peak assignment and interpretation. *J. Phys.: Condens. Matter* **21**, 104215.

Mizoguchi, T; Tanaka, I; Gao, S.P; Pickard, C.J. 2009a. First-principles calculation of spectral features, chemical shift and absolute threshold of ELNES and XANES using a plane wave pseudopotential method. *J. Phys.: Condens. Matter* **21**, 104204.

Mo, S,-D; Ching, W.Y. 2000. *Ab initio* calculation of the core-hole effect in the electron energy-loss near-edge structure. *Phys. Rev. B* **62**, 7901.

Monkhorst, H.J; Pack, J.D. 1976. Special points for Brillouin-zone integrations. *Phys. Rev. B* **13**, 5188.

Moreau, P; Boucher, F; Goglio, G; Foy, D; Mauchamp, V; Ouvrard, G. 2006. Electron energy-loss spectra calculations and experiments as a tool for the identification of a lamellar C_3N_4 compound. *Phys. Rev. B* **73**, 195111.

Muller, D.A; Singh, D.J; Silcox, J. 1998. Connections between the electron-energy-loss spectra, the local electronic structure, and the physical properties of a material: A study of nickel aluminum alloys. *Phys. Rev. B* **57**, 8181.

Muller, D.A. 2009. Structure and bonding at the atomic scale by scanning transmission electron microscopy. *Nature Materials* **8**, 263.

Müller, E.W. 1970. The atom-probe field ion microscope. *Naturwissenschaften* **57**, 222.

Münz, W.-D; Schulze, D; Hauzer, F.J.M. 1992. A new method for hard coatings: ABSTM (arc bond sputtering). *Surf. Coat. Technol.* **50**, 169.

Münz, W.-D; Lewis, D.B; Hovsepian, P. Eh; Schonjahn, C; Ehiasarian, A; Smith, I.J. 2001. Industrial scale manufactured superlattice hard PVD coatings. *Surf. Eng.* **17**, 15.

Nicholls, R.J; Scott, A.J. Practical approaches to the accurate modelling of EELS edges using density functional theory. J. Phys. : Conf. Ser. 126 (2008) 012038.

de Novion, C.H; Landesman, J.P. 1985. Order and disorder in transition metal carbides and nitrides: experimental and theoretical aspects. *Pure & Appl. Chem.* **57**, 1391.

Ogasawara, K; Iwata, T; Koyama, Y; Ishii, T; Tanaka, I; Adachi, H. Relativistic cluster calculation of ligand-field multiplet effects on cation $L_{2,3}$ X-ray absorption edges of $SrTiO_3$, NiO, and CaF_2. *Phys. Rev. B* **64** (2001) 115413.

Ohno, M. Lifetime of core two-hole states in atoms. 2005. *J. Electron. Spectrosc.* **148**, 41.

Palmer, C. 2005. *Diffraction Grating Handbook*, 6th edn. Newport Corporation.

Panjan, M; Šturma, S; Panjan, P; Čekada, M. 2007. TEM investigation of TiAlN/CrN multilayer coatings prepared by magnetron sputtering. *Surf. Coat. Technol.* **202**, 815.

Paxton, A.T; van Schilfgaarde, M; MacKenzie, M; Craven, A.J. 2000. The near-edge structure in energy-loss spectroscopy: many-electron and magnetic effects in transition metal nitrides and carbides. *J. Phys.: Condens. Matter* **12**, 729.

Paxton, A.T; Craven, A.J; Gregg, J.M; McComb, D.W. 2003. Bandstructure approach to near edge structure. *J. Microscopy* **210**, 35.

Payne, M.C; Teter, M.P; Allan, D.C; Arias, T.A; Joannopoulos, J.D. 1992. Iterative minimization techniques for ab initio total-energy calculations: molecular dynamics and conjugate gradients. *Rev. Mod. Phys.* **64**, 1045.

Pedrotti, F.L; Pedrotti, L.M; Pedrotti, L.S. 2006. *Introduction to Optics*, 3rd edn. Prentice Hall.

Perdew, J.P; Yue, W. 1986. Accurate and simple density functional for the electronic exchange energy: Generalized gradient approximation. *Phys. Rev. B* **33**, 8800.

Perdew, J.P; Burke, K; Ernzerhof, M. 1996. Generalized Gradient Approximation Made Simple. *Phys. Rev. Lett.* **77** 3865.

Perkins, J.M; Wang, Y; Shollock, B; Ardakani, M; McComb, D.W. 2007. Initial results from the first monochromated FEI Titan 80/300 in the UK. *Microsc. Microanal.* **13**, 1244.

Persson, C; Janzén, E. 1998. Electronic band structure in hexagonal close-packed Si polytypes. *J. Phys.: Condens. Matter* **10**, 10549.

Pfrommer, B.G; Côté, M; Louie, S.G; Cohen, M.L. 1997. Relaxation of Crystals with the Quasi-Newton Method. *Journal of Computational Physics* **131**, 233.

Pickard, C.J. 1997. Ph.D. Thesis, University of Cambridge.

Rainforth, W.M. 2000. Opportunities and pitfalls in characterisation of nanoscale features. *Materials Science and Technology* **16**, 1349.

Ratcliff, L; Haynes, P. 2010. Towards the calculation of experimental spectra using O(N) DFT. ONETEP Workshop (Cambridge), private communication.

Reetz, M.T; Helbig, W; Quaiser, S.A; Stimming, U; Breuer, N; Vogel, R. 1995. Visualization of Surfactants on Nanostructured Palladium Clusters by a Combination of STM and High-Resolution TEM. *Science* **20**, 367.

Rehr, J.J; Albers, R.C; Zabinsky, S.I. 1992. High-Order Multiple-Scattering Calculations of X-Ray Absorption Fine Structure. *Phys. Rev. Lett.* **69**, 3397.

Renner, Ch; Revaz, B; Genoud, J.-Y; Kadowaki, H; Fischer, Ø. 1998. Pseudogap Precursor of the Superconducting Gap in Under- and Overdoped $Bi_2Sr_2CaCu_2O_{8+\delta}$. *Phys. Rev. Lett.* **80**, 149.

Rez, P. 2006. Perfection in Theoretical Modeling of Electron Energy Loss Spectra: Is it attainable? *Microsc. Microanal.* **12** (Supp 2) 108.

Rez, P; Muller, D.A. 2008. The Theory and Interpretation of Electron Energy Loss Near-Edge Fine Structure. *Annu. Rev. Mater. Res.* **38**, 535.

Rohlfing, M; Wang, N.P; Krüger, P; Pollmann, J. 2003. Image states and excitons at insulator surfaces with negative electron affinity. *Phys. Rev. Lett.* **91**, 256802.

Ross, I.M; Rainforth, W.M; Seabourne, C.R; Scott, A.J; Wang, P; Mendis, B.G; Bleloch, A.L; Reinhard, C; Hovsepian, P. Eh. 2010. Nano-scale electron energy loss spectroscopy of CrAlYN/CrN – CrAlY(O)N/Cr(O)N multilayer coatings deposited by unbalanced magnetron sputtering. *Thin Solid Films* **518**, 5121.

Ruska, E. 1943. The origin of fringes about particles in electron microscope images and their change with focus. *Kolloid Zeits.* **105**, 43.

Scherzer, O. 1936. Über einige Fehler von Elektronenlinsen (About some of the errors in electron-lenses). *Z. Phys. A-Hadron Nucl.* **101**, 593.

Schonhense, G; Elmers, H.J; Nepijko, S.A; Schneider, C.M. 2006. Time-resolved Photoemission Electron Microscopy, in *Advances in Imaging and Electron Physics* (edited by P.W.Hawkes) **142**, 159.

Schwarz, K; Blaha, P; Madsen, G.K.H. 2002. Electronic structure calculations of solids using the WIEN2k package for material sciences. *Comp. Phys. Comm.* **147**, 71.

Scott, A.J; Brydson, R; MacKenzie, M; Craven, A.J. 2001. Theoretical investigation of the ELNES of transition metal carbides for the extraction of structural and bonding information. *Phys. Rev. B* **63**, 245105.

Scott, J; Thomas, P.J; MacKenzie, M; McFadzean, S; Wilbrink, J; Craven, A.J; Nicholson, P.A.W. 2008. Near-simultaneous dual energy range EELS spectrum imaging. *Ultramicroscopy* **108**, 1586.

Seabourne, C.R; Scott, A.J; Brydson, R; Nicholls, R.J. 2009. A systematic approach to choosing parameters for modelling fine structure in electron energy-loss spectroscopy. *Ultramicroscopy* **109**, 1374.

Seabourne, C.R; Scott, A.J; Vaughan, G; Brydson, R; Wang, S.G; Ward, R.C.C; Wang, C; Kohn, A; Mendis, B; Petford-Long, A.K. 2010. Analysis of computational EELS modelling results for MgO-based systems. *Ultramicroscopy* **110**, 1059.

Seabourne, C.R; Ross, I.M; Rainforth, W.M; Scott, A.J; Mendis, B.G; Hovespian, P. Eh. 2010a. EELS and ELNES studies of nano-scale nitride multilayers deposited by unbalanced magnetron sputtering. *J. Phys.: Conf. Ser.* **241**, 012046.

Seah, M.P; Dench, W.A. 1979. Quantitative electron spectroscopy of surfaces: A standard data base for electron inelastic mean free paths in solids. *Surf. Interface Anal.* **1**, 2.

Segall, M.D; Lindan, P.L.D; Probert, M.J; Pickard, C.J; Hasnip, P.J; Clark, S.J; Payne, M.C. 2002. First principles methods using CASTEP. *J. Phys-Condens. Mat.* **14**, 2717.

Seidman, D.N. 2007. Three-Dimensional Atom-Probe Tomography: Advances and Applications. *Annu. Rev. Mater. Res.* **37**, 127.

Serin, V; Andrieu, S; Serra, R; Bonell, F; Tiusan, C; Calmels, L; Varela, M; Pennycook, S.J; Snoeck, E; Walls, M; Colliex, C. 2009. TEM and EELS measurements of interface roughness in epitaxial Fe/MgO/Fe magnetic tunnel junctions. *Phys. Rev. B* **79**, 144413.

Shin, C.-S; Gall, D; Hellgren, N; Patscheider, J; Petrov, I; Greene, J.E. 2003. Vacancy hardening in single-crystal TiN_x(001) layers. *Journal of Applied Physics* **93**, 6025.

Skylaris, C.-K; Haynes, P.D; Mostofi, A.A; Payne, M.C. 2005. Introducing ONETEP: Linear-scaling density functional simulations on parallel computers. *J. Chem. Phys.* **122**, 084119.

Smart, L.E; E.A. Moore. 2005. Solid State Chemistry: An Introduction. CRC Press: Florida.

Smolik, J; Zdunek, K. 1999. Effect of interlayer composition on the tribological properties of TiC/Ti(C_x, N_{1-x})/TiN anti-abrasive multi-layer coatings. *Vacuum* **55**, 147.

Storms, E.K. 1967. *The Refractory Carbides.* Academic Press, New York.

Su, D.S; Hébert, C; Willinger, M; Schlögl, R. 2003. Anisotropy and collection angle dependence of the oxygen K ELNES in V_2O_5: a band-structure calculation study. *Micron* **34**, 227.

Svane, A; Gunnarsson, O. 1990. Transition-metal oxides in the self-interaction-corrected density functional formulism. *Phys. Rev. Lett.* **65**, 1148.

Tamboli, S.H; Patil, R.B; Kamat, S.V; Puri, V; Puri, R.K. 2009. Modification of optical properties of MgO thin films by vapour chopping. *J. Alloys Compd.* **477**, 855.

Tanaka, I; Mizoguchi, T; Yoshiya, M; Ogasawara, K; Adachi, H; Mo, S-D; Ching, W.Y. 2003. First principles calculation of ELNES by LCAO methods. *J. Electron Microsc.* **51**, 107.

Tanaka, I; Mizoguchi, T. 2009. First-principles calculations of x-ray absorption near edge structure and energy loss near edge structure: present and future *J. Phys.: Condens. Matter* **21**, 104201.

Tashmetov, M. Yu; Em, V.T; Lee, C.H; Shim, H.-S; Choi, Y.-N; Lee, J.-S. 2002. Neutron diffraction study of the ordered structures of nonstoichiometric titanium carbide. *Physica B: Condensed Matter* **311**, 318.

Terauchi, M; Tanaka, M; Tsuno, K; Ishida, M. 1999. Development of a high energy resolution electron energy-loss spectroscopy microscope. *J. Microscopy* **194**, 203.

Tönshoff, K; Karpuschewski, B; Mohlfeld, A; Leyendecker, T; Erkens, G; Fuß, H.G; Wenke, R. 1998. Performance of oxygen-rich TiALON coatings in dry cutting applications. *Surf. Coat. Technol.* **108-109**, 535.

Tortonese, M; Barrett, R.C; Quate, C.F. 1993. Atomic resolution with an atomic force microscope using piezoresistive detection. *Appl. Phys. Lett.* **62**, 834.

Trebbia, P; Mory, C. 1990. EELS elemental mapping with unconventional methods II. Applications to biological specimens. *Ultramicroscopy* **34**, 179.

Tsujimoto, M; Kurata, H; Nemoto, T; Isoa, S; Terada, S; Kaji. K. 2005. Influence of nitrogen vacancies on the N K-ELNES spectrim of titanium nitride. *J. Electron Spectrosc.* **143**, 159.

Urban, K.W. 2008. Studying Atomic Structures by Aberration-Corrected Transmission Electron Microscopy. *Science* **321**, 506.

Wang, C; Wang, S; Kohn, A; Ward, R.C.C; Petford-Long, A.K. 2007. Transmission Electron Microscopy Study of the Fe(001) MgO(001) Interface for Magnetic Tunnel Junctions. *IEEE Trans. Magn.* **43**, 2779.

Wang, S.G; Ward, R.C.C; G.X Du, X.F. Han, C. Wang, A. Kohn. 2008. Temperature dependence of giant tunnel magnetoresistance in epitaxial Fe/MgO/Fe magnetic tunnel junctions. *Phys. Rev. B* **78**, 180411.

Welford, W.T. 1986. *Aberrations of Optical Systems: (The Adam Hilger Series On Optics & Optoelectronics).* Taylor & Francis Ltd, New York.

Weng, X; Rez, P. 1989. Multiple-scattering approach to oxygen K near-edge structures in electron-energy-loss spectroscopy of alkaline earths. *Phys. Rev. B* **39**, 7405.

Wollschläger, J; Viernow, J; Tegenkamp, C; Erdös, D; Schröder, K.M; Pfnür, H. 1999. Stoichiometry and morphology of MgO films grown reactively on Ag(100). *Appl. Surf. Sci.* **142**, 129.

Yang, S; Wiemann, E; Teer, D.G. 2004. The properties and performance of Cr-based multilayer nitride hard coatings using unbalanced magnetron sputtering and elemental metal targets. *Surf. Coat. Technol.* **188-189**, 662.

Yuasa, S; Nagahama, T; Fukushima, A; Suzuki, Y; Ando, K. 2004. Spin-Polarized Resonant Tunneling in Magnetic Tunnel Junctions. *Nature Mater.* **3**, 868.

Zhang, Y; Holzwarth, N.A.W. 1998. Electronic band structures of the scheelite materials $CaMoO_4$, $CaWO_4$, $PbMoO_4$, and $PbWO_4$. *Phys. Rev.* **57**, 12738.

Zhou, Z; Rainforth, W.M; Lewis, D.B; Creasy, S; Forsyth, J.J; Clegg, F; Ehiasarian, A.P; Hovespian, P. Eh; Münz, W.-D. 2004. Oxidation behaviour of nanoscale TiAlN/VN multilayer coatings. *Surf. Coat. Technol.* **177-178**, 198.

Zhu, J; Gao, S.P; Zhang, A.H; Yuan, J. 2005. Theoretical electron energy-loss spectroscopy and its application in materials research. *J. Electron Micros.* **54**, 293.

Zhu, J; Zhao, D; Luo, W.B; Zhang, Y; Li, Y.R. 2008. Epitaxial growth of cubic AlN films on $SrTiO_3$ (100) substrates by pulsed laser deposition. *Journal of Crystal Growth* **310**, 731.

Zueva, L.V; Lipatnikov, V.N; Gusev, A.I. 2000. Ordering Effects on the Microstructure and Microhardness of Nonstoichiometric Titanium Carbide TiC_y. *Inorganic Materials* **36**, 695.

11. Appendix

11.1 Prizes and awards won during PhD studies

1) 2007 - Present. Frank Parkinson Scholar, University of Leeds.

    - £8000 per annum scholarship for PhD study in the Institute for Materials Research.
    - Based on undergraduate achievements and future potential.

2) September 2009. Institute of Physics grant.

    - Grant of £185 to attend the Electron Microscopy and Analysis Group (EMAG) Conference, Sheffield.

3) March 2009. Institute of Materials, Minerals and Mining award.

    - Award of £100 for winning the Leeds Bradford Materials Society Young Persons' Lecture contest.

4) June 2008. European Microscopy Society grant.

    - Grant of over £200 obtained to assist with presentation of research at the European Microscopy Congress, Aachen 2008.

11.2 Conferences and funding during PhD studies

1) November 2009. Invited Lecture, Queen's University Belfast.

    - National Grid Service computing facility: invite to speak about computational electron microscopy in Belfast.

2) September 2009. EMAG 2009 conference, Sheffield.

    - Leading UK conference on electron microscopy.
    - Gave an oral presentation which was well received.

3) May 2009. Enhanced Data Generated by Electrons (EDGE) conference, Banff, Canada.

    - Held every four years this is the major conference in the field of EELS in particular.
    - I presented a poster that stimulated wide-ranging discussion.

4) April 2009. ‘Realising the potential’ conference in Electron Microscopy, Imperial College London.
    - Major topics – EELS, imaging techniques and modelling.
5) January 2009. Institute of Materials, Minerals and Mining Literature Review Competition.
    - Reached the final six in the competition.
    - Attended a masterclass in London on scientific writing.
6) September 2008. European Microscopy Congress, Aachen.
    - Presented a successful poster, and obtained several useful contacts.
7) July 2008. HECToR computing service resource allocation.
    - Awarded 100,000 units of computing time on the HECToR high performance computing facility.
    - Estimated financial value of this award is in excess of £5000.
    - HECToR is arguably the UK’s leading high performance computing service.
8) December 2007. National Grid Service computing resource allocation.
    - Awarded 5000 (increased to over 400,000) hours of computing time on the National Grid Service network.